Lehrstuhl für Kommunikation und Navigation

Enhanced Sensitivity for Galileo and GPS Receivers

Andreas Schmid

Vollständiger Abdruck der von der Fakultät für Elektrotechnik und Informationstechnik der Technischen Universität München zur Erlangung des akademischen Grades eines

Doktor–Ingenieurs

genehmigten Dissertation.

Vorsitzender:		.....
Prüfer der Dissertation:	1.	.....
	2.	.....
	3.	.....

Die Dissertation wurde am ..... bei der Technischen Universität München eingereicht und durch die Fakultät für Elektrotechnik und Informationstechnik am ..... angenommen.

Acknowledgements

To a casual observer, a doctoral dissertation may appear to be solitary work. However, to complete a project of this magnitude requires a network of support, and I am indebted to many people.

This dissertation could not have been written without Prof. Dr. sc. nat. Christoph Günther who not only served as my supervisor but also encouraged and challenged me throughout the project. He patiently guided me through the thesis process, never accepting less than my best efforts. I am grateful in every way and hope to keep our collaboration in the future.

A special thanks goes to my co-supervisor Prof. Dr.-ir. A. J. Han Vinck for his time and effort. I am grateful that in the midst of all his activities he accepted to be a member of my examination committee.

Infineon Technologies AG has provided the funding, support, and equipment I have needed to produce and complete my thesis. Thanks to all my colleagues at Infineon for providing an inspiring working atmosphere. Prof. Dr.-Ing. André Neubauer deserves special mention for making this a personally and professionally rewarding experience.

Most importantly, I thank my wife, Shri, for her unconditional love and understanding throughout the countless evenings of writing this dissertation. Finally, I want to thank my parents, Franz and Renate, for all their support.

Duisburg, January 2007 Andreas Schmid

Abstract

The success of satellite navigation in the mass consumer market will depend greatly on the service availability in urban canyons and moderate indoor environments. In order to meet these requirements the reception sensitivity of GPS and Galileo receivers will have to be substantially enhanced. This thesis introduces new ranging techniques that have been shown to improve the reception sensitivity and positioning accuracy of GPS and Galileo receivers. These can be implemented with low complexity and in addition to existing methods. The sensitivity enhancements are based on differential correlation techniques that utilize the statistical properties of Galileo/GPS signals and also permit the estimation of important signal parameters with low complexity. The probability density functions of the signals are algebraically derived at each processing step. Extensive simulations are provided to analyze the performance of the algorithms and architectures developed for this theses.

All techniques presented rely on the *differential correlation* which serves as a replacement for the state-of-the-art noncoherent integration. The differential correlation improves the reception sensitivity and positioning accuracy since it multiplies statistically independent signal samples, while noncoherent integration squares identical samples. In order to mitigate the limiting effect of the out-of-phase autocorrelation values, a mechanism is devised to adapt the detection threshold as a function of the statistical properties of the differential correlation. The differential correlation provides an elegant way to estimate the residual Doppler frequency offset with very little effort. This in turn allows for the incremental reduction of the frequency offset during the differential correlation process, leading to a further increase in reception sensitivity and positioning accuracy. The frequency adjustment causes phase fluctuations in the differential correlation function, which are compensated by another mechanism. As a result, the major part of the correlation power is accumulated in the inphase component, which can then be leveraged for simplified receiver architectures with reduced implementation expenses. The reduced frequency offset furthermore allows for an incremental extension of the coherent integration intervals during the differential correlation process. The combined benefit of these techniques is a Galileo/GPS receiver which enhances the reception sensitivity by up to 17.3 dB and increases the range measurement accuracy by up to 483 % as compared to the noncoherent integration.

Contents

Chapter 1

Introduction

The Global Positioning System (GPS) has become the prerequisite for a wide range of applications. Many emerging applications of GPS require positioning in deep urban and moderate indoor environments. Current GPS receivers only provide limited service availability in these environments. This thesis aims at improving the situation with new signal estimation techniques targeted to enhance the positioning availability and accuracy in urban and indoor environments.

The key to increasing the availability is enhancing the reception sensitivity. The attenuation, shadowing, and multipath fading effects in urban canyons and indoor areas frequently degrade the received GPS signal power by 30 dB or more [1, 2, 3]. While the minimum reception levels for indoor coverage of GSM and UMTS mobile phones are specified as -102 dBm and -117 dBm respectively, Galileo and GPS signals with 30 dB attenuation have around -158 dBm signal power [1] [4, 5].

Chapter 2 summarizes the current techniques for GPS reception with enhanced sensitivity. The reception sensitivity of a Galileo/GPS receiver can generally be increased by extending the observation period and thus collecting more signal energy. Doubling the coherent integration time potentially increases the reception sensitivity by around 3 dB. However, the maximum coherent integration period is limited by the residual frequency deviation, the stability of the local oscillator, and the coherence time of the propagation channel. The state-of-the-art technique to further enhance the reception sensitivity is noncoherent integration, which can extend the observation period indefinitely without further limiting the frequency deviation. The squaring process of the noncoherent integration, however, increases the noise level and hence yields an inferior sensitivity gain. Doubling the noncoherent integration period increases the reception sensitivity only by around 1.5 dB.

Chapter 3 introduces the differential correlation technique. It can also extend the observation period indefinitely without having to reduce the residual frequency deviation. Differential correlation multiplies statistically independent noise samples instead of squaring them. The noise level is hence not being raised as much as by the squaring process of the noncoherent integration. The resulting sensitivity gain of the differential correlation technique versus

[1] signal power C in dBm refers to $C = 10\log(\tilde{C}/(1\,\mathrm{mW}))$, where $\tilde{C}$ is the power measured in W.

the noncoherent integration method is algebraically derived and verified by simulations using GPS and Galileo signals in the L1/E1 frequency band. Differential correlation furthermore yields a positioning accuracy improvement, which is also algebraically derived and verified by simulations using L1/E1 GPS and Galileo signals.

In order to fully leverage the potential of enhanced sensitivity Galileo/GPS reception in highly dynamic environments, a technique to adaptively adjust the detection threshold is required. Chapter 4 derives such a mechanism, which yields a substantial sensitivity improvement.

The differential correlation technique furthermore provides an elegant way to estimate the residual frequency offset between the received signal and the down-conversion frequency. Chapter 5 utilizes this property to introduce a technique to estimate and adaptively correct the residual frequency offset. The benefit is not only a gain in reception sensitivity, but an improvement in positioning accuracy as well.

The adaptive correction of the residual frequency offset, however, introduces phase fluctuations within the differential correlation process. Chapter 6 presents a technique to compensate for these fluctuations with the merit of further enhancing reception sensitivity and positioning accuracy.

Since the residual frequency derivation is incrementally reduced, it is furthermore possible to iteratively increase the coherent integration time. Chapter 7 hence presents a mechanism, which dynamically adjusts the coherent integration period once the residual frequency deviation is sufficiently low. This process increases reception sensitivity and positioning accuracy even more.

Satellite navigation, in deep urban and moderate indoor environments, not only has to address the signal attenuation but also the multipath fading effects. In a standard Galileo/GPS receiver architecture, the multipath fading might result in excessive false acquisitions. In order to suppress this behavior, Chapter 8 extends the adaptation technique of Chapter 4 to dynamically adjust the detection threshold as a function of both the signal-to-noise ratio and the fading characteristics. It is shown to reduce the false acquisition probability to the desired level.

Finally, the appendix presents some details of a microchip design with the differential correlation technique. The appendix compares the quantization noise, silicon area, and power consumption of differential correlation versus noncoherent integration.

The relevance of this work has its roots in the rising demand for mobile phone positioning. Almost all wireless carriers are planning to implement location based services in order to participate in the predicted multi-billion dollar market [6, 7, 8]. Moreover, virtually all manufacturers of mobile phones have decided to utilize satellite navigation [9, 10, 11].

Chapter 2

Known Methods to Enhance Sensitivity

The reception sensitivity of a Galileo/GPS receiver is usually defined as the minimum signal power required to achieve a certain probability of detection. Positioning, in deep urban and moderate indoor environments, requires increased sensitivity due to signal attenuation by walls and ceilings, shadowing by buildings, and multipath fading caused by reflections [3, 12, 13]. This chapter summarizes state-of-the-art techniques to enhance reception sensitivity. All but one of the presented methods serve as a foundation and will be incorporated in the new approaches described later on. The noncoherent integration method, however, will be replaced by techniques based on differential correlation. It serves as reference to quantify the sensitivity gain of the new developments.

2.1 Assisted Satellite Navigation

Aiding the satellite navigation with assistance data can improve reception sensitivity substantially. Assistance protocols are specified for most mobile communication standards [14, 15, 16]. Reference receivers continuously track all satellite signals and maintain a database of relevant signal parameters. The entire navigation data messages of the satellite signals can then be supplied via the wireless communications link, such that the Assisted-Galileo/GPS receiver only needs to perform signal acquisition [17, 18]. The subsequent signal tracking for the navigation messages becomes redundant.

The receiver only needs to estimate the spreading code phases so that its location can be calculated with the help of assistance data [19, 20]. This method substantially reduces the power consumption, another key requirement for emerging Galileo/GPS applications [21, 22]. The acquisition search space and thereby the acquisition time is also reduced by a narrower Doppler frequency uncertainty. Longer coherent integration times, which yield higher reception sensitivities at the expense of narrower frequency search bins, are also possible with good Doppler frequency estimates. The supplied navigation data messages also allow observation times in excess of the data bit period, effectively improving the reception

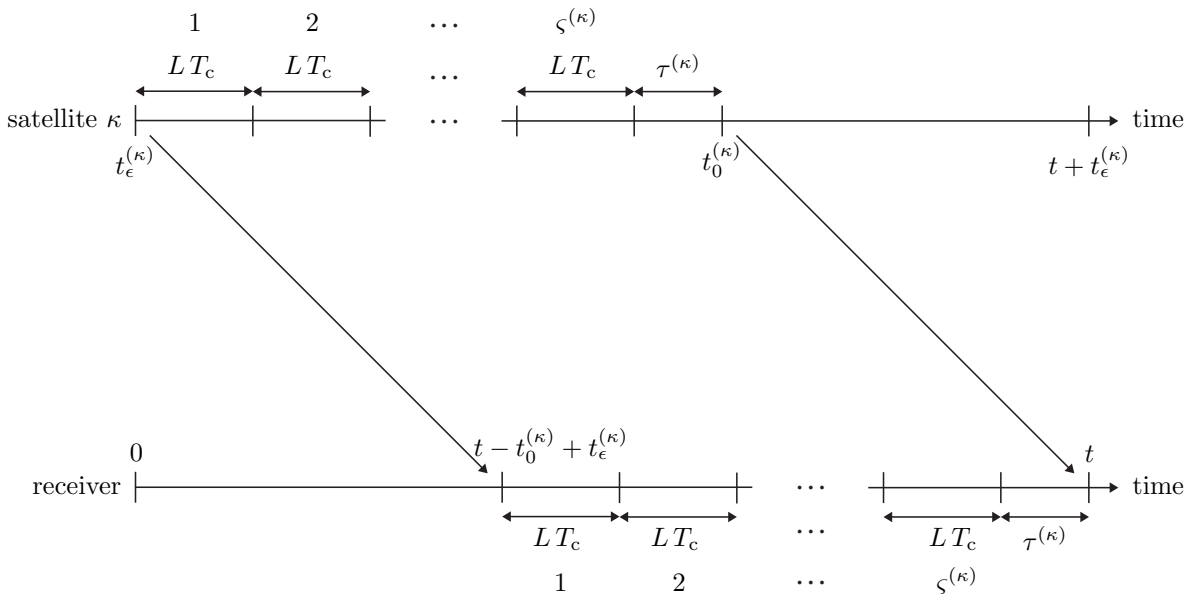

Figure 2.1: Satellite and receiver time lines for single shot positioning.

sensitivity. The increased reception sensitivity allows the reception of more satellite signals, which in turn improves the positioning accuracy.

2.2 Single Shot Positioning

Assisted satellite navigation enables single shot positioning by providing the navigation message via a communications link. Single shot positioning as opposed to conventional positioning works with just signal acquisition and no signal tracking [19, 20]. The time-consuming signal tracking until the ephemeris and almanac data are received can be skipped to reduce power consumption and positioning latency. Strongly attenuated signals also do not permit navigation message extraction, since the observation period has to be increased beyond the data bit boundaries [21, 23]. Assisted satellite navigation combined with single shot positioning hence allows positioning with increased observation times, which yields enhanced reception sensitivity [24].

Without loss of generality, it shall be assumed that all signals are received simultaneously at time t. When the receiver only estimates the code phase without tracking the signal, the transmission time $t_0^{(\kappa)}$ of the received signal remains unknown. The index $\kappa \in \{1, \ldots K_\mathrm{S}\}$ represents the different visible satellites and K_S the number of visible satellites. Fig. 2.1 illustrates time lines at a satellite and the receiver. The transmission time can be expressed as an integer multiple $\varsigma^{(\kappa)} \in \mathbb{Z}$ of the spreading code period $L\,T_\mathrm{c}$ plus the code phase $\tau^{(\kappa)}$ and the clock difference between satellite and system time $t_\epsilon^{(\kappa)}$

$$t_0^{(\kappa)} = \varsigma^{(\kappa)}\,L\,T_\mathrm{c} + \tau^{(\kappa)} + t_\epsilon^{(\kappa)}\ . \tag{2.1}$$

The spreading code length is denoted by L and the spreading chip period by T_c. When the signal is transmitted from the satellite at time $t_0^{(\kappa)}$, the code phase $\tau^{(\kappa)}$ has an arbitrary value. However, when the signal is received later at time t, the code phase still has the same value

$\tau^{(\kappa)}$. Each satellite clock difference $t_\epsilon^{(\kappa)}$ relative to the system time t is supplied as assistance data. The distance between the receiver location $\mathbf{p}_\mathrm{r} \in \mathbb{R}^3$ and each satellite location $\mathbf{p}_\mathrm{s}^{(\kappa)} \in \mathbb{R}^3$ can be expressed as

$$\rho^{(\kappa)} = \left\| \mathbf{p}_\mathrm{s}^{(\kappa)} - \mathbf{p}_\mathrm{r} \right\|_2 = \mathrm{c} \left(t - t_0^{(\kappa)} \right) , \tag{2.2}$$

where c is the speed of light and $\| \cdot \|_2$ the EUCLIDIAN norm.

An approximate location $\mathbf{p}_\mathrm{a} \in \mathbb{R}^3$ and time t_a can be supplied with the assistance data and utilized to calculate the integer multiple $\varsigma^{(\kappa)}$. Solving (2.2) and (2.1) for $\varsigma^{(\kappa)}$ yields

$$\varsigma^{(\kappa)} = \frac{1}{L\,T_\mathrm{c}} \left(t_0^{(\kappa)} - \tau^{(\kappa)} - t_\epsilon^{(\kappa)} \right) = \frac{1}{L\,T_\mathrm{c}} \left(t - \frac{\rho^{(\kappa)}}{\mathrm{c}} - \tau^{(\kappa)} - t_\epsilon^{(\kappa)} \right) . \tag{2.3}$$

Inserting the approximate distance between each satellite and the receiver

$$\rho^{(\kappa)} \simeq \left\| \mathbf{p}_\mathrm{s}^{(\kappa)} - \mathbf{p}_\mathrm{a} \right\|_2 , \tag{2.4}$$

as well as the approximate time

$$t \simeq t_\mathrm{a} \tag{2.5}$$

into (2.3) and rounding to the nearest integer, denoted by $\langle \cdot \rangle$, resolves the ambiguity

$$\boxed{\varsigma^{(\kappa)} = \left\langle \frac{1}{L\,T_\mathrm{c}} \left(t_\mathrm{a} - \frac{\left\| \mathbf{p}_\mathrm{s}^{(\kappa)} - \mathbf{p}_\mathrm{a} \right\|_2}{\mathrm{c}} - \tau^{(\kappa)} - t_\epsilon^{(\kappa)} \right) \right\rangle} . \tag{2.6}$$

The tolerable errors for the approximate location and time are

$$\left| t_\mathrm{a} - \frac{\left\| \mathbf{p}_\mathrm{s}^{(\kappa)} - \mathbf{p}_\mathrm{a} \right\|_2}{\mathrm{c}} - t + \frac{\rho^{(\kappa)}}{\mathrm{c}} \right| < \frac{L\,T_\mathrm{c}}{2} . \tag{2.7}$$

Since $\mathrm{c}\,L\,T_\mathrm{c}$ equals 300 km for the GPS L1-C/A code, the cell location of the mobile phone and an approximate time with some 100 μs accuracy is already sufficient. This timing accuracy can be provided by most cellular communication networks [25]. The longer Galileo spreading codes yield further relaxed requirements on the approximate location and time. A sufficiently accurate approximate time t_a can also be obtained if just one satellite signal is strong enough to align the navigation message from the assistance data with the navigation message from the satellite signal.

The precise system time t is typically unknown. If $K_\mathrm{S} \geqslant 4$ satellites are visible, the receiver position $\mathbf{p}_\mathrm{r}$ and time t can be estimated with the nonlinear Weighted Least Square Error (WLSE) estimation

$$\begin{aligned} \left(\widehat{\mathbf{p}}_\mathrm{r},\, \widehat{t}\, \right) &= \underset{\substack{\widehat{\mathbf{p}}_\mathrm{r} \in \mathbb{R}^3 \\ \widehat{t} \in \mathbb{R}}}{\operatorname{argmin}} \sum_{\kappa=1}^{K_\mathrm{S}} \frac{1}{\sigma^2_{\widehat{\rho}^{(\kappa)}}} \left(\widehat{\rho}^{(\kappa)} - \left\| \mathbf{p}_\mathrm{s}^{(\kappa)} - \widehat{\mathbf{p}}_\mathrm{r} \right\|_2 \right)^2 \\ &= \underset{\substack{\widehat{\mathbf{p}}_\mathrm{r} \in \mathbb{R}^3 \\ \widehat{t} \in \mathbb{R}}}{\operatorname{argmin}} \sum_{\kappa=1}^{K_\mathrm{S}} \frac{1}{\sigma^2_{\widehat{\rho}^{(\kappa)}}} \left(\mathrm{c} \left(\widehat{t} - t_0^{(\kappa)} \right) - \left\| \mathbf{p}_\mathrm{s}^{(\kappa)} - \widehat{\mathbf{p}}_\mathrm{r} \right\|_2 \right)^2 \end{aligned} \tag{2.8}$$

$$\boxed{\left(\widehat{\mathbf{p}}_\mathrm{r},\, \widehat{t}\, \right) = \underset{\substack{\widehat{\mathbf{p}}_\mathrm{r} \in \mathbb{R}^3 \\ \widehat{t} \in \mathbb{R}}}{\operatorname{argmin}} \sum_{\kappa=1}^{K_\mathrm{S}} \frac{1}{\sigma^2_{\widehat{\rho}^{(\kappa)}}} \left(\mathrm{c} \left(\widehat{t} - \varsigma^{(\kappa)}\, L\, T_\mathrm{c} - \tau^{(\kappa)} - t_\epsilon^{(\kappa)} \right) - \left\| \mathbf{p}_\mathrm{s}^{(\kappa)} - \widehat{\mathbf{p}}_\mathrm{r} \right\|_2 \right)^2} .$$

The variance of the estimated satellite to receiver distance is denoted by $\sigma^2_{\widehat{\rho}^{(\kappa)}}$ and can be estimated by the receiver, e.g. with signal-to-noise ratio measurements [26]. The receiver time $\widehat{t}$ and location $\widehat{\mathbf{p}}_\mathrm{r}$ are calculated with (2.8). The integer multiples $\varsigma^{(\kappa)}$ are calculated with (2.3). The satellite clock differences $t_\epsilon^{(\kappa)}$ and the satellite locations $\mathbf{p}_\mathrm{s}^{(\kappa)}$ are supplied with the assistance data. The only task left for the Assisted-Galileo/GPS receiver is hence to estimate the code delays $\tau^{(\kappa)}$ [19, 20]. In order to provide high high availability for emerging applications in urban environments, the code phase estimations have to be performed for low signal-to-noise ratios. The more code delays can be estimated, the more accurate the position fix.

2.3 Highly Parallel Correlation

The code phase $\tau^{(\kappa)}$ can be approximated as uniformly distributed within $[0,\, L\,T_\mathrm{c}]$. If the received thermal noise is additionally modelled as white Gaussian noise, the Minimum Mean Squared Error (MMSE) estimation

$$\widehat{\tau}^{(\kappa)} = \underset{\widehat{\tau}^{(\kappa)}\in[0,\,L\,T_\mathrm{c}]}{\operatorname{argmin}} \int_0^{T_\mathrm{i}} \left| r(t) - x^{(\kappa)}\big(t-\widehat{\tau}^{(\kappa)}\big)\right|^2 dt \tag{2.9}$$

corresponds to the Maximum A Posteriori (MAP) and the Maximum Likelihood (ML) estimation [27, 28]. The coherent integration time T_i is usually a multiple of $L\,T_\mathrm{c}$. The received Galileo/GPS signal is expressed by $r(t)$ and a local replica of the transmitted signal by $x^{(\kappa)}(t)$.

The ML estimation of the code phase can be achieved by maximizing the correlation

$$\begin{aligned}\widehat{\tau}^{(\kappa)} &= \underset{\widehat{\tau}^{(\kappa)}\in[0,\,L\,T_\mathrm{c}]}{\operatorname{argmin}} \int_0^{T_\mathrm{i}} |r(t)|^2 - 2\,\Re\big\{r(t)\,x^{*(\kappa)}\big(t-\widehat{\tau}^{(\kappa)}\big)\big\} + \left|x^{(\kappa)}\big(t-\widehat{\tau}^{(\kappa)}\big)\right|^2 dt \\ &= \underset{\widehat{\tau}^{(\kappa)}\in[0,\,L\,T_\mathrm{c}]}{\operatorname{argmax}} \int_0^{T_\mathrm{i}} \Re\big\{r(t)\,x^{*(\kappa)}\big(t-\widehat{\tau}^{(\kappa)}\big)\big\}\, dt\end{aligned} \tag{2.10}$$

of the received signal $r(t)$ with the complex conjugate of the locally generated replica of the signal $x^{*(\kappa)}\big(t-\widehat{\tau}^{(\kappa)}\big)$ [27, 28]. If the received signal phase is assumed to be random and uniformly distributed, and the thermal noise is modelled as zero-mean white Gaussian noise, then the optimal estimation evaluates the magnitude or the squared magnitude of the correlation [27, 28]

$$\boxed{\widehat{\tau}^{(\kappa)} = \underset{\widehat{\tau}^{(\kappa)}\in[0,\,L\,T_\mathrm{c}]}{\operatorname{argmax}} \left| \int_0^{T_\mathrm{i}} r(t)\,x^{*(\kappa)}\big(t-\widehat{\tau}^{(\kappa)}\big)\, dt\right|^2}. \tag{2.11}$$

The squared magnitude usually causes less implementation expense.

The spreading code length of the GPS L1-C/A signal is 1023 chips. The GPS orbits at an altitude of 20,183 km combined with the carrier frequency of $f_\mathrm{c} = 1575.42$ MHz cause Doppler frequency shifts in the range of approximately ± 6 kHz [29]. Fig. 2.2 and 2.3 illustrate the code/frequency search space for the GPS L1-C/A signal. Fig. 2.2 shows the

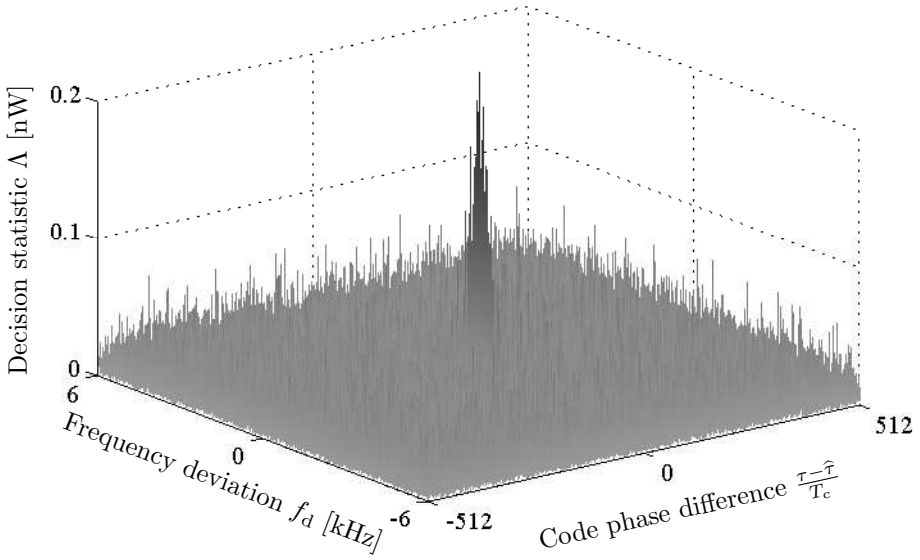

Figure 2.2: GPS L1-C/A search space for 2 dB signal attenuation and $T_\mathrm{i} = 1\,\mathrm{ms}$.

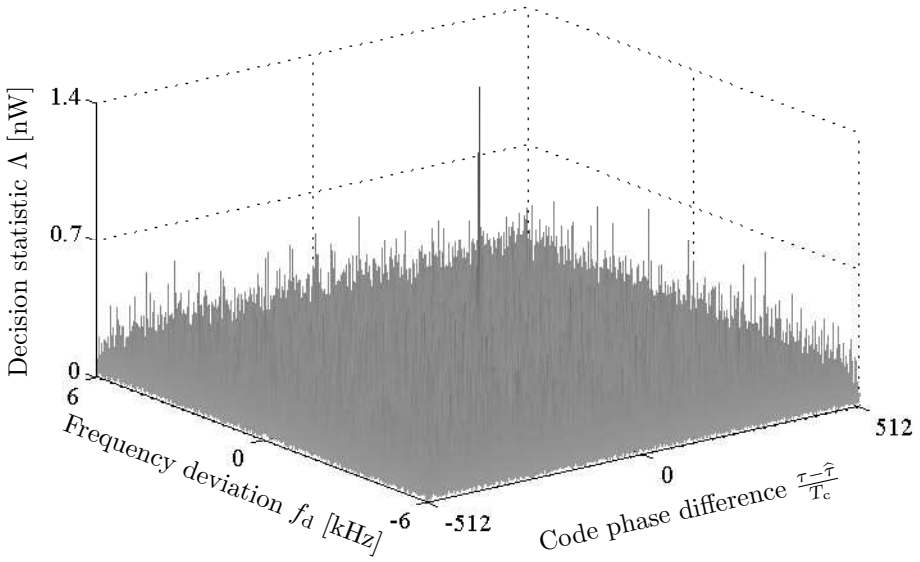

Figure 2.3: GPS L1-C/A search space for 11 dB signal attenuation and $T_\mathrm{i} = 8\,\mathrm{ms}$.

search space for the short coherent integration period $T_\mathrm{i} = 1\,\mathrm{ms}$ and just 2 dB signal attenuation. Doubling the coherent integration interval potentially increases the reception sensitivity by 3 dB. Fig. 2.3 shows the search space for a signal that is 11 dB attenuated. In order to achieve the sensitivity enhancement of $3 \times 3\,\mathrm{dB}$, the coherent integration period in Fig. 2.3 has been doubled three times to $T_\mathrm{i} = 8\,\mathrm{ms}$. It can be observed that the correlation peak is separated from the noise floor by a similar distance. In order to produce a local replica $x^{(\kappa)}(t)$ of the received signal $r(t)$, the receiver has to determine which of the satellites are currently visible, which DOPPLER frequency shifts they expose, and finally which code delays are correct. The receiver has to narrow down the code delay and DOPPLER frequency shift to an extend where Fig. 2.2 and 2.3 show the correlation peak. While Fig. 2.2 presents the search space for a receiver with the short coherent integration period $T_\mathrm{i} = 1\,\mathrm{ms}$, Fig. 2.3

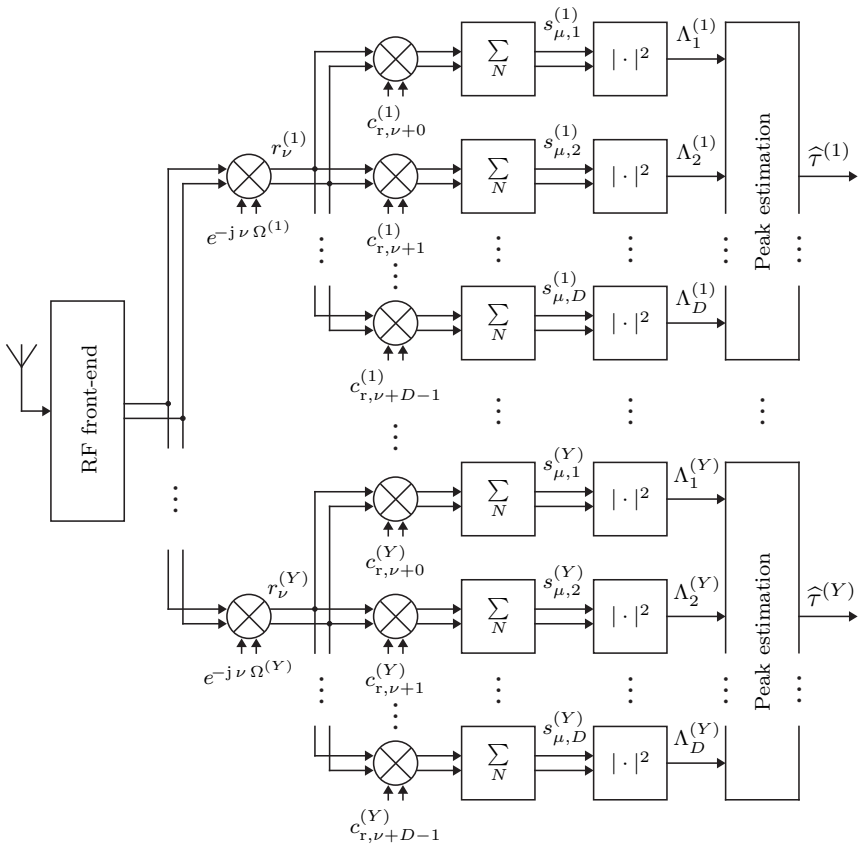

Figure 2.4: Highly parallel correlation technique.

illustrates the longer coherent integration period $T_\mathrm{i} = 8\,\mathrm{ms}$. It can be observed that the correlation peak becomes narrower in the dimension of the frequency deviation as the coherent integration period increases. The exact mathematical relationship will be derived in the next chapter in Section 3.3. The narrow correlation peak, in turn, requires a more fine-grained search in the frequency dimension. Increasing the coherent integration period, reduces the size of the search bins in the frequency dimension and hence increases the number of bins to be searched. Conventional GPS receivers sequentially perform correlations with different code delays, DOPPLER shifts, and spreading codes until they hit the correlation peak [30, 31]. This is very time consuming, drains batteries and challenges the user's patience [21]. Furthermore, the sequential search times increases quadratically with the increase in coherent integration period, since doubling the integration period also doubles the number of frequency search bins. The result is that the achievable reception sensitivity of sequential search is low, because long coherent integration times T_i per search bin are not affordable [23, 32].

The solution for this problem are highly parallel correlation techniques, as illustrated in Fig. 2.4. They can calculate a large number of correlation results simultaneously and hence acquire weak signals with sufficiently low latency [22, 23, 32]. Parallel correlation techniques provide the possibility to scan the inflated search space due to extended coherent integration intervals more effectively. The receiver architecture in Fig. 2.4 performs the subsequently described operations. The radio frequency (RF) front-end converts the received signal to intermediate frequency and samples it at time instances $\nu\,T_\mathrm{s}$, where T_s denotes the sample

period. The digital down-conversion with

$$\Omega^{(\kappa)} = 2\,\pi\,f_{\mathrm{LO}}^{(\kappa)}\,T_{\mathrm{s}}\;, \quad \kappa \in Y\;, \tag{2.12}$$

where $f_{\mathrm{LO}}^{(\kappa)}$ is the local oscillator frequency, implements the frequency search of Y frequency bins in parallel and yields the baseband samples $r_{\nu}^{(\kappa)}$. The parallel search of D code phase bins is indexed with ι. The code phase of the receiver path number ι is hence denoted $\widehat{\tau}_{\iota}$. The receiver in Fig. 2.4 despreads the received signal with all D possible code phases of the reference code $c_{\lfloor(\nu\,T_{\mathrm{s}}+\widehat{\tau}_{\iota})/T_{\mathrm{c}}\rfloor}$. The subsequent coherent accumulation of N samples yields the predetection values

$$s_{\mu,\iota}^{(\kappa)} = \sum_{\nu=(\mu-1)N+1}^{\mu N} r_{\nu}^{(\kappa)}\,c_{\lfloor(\nu\,T_{\mathrm{s}}+\widehat{\tau}_{\iota})/T_{\mathrm{c}}\rfloor}^{(\kappa)}\;, \tag{2.13}$$

with $\langle\,\cdot\,\rangle$ being the floor function for rounding to the nearest integer less or equal. The decision statistic for the code phase estimation is then

$$\boxed{\Lambda_{\iota}^{(\kappa)} = \left|s_{\mu,\iota}^{(\kappa)}\right|^2}\,. \tag{2.14}$$

Depending on the system configuration and which hardware resources are available, the parallel correlation results may either be calculated in the time domain or the frequency domain. The correlation in the time domain corresponds to a multiplication in the frequency domain. The frequency domain approach can be implemented with efficient hardware and software techniques, such as different variations of the Fast Fourier Transform (FFT) [23, 33, 34]. A big benefit of it is that the correlation values of all code delays can be calculated simultaneously [35, 36, 37]. Other proprietary techniques can be applied for efficient correlation in the time domain [32, 38]. The benefit of time domain correlation is that the correlation values can be continuously monitored, enabling the integration time T_{i} to rise until the signal-to-noise ratio is sufficiently large [39, 40]. More details on the implementation aspects of an enhanced sensitivity Galieo/GPS receiver are covered in the appendix.

2.4 Noncoherent Integration

Enhanced reception sensitivity is a key requirement for successful mobile phone positioning and location based services. A longer coherent integration time T_{i} in (2.11) leads to a higher reception sensitivity. However, the maximum coherent integration time is limited by different factors.

Firstly, the size of each frequency search bin is inversely proportional to the coherent integration time T_{i}. Fig. 2.2 and Fig. 2.3 show the GPS L1-C/A code/frequency search space for $T_{\mathrm{i}} = 1\,\mathrm{ms}$ and $T_{\mathrm{i}} = 8\,\mathrm{ms}$, respectively. It can be observed that the correlation peak becomes narrower in the frequency dimension. Thus, doubling the coherent integration time T_{i} doubles the number of frequency search bins, which either increases the time-to-fix or doubles the required number of parallel correlation channels.

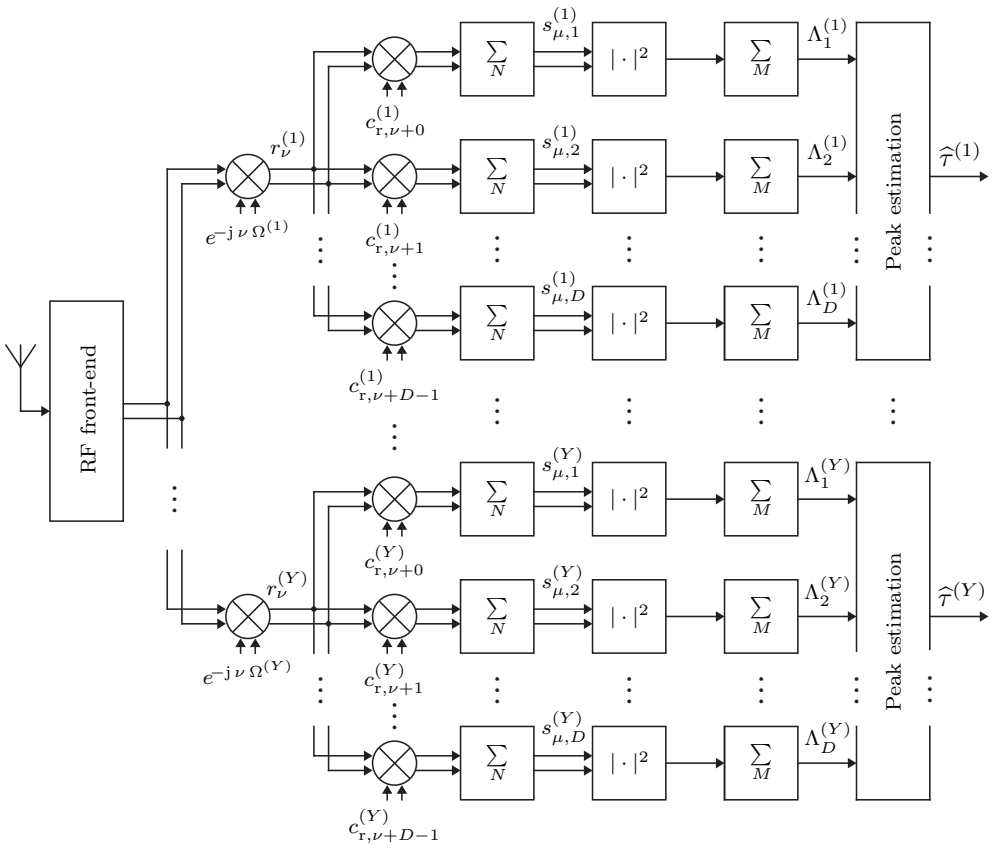

Figure 2.5: Highly parallel correlation technique with the noncoherent integration method.

Secondly, consumer market receivers have oscillators with limited frequency stability. This causes variations in the down-conversion factor $\Omega^{(\kappa)}$ and effectively limits the maximum coherent integration time T_i. Each frequency bin has to be kept wide enough to contain the fluctuation of the down-conversion frequency.

Thirdly, the coherence time of the signal propagation channel can also be a limiting factor, particularly for high user motion, such as vehicular environments. Variations in the user motion cause fluctuations in the Doppler frequency shift. The Doppler fluctuations add to the fluctuations of the down-conversion frequency and the width of the frequency bins has to be sufficient to contain this sum.

Noncoherent integration, on the other hand, can extend the observation period indefinitely without affecting the size of the frequency search bins. For positioning in deep urban and moderate indoor environments, where enhanced reception sensitivity is a prerequisite, noncoherent integration has become the state-of-the-art technique [21, 22, 23]. Fig. 2.5 shows the corresponding signal flow. The only difference to the receiver architecture in Fig. 2.4 is the additional accumulation block, which performs the operation

$$\boxed{\Lambda_\iota^{(\kappa)} = \sum_{\mu=1}^{M} \left| s_{\mu,\iota}^{(\kappa)} \right|^2}, \tag{2.15}$$

where the coherently integrated predetection values $s_{\mu,\iota}^{(\kappa)}$ are defined in (2.13) [36, 41]. Fig. 2.6 and 2.7 demonstrate that the width of the correlation peak is independent of the noncoherent

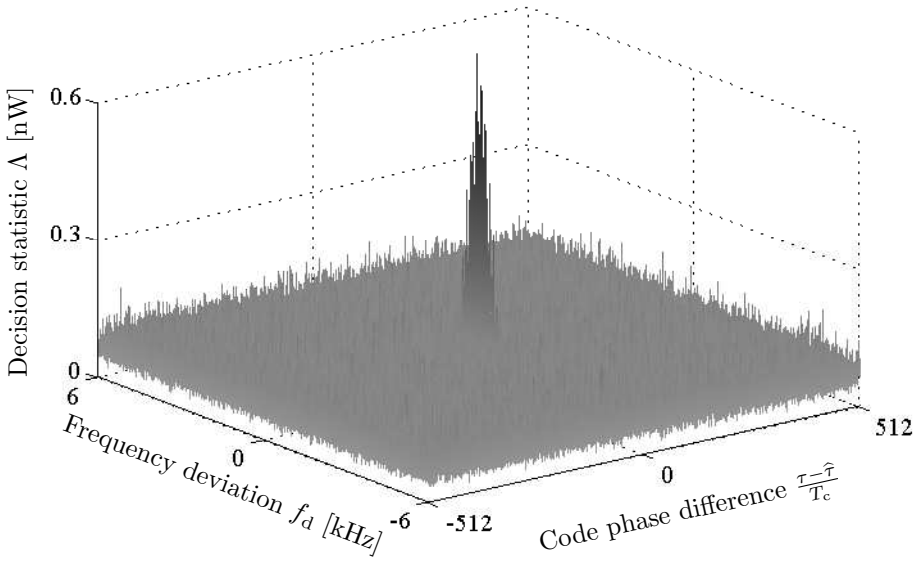

Figure 2.6: GPS L1-C/A search space for 6.5 dB signal attenuation, $T_\mathrm{i} = 1\,\mathrm{ms}$, and $M = 8$.

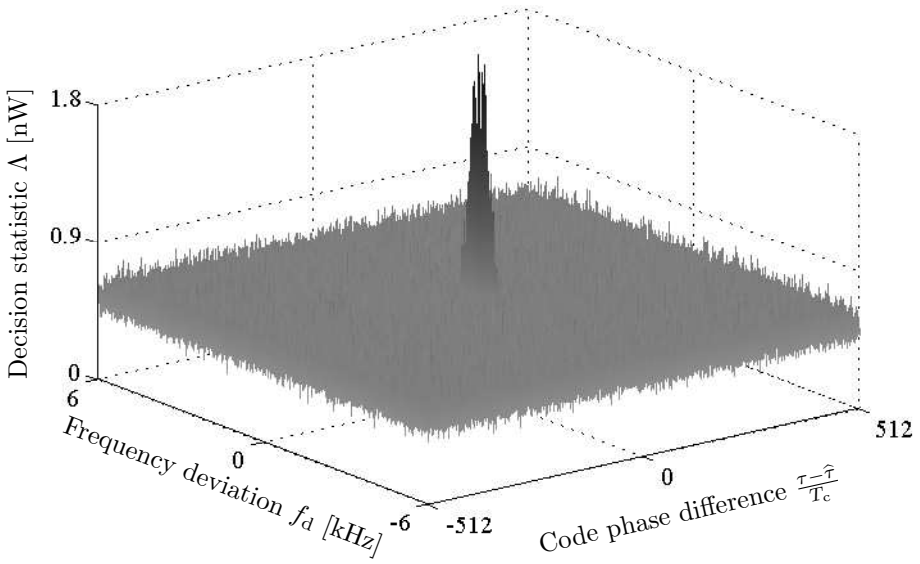

Figure 2.7: GPS L1-C/A search space for 11 dB signal attenuation, $T_\mathrm{i} = 1\,\mathrm{ms}$, and $M = 64$.

integration number M. The number of frequency bins hence does not increase with an increasing noncoherent integration number M [32, 34]. However, it can also be observed in Fig. 2.6 and 2.7 that the noise floor rises with an increasing noncoherent integration number M. This effect is caused by the squaring of the zero-mean additive noise samples, which turns them into non-zero-mean noise samples. The subsequent accumulation of the non-zero-mean noise samples raises the noise floor, which results in decreased sensitivity gain. While doubling the coherent integration period increases the reception sensitivity by approximately 3 dB, doubling the noncoherent integration number increases the reception sensitivity only by approximately 1.5 dB [21, 32]. The noncoherent integration number $M = 8$ in Fig. 2.6 achieves a sensitivity gain of around $3 \times 1.5\,\mathrm{dB}$. In order to obtain a sensitivity gain of 9 dB as in Fig. 2.3, around $M = 64$ as in Fig. 2.7 is required. Unlike Fig. 2.3, the correlation peak

is still wide in Fig. 2.7. The noncoherent integration does not increase the complexity of the frequency search. The price for this benefit is a substantial increase in required observation time. The sensitivity gain that is achieved in 8 ms in Fig. 2.3 takes 64 ms in Fig. 2.7.

2.5 Combined Galileo and GPS Reception

Mobile phone positioning benefits greatly from the combined use of Galileo and GPS signals. The GPS satellite visibility in urban environments is limited, with only three or less satellites above 30° elevation 80 % of the time [11, 42, 43]. However, as shown in Section 2.2, four satellites are required for three-dimensional (3D) positioning. Even when four GPS satellites are visible, the satellite geometry often remains poor, resulting in a degraded positioning accuracy. Simulations for the combined constellations of GPS and Galileo show that seven or more satellites are visible all the time with a 30° masking angle [11]. A total of 11–20 GPS and Galileo satellites are visible above 10° elevation [13, 44]. While neither GPS nor Galileo alone can provide accurate 3D positioning at a 30° masking angle, the combination of both allows positioning with horizontal and vertical errors within 12 m and 30 m respectively, for 95 % of the measurements [11, 42].

In high-rise urban environments, GPS is reported to provide a 20 m horizontal accuracy in just 15 % – 30 % of the sites [42, 43, 45]. This improves to 80 % – 90 % for combined Galileo/GPS reception. The remaining 10 % – 20 % of the sites can then be served with a combined trilateration of Galileo, GPS, and mobile telephone signals [41, 43]. The availability in low-rise urban areas improves from around 70 % to 100 % for the combined Galileo/GPS reception. Even for suburban environments, the horizontal accuracy of the combined Galileo/GPS reception is simulated to improve by around 400 % to less than 8 m, while 3 m appear achievable in open sky environments [11, 42, 45].

It is therefore essential for future satellite navigation receivers in urban environments to support simultaneous reception of Galileo and GPS. Since the GPS L1-C/A signal is transmitted with the same carrier frequency as the Galileo E1-B/C signals, a combined receiver for these signals requires only a single radio frequency front-end [4, 5]. This work hence provides simulation results for the reception of the GPS L1-C/A and the Galileo E1-B/C signals.

2.6 Conclusion

Enhancing the reception sensitivity is a prerequisite for many emerging Galileo/GPS applications in deep urban and moderate indoor environments. At the same time, low positioning latency is also required. Assistance data provides aiding information to support the acquisition of weak signals. When the observation period is extended beyond the data bit boundaries to collect more signal energy, the navigation messages of the Galileo/GPS signals cannot be received any more. The combination of assistance data and single shot positioning allows calculating the navigation solution in this situation. The task of the Galileo/GPS

receiver can then be reduced to the measurement of the spreading code phases. Sequential acquisition search with an extended observation period leads to unacceptable delays. The positioning latency can be substantially reduced by parallelizing the signal processing to calculate the correlation result for multiple code phases simultaneously. The maximum coherent integration interval is limited, as it increases the size of the acquisition search space. The stability of the local oscillator and the coherence time of the propagation channel are further limiting factors. The state-of-the-art technique for GPS reception in deep urban and moderate indoor environments is noncoherent integration, as it allows to extend the observation period without increasing the size of the acquisition search space. The drawback of noncoherent integration is that it raises the noise floor. The sensitivity gain from doubling the noncoherent integration interval is only around 1.5 dB, as opposed to the 3 dB gain from doubling the coherent integration interval. Both, Galileo and GPS receivers suffer from poor visibility in urban canyons. The best choice in urban environments is to combine both for improved service availability.

Chapter 3

Differential Correlation

This chapter introduces the *differential correlation* technique as a potential replacement for the *noncoherent integration*. The state-of-the-art method for GPS reception in deep urban and moderate indoor areas is noncoherent integration [22, 23, 32]. It can extend the observation period indefinitely without reducing the size of the frequency bins. Differential correlation has the same property, as will be shown subsequently. Noncoherent integration raises the noise floor by squaring the received noise samples. Differential correlation multiplies subsequent noise samples, which are statistically independent. The resulting noise power of differential correlation is therefore less than that of noncoherent integration.

The following sections derive the probability distributions of the decision statistics for differential correlation and noncoherent integration. These distributions are then evaluated for GPS and Galileo signals in the E1/L1 frequency band with various receiver settings and various Doppler frequency shifts. It is shown that differential correlation provides improved reception sensitivity over the whole range of frequency shifts and receiver settings. The findings are verified by extensive simulations. In order to evaluate the positioning accuracy, the standard deviations of the estimated distances between receiver and satellites are also derived for differential correlation and noncoherent integration. These standard deviations are evaluated for various E1/L1 Galileo/GPS receiver parameters and frequency offsets. The results show that differential correlation not only improves reception sensitivity, but also increases positioning accuracy.

Fig. 3.1 provides an overview of the receiver architecture for differential correlation. Each of the signal processing steps will be described subsequently and the probability density function of the signal will be derived at each processing stage. While the noncoherent integration method squares the predetection samples s_μ, the differential correlation technique multiplies each predetection sample with the complex conjugate of the previous predetection sample. This technique is inspired by the differential demodulation method in digital communications [46, 47]. The important distinction to noncoherent integration is the additional delay element, denoted by z^{-1} in Fig. 3.1. The complex conjugate operation is denoted by the symbol $(\cdot)^*$. As will be shown in Section 3.4, the improved reception sensitivity of the differential correlation originates from the fact that subsequent predetection samples are statistically independent. The products of the statistically independent predetection samples have a lower variance than that of the squared predetection samples.

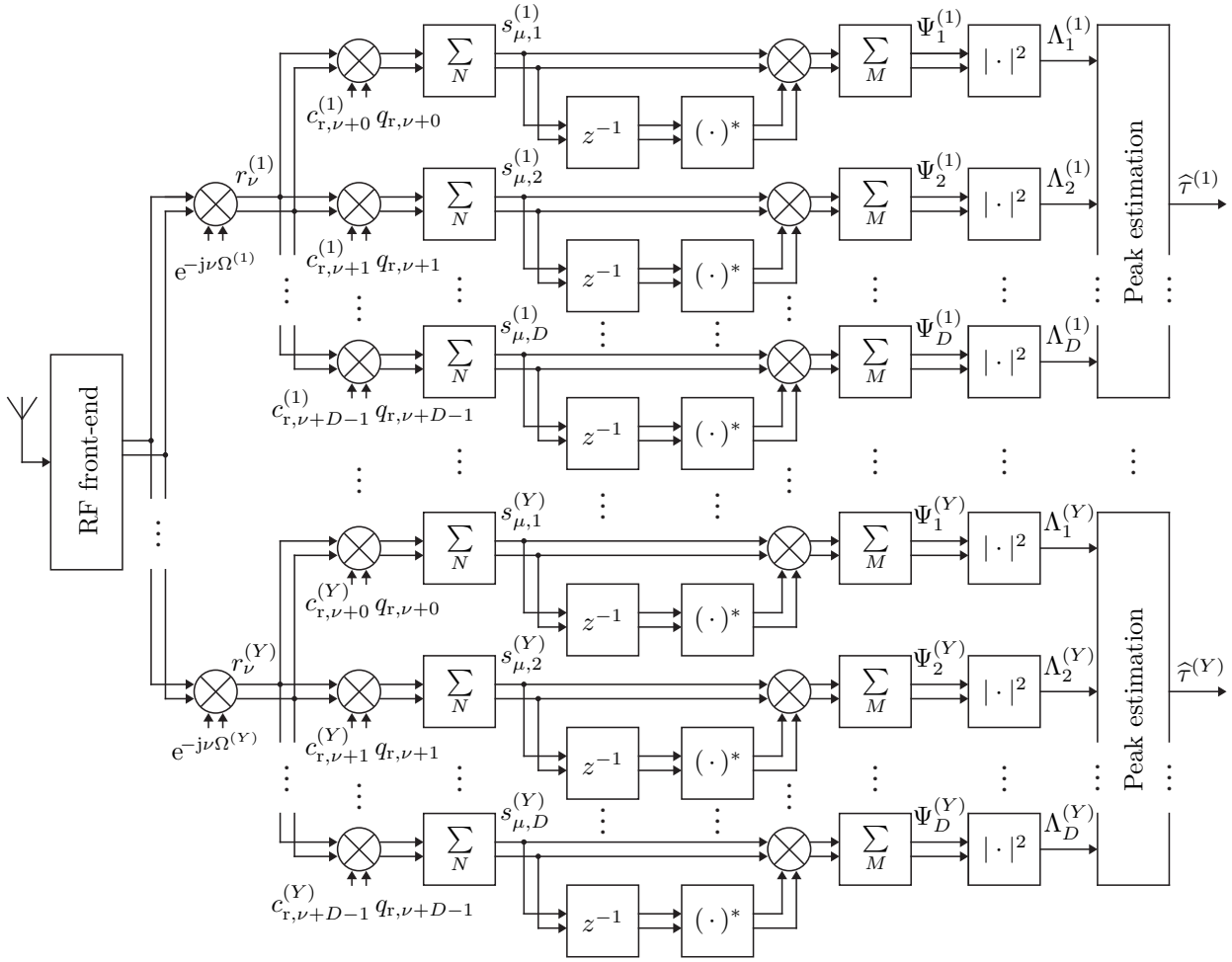

Figure 3.1: Highly parallel reception with the differential correlation technique.

3.1 Galileo/GPS Signal Specification

The Galileo and GPS signals are spread spectrum signals. They are characterized by their carrier frequency f_c, carrier power C, data bit stream d_μ, data bit period T_d, spreading code c_ν, chip period T_c, code length L, square-wave subcarrier $q(t)$, and spreading pulse form $p(t)$. A generalized formulation of the Galileo/GPS transmit signals can be expressed in lowpass equivalent notation as

$$x(t) = \sqrt{2\,C} \sum_{\mu=-\infty}^{\infty} d_\mu \sum_{\nu=0}^{G-1} c_\nu \; q(t)\, p(t - \mu\, T_\mathrm{d} - \nu\, T_\mathrm{c}) \;, \tag{3.1}$$

with

$$G = \frac{T_\mathrm{d}}{L\, T_\mathrm{c}} \;. \tag{3.2}$$

Table 3.1 summarizes the values of the parameters for the Galileo and modernized GPS signals [4, 5, 48]. The Galileo E1-B/C signals use the Binary Offset Carrier (BOC) modulation, which utilizes the square-wave subcarrier

$$q(t) = \mathrm{sign}\left[\sin\left(\frac{2\,\pi\, t}{T_\mathrm{c}}\right)\right] \;, \tag{3.3}$$

Component name	Modulation scheme	Carrier frequency f_c [MHz]	Carrier power C [dBm]	Spreading chip period T_c [μs]	Primary code length L [chips]	Secondary code length U [chips]	Data bit period T_d [ms]
Galileo E1-B	BOC(1, 1)	1575.42	-130	1/1.023	4092	none	4
Galileo E1-C	BOC(1, 1)	1575.42	-130	1/1.023	4092	25	pilot
Galileo E5a-I	BPSK(10)	1176.45	-128	1/10.23	10230	20	20
Galileo E5a-Q	BPSK(10)	1176.45	-128	1/10.23	10230	100	pilot
Galileo E5b-I	BPSK(10)	1207.14	-128	1/10.23	10230	4	4
Galileo E5b-Q	BPSK(10)	1207.14	-128	1/10.23	10230	100	pilot
Galileo E6-B	BPSK(5)	1278.75	-128	1/5.115	5115	none	1
Galileo E6-C	BPSK(5)	1278.75	-128	1/5.115	5115	100	pilot
GPS L1-C/A	BPSK(1)	1575.42	-128.5	1/1.023	1023	none	20
GPS L2-CM	BPSK(1)	1227.60	-130	1/1.023	10230	none	20
GPS L2-CL	BPSK(1)	1227.60	-130	1/1.023	767250	none	pilot
GPS L5-I	BPSK(10)	1176.45	-127.9	1/10.23	10230	10	10
GPS L5-Q	BPSK(10)	1176.45	-127.9	1/10.23	10230	20	pilot

Table 3.1: Galileo and modernized GPS civilian signal parameters [4, 5, 48].

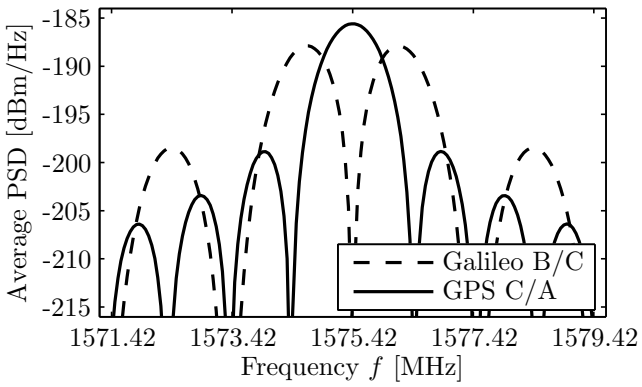

Figure 3.2: Average E1/L1-band power density spectrum for the approximation of c_ν, g_μ and d_κ as zero-mean white noise processes and $p(t)$ as rectangular pulse.

where sign($\cdot$) is the signum function. The signals modulated with Binary Phase Shift Keying (BPSK) are modeled with $q(t) = 1$. Some signals are modulated with a secondary spreading code, which has a chip period equal to the full primary code period [5, 48]. The *pilot* signals contain no data message and are modelled as $d_\mu = 1$. Fig. 3.2 presents the average E1/L1-band Power Spectral Density (PSD)[1] for the approximation of c_ν and d_μ as zero-mean white noise processes and $p(t)$ as a rectangular pulse. It can be observed that the zero-to-zero bandwidth for the GPS L1-C/A signal is $B = 2.046\,\text{MHz}$, while it is $B = 4.092\,\text{MHz}$ for the Galileo L1-B/C signal.

When the Galileo/GPS signals reach the earth surface, they also display a propagation

[1] $P(f)$ in dBm/Hz refers to $P(f) = 10\log(\tilde{P}(f)/(1\,\text{mW/Hz}))$, where $\tilde{P}(f)$ is the power spectral density measured in W/Hz.

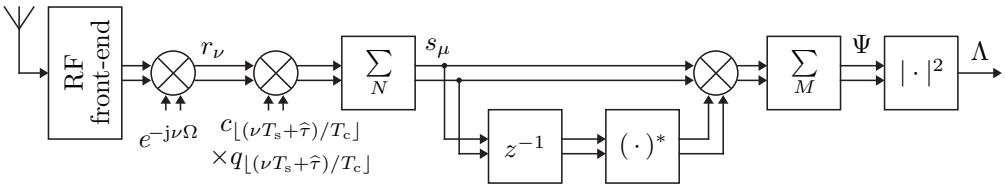

Figure 3.3: Receiver channel with the differential correlation technique.

delay T_p, DOPPLER frequency shift f_D, carrier phase φ_c, and additive thermal band-pass noise $n_\mathrm{bp}(t)$. The received signals can therefore be expressed in bandpass notation as

$$r_\mathrm{bp}(t) = x(t - T_\mathrm{p})\,\cos[2\,\pi\,(f_\mathrm{c} + f_\mathrm{D})\,(t - T_\mathrm{p}) + \varphi_\mathrm{c}] + n_\mathrm{bp}(t)\;. \tag{3.4}$$

3.2 Down-Conversion and Doppler Compensation

It is shown in Section 2.2 that instead of estimating the propagation time T_p it is sufficient to estimate the code phase τ within a single code sequence period $[0,\, L\,T_\mathrm{c}]$. The single shot positioning algorithm of Section 2.2 can determine how many integer multiples ς of the chip period have passed at the time the signal was transmitted. The transmission time therefore is

$$t_0 = t - T_\mathrm{p} = \varsigma\,L\,T_\mathrm{c} + \tau \quad ;\varsigma \in \mathbb{Z} \quad ;\tau \in [0,\, L\,T_\mathrm{c}]\;. \tag{3.5}$$

Section 2.3 concludes that the code phase τ can be best estimated by maximizing the squared magnitude of the correlation between the received signal and a locally generated replica of the signal.

Before the correlation value can be calculated, the DOPPLER frequency shift of the received signal has to be compensated. This is typically accomplished with the down-conversion to baseband. Subsequently, a single channel of the differential correlation receiver in Fig. 3.1 with one down-conversion factor Ω, one reference code $c_{\lfloor(\nu\,T_\mathrm{s}+\widehat{\tau})/T_\mathrm{c}\rfloor}$, and one subcarrier $q_{\lfloor(\nu\,T_\mathrm{s}+\widehat{\tau})/T_\mathrm{c}\rfloor}$ is analyzed. The corresponding signal processing stages of the single channel are presented in Fig. 3.3. The Radio Frequency (RF) front-end converts the received signal to the intermediate frequency f_IF and samples it at time instances $\nu\,T_\mathrm{s}$, where T_s denotes the sampling period. The spreading pulse form is approximated as the rectangular function

$$p(t) \simeq \mathrm{rect}\!\left(\frac{t}{T_\mathrm{c}} - \frac{1}{2}\right). \tag{3.6}$$

The digital down-conversion with

$$\Omega = 2\,\pi\,f_\mathrm{LO}\,T_\mathrm{s} \tag{3.7}$$

yields the baseband samples r_ν. However, the exact DOPPLER frequency shift f_D is generally unknown. It is searched for with a discrete frequency grid. The center frequency of each frequency search bin is applied as the down-conversion frequency f_LO. If the subsequent correlation is successful, then the correct frequency bin has been found. This discrete frequency search is not generally able to exactly compensate for the unknown DOPPLER frequency shift. The sampled baseband Galileo/GPS signal

$$r_\nu = \sqrt{2\,C}\,d_{\lfloor(\nu\,T_\mathrm{s}+\tau)/T_\mathrm{d}\rfloor}\,c_{\lfloor(\nu\,T_\mathrm{s}+\tau)/T_\mathrm{c}\rfloor}\,q_{\lfloor(\nu\,T_\mathrm{s}+\tau)/T_\mathrm{c}\rfloor}\,\mathrm{e}^{\mathrm{j}\,[2\,\pi\,f_\mathrm{d}\,(\nu\,T_\mathrm{s}+\tau)+\varphi_\mathrm{c}]} + n_\nu \tag{3.8}$$

is hence left with the residual frequency deviation

$$\boxed{f_\mathrm{d} = f_\mathrm{IF} + f_\mathrm{D} - f_\mathrm{LO}}\,. \tag{3.9}$$

The possible range of the residual frequency deviation depends on the size of the frequency search bins.

The lowpass equivalent received thermal noise n_ν can be modelled as complex-valued zero-mean white GAUSSIAN noise, which has the probability distribution

$$p_n(\Re\{n\},\,\Im\{n\}) = \frac{1}{\pi\,\sigma_n^2}\,\exp\!\left(-\frac{\Re\{n\}^2}{\sigma_n^2} - \frac{\Im\{n\}^2}{\sigma_n^2}\right), \tag{3.10}$$

where $\Re\{\,\cdot\,\}$ denotes the real part and $\Im\{\,\cdot\,\}$ the imaginary part [28, 49]. The noise variance is

$$\sigma_n^2 = \mathrm{E}\{|n|^2\} = 2\,\mathrm{E}\{\Re\{n\}^2\} = 2\,\mathrm{E}\{\Im\{n\}^2\} = 2\,\mathcal{N}_0\,B\,F\,, \tag{3.11}$$

where $\mathrm{E}\{\,\cdot\,\}$ is the operator for the expectation value,

$$\mathcal{N}_0 = k\,T_0 \tag{3.12}$$

denotes the noise Power Spectral Density (PSD), B the noise bandwidth, F the front-end noise figure, $k = 1.381\times10^{-23}\,\mathrm{W\,s/K}$ the BOLTZMAN constant, and T_0 the noise temperature [29, 50]. The real and imaginary part of n_ν are uncorrelated [49]

$$\mathrm{E}\{\Re\{n\}\,\Im\{n\}\} = 0\,. \tag{3.13}$$

The noise temperature $T_0 = 290\,\mathrm{K}$ and the front-end noise figure $F = 3\,\mathrm{dB}$ are applied for all subsequent simulations, as they are typical values used in literature.

3.3 Despreading and Coherent Integration

As introduced in Section 2.3, the baseband signal is despread with the spreading code $c_{\lfloor(\nu\,T_\mathrm{s}+\widehat{\tau})/T_\mathrm{c}\rfloor}$ and the subcarrier $q_{\lfloor(\nu\,T_\mathrm{s}+\widehat{\tau})/T_\mathrm{c}\rfloor}$, where $\widehat{\tau}$ is the estimated code phase. Since the primary spreading code repeats every $L\,T_\mathrm{c}/T_\mathrm{s}$ samples, the code phase is estimated within the range $[0,\,L\,T_\mathrm{c}]$ and the integer multiples of the code period are determined with the single shot positioning algorithm in Section 2.3. The predetection values are obtained by the despreading and coherent accumulation of N samples

$$\boxed{s_\mu = \sum_{\nu=\mu\,N}^{(\mu+1)\,N-1} r_\nu\,c_{\lfloor(\nu\,T_\mathrm{s}+\widehat{\tau})/T_\mathrm{c}\rfloor}\,q_{\lfloor(\nu\,T_\mathrm{s}+\widehat{\tau})/T_\mathrm{c}\rfloor} = y_\mu + w_\mu}\,. \tag{3.14}$$

The deterministic signal component is denoted by

$$\boxed{\begin{aligned} y_\mu = \sqrt{2\,C}\sum_{\nu=\mu\,N}^{(\mu+1)\,N-1} \Big[& d_{\lfloor(\nu\,T_\mathrm{s}+\tau)/T_\mathrm{d}\rfloor}\,c_{\lfloor(\nu\,T_\mathrm{s}+\tau)/T_\mathrm{c}\rfloor}\,q_{\lfloor(\nu\,T_\mathrm{s}+\tau)/T_\mathrm{c}\rfloor} \\ & \times c_{\lfloor(\nu\,T_\mathrm{s}+\widehat{\tau})/T_\mathrm{c}\rfloor}\,q_{\lfloor(\nu\,T_\mathrm{s}+\widehat{\tau})/T_\mathrm{c}\rfloor}\,\mathrm{e}^{\mathrm{j}\,[2\,\pi\,f_\mathrm{d}\,(\nu\,T_\mathrm{s}+\tau)+\varphi_\mathrm{c}]}\Big] \end{aligned}} \tag{3.15}$$

and the zero-mean white GAUSSIAN noise component by

$$\boxed{w_\mu = \sum_{\nu=\mu\,N}^{(\mu+1)\,N-1} n_\nu \, c_{\lfloor(\nu\,T_\mathrm{s}+\widehat{\tau})/T_\mathrm{c}\rfloor} \, q_{\lfloor(\nu\,T_\mathrm{s}+\widehat{\tau})/T_\mathrm{c}\rfloor}} \; . \tag{3.16}$$

If the sampling rate does not exceed the NYQUIST rate with

$$T_\mathrm{s} = \frac{1}{B} \; , \tag{3.17}$$

then the subsequent noise samples are uncorrelated

$$\mathrm{E}\big\{ n_\nu \, n_{\nu+1}^* \big\} = 0 \; . \tag{3.18}$$

The accumulated noise variance results in

$$\boxed{\sigma_w^2 = \mathrm{E}\big\{|w|^2\big\} = 2\,\mathrm{E}\big\{\Re\{w\}^2\big\} = 2\,\mathrm{E}\big\{\Im\{w\}^2\big\} = N\,\sigma_n^2 = 2\,N k\,T_0\,B\,F} \; . \tag{3.19}$$

Subsequent predetection noise samples are then also uncorrelated

$$\mathrm{E}\big\{ w_\mu \, w_{\mu+1}^* \big\} = 0 \; . \tag{3.20}$$

If the coherent integration takes place within the data bit boundaries and the estimated code phase $\widehat{\tau}$ equals the actual code phase τ, then the deterministic component equals the geometric series

$$\begin{aligned} y_\mu\big|_{\widehat{\tau}=\tau} &= \sqrt{2\,C}\, d_{\mathrm{s},\mu} \sum_{\nu=\mu\,N}^{(\mu+1)\,N-1} \mathrm{e}^{\mathrm{j}\,[2\,\pi\,f_\mathrm{d}\,(\nu\,T_\mathrm{s}+\tau)+\varphi_\mathrm{c}]} \\ &= \sqrt{2\,C}\, d_{\mathrm{s},\mu} \left(\frac{1-\mathrm{e}^{\mathrm{j}\,2\,\pi\,f_\mathrm{d}\,(\mu+1)\,N\,T_\mathrm{s}}}{1-\mathrm{e}^{\mathrm{j}\,2\,\pi\,f_\mathrm{d}\,T_\mathrm{s}}} - \frac{1-\mathrm{e}^{\mathrm{j}\,2\,\pi\,f_\mathrm{d}\,\mu\,N\,T_\mathrm{s}}}{1-\mathrm{e}^{\mathrm{j}\,2\,\pi\,f_\mathrm{d}\,T_\mathrm{s}}} \right) \mathrm{e}^{\mathrm{j}\,(2\,\pi\,f_\mathrm{d}\,\tau+\varphi_\mathrm{c})} \\ &= \sqrt{2\,C}\, d_{\mathrm{s},\mu}\, \mathrm{e}^{\mathrm{j}\,(2\,\pi\,f_\mathrm{d}\,\tau+\varphi_\mathrm{c})} \frac{\mathrm{e}^{\mathrm{j}\,2\,\pi\,f_\mathrm{d}\,\mu\,N\,T_\mathrm{s}} - \mathrm{e}^{\mathrm{j}\,2\,\pi\,f_\mathrm{d}\,(\mu+1)\,N\,T_\mathrm{s}}}{1-\mathrm{e}^{\mathrm{j}\,2\,\pi\,f_\mathrm{d}\,T_\mathrm{s}}} \\ &= \sqrt{2\,C}\, d_{\mathrm{s},\mu}\, \mathrm{e}^{\mathrm{j}\,(2\,\pi\,f_\mathrm{d}\,[(\mu+1/2)\,N\,T_\mathrm{s}+\tau]+\varphi_\mathrm{c})} \frac{\mathrm{e}^{-\mathrm{j}\,\pi\,f_\mathrm{d}\,N\,T_\mathrm{s}} - \mathrm{e}^{\mathrm{j}\,\pi\,f_\mathrm{d}\,N\,T_\mathrm{s}}}{1-\mathrm{e}^{\mathrm{j}\,2\,\pi\,f_\mathrm{d}\,T_\mathrm{s}}} \end{aligned} \tag{3.21}$$

with the data stream

$$d_{\mathrm{s},\mu} = d_{\lfloor(\mu\,N\,T_\mathrm{s}+\tau)/T_\mathrm{d}\rfloor} \; . \tag{3.22}$$

The term $\mathrm{e}^{\mathrm{j}\,2\,\pi\,f_\mathrm{d}\,T_\mathrm{s}}$ can expressed by the TAYLOR series

$$\mathrm{e}^{\mathrm{j}\,2\,\pi\,f_\mathrm{d}\,T_\mathrm{s}} = \sum_{\nu=0}^{\infty} \frac{(\mathrm{j}\,2\,\pi\,f_\mathrm{d}\,T_\mathrm{s})^\nu}{\nu!} = 1 + \mathrm{j}\,2\,\pi\,f_\mathrm{d}\,T_\mathrm{s} + \frac{(\mathrm{j}\,2\,\pi\,f_\mathrm{d}\,T_\mathrm{s})^2}{2} + \frac{(\mathrm{j}\,2\,\pi\,f_\mathrm{d}\,T_\mathrm{s})^3}{6} + \ldots \quad . \tag{3.23}$$

For the relevant cases, the argument $\mathrm{j}\,2\,\pi\,f_\mathrm{d}\,T_\mathrm{s}$ has a magnitude much smaller than one, since the receiver has to ensure that the signal phase $\mathrm{e}^{\mathrm{j}\,[2\,\pi\,f_\mathrm{d}\,(\nu\,T_\mathrm{s}+\tau)+\varphi_\mathrm{c}]}$ does not rotate by more than around π within the coherent integration period $N\,T_\mathrm{s} \geqslant L\,T_\mathrm{c}$. The case of $T_\mathrm{c} = 1/1023\,\mathrm{ms}$, $T_\mathrm{s} = T_\mathrm{c}/2$ and $|f_\mathrm{d}| \leqslant 500\,\mathrm{Hz}$ yields $|\mathrm{j}\,2\,\pi\,f_\mathrm{d}\,T_\mathrm{s}| \leqslant 0.00156$. The receiver

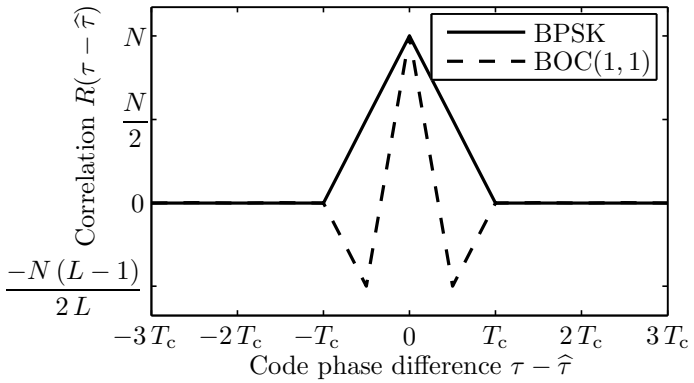

Figure 3.4: Correlation peak for BPSK and BOC(1, 1) modulation.

partitions the frequency search space into search bins and within the correct bin, the term $\mathrm{e}^{\mathrm{j}\,2\,\pi\,f_\mathrm{d}\,T_\mathrm{s}}$ can be well approximated by the first two terms of its TAYLOR series

$$\mathrm{e}^{\mathrm{j}\,2\,\pi\,f_\mathrm{d}\,T_\mathrm{s}} \simeq 1 + \mathrm{j}\,2\,\pi\,f_\mathrm{d}\,T_\mathrm{s}\;. \tag{3.24}$$

Substituting (3.24) into (3.21) yields

$$\begin{aligned} y_\mu\big|_{\widehat{\tau}=\tau} &\simeq \sqrt{2\,C}\,d_{\mathrm{s},\mu}\,\mathrm{e}^{\mathrm{j}\,(2\,\pi\,f_\mathrm{d}\,[(\mu+1/2)\,N\,T_\mathrm{s}+\tau]+\varphi_\mathrm{c})}\,\frac{\mathrm{e}^{-\mathrm{j}\,\pi\,f_\mathrm{d}\,N\,T_\mathrm{s}} - \mathrm{e}^{\mathrm{j}\,\pi\,f_\mathrm{d}\,N\,T_\mathrm{s}}}{-\mathrm{j}\,2\,\pi\,f_\mathrm{d}\,T_\mathrm{s}} \\ &\simeq \sqrt{2\,C}\,d_{\mathrm{s},\mu}\,N\,\mathrm{sinc}(f_\mathrm{d}\,N\,T_\mathrm{s})\,\mathrm{e}^{\mathrm{j}\,(2\,\pi\,f_\mathrm{d}\,[(\mu+1/2)\,N\,T_\mathrm{s}+\tau]+\varphi_\mathrm{c})} \end{aligned} \tag{3.25}$$

with the normalized sinc-function

$$\mathrm{sinc}(\alpha) = \frac{\sin(\pi\,\alpha)}{\pi\,\alpha}\;. \tag{3.26}$$

The coherent integration time $N\,T_\mathrm{s}$ should be chosen as a multiple of the primary spreading code period $L\,T_\mathrm{c}$. The deterministic component for a frequency deviation of zero and an arbitrary code phase $\widehat{\tau} \neq \tau$

$$y_\mu\big|_{f_\mathrm{d}=0} = \sqrt{2\,C}\,d_{\mathrm{s},\mu}\,R(\tau-\widehat{\tau})\,\mathrm{e}^{\mathrm{j}\,\varphi_\mathrm{c}} \tag{3.27}$$

can then be described with help of the correlation function

$$\boxed{\begin{aligned} R(\tau-\widehat{\tau}) &= \sum_{\nu=0}^{N-1}\Big[c_{\lfloor(\nu\,T_\mathrm{s}+\tau)/T_\mathrm{c}\rfloor}\,q_{\lfloor(\nu\,T_\mathrm{s}+\tau)/T_\mathrm{c}\rfloor}\,c_{\lfloor(\nu\,T_\mathrm{s}+\widehat{\tau})/T_\mathrm{c}\rfloor}\,q_{\lfloor(\nu\,T_\mathrm{s}+\widehat{\tau})/T_\mathrm{c}\rfloor}\Big] \\ &\simeq \frac{1}{T_\mathrm{s}}\int_0^{N\,T_\mathrm{s}} c(t+\tau)\,q(t+\tau)\,c(t+\widehat{\tau})\,q(t+\widehat{\tau})\;dt \end{aligned}}\;, \tag{3.28}$$

where $c_{\lfloor(\nu\,T_\mathrm{s}+\tau)/T_\mathrm{c}\rfloor}$ denotes the sampled spreading code, $q_{\lfloor(\nu\,T_\mathrm{s}+\tau)/T_\mathrm{c}\rfloor}$ the sampled subcarrier, $c(t)$ the time-continuous spreading code, and $q(t)$ the time-continuous subcarrier. The time-continuous correlation function in (3.28) can be well approximated with digital signal processing by utilizing *non-commensurate sampling rates* [51]. Fig. 3.4 shows the correlation peaks for BPSK and BOC(1, 1) modulated signals in the center at $\tau - \widehat{\tau} \sim 0$. It can be observed how the subcarrier of the BOC signal narrows the correlation peak and leads to

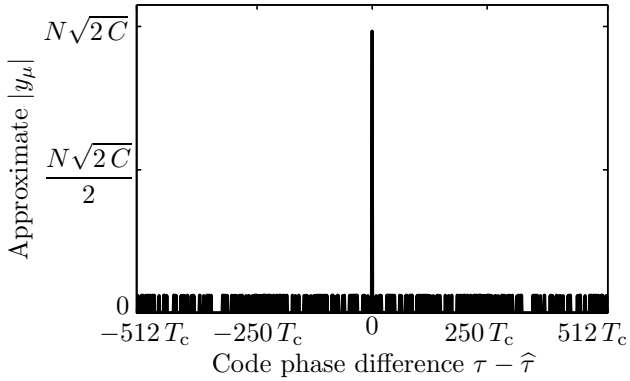

(a) Approximation in (3.31) for $f_\mathrm{d} = 100\,\mathrm{Hz}$.

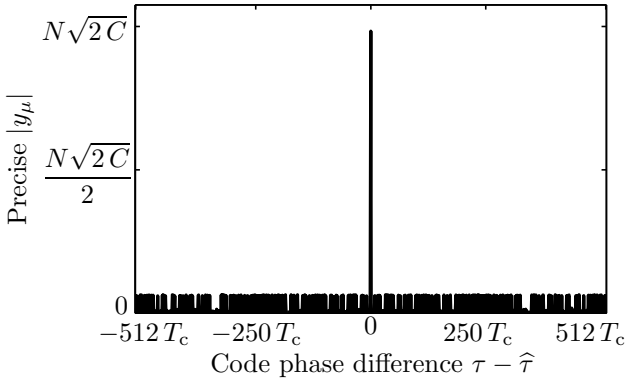

(b) Precise result in (3.15) for $f_\mathrm{d} = 100\,\mathrm{Hz}$.

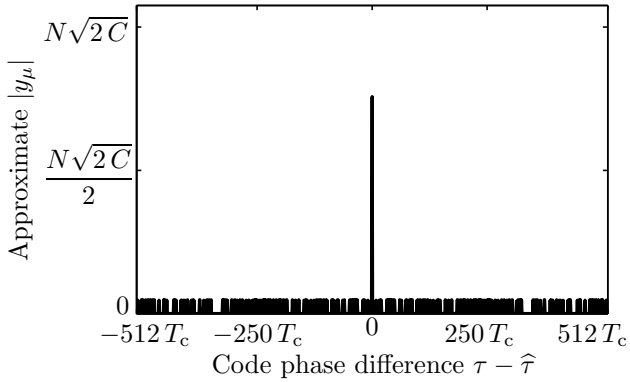

(c) Approximation in (3.31) for $f_\mathrm{d} = 240\,\mathrm{Hz}$.

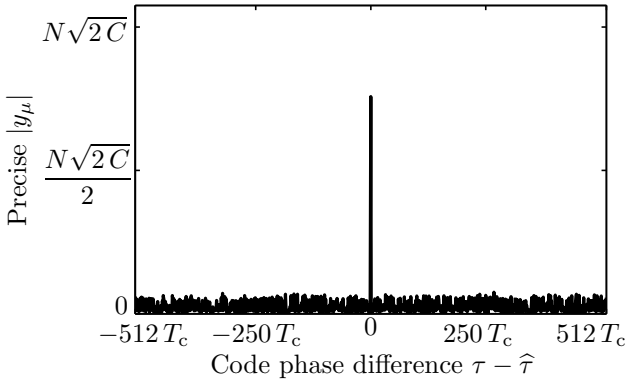

(d) Precise result in (3.15) for $f_\mathrm{d} = 240\,\mathrm{Hz}$.

Figure 3.5: Comparison of the approximate of y_μ in (3.31) for GPS L1-C/A versus the precise result in (3.15).

negative side-peaks. The possible correlation values of BPSK modulated GOLD codes of length L at code phase differences of multiple chips are [52]

$$R(\tau - \widehat{\tau})\Big|_{\substack{\tau-\widehat{\tau}=\nu\,T_\mathrm{c} \\ \nu\in\mathbb{Z}}} \in \left\{ N,\ \frac{(\beta-2)\,N}{L},\ -\frac{N}{L},\ -\frac{\beta\,N}{L} \right\}, \tag{3.29}$$

with

$$\beta = 1 + 2^{\lfloor(\log_2(L+1)+2)/2\rfloor}\ . \tag{3.30}$$

The GPS L1-C/A signals utilize GOLD codes of length $L = 1023$, where the correlation values $R(\tau - \widehat{\tau})|_{\tau-\widehat{\tau}=\nu\,T_\mathrm{c}} = -(65\,N)/1023$ and $R(\tau - \widehat{\tau})|_{\tau-\widehat{\tau}=\nu\,T_\mathrm{c}} = (63\,N)/1023$ each have a 12.5 % occurrence rate [29]. The Galileo signals utilize spreading codes that have been found by computer simulation. The maximum out-of-phase autocorrelation value for despreading the Galileo E1-B/C signals with the Galileo E1-B codes or the the Galileo E1-C codes is $R_\mathrm{m} = 0.094\,N$ [5].

By combining the previous results for sufficiently low frequency deviations f_d, the deterministic component of the predetection samples can be approximated by

$$\boxed{y_\mu \simeq \sqrt{2\,C}\,d_{\mathrm{s},\mu}\,R(\tau - \widehat{\tau})\,\mathrm{sinc}(f_\mathrm{d}\,N\,T_\mathrm{s})\,\mathrm{e}^{\mathrm{j}\,(2\,\pi\,f_\mathrm{d}\,[(\mu+1/2)\,N\,T_\mathrm{s}+\tau]+\varphi_\mathrm{c})}}\ . \tag{3.31}$$

Fig. 3.5 compares the approximation of $|y_\mu|$ in (3.31) versus the exact result in (3.15). The correlation peak is visible in the middle and the out-of-phase autocorrelation values to the

left and right of the peak. It can be seen that the approximations for the correlation peak and the average of the out-of-phase correlation values match with a sufficiently high degree of accuracy. The nonzero out-of-phase correlation values limit the reception sensitivity, since the detection threshold has to be higher than the out-of-phase correlation plus the added thermal noise.

3.4 Differential Correlation Mean

As illustrated in Fig. 3.1 the distinction of differential correlation as opposed to noncoherent integration is the additional delay element. As formulated in (3.32), each coherently integrated predetection sample is multiplied with the complex conjugate of the *previous* predetection sample. This results in a sensitivity gain when compared to noncoherent integration, since subsequent predetection samples are uncorrelated. These products are then further accumulated to form the differential correlation result

$$\boxed{\Psi = \sum_{\mu=1}^{M-1} s_\mu \, s_{\mu-1}^* = m_\Psi + u + v} \, , \tag{3.32}$$

$$m_\Psi = \sum_{\mu=1}^{M-1} y_\mu \, y_{\mu-1}^* \, , \tag{3.33}$$

$$u = \sum_{\mu=1}^{M-1} \left(w_\mu \, y_{\mu-1}^* + y_\mu \, w_{\mu-1}^* \right) \, , \tag{3.34}$$

$$v = \sum_{\mu=1}^{M-1} w_\mu \, w_{\mu-1}^* \, , \tag{3.35}$$

where s_μ, y_μ, and w_μ are defined in (3.14), (3.31), and (3.16), respectively. The probability density function of the differential correlation result Ψ is subsequently derived.

It can be concluded from (3.10) and (3.16) that the noise w_μ is zero-mean GAUSSIAN distributed and complex-valued. It follows from (3.13) that the real and imaginary parts of w_μ are statistically independent with

$$\mathrm{E}\{\Re\{w\} \, \Im\{w\}\} = 0 \, . \tag{3.36}$$

It can be seen in (3.18) that subsequent samples of w_μ are statistically independent with

$$\mathrm{E}\left\{ w_\mu \, w_{\mu-1}^* \right\} = 0 \tag{3.37}$$

since the noise samples are derived from disjoint intervals. The expectation value of the

differential correlation result is

$$\begin{aligned} m_\Psi = \mathrm{E}\{\Psi\} &= \mathrm{E}\left\{ \sum_{\mu=1}^{M-1} s_\mu \, s_{\mu-1}^* \right\} = \mathrm{E}\left\{ \sum_{\mu=1}^{M-1} (y_\mu + w_\mu) \, (y_{\mu-1}^* + w_{\mu-1}^*) \right\} = \sum_{\mu=1}^{M-1} y_\mu \, y_{\mu-1}^* \\ &= \sum_{\mu=1}^{M-1} \Big[\sqrt{2\,C}\, d_{\mathrm{s},\mu} \, R(\tau - \widehat{\tau}) \, \mathrm{sinc}(f_\mathrm{d} \, N \, T_\mathrm{s}) \, \mathrm{e}^{\mathrm{j}\,[(2\,\mu+1)\,\pi\, f_\mathrm{d}\, N\, T_\mathrm{s} + \varphi_\mathrm{c}]} \\ &\qquad \times \sqrt{2\,C}\, d_{\mathrm{s},\mu-1} \, R(\tau - \widehat{\tau}) \, \mathrm{sinc}(f_\mathrm{d} \, N \, T_\mathrm{s}) \, \mathrm{e}^{-\mathrm{j}\,[(2\,\mu-1)\,\pi\, f_\mathrm{d}\, N\, T_\mathrm{s} + \varphi_\mathrm{c}]} \Big] \\ \boxed{m_\Psi = 2\,C\, R^2(\tau - \widehat{\tau}) \, \mathrm{sinc}^2(f_\mathrm{d} \, N \, T_\mathrm{s}) \, \mathrm{e}^{\mathrm{j}\,2\,\pi\, f_\mathrm{d}\, N\, T_\mathrm{s}} \sum_{\mu=1}^{M-1} d_{\mathrm{s},\mu} \, d_{\mathrm{s},\mu-1}} \, . \end{aligned} \tag{3.38}$$

It can be observed in (3.38) that data bit transitions may lead to a degradation of the differential correlation result. The data bit value in the μ-th integration interval is denoted by $d_{\mathrm{s},\mu}$. However, as shown in Table 3.1, there are various GPS and Galileo pilot signals without navigation data, which gives $d_{\mathrm{s},\mu} = 1$. The sequence of a secondary spreading code on the other hand is known a-priori, such that it can be acquired just like the primary spreading code. Furthermore, as shown in Section 2.1, the navigation data streams are supplied by assistance data, such that they can be compensated. In order to reduce the acquisition complexity, the secondary spreading code phase could also be supplied as assistance data. Once the data stream is known, the coherent predetection results s_μ can be multiplied with the data bit value, resulting in

$$\boxed{m_\Psi|_{d_{\mathrm{s},\mu}=1} = 2\,(M-1)\,C\, R^2(\tau - \widehat{\tau}) \, \mathrm{sinc}^2(f_\mathrm{d} \, N \, T_\mathrm{s}) \, \mathrm{e}^{\mathrm{j}\,2\,\pi\, f_\mathrm{d}\, N\, T_\mathrm{s}}} \, . \tag{3.39}$$

If the differential correlation technique is applied to the data modulated GPS L1-C/A signal with the coherent integration time $N\,T_\mathrm{s} = 1\,\mathrm{ms}$, the bit transitions only occur in average on 2.5 % of the products $d_{\mathrm{s},\mu}\, d_{\mathrm{s},\mu-1}$. This translates to a degradation of the signal power by just 0.22 dB. The degradation is so low, because only opposite signs of $d_{\mathrm{s},\mu}$ and $d_{\mathrm{s},\mu-1}$ reduce the correlation power. No matter what sign the two have, their product is always positive as long as the signs are equal.

3.5 Differential Correlation Variance

The second component u of the differential correlation result Ψ in (3.32) originates from the multiplication of the deterministic predetection result y_μ and the zero-mean white Gaussian variable w_μ. The differential correlation interval is $\mu \in [0,\, M-1]$. Using

$$y_{-1} = y_M = 0 \, , \tag{3.40}$$

the accumulation of the zero-mean white Gaussian noise component in (3.32) is rearranged into

$$u = \sum_{\mu=1}^{M-1} \left(w_\mu \, y_{\mu-1}^* + y_\mu \, w_{\mu-1}^* \right) = \sum_{\mu=0}^{M-1} \left(w_\mu \, y_{\mu-1}^* + w_\mu^* \, y_{\mu+1} \right) . \tag{3.41}$$

Since the noise samples w_μ are statistically independent for different sample indices μ, the variance of the inphase component of the zero-mean white GAUSSIAN noise component is calculated as

$$\begin{aligned}
&\mathrm{E}\big\{(\Re\{u\})^2\big\} = \mathrm{E}\left\{\left(\Re\left\{\sum_{\mu=0}^{M-1}\left(w_\mu\, y_{\mu-1}^* + w_\mu^*\, y_{\mu+1}\right)\right\}\right)^2\right\} \\
&= \sum_{\mu=0}^{M-1}\mathrm{E}\Big\{\big(\Re\big\{w_\mu\, y_{\mu-1}^* + w_\mu^*\, y_{\mu+1}\big\}\big)^2\Big\} = \sum_{\mu=0}^{M-1}\mathrm{E}\Big\{\big(\Re\{w_\mu\ (y_{\mu-1} + y_{\mu+1})^*\}\big)^2\Big\} \\
&= \sum_{\mu=0}^{M-1}\big[\mathrm{E}\big\{(\Re\{w_\mu\})^2\big\}\ (\Re\{\,y_{\mu-1} + y_{\mu+1}\})^2 + \mathrm{E}\big\{(\Im\{w_\mu\})^2\big\}\ (\Im\{\,y_{\mu-1} + y_{\mu+1}\})^2\big] \\
&= \frac{\sigma_w^2}{2}\sum_{\mu=0}^{M-1}|y_{\mu+1} + y_{\mu-1}|^2 \\
&= \sigma_w^2\, C\, R^2(\tau - \widehat{\tau})\,\mathrm{sinc}^2(f_\mathrm{d}\, N\, T_\mathrm{s})\left[2 + \sum_{\mu=1}^{M-2}\left|d_{\mathrm{s},\mu+1}\,\mathrm{e}^{\mathrm{j}\,2\,\pi\,f_\mathrm{d}\,N\,T_\mathrm{s}} + d_{\mathrm{s},\mu-1}\mathrm{e}^{-\mathrm{j}\,2\,\pi\,f_\mathrm{d}\,N\,T_\mathrm{s}}\right|^2\right].
\end{aligned} \tag{3.42}$$

The quadrature variance correspondingly results in

$$\begin{aligned}
&\mathrm{E}\big\{(\Im\{u\})^2\big\} = \mathrm{E}\left\{\left(\Im\left\{\sum_{\mu=0}^{M-1}\left(w_\mu\, y_{\mu-1}^* + w_\mu^*\, y_{\mu+1}\right)\right\}\right)^2\right\} \\
&= \sum_{\mu=0}^{M-1}\mathrm{E}\Big\{\big(\Im\big\{w_\mu\, y_{\mu-1}^* + w_\mu^*\, y_{\mu+1}\big\}\big)^2\Big\} = \sum_{\mu=0}^{M-1}\mathrm{E}\Big\{\big(\Im\{w_\mu\ (y_{\mu-1} - y_{\mu+1})^*\}\big)^2\Big\} \\
&= \sum_{\mu=0}^{M-1}\big[\mathrm{E}\big\{(\Re\{w_\mu\})^2\big\}\ (\Re\{\,y_{\mu-1} - y_{\mu+1}\})^2 + \mathrm{E}\big\{(\Im\{w_\mu\})^2\big\}\ (\Im\{\,y_{\mu-1} - y_{\mu+1}\})^2\big] \\
&= \frac{\sigma_w^2}{2}\sum_{\mu=0}^{M-1}|y_{\mu+1} - y_{\mu-1}|^2 \\
&= \sigma_w^2\, C\, R^2(\tau - \widehat{\tau})\,\mathrm{sinc}^2(f_\mathrm{d}\, N\, T_\mathrm{s})\left[2 + \sum_{\mu=1}^{M-2}\left|d_{\mathrm{s},\mu+1}\,\mathrm{e}^{\mathrm{j}\,2\,\pi\,f_\mathrm{d}\,N\,T_\mathrm{s}} - d_{\mathrm{s},\mu-1}\mathrm{e}^{-\mathrm{j}\,2\,\pi\,f_\mathrm{d}\,N\,T_\mathrm{s}}\right|^2\right].
\end{aligned} \tag{3.43}$$

The third component v of the differential correlation result Ψ in (3.32) originates from multiplications of two statistically independent zero-mean GAUSSIAN variables w_μ and $w_{\mu-1}$. The product $\gamma = \alpha\,\beta$ of two uncorrelated real-valued zero-mean GAUSSIAN variables α and β with equal variances $\sigma_w^2/2$ obeys the normal product distribution [53]

$$p_\gamma(\gamma) = \int_{-\infty}^{\infty}\int_{-\infty}^{\infty}\frac{\exp\!\left(\frac{-\alpha^2}{\sigma_w^2}\right)}{\sqrt{\pi}\,\sigma_w}\,\frac{\exp\!\left(\frac{-\beta^2}{\sigma_w^2}\right)}{\sqrt{\pi}\,\sigma_w}\,\delta(\alpha\,\beta - \gamma)\,d\alpha\,d\beta = \frac{2\,\mathrm{K}_0\!\left(\frac{2|\gamma|}{\sigma_w^2}\right)}{\pi\,\sigma_w^2}\,, \tag{3.44}$$

where $\delta(\,\cdot\,)$ is the DIRAC delta distribution and

$$\mathrm{K}_0(\alpha) = \int_0^{\infty}\cos(\alpha\,\sinh(\beta))\,d\beta \tag{3.45}$$

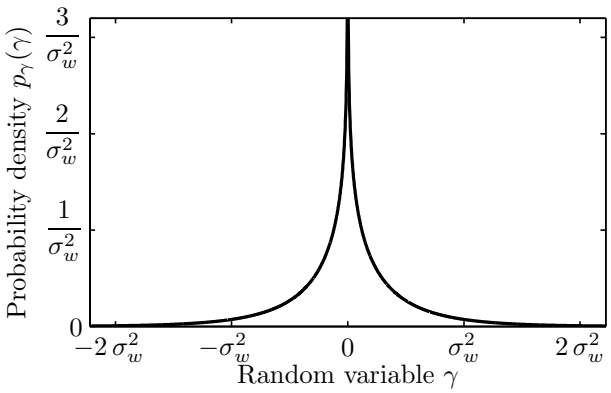

Figure 3.6: Normal product distribution.

the modified Bessel function of the second kind and zero order [54]. Fig. 3.6 illustrates the normal product distribution. The variance of the normal product distribution is

$$\begin{aligned} \mathrm{E}\{\gamma^2\} &= \int_{-\infty}^{\infty} \gamma^2\, p_\gamma(\gamma)\, d\gamma = \int_{-\infty}^{\infty}\int_{-\infty}^{\infty} \alpha^2\,\beta^2\, \frac{\exp\!\left(\frac{-\alpha^2}{\sigma_w^2}\right)}{\sqrt{\pi}\,\sigma_w}\, \frac{\exp\!\left(\frac{-\beta^2}{\sigma_w^2}\right)}{\sqrt{\pi}\,\sigma_w}\, d\alpha\, d\beta \\ &= \int_{-\infty}^{\infty} \alpha^2\, \frac{\exp\!\left(\frac{-\alpha^2}{\sigma_w^2}\right)}{\sqrt{\pi}\,\sigma_w}\, d\alpha \int_{-\infty}^{\infty} \gamma^2\, \frac{\exp\!\left(\frac{-\beta^2}{\sigma_w^2}\right)}{\sqrt{\pi}\,\sigma_w}\, d\beta = \frac{\sigma_w^2}{2}\,\frac{\sigma_w^2}{2} = \frac{\sigma_w^4}{4}\,. \end{aligned} \tag{3.46}$$

The last summand in (3.32) constitutes an accumulation of the four normal product distributed variables

$$\begin{aligned} v = \sum_{\mu=1}^{M-1} w_\mu\, w_{\mu-1}^* = \sum_{\mu=1}^{M-1} \big[&\Re\{w_\mu\}\,\Re\{w_{\mu-1}\} + \Im\{w_\mu\}\,\Im\{w_{\mu-1}\} \\ &+ \mathrm{j}\,(\Im\{w_\mu\}\,\Re\{w_{\mu-1}\} - \Re\{w_\mu\}\,\Im\{w_{\mu-1}\})\big]. \end{aligned} \tag{3.47}$$

Using the central limit theorem, for a sufficiently large M, the variable v converges to a zero-mean Gaussian variable with the variance

$$\begin{aligned} \mathrm{E}\{|v|^2\} = \mathrm{E}\left\{\left|\sum_{\mu=1}^{M-1} w_\mu\, w_{\mu-1}^*\right|^2\right\} &= \sum_{\mu=1}^{M-1} \mathrm{E}\Big\{\big(\Re\{w_\mu\, w_{\mu-1}^*\}\big)^2 + \big(\Im\{w_\mu\, w_{\mu-1}^*\}\big)^2\Big\} \\ &= (M-1)\,\sigma_w^4\,. \end{aligned} \tag{3.48}$$

Fig. 3.7 compares the Gaussian approximation of v in (3.47) to simulation results where v is precisely calculated. It can be seen that the approximation holds with a high degree of accuracy even for low values of the noncoherent integration number M in the order of 10. However, large values of M in the order of 100–1000 are typical for enhanced sensitivity Galileo/GPS reception and result in virtually no difference between the Gaussian approximation and the precise result.

By combining (3.42), (3.43), and (3.48), the differential correlation result Ψ in (3.32) can be approximated for sufficiently large M as Gaussian distributed with the mean given in (3.39). The inphase and quadrature components are statistically independent. The inphase

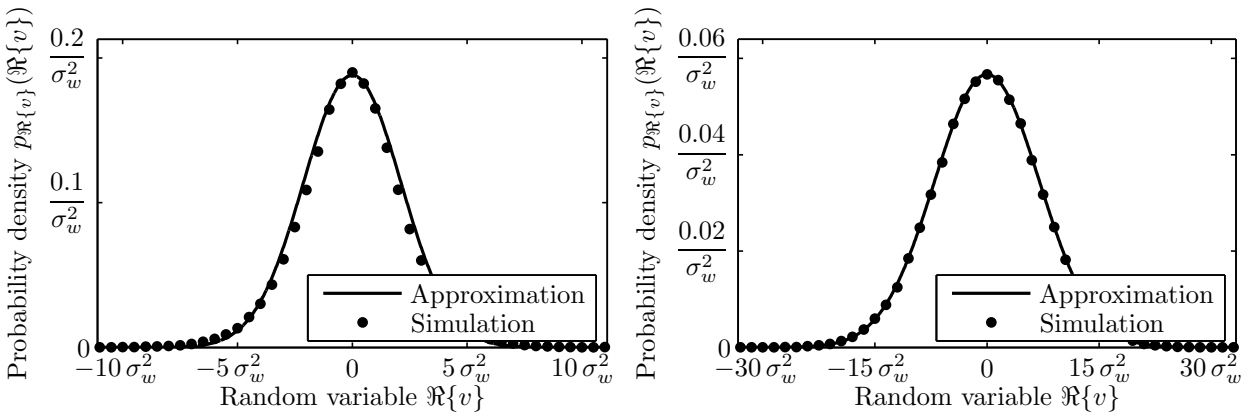

(a) $M = 10$. (b) $M = 100$.

Figure 3.7: Comparison of the GAUSSIAN approximation of v in (3.47) versus the simulation results.

variance is

$$\boxed{\sigma_{\Psi,\mathrm{I}}^2 = \mathrm{E}\big\{\Re\{\Psi - \mathrm{E}\{\Psi\}\}^2\big\} = \frac{(M-1)\,\sigma_w^4}{2} + \sigma_w^2\,C\,R^2(\tau-\widehat{\tau})\,\mathrm{sinc}^2(f_\mathrm{d}\,N\,T_\mathrm{s}) \left[2 + \sum_{\mu=1}^{M-2}\left|d_{\mathrm{s},\mu+1}\,\mathrm{e}^{\mathrm{j}\,2\,\pi\,f_\mathrm{d}\,N\,T_\mathrm{s}} + d_{\mathrm{s},\mu-1}\mathrm{e}^{-\mathrm{j}\,2\,\pi\,f_\mathrm{d}\,N\,T_\mathrm{s}}\right|^2\right]} \tag{3.49}$$

and the quadrature variance is

$$\boxed{\sigma_{\Psi,\mathrm{Q}}^2 = \mathrm{E}\big\{\Im\{\Psi - \mathrm{E}\{\Psi\}\}^2\big\} = \frac{(M-1)\,\sigma_w^4}{2} + \sigma_w^2\,C\,R^2(\tau-\widehat{\tau})\,\mathrm{sinc}^2(f_\mathrm{d}\,N\,T_\mathrm{s}) \left[2 + \sum_{\mu=1}^{M-2}\left|d_{\mathrm{s},\mu+1}\,\mathrm{e}^{\mathrm{j}\,2\,\pi\,f_\mathrm{d}\,N\,T_\mathrm{s}} - d_{\mathrm{s},\mu-1}\mathrm{e}^{-\mathrm{j}\,2\,\pi\,f_\mathrm{d}\,N\,T_\mathrm{s}}\right|^2\right]}. \tag{3.50}$$

The variables σ_w^2, $R(\tau-\widehat{\tau})$, f_d, and $d_{\mathrm{s},\mu}$ are specified in (3.19), (3.28), (3.9), and (3.22), respectively. Using $y_{-1} = y_M = 0$, the combined inphase and quadrature variance is

$$\begin{aligned}
\sigma_\Psi^2 &= \mathrm{E}\big\{|\Psi - \mathrm{E}\{\Psi\}|^2\big\} = \sigma_{\Psi,\mathrm{I}}^2 + \sigma_{\Psi,\mathrm{Q}}^2 \\
&= (M-1)\,\sigma_w^4 + \frac{\sigma_w^2}{2}\sum_{\mu=0}^{M-1}|y_{\mu+1} + y_{\mu-1}|^2 + \frac{\sigma_w^2}{2}\sum_{\mu=0}^{M-1}|y_{\mu+1} - y_{\mu-1}|^2 \\
&= (M-1)\,\sigma_w^4 + \sigma_w^2\sum_{\mu=1}^{M-1}\left(|y_\mu|^2 + |y_{\mu-1}|^2\right) \\
&= (M-1)\,\sigma_w^4 + 2\,\sigma_w^2\,C\,R^2(\tau-\widehat{\tau})\,\mathrm{sinc}^2(f_\mathrm{d}\,N\,T_\mathrm{s}) \\
&\quad \sum_{\mu=1}^{M-1}\left(\left|d_{\mathrm{s},\mu}\,\mathrm{e}^{\mathrm{j}\,2\,\pi\,f_\mathrm{d}\,N\,T_\mathrm{s}}\right|^2 + \left|d_{\mathrm{s},\mu-1}\mathrm{e}^{-\mathrm{j}\,2\,\pi\,f_\mathrm{d}\,N\,T_\mathrm{s}}\right|^2\right) \\
&\boxed{\sigma_\Psi^2 = (M-1)\,\sigma_w^4 + 4\,(M-1)\,\sigma_w^2\,C\,R^2(\tau-\widehat{\tau})\,\mathrm{sinc}^2(f_\mathrm{d}\,N\,T_\mathrm{s})}\,.
\end{aligned} \tag{3.51}$$

As elaborated in Section 3.4, the new pilot signals without data stream offer the advantage of extended coherent integration intervals to enhance the reception sensitivity. The data

streams of the non-pilot signals can be provided as assistance data for the same reason. If the modulation by the navigation data is eliminated or the received signal is a pilot signal such that $d_{\mathrm{s},\mu} = 1$, then (3.49) and (3.50) can be simplified to

$$\boxed{\sigma^2_{\Psi,\mathrm{I}}\big|_{d_{\mathrm{s},\mu}=1} = \frac{(M-1)\,\sigma_w^4}{2} + 2\,\sigma_w^2\,C\,R^2(\tau-\widehat{\tau})\,\mathrm{sinc}^2(f_\mathrm{d}\,N\,T_\mathrm{s})\\ \big[1+2\,(M-2)\,\cos^2(2\,\pi\,f_\mathrm{d}\,N\,T_\mathrm{s})\big]}\,, \tag{3.52}$$

and

$$\boxed{\sigma^2_{\Psi,\mathrm{Q}}\big|_{d_{\mathrm{s},\mu}=1} = \frac{(M-1)\,\sigma_w^4}{2} + 2\,\sigma_w^2\,C\,R^2(\tau-\widehat{\tau})\,\mathrm{sinc}^2(f_\mathrm{d}\,N\,T_\mathrm{s})\\ \big[1+2\,(M-2)\,\sin^2(2\,\pi\,f_\mathrm{d}\,N\,T_\mathrm{s})\big]}\,. \tag{3.53}$$

It can be observed that the variances of the inphase and quadrature components differ. For mathematical simplicity and since it is advantageous for indoor reception, the pilot signals or signals with eliminated navigation data stream are subsequently considered.

3.6 Synchronization Detection

The differential correlation result Ψ as specified in (3.39), (3.52), and (3.53) is complex-valued, has an unknown signal phase, and is buried in zero-mean complex-valued white Gaussian noise. As derived in Section 2.3, the estimation of the unknown code phase τ is best accomplished by maximizing the magnitude or squared magnitude of the differential correlation result [27, 28]

$$\boxed{\Lambda = |\Psi|^2 = \Re\{\Psi\}^2 + \Im\{\Psi\}^2}\,. \tag{3.54}$$

The squared magnitude usually causes less implementation expenses. The corresponding signal processing flow is illustrated in Fig. 3.3.

The real and imaginary components of Ψ are Gaussian distributed and have a nonzero mean. Squaring them leads to a noncentral Chi-squared distributed variable with two degrees of freedom [28, 55]. The decision statistic Λ is thus the sum of two statistically independent noncentral Chi-squared distributed variables with different variances. It therefore obeys the probability density [56]

$$\begin{aligned} p_\Lambda(\Lambda) =& \frac{1}{2\,\sigma_{\Psi,\mathrm{I}}\,\sigma_{\Psi,\mathrm{Q}}}\exp\!\left(-\frac{\Lambda}{2\,\sigma^2_{\Psi,\mathrm{I}}} - \frac{\Re\{m_\Psi\}^2}{2\,\sigma^2_{\Psi,\mathrm{I}}} - \frac{\Im\{m_\Psi\}^2}{2\,\sigma^2_{\Psi,\mathrm{Q}}}\right)\sum_{\alpha=0}^{\infty}\sum_{\beta=0}^{\infty}\left[\frac{\Gamma\!\left(\frac{1}{2}+\alpha+\beta\right)}{\alpha!\,\beta!\,\Gamma\!\left(\frac{1}{2}+\beta\right)}\right.\\ &\left.\times\left(\frac{\sqrt{\Lambda}\,\Im\{m_\Psi\}^2\,\sigma^2_{\Psi,\mathrm{I}}}{2\,\Re\{m_\Psi\}\,\sigma^4_{\Psi,\mathrm{Q}}}\right)^{\beta}\left(\frac{\sqrt{\Lambda}\,\left(\sigma^2_{\Psi,\mathrm{Q}}-\sigma^2_{\Psi,\mathrm{I}}\right)}{\Re\{m_\Psi\}\,\sigma^2_{\Psi,\mathrm{Q}}}\right)^{\alpha}\mathrm{I}_{\alpha+\beta}\!\left(\frac{\sqrt{\Lambda}\,\Re\{m_\Psi\}}{\sigma^2_{\Psi,\mathrm{I}}}\right)\right], \end{aligned} \tag{3.55}$$

where

$$\Gamma(\alpha) = \int_0^\infty \beta^{\alpha-1}\exp(-\beta)\,\mathrm{d}\beta \tag{3.56}$$

is the Gamma function and

$$\mathrm{I}_\kappa(\alpha) = \frac{1}{\pi}\int_0^\pi \exp[\alpha\,\cos(\beta)]\,\cos(\kappa\,\beta)\,d\beta \tag{3.57}$$

is the modified BESSEL function of the first kind and order κ [53, 54]. The mean value m_Ψ, the inphase variance $\sigma^2_{\Psi,\mathrm{I}}$, and the quadrature variance $\sigma^2_{\Psi,\mathrm{Q}}$ are specified in (3.39), (3.52), and (3.53), respectively. The corresponding cumulative distribution is [56]

$$\begin{aligned} P_\Lambda(\Lambda) =& \frac{\sigma_{\Psi,\mathrm{I}}}{\sigma_{\Psi,\mathrm{Q}}} \exp\!\left(-\frac{\Im\{m_\Psi\}^2}{2\,\sigma^2_{\Psi,\mathrm{Q}}}\right) \sum_{\alpha=0}^{\infty}\sum_{\beta=0}^{\infty} \left(\frac{\Gamma\!\left(\frac{1}{2}+\alpha+\beta\right)}{\alpha!\,\beta!\,\Gamma\!\left(\frac{1}{2}+\beta\right)}\right) \left(\frac{\Im\{m_\Psi\}^2\,\sigma^2_{\Psi,\mathrm{I}}}{2\,\sigma^2_{\Psi,\mathrm{Q}}}\right)^{\beta} \\ & \times \left(\frac{\sigma^2_{\Psi,\mathrm{Q}}-\sigma^2_{\Psi,\mathrm{I}}}{\sigma^2_{\Psi,\mathrm{Q}}}\right)^{\alpha} \left[1-\mathrm{Q}_{1+\alpha+\beta}\!\left(\frac{\Re\{m_\Psi\}}{\sigma_{\Psi,\mathrm{I}}},\,\frac{\sqrt{\Lambda}}{\sigma_{\Psi,\mathrm{I}}}\right)\right]\Bigg), \end{aligned} \tag{3.58}$$

where

$$\mathrm{Q}_M(\alpha,\,\beta) = \exp\!\left(-\frac{\alpha^2+\beta^2}{2}\right) \sum_{\kappa=1-M}^{\infty} \left(\frac{\alpha}{\beta}\right)^{\kappa} \mathrm{I}_\kappa(\alpha\,\beta) \tag{3.59}$$

is the MARCUM-Q function of order M [28].

The reception sensitivity can be approximated with a high degree of accuracy by substituting the inphase and quadrature variances $\sigma^2_{\Psi,\mathrm{I}}$ and $\sigma^2_{\Psi,\mathrm{Q}}$ by half of their combined variance σ^2_Ψ as specified in (3.51). Simulations of the precise probability of detection for the differential correlation technique will be presented later in Section 3.8. The simulation feeds the algorithm in (3.32) with the GAUSSIAN distributed predetection samples s_μ as specified in (3.14), (3.19), and (3.31). There is no observable difference to the approximated result for long observation periods $M\,N\,T_\mathrm{s}$. In case of short observation periods, the approximation delivers slightly lower probabilities of detection P_d where P_d is low, but both match for $P_\mathrm{d} = 90\,\%$, which is typically used to express the reception sensitivity of navigation receivers. The approximation of Λ obeys the noncentral CHI-SQUARED distribution [28, 56]

$$p_\Lambda(\Lambda) \simeq \frac{1}{\sigma^2_\Psi} \exp\!\left(-\frac{\Lambda+|m_\Psi|^2}{\sigma^2_\Psi}\right) \mathrm{I}_0\!\left(\frac{2\sqrt{\Lambda\,|m_\Psi|^2}}{\sigma^2_\Psi}\right). \tag{3.60}$$

The corresponding noncentral CHI-SQUARED cumulative distribution is [28, 56]

$$P_\Lambda(\Lambda) \simeq 1-\mathrm{Q}_1\!\left(\sqrt{\frac{2\,|m_\Psi|^2}{\sigma^2_\Psi}},\,\sqrt{\frac{2\Lambda}{\sigma^2_\Psi}}\right). \tag{3.61}$$

3.7 Detection Threshold

The expectation value of the decision statistic Λ is maximal, if the estimated code phase $\widehat{\tau}$ matches the actual code phase τ. However, the signal-to-noise ratio of Λ can become very low if the satellite signal is heavily attenuated or blocked. The lower the signal-to-noise ratio of Λ is, the higher the chance that an out-of-phase autocorrelation value combined with the received noise exceeds the actual correlation peak plus noise. Due to the unknown signal attenuation, it is not reliable to just determine the code phase τ based on the highest value of Λ. Instead, the highest value of Λ also has to be sufficiently large, such that a correlation peak can be assumed. It is therefore compared to a detection threshold λ. If Λ exceeds the

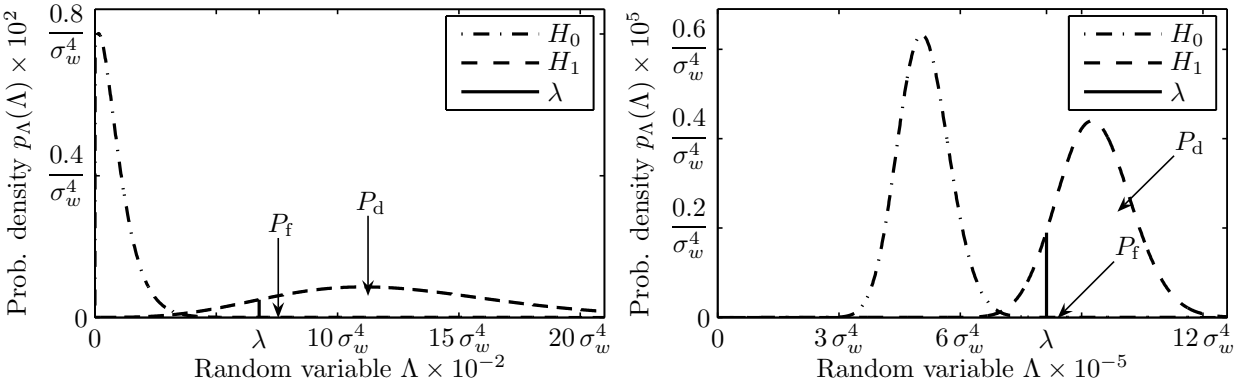

(a) $M = 25$ and $C/\mathcal{N}_0 = 28.5\,\mathrm{dBHz}$. (b) $M = 2500$ and $C/\mathcal{N}_0 = 22.85\,\mathrm{dBHz}$.

Figure 3.8: Probability distributions of the decision statistic Λ for GPS L1-C/A with $T_0 = 290\,\mathrm{K}$, $B = 4.092\,\mathrm{MHz}$, $F = 3\,\mathrm{dB}$, $N\,T_\mathrm{s} = 4\,\mathrm{ms}$, $P_\mathrm{f} = 10^{-5}$, and $P_\mathrm{d} = 90\,\%$.

threshold, hypothesis H_1 is assumed

$$\boxed{\Lambda \underset{\mathrm{H}_0}{\overset{\mathrm{H}_1}{\gtrless}} \lambda}\,. \tag{3.62}$$

Hypothesis H_1 represents the case where the estimated code phase $\widehat{\tau}$ corresponds to the actual code phase τ. Hypothesis H_0 represents the out-of-phase correlation and is assumed if Λ does not exceed the threshold.

The detection threshold λ of satellite navigation receivers is typically determined with the Neyman-Pearson criterion [30, 31]. It maximizes the probability of detection P_d for a given false detection probability P_f [27].

The probability of false detection

$$P_\mathrm{f} = \Pr\{\Lambda \geqslant \lambda | \mathrm{H}_0\} = \int_\lambda^\infty p_{\Lambda|\mathrm{H}_0}(\Lambda)\,d\Lambda = 1 - P_{\Lambda|\mathrm{H}_0}(\lambda) = \mathrm{Q}_1\left(\sqrt{\frac{2\,|m_{\Psi,\mathrm{H}_0}|^2}{\sigma^2_{\Psi,\mathrm{H}_0}}},\, \sqrt{\frac{2\,\lambda}{\sigma^2_{\Psi,\mathrm{H}_0}}}\right) \tag{3.63}$$

with

$$m_{\Psi,\mathrm{H}_0} = m_\Psi\big|_{R^2(\tau-\widehat{\tau})=R^2_\mathrm{m}}\,, \quad \sigma^2_{\Psi,\mathrm{H}_0} = \sigma^2_\Psi\big|_{R^2(\tau-\widehat{\tau})=R^2_\mathrm{m}} \tag{3.64}$$

is the probability that the maximum out-of-phase autocorrelation value R_m leads to a false detection [29]. The maximum out-of-phase autocorrelation values for zero frequency deviation are $R_\mathrm{m} = 65\,N/1023$ for GPS L1-C/A and $R_\mathrm{m} = 0.094\,N$ for Galileo E1-C [5, 29]. Fig. 3.8 illustrates the probability distributions of Λ for hypothesis H_0 and H_1. Since Fig. 3.8.a and 3.8.b illustrate the distributions for different accumulation numbers M, different $C/\mathcal{N}_0$ values have been chosen to plot hypothesis H_1. The $C/\mathcal{N}_0$ values have been selected to illustrate the case for $P_\mathrm{d} \simeq 90\,\%$. The detection thresholds λ are inserted for the false detection probability of $P_\mathrm{f} = 10^{-5}$. Without a-priori information, the received signal power C has to be assumed to be the line-of-sight signal power, as specified in Table 3.1.

The receiver parameters in Fig. 3.8 are typical values frequently used in similar publications. The noise temperature $T_0 = 290\,\mathrm{K}$ is a typical indoor temperature. The front-end filter bandwidth $B = 4.092\,\mathrm{MHz}$ is the zero-to-zero bandwidth of the Gaileo E1-B/C signals. The GPS L1-C/A zero-to-zero bandwidth is only half this value. However, the reception sensitivity is not degraded by extending the bandwidth, as long as the NYQUIST sampling rate is met. The front-end noise figure $F = 3\,\mathrm{dB}$ is a typical value for enhanced sensitivity GPS receivers. A single shot positioning receiver typically requires a lower false detection probability P_f per code phase search bin than a conventional tracking receiver. If false detection occurs during the acquisition process of a tracking receiver, it will be discovered during the tracking operation and reacquisition takes place until the correct code phase is determined. However, a single shot positioning receiver only performs the acquisition process and not the tracking operation. Based on the code phase estimates of the acquisition process, it immediately calculates the position. Depending on the navigation algorithm and the amount of code phase error, the false detection may thus go unnoticed, resulting in a large positioning error. Experience indicates that a false detection probability in the order of $P_\mathrm{f} = 10^{-5}$ offers a good trade-off for highly parallel correlation engines, which calculate several 10,000 correlation results simultaneously. The probability of a false detection for the complete search is the false detection probability per search bin times the total number of search bins. The probability of detection $P_\mathrm{d} = 90\,\%$ is often cited in literature to compare the reception sensitivity of different receiver techniques.

With (3.63), the optimal detection threshold

$$\boxed{\lambda = P^{-1}_{\Lambda|\mathrm{H}_0}(1-P_\mathrm{f}) = \frac{\sigma^2_{\Psi,\mathrm{H}_0}}{2}\left[\mathrm{Q}^{-1}_{1,\beta}\left(\sqrt{\frac{2\,|m_{\Psi,\mathrm{H}_0}|^2}{\sigma^2_{\Psi,\mathrm{H}_0}}},\, P_\mathrm{f}\right)\right]^2} \tag{3.65}$$

equals the inverse cumulative distribution of Λ for the false detection hypothesis $P^{-1}_{\Lambda|\mathrm{H}_0}(\cdot)$, which can be obtained with the inverse first-order MARCUM-Q function with respect to its second argument $\mathrm{Q}^{-1}_{1,\beta}(\alpha,\,\gamma)$. The inverse MARCUM-Q function can be solved by numerical methods [57].

3.8 Differential Correlation Sensitivity

The probability of detection

$$\boxed{P_\mathrm{d} = \Pr\{\Lambda \geqslant \lambda|\mathrm{H}_1\} = \int_\lambda^\infty p_{\Lambda|\mathrm{H}_1}(\Lambda)\,d\Lambda = 1 - P_{\Lambda|\mathrm{H}_1}(\lambda) = \mathrm{Q}_1\left(\sqrt{\frac{2\,|m_{\Psi,\mathrm{H}_1}|^2}{\sigma^2_{\Psi,\mathrm{H}_1}}},\,\sqrt{\frac{2\,\lambda}{\sigma^2_{\Psi,\mathrm{H}_1}}}\right)} \tag{3.66}$$

with

$$m_{\Psi,\mathrm{H}_1} = m_\Psi\big|_{R^2(\tau-\widehat{\tau})=N^2}\,, \quad \sigma^2_{\Psi,\mathrm{H}_1} = \sigma^2_\Psi\big|_{R^2(\tau-\widehat{\tau})=N^2} \tag{3.67}$$

is the probability that the decision statistic Λ is above the detection threshold λ when the estimated code phase equals the actual code phase $\widehat{\tau} = \tau$. Fig. 3.9 compares the resulting theoretical probabilities of detection P_d to the precise simulation results without using the

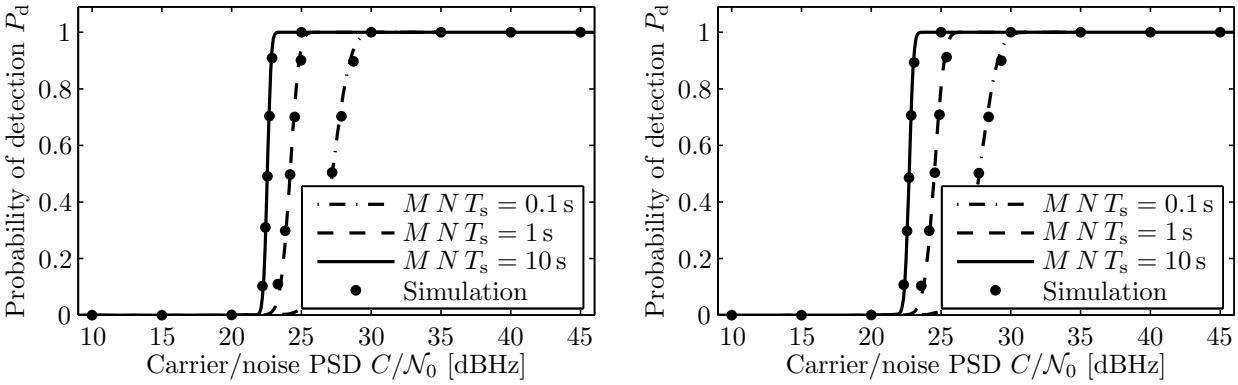

(a) GPS L1-C/A with $f_d = 0$. (b) GPS L1-C/A with $f_d = 60\,\text{Hz}$.

Figure 3.9: Detection probability with the differential correlation technique for $T_0 = 290\,\text{K}$, $F = 3\,\text{dB}$, $N\,T_s = 4\,\text{ms}$, and $P_f = 10^{-5}$.

presented approximations. The dots denoted *Simulation* in Fig. 3.9 and all corresponding subsequent figures represent actual simulation results without using any of the approximations introduced by this work. The dots represent simulations of the signal flow in Fig. 3.3, where the Galileo/GPS signal plus additive white GAUSSIAN noise samples are used as input. These true simulations are supplied to validate the theoretical derivations of this work. The solid and dashed lines in Fig. 3.9, on the other hand, are calculated with (3.66) using (3.65). The sensitivity limit can be found in Fig. 3.9, where the detection probability suddenly decreases. The longer the coherent integration period $M\,N\,T_s$, the better the reception sensitivity. To compare different receiver techniques, the $C/\mathcal{N}_0$ value for $P_d = 90\,\%$ is often quoted.

It can be observed that the theoretical result matches the simulation result with a very high degree of accuracy. The detection probability of 90 % will be subsequently used to characterize the reception sensitivity. In Fig. 3.9 there is no relevant difference between the simulation and the theoretical derivation for $P_d = 90\,\%$. The applied receiver parameters of $T_0 = 290\,\text{K}$, $F = 3\,\text{dB}$, and $P_f = 10^{-5}$ are reasonable values for enhanced sensitivity reception. They are elaborated in Section 3.7 and found frequently in literature to compare receiver algorithms. The reception sensitivity is independent of the front-end bandwidth B, as long as the bandwidth is sufficiently wide to capture the signal energy, the corresponding NYQUIST sampling rate is applied, and no interference other than white thermal noise is considered. The highest $C/\mathcal{N}_0$ value in Fig. 3.9 of 45.5 dBHz corresponds to the line-of-sight signal power without attenuation. The lowest $C/\mathcal{N}_0$ value of 10 dBHz is reached by the combination of all techniques subsequently presented in this work. The noise power spectral density $\mathcal{N}_0$ is defined in (3.12) and does not include the noise figure F.

Fig. 3.10 summarizes the carrier-to-noise PSD values $C_D/\mathcal{N}_0$, where the differential correlation yields the detection probability $P_d = 90\,\%$. The range for $C_D/\mathcal{N}_0$ is chosen equal to the total dynamic range that is achieved by the correlation techniques in the subsequent chapters. All figures summarizing the reception sensitivities in this work are plotted in the same range of 10–35 dBHz to ease the comparison of the different techniques. The maximum reception sensitivity in Fig. 3.10 appears to be bound. This effect is due to the out-of-phase autocorrelation properties of the spreading code. The correlation functions for GPS and

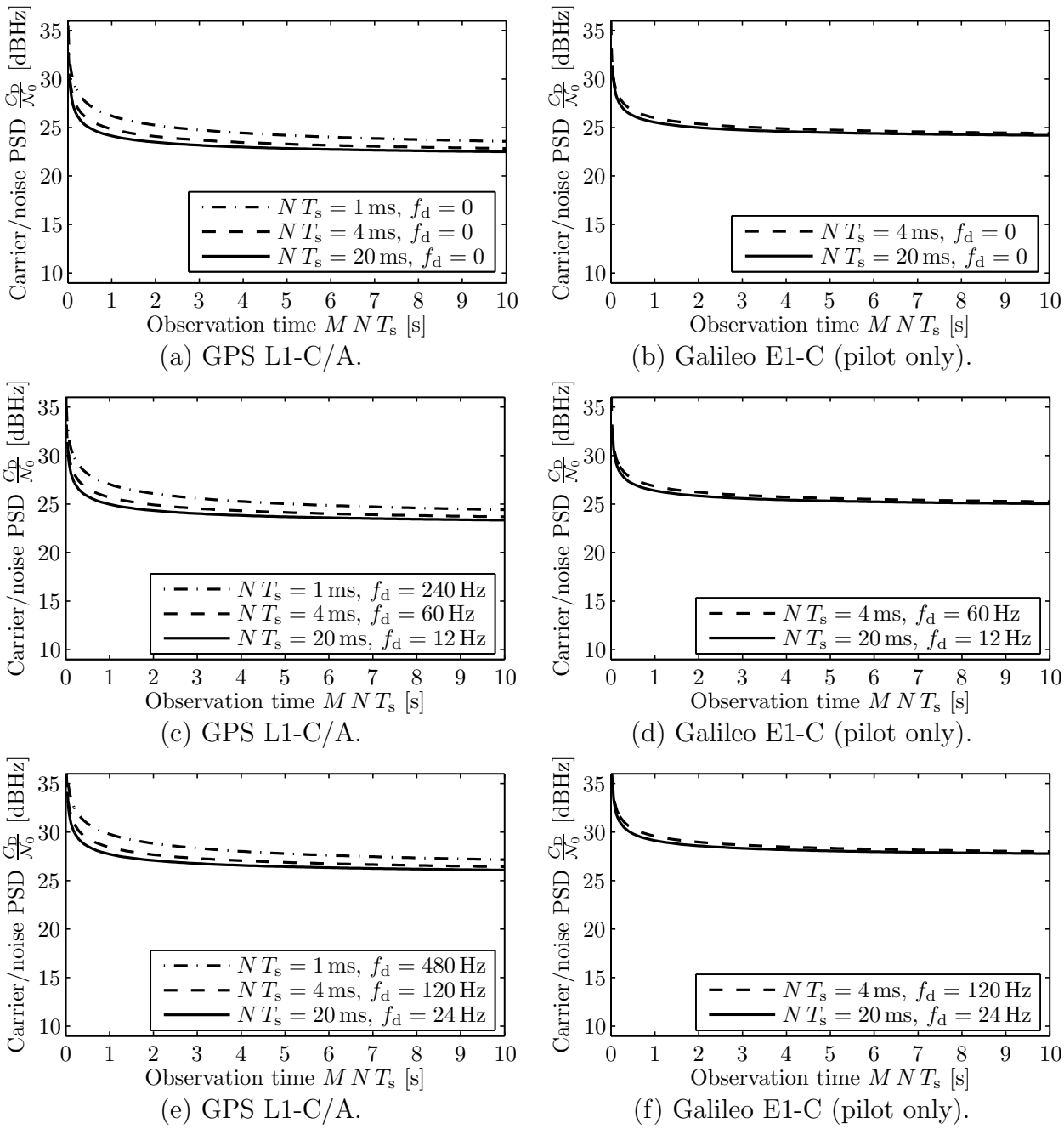

(a) GPS L1-C/A. (b) Galileo E1-C (pilot only).

(c) GPS L1-C/A. (d) Galileo E1-C (pilot only).

(e) GPS L1-C/A. (f) Galileo E1-C (pilot only).

Figure 3.10: Reception sensitivity with the differential correlation technique for $T_0 = 290\,\mathrm{K}$, $F = 3\,\mathrm{dB}$, $P_\mathrm{f} = 10^{-5}$, and $P_\mathrm{d} = 90\,\%$.

Galileo have been introduced in Section 3.3. The maximum out-of-phase correlation value of the GPS L1-C/A spreading codes is $R_\mathrm{m} = 65\,N/1023$ [29]. The Galileo E1-B (data) and E1-C (pilot) signals are transmitted jointly on the inphase component of a single carrier. The maximum out-of-phase autocorrelation value for despreading the Galileo E1-B/C signals with the Galileo E1-B or the Galileo E1-C codes is $R_\mathrm{m} = 0.094\,N$ [5]. It is slightly larger than for GPS L1-C/A due to cross-correlation between the Galileo E1-B and E1-C signals. For this reason, the maximum reception sensitivity in Fig. 3.10 is slightly worse for Galileo E1-C than for GPS L1-C/A. However, the next chapter will introduce an *adaptive detection threshold* method, which allows the reception of significantly weaker signals. This technique will also neutralize the difference between GPS and Galileo in Fig. 3.10.

3.9 Coherent Integration Sensitivity

As summarized in Sections 2.3 and 2.4, current state-of-the-art GPS receivers utilize either the squared magnitude of the predetection samples s_μ in (3.14) or a noncoherent accumulation of the squared magnitudes of the predetection samples as the decision statistic Λ. This section compares the reception sensitivities of the *differential correlation* method to the technique of *long coherent integration*.

The squared magnitude of the coherently integrated predetection samples

$$\Lambda = |s_\mu|^2 = |y_\mu + w_\mu|^2 \tag{3.68}$$

obeys the noncentral CHI-SQUARED distribution with the cumulative density function [28, 56]

$$P_\Lambda(\Lambda) = 1 - \mathrm{Q}_1\left(\sqrt{\frac{2\,|y_\mu|^2}{\sigma_w^2}},\, \sqrt{\frac{2\Lambda}{\sigma_w^2}}\right). \tag{3.69}$$

The optimal detection threshold

$$\lambda = P^{-1}_{\Lambda|\mathrm{H}_0}(1 - P_\mathrm{f}) = \frac{\sigma_w^2}{2}\left[\mathrm{Q}^{-1}_{1,\beta}\left(\sqrt{\frac{2\,|y_{\mu,\mathrm{H}_0}|^2}{\sigma_w^2}},\, P_\mathrm{f}\right)\right]^2 \tag{3.70}$$

with

$$y_{\mu,\mathrm{H}_0} = y_\mu\big|_{R(\tau-\widehat{\tau})=R_\mathrm{m}} \tag{3.71}$$

can therefore be obtained with the inverse first-order MARCUM-Q function with respect to its second argument $\mathrm{Q}^{-1}_{1,\beta}(\alpha,\, P_\mathrm{f})$. The variables σ_w^2 and f_d are specified in (3.19) and (3.9). The resulting probability of detection is

$$P_\mathrm{d} = \Pr\{\Lambda > \lambda|\mathrm{H}_1\} = 1 - P_{\Lambda|\mathrm{H}_1}(\lambda) = \mathrm{Q}_1\left(\sqrt{\frac{2\,|y_{\mu,\mathrm{H}_1}|^2}{\sigma_w^2}},\, \sqrt{\frac{2\lambda}{\sigma_w^2}}\right), \tag{3.72}$$

with

$$y_{\mu,\mathrm{H}_1} = y_\mu\big|_{R(\tau-\widehat{\tau})=N}. \tag{3.73}$$

Fig. 3.11 illustrates the probabilities of detection P_d. For $f_\mathrm{d} = 0$ in Fig. 3.11.a, the reception sensitivity increases with increasing coherent integration period. However, for $f_\mathrm{d} = 60\,\mathrm{Hz}$ in Fig. 3.11.b, the long integration $N\,T_\mathrm{s} = 20\,\mathrm{ms}$ is already too long and delivers a worse performance than $N\,T_\mathrm{s} = 1\,\mathrm{ms}$. The reason is that extending the coherent integration reduces the size of the frequency search bins. The frequency deviation of 60 Hz is already outside the search bin for $N\,T_\mathrm{s} = 20\,\mathrm{ms}$.

Fig. 3.12 summarizes the achievable reception sensitivities for $P_\mathrm{d} = 90\,\%$. This figure shows the vulnerability of long coherent integration intervals to nonzero frequency deviations f_d, which makes it unsuitable for deep urban and moderate indoor reception. If the frequency deviation f_d leads to a signal phase in (3.8) which extends too far, then the term $\mathrm{sinc}(f_\mathrm{d}\,N\,T_\mathrm{s})$ in (3.39) has a low value, such that the deterministic component of Λ becomes low. Thus, the probability of detection may decrease with a growing integration period $N\,T_\mathrm{s}$. It can be

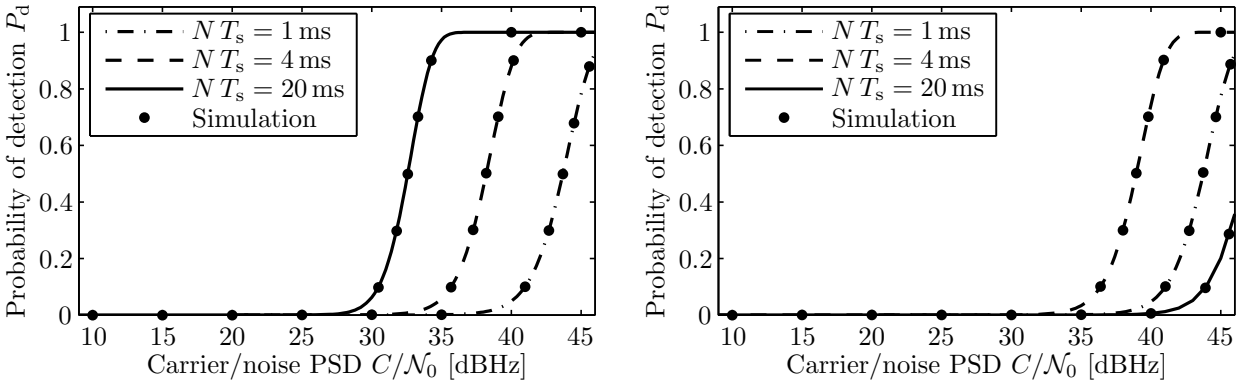

(a) GPS L1-C/A with $f_d = 0$. (b) GPS L1-C/A with $f_d = 60\,\text{Hz}$.

Figure 3.11: Detection probability with the long coherent integration method for $T_0 = 290\,\text{K}$, $F = 3\,\text{dB}$, and $P_f = 10^{-5}$.

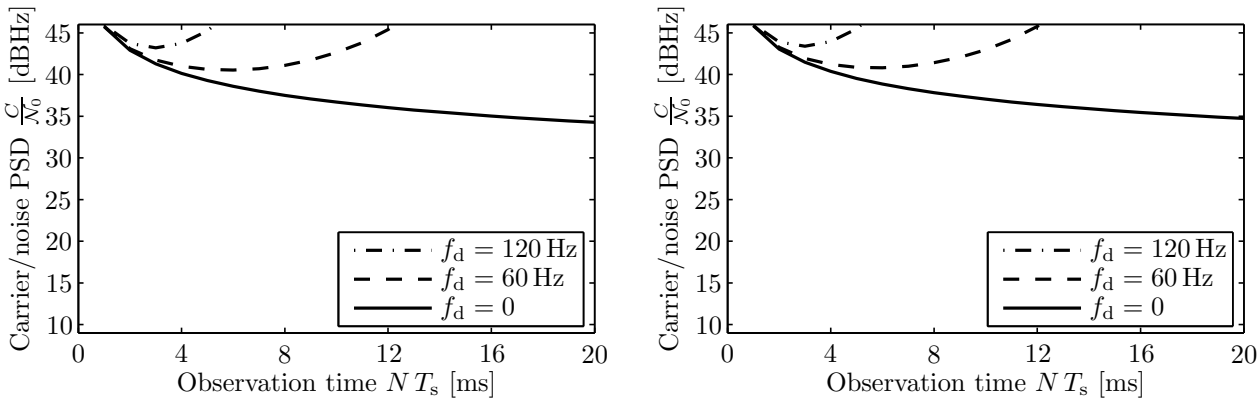

(c) GPS L1-C/A. (d) Galileo E1-C (pilot only).

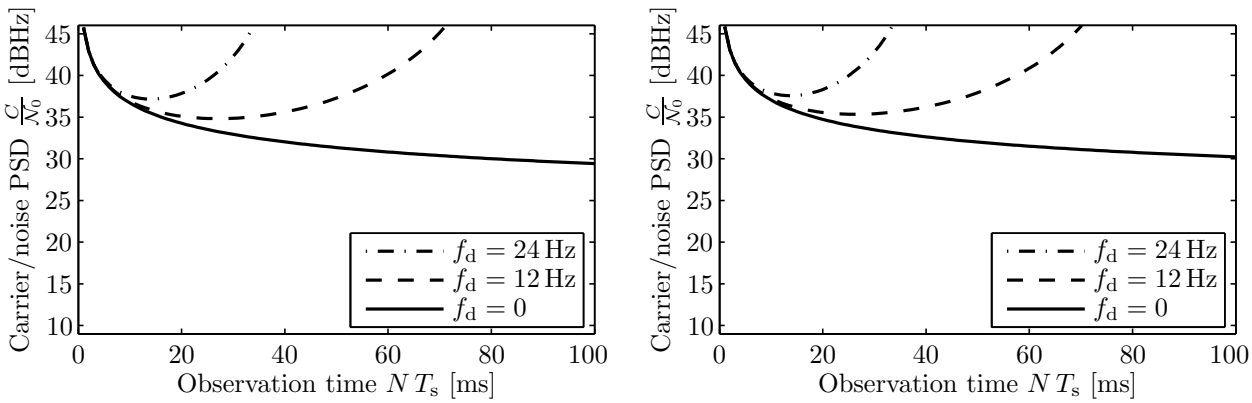

(a) GPS L1-C/A. (b) Galileo E1-C (pilot only).

Figure 3.12: Reception sensitivity with the long coherent integration method for $T_0 = 290\,\text{K}$, $F = 3\,\text{dB}$, $P_f = 10^{-5}$, and $P_d = 90\,\%$.

observed in Fig. 3.12 that the coherent integration periods $N\,T_s = 1\,\text{ms}$, $N\,T_s = 4\,\text{ms}$, and $N\,T_s = 20\,\text{ms}$ are suitable for frequency deviations of up to $f_d = 480\,\text{Hz}$, $f_d = 120\,\text{Hz}$, and $f_d = 24\,\text{Hz}$ respectively. The differential correlation technique introduced earlier does not show this vulnerability to nonzero frequency deviations f_d. It can extend the observation period indefinitely without degrading the reception sensitivity, as illustrated in Fig. 3.10.

3.10 Noncoherent Integration Sensitivity

Section 2.4 outlines the noncoherent integration as the current state-of-the art method for enhanced sensitivity reception. As opposed to very long coherent integration intervals, the noncoherent integration can sustain a certain degree of frequency deviation. Since s_μ is a nonzero-mean white GAUSSIAN variable, the decision statistic of the noncoherent integration

$$\Lambda = \sum_{\mu=1}^{M} |s_\mu|^2 = \sum_{\mu=1}^{M} |y_\mu + w_\mu|^2 \tag{3.74}$$

obeys the noncentral CHI-SQUARED distribution with the cumulative probability density function [28, 56]

$$P_\Lambda(\Lambda) = 1 - \mathrm{Q}_M\left(\sqrt{\frac{2\,M\,|y_\mu|^2}{\sigma_w^2}},\, \sqrt{\frac{2\Lambda}{\sigma_w^2}}\right). \tag{3.75}$$

The detection threshold

$$\lambda = \frac{\sigma_w^2}{2}\left[\mathrm{Q}_{M,\beta}^{-1}\left(\sqrt{\frac{2\,M\,|y_{\mu,\mathrm{H}_0}|^2}{\sigma_w^2}},\, P_\mathrm{f}\right)\right]^2 \tag{3.76}$$

can be calculated for a given false detection probability

$$P_\mathrm{f} = \Pr\{\Lambda \geqslant \lambda|\mathrm{H}_0\} = 1 - P_{\Lambda|\mathrm{H}_0}(\lambda) = \mathrm{Q}_M\left(\sqrt{\frac{2\,M\,|y_{\mu,\mathrm{H}_0}|^2}{\sigma_w^2}},\, \sqrt{\frac{2\,\lambda}{\sigma_w^2}}\right) \tag{3.77}$$

with the inverse M-th order MARCUM-Q function with respect to its second argument $\mathrm{Q}_{M,\beta}^{-1}(\alpha,\, P_\mathrm{f})$ [57]. This threshold yields the probability of detection

$$P_\mathrm{d} = \Pr\{\Lambda > \lambda|\mathrm{H}_1\} = 1 - P_{\Lambda|\mathrm{H}_1}(\lambda) = \mathrm{Q}_M\left(\sqrt{\frac{2\,M\,|y_{\mu,\mathrm{H}_1}|^2}{\sigma_w^2}},\, \sqrt{\frac{2\lambda}{\sigma_w^2}}\right). \tag{3.78}$$

Fig. 3.13 illustrates the resulting probabilities of detection P_d. Fig. 3.14 summarizes the carrier-to-noise PSD values $C_\mathrm{N}/\mathcal{N}_0$ where the noncoherent integration yields the probability of detection $P_\mathrm{d} = 90\,\%$. The figures show that the sensitivity of noncoherent integration improves with increasing observation time. Unlike the coherent integration in Fig. 3.12, the noncoherent integration does not narrow the frequency search bins. The reception sensitivity of the noncoherent integration appears quite similar to the one for the differential correlation in Fig. 3.10. The sensitivities in Fig. 3.14 are compared to the sensitivities of the differential correlation method in the next section to determine the sensitivity gain of the differential correlation technique. Both methods seem to converge to a sensitivity boundary, which is slightly higher for Galileo than for GPS. The bound is due to the non-zero out-of-phase autocorrelation values of the spreading codes. The bound for Galileo is slightly higher due to the cross-correlation between the Galileo E1-B and E1-C signals. The details are elaborated in Section 3.8. The sensitivity bound will be significantly lowered by the technique to adaptively lower the detection threshold, which is introduced in Chapter 4. This method will also balance the difference between Galileo and GPS.

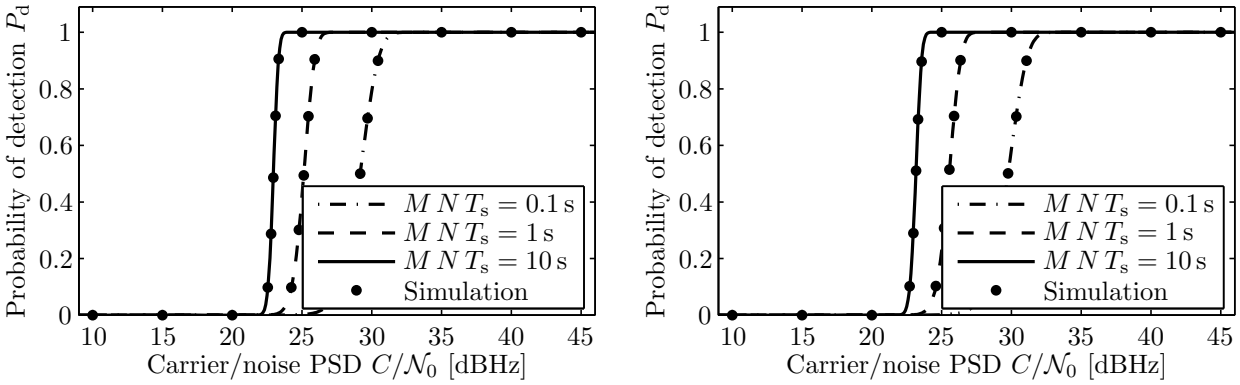

(a) GPS L1-C/A with $f_\mathrm{d} = 0$. (b) GPS L1-C/A with $f_\mathrm{d} = 60\,\mathrm{Hz}$.

Figure 3.13: Detection probability with the noncoherent integration method for $T_0 = 290\,\mathrm{K}$, $F = 3\,\mathrm{dB}$, $N\,T_\mathrm{s} = 4\,\mathrm{ms}$, and $P_\mathrm{f} = 10^{-5}$.

3.11 Sensitivity Gain

Fig. 3.15 shows the sensitivity gain $C_\mathrm{N}/C_\mathrm{D}$ of the differential correlation as described in Section 3.8 versus the state-of-the-art noncoherent integration method described in Section 3.10. The gain in dB is the difference between the values of Fig. 3.10 and 3.14. Since the reception sensitivity of differential correlation and noncoherent integration degrade the same way for an increasing frequency deviation f_d, their difference becomes independent of f_d. The gain in Fig. 3.15 is not parameterized by f_d as it applies to an arbitrary f_d within the correct frequency search bin. It can be observed that the sensitivity gain is initially higher for short observation periods $M\,N\,T_\mathrm{s}$ and reaches values of up to 2.7 dB. However, the gain decreases for longer observation periods. The reason for it is that the sensitivities in Fig. 3.10 and 3.14 are bound by the out-of-phase autocorrelation property of the spreading code. The *adaptive detection threshold* solution in the next chapter further improves the sensitivity gain of the differential correlation compared to the noncoherent integration.

3.12 Code Phase Estimation

The signal acquisition method described in Section 3.6 is the first step to estimate the code phase τ. It allows the unknown code phase to be narrowed down. Fig. 3.1 illustrates the highly parallel correlation engine, which simultaneously calculates the decision statistics Λ_ι for all possible fractional code delays $\widehat{\tau}_\iota$. To prevent false acquisitions, the decision statistic Λ_ι has to be higher than the detection threshold λ. In case multiple Λ_ι exceed λ, many different strategies are possible. Amongst others, one could accumulate all Λ_ι over the length of the correlation peak. Alternatively one could continue the integration until only a single block of neighboring Λ_ι exceeds all other Λ_ι by a certain amount. These strategies allow selecting the code phase search bin, which is assumed to contain the correct code phase τ. However, this limits the resolution of the estimated code phase $\widehat{\tau}$ to the size of the code phase search bins, which is insufficient for most positioning applications. A higher accuracy can be obtained by interpolating the actual code phase τ in between the samples of the correlation peak. Many different interpolation schemes are possible. The standard approach for GPS

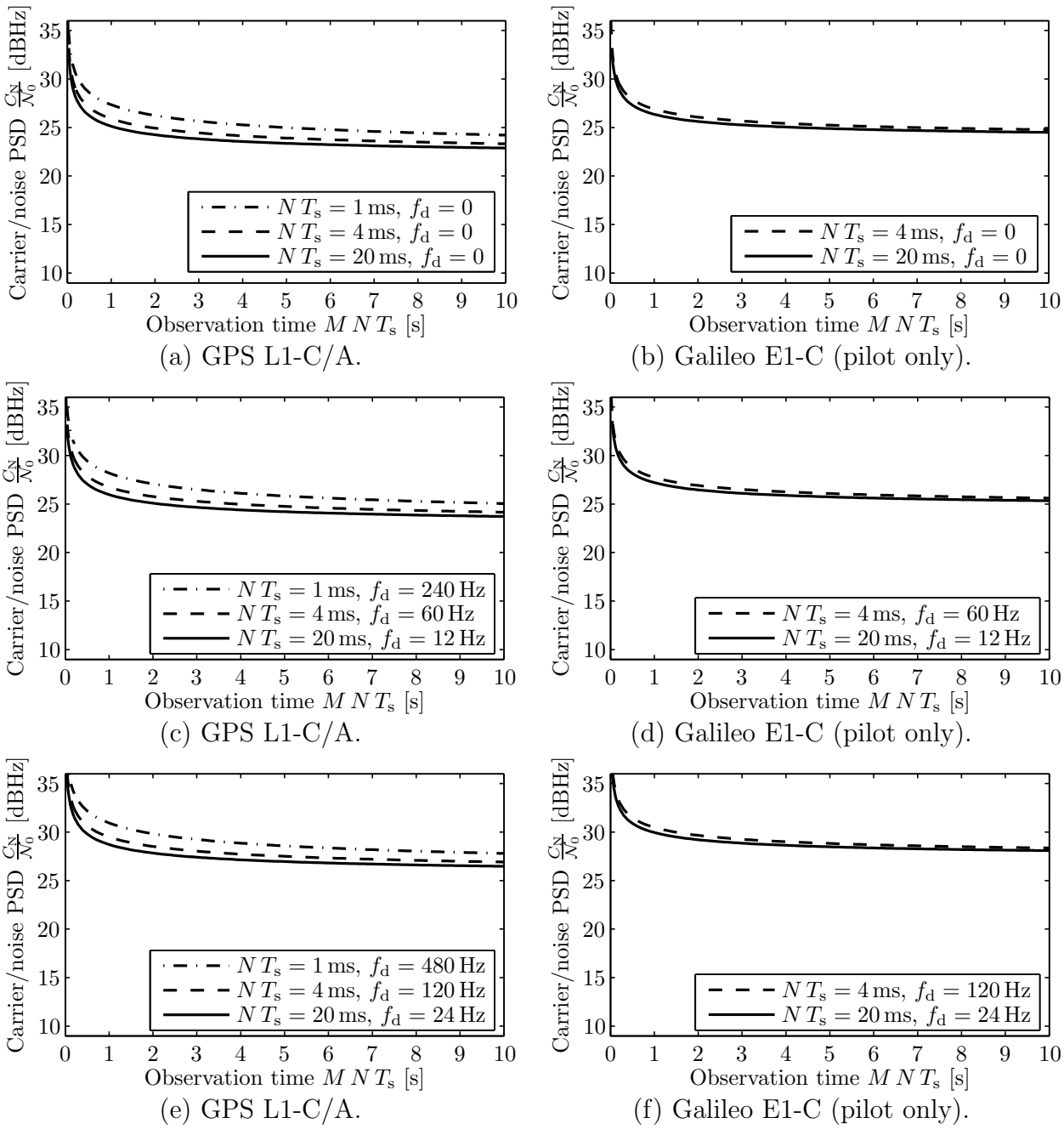

(a) GPS L1-C/A. (b) Galileo E1-C (pilot only).

(c) GPS L1-C/A. (d) Galileo E1-C (pilot only).

(e) GPS L1-C/A. (f) Galileo E1-C (pilot only).

Figure 3.14: Reception sensitivity with the noncoherent integration method for $T_0 = 290\,\text{K}$, $F = 3\,\text{dB}$, $P_f = 10^{-5}$, and $P_d = 90\,\%$.

receivers is early-late discrimination [58, 59]. This method arises automatically when the rectangular spreading pulse form is considered. The added advantage of this method is that its accuracy can be derived in closed form [58, 60]. The target of this work is to evaluate the performance of the differential correlation technique. After evaluating the reception sensitivity, the second question to be answered is how does it affect the positioning accuracy. The performance of early-late discrimination for noncoherent integration is well-published in literature [60, 61]. It is also possible to algebraically derive the accuracy of early-late discrimination for differential correlation in closed form. The early-late method therefore offers the opportunity to compare the accuracy of differential correlation and noncoherent integration in all details for the most widely used code phase interpolation method.

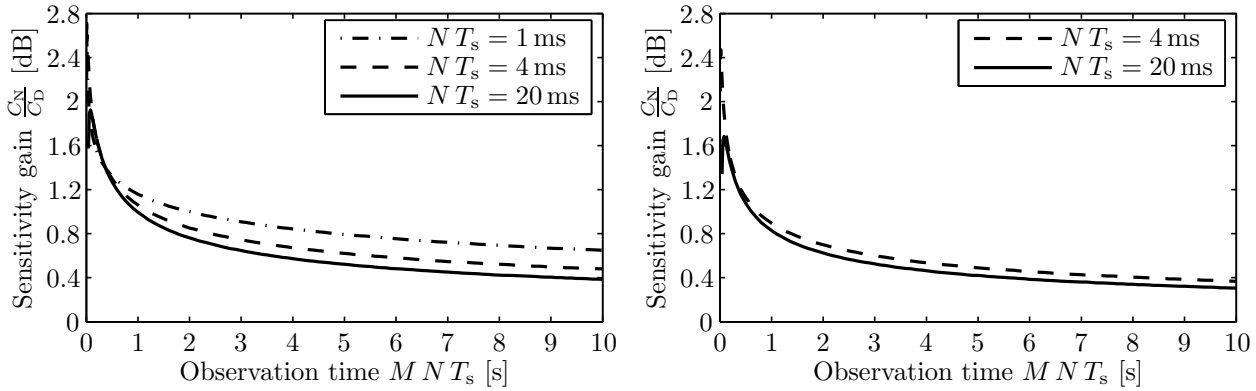

(a) GPS L1-C/A. (b) Galileo E1-C (pilot only).

Figure 3.15: Sensitivity gain of the differential correlation technique for $T_0 = 290\,\text{K}$, $F = 3\,\text{dB}$, $P_\text{f} = 10^{-5}$, and $P_\text{d} = 90\,\%$.

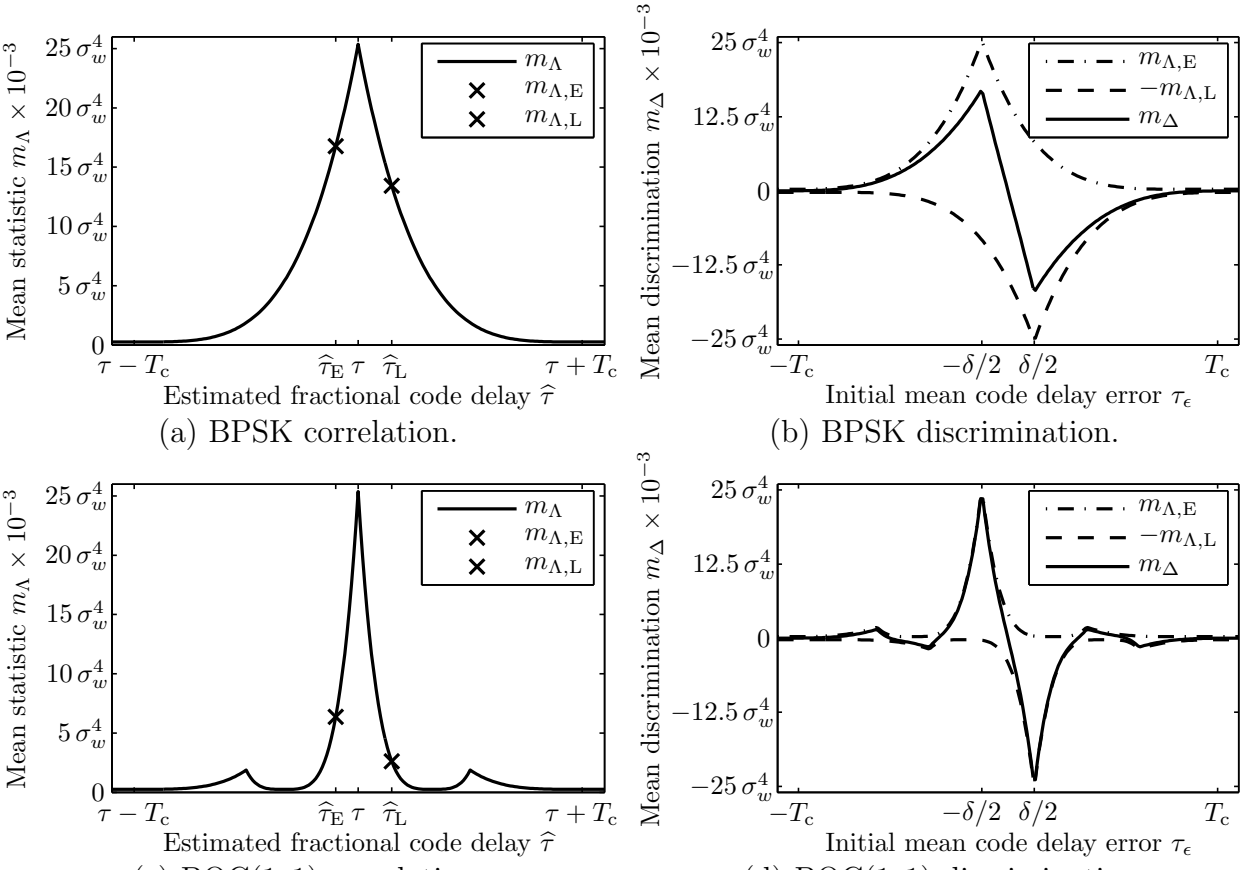

(a) BPSK correlation. (b) BPSK discrimination.

(c) BOC(1, 1) correlation. (d) BOC(1, 1) discrimination.

Figure 3.16: Code discrimination function for $T_0 = 290\,\text{K}$, $F = 3\,\text{dB}$, $\delta = 1/B$, $B = 4.092\,\text{MHz}$, $C/\mathcal{N}_0 = 25\,\text{dBHz}$, $N\,T_s = 4\,\text{ms}$, $M\,N\,T_s = 1\,\text{s}$.

3.13 Early-Late Discrimination Function

With early-late discrimination, the two correlation values to both sides of the code phase search bin are evaluated. Fig. 3.16.a shows a BPSK correlation peak, while Fig. 3.16.c illustrates a BOC(1, 1) correlation peak. Two decision statistics are marked with a cross in each of the plots. The decision statistic to the left of the code phase interval is denoted as the early decision statistic $\Lambda_\text{E} = |\Psi_\text{E}|^2$. It originates from the early estimated code phase $\widehat{\tau}_\text{E}$ and

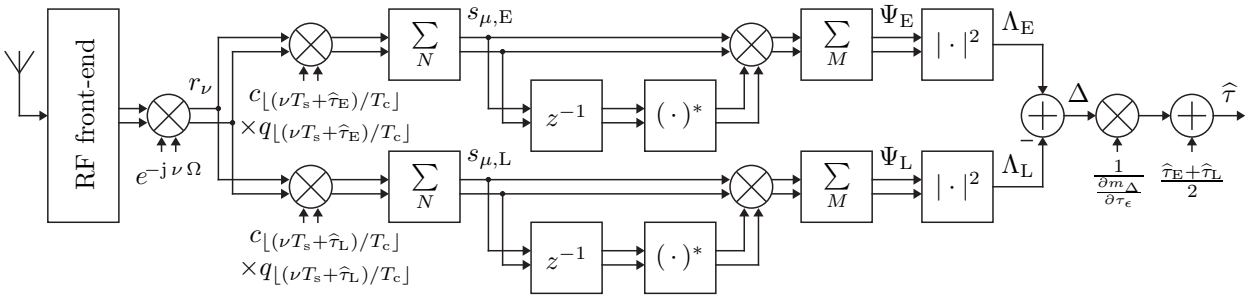

Figure 3.17: Fractional code phase estimation with differential correlation technique.

has the mean

$$m_{\Lambda,\mathrm{E}} = \mathrm{E}\{\Lambda_\mathrm{E}\} = \mathrm{E}\big\{|\Psi_\mathrm{E}|^2\big\} = |m_{\Psi,\mathrm{E}}|^2 + \sigma^2_{\Psi,\mathrm{E}} \tag{3.79}$$

with

$$m_{\Psi,\mathrm{E}} = m_\Psi\big|_{R^2(\tau-\widehat{\tau})=R^2(\tau-\widehat{\tau}_\mathrm{E})}\,, \quad \sigma^2_{\Psi,\mathrm{E}} = \sigma^2_\Psi\big|_{R^2(\tau-\widehat{\tau})=R^2(\tau-\widehat{\tau}_\mathrm{E})}\,. \tag{3.80}$$

The decision statistic to the right of the code phase interval is denoted as the late decision statistic $\Lambda_\mathrm{L} = |\Psi_\mathrm{L}|^2$. It originates from the late estimated code phase $\widehat{\tau}_\mathrm{L}$ and has the mean

$$m_{\Lambda,\mathrm{L}} = \mathrm{E}\{\Lambda_\mathrm{L}\} = \mathrm{E}\big\{|\Psi_\mathrm{L}|^2\big\} = |m_{\Psi,\mathrm{L}}|^2 + \sigma^2_{\Psi,\mathrm{L}} \tag{3.81}$$

with

$$m_{\Psi,\mathrm{L}} = m_\Psi\big|_{R^2(\tau-\widehat{\tau})=R^2(\tau-\widehat{\tau}_\mathrm{L})}\,, \quad \sigma^2_{\Psi,\mathrm{L}} = \sigma^2_\Psi\big|_{R^2(\tau-\widehat{\tau})=R^2(\tau-\widehat{\tau}_\mathrm{L})}\,. \tag{3.82}$$

In a second step, the true code phase τ is estimated with the code discrimination function

$$\boxed{\Delta = \Lambda_\mathrm{E} - \Lambda_\mathrm{L} = |\Psi_\mathrm{E}|^2 - |\Psi_\mathrm{L}|^2}\,. \tag{3.83}$$

Fig. 3.17 shows the corresponding signal processing steps. It illustrates the two pathes of the receiver that are utilized to calculate the discrimination function. The expectation value of the discrimination function is

$$\begin{aligned} m_\Delta &= \mathrm{E}\{\Delta\} = \mathrm{E}\big\{|\Psi_\mathrm{E}|^2 - |\Psi_\mathrm{L}|^2\big\} = \sigma^2_{\Psi,\mathrm{E}} + |m_{\Psi,\mathrm{E}}|^2 - \sigma^2_{\Psi,\mathrm{L}} - |m_{\Psi,\mathrm{L}}|^2 \\ &= 4\,(M-1)\,\sigma_w^2\,C\,\big[R^2(\tau-\widehat{\tau}_\mathrm{E}) - R^2(\tau-\widehat{\tau}_\mathrm{L})\big]\,\mathrm{sinc}^2(f_\mathrm{d}\,N\,T_\mathrm{s}) \\ &\quad + 4\,(M-1)^2\,C^2\,\big[R^4(\tau-\widehat{\tau}_\mathrm{E}) - R^4(\tau-\widehat{\tau}_\mathrm{L})\big]\,\mathrm{sinc}^4(f_\mathrm{d}\,N\,T_\mathrm{s})\,. \end{aligned} \tag{3.84}$$

Fig. 3.16 illustrates the relationship between the decision statistics and the code discrimination function. Fig. 3.16.a and 3.16.b present the decision statistic Λ as a function of the estimated code phase $\widehat{\tau}$. They show the correlation peak and two exemplary early and late sampling values Λ_E and Λ_L. The discrimination function Δ is provided in Fig. 3.16.c and 3.16.d. It indicates whether the true correlation peak is to the left or to the right of the initial mean code phase estimation error

$$\tau_\epsilon = \tau - \frac{\widehat{\tau}_\mathrm{E} + \widehat{\tau}_\mathrm{L}}{2}\,, \tag{3.85}$$

where τ is the true code phase. The distance between the early and late code phase is subsequently denoted as

$$\delta = \widehat{\tau}_\mathrm{L} - \widehat{\tau}_\mathrm{E}\,. \tag{3.86}$$

A large positive value of Δ originates from a large negative value of τ_ϵ and vice versa. The initial mean code phase estimation error can be obtained from the linear part of the discrimination function as

$$\tau_\epsilon = \frac{m_\Delta}{\frac{\partial m_\Delta}{\partial \tau_\epsilon}} \,. \tag{3.87}$$

With (3.85) and (3.87), the actual code phase is given by

$$\tau = \frac{\widehat{\tau}_\mathrm{E} + \widehat{\tau}_\mathrm{L}}{2} + \frac{m_\Delta}{\frac{\partial m_\Delta}{\partial \tau_\epsilon}} \,. \tag{3.88}$$

Fig. 3.16.c and 3.16.d show that the linear part of the discrimination function approximates the discrimination function with a high degree of accuracy. For sufficiently small code phase errors τ_ϵ, the code phase can be estimated as

$$\boxed{\widehat{\tau} = \frac{\widehat{\tau}_\mathrm{E} + \widehat{\tau}_\mathrm{L}}{2} + \frac{\Delta}{\frac{\partial m_\Delta}{\partial \tau_\epsilon}\Big|_{\tau_\epsilon = 0}}} \,. \tag{3.89}$$

3.14 Differential Correlation Accuracy

The ranging accuracy of the code phase estimation with the differential correlation method is derived in this section. The estimation of τ in (3.89) has the mean

$$m_{\widehat{\tau}} = \mathrm{E}\{\widehat{\tau}\} = \frac{\widehat{\tau}_\mathrm{E} + \widehat{\tau}_\mathrm{L}}{2} + \frac{\mathrm{E}\{\Delta\}}{\frac{\partial m_\Delta}{\partial \tau_\epsilon}\Big|_{\tau_\epsilon = 0}} = \frac{\widehat{\tau}_\mathrm{E} + \widehat{\tau}_\mathrm{L}}{2} + \frac{m_\Delta}{\frac{\partial m_\Delta}{\partial \tau_\epsilon}\Big|_{\tau_\epsilon = 0}} \tag{3.90}$$

and the variance

$$\sigma^2_{\widehat{\tau}} = \mathrm{E}\left\{(\widehat{\tau} - m_{\widehat{\tau}})^2\right\} = \frac{\mathrm{E}\left\{(\Delta - m_\Delta)^2\right\}}{\left(\frac{\partial m_\Delta}{\partial \tau_\epsilon}\right)^2} = \frac{\sigma^2_\Delta}{\left(\frac{\partial m_\Delta}{\partial \tau_\epsilon}\right)^2} \,. \tag{3.91}$$

In order to derive $\sigma^2_{\widehat{\tau}}$, the derivative $\partial m_\Delta / \partial \tau_\epsilon$ is calculated next and the variance σ^2_Δ thereafter.

If the initial mean code phase error is bound by the size of the code phase search bin

$$-\frac{\delta}{2} \leqslant \tau_\epsilon \leqslant \frac{\delta}{2} \,, \tag{3.92}$$

then the early and late correlation functions can be expressed as

$$\begin{aligned} R(\tau - \widehat{\tau}_\mathrm{E}) &= R\left(\tau - \frac{\widehat{\tau}_\mathrm{E} + \widehat{\tau}_\mathrm{L}}{2} + \frac{\delta}{2}\right) = R\left(\tau_\epsilon + \frac{\delta}{2}\right) \\ &= \left(1 - \frac{|\tau_\epsilon + \delta/2|}{\eta\, T_\mathrm{c}}\right) N = \left(1 - \frac{\delta}{2\,\eta\, T_\mathrm{c}} - \frac{\tau_\epsilon}{\eta\, T_\mathrm{c}}\right) N \end{aligned} \tag{3.93}$$

and

$$\begin{aligned} R(\tau - \widehat{\tau}_\mathrm{L}) &= R\left(\tau - \frac{\widehat{\tau}_\mathrm{E} + \widehat{\tau}_\mathrm{L}}{2} - \frac{\delta}{2}\right) = R\left(\tau_\epsilon - \frac{\delta}{2}\right) \\ &= \left(1 - \frac{|\tau_\epsilon - \delta/2|}{\eta\, T_\mathrm{c}}\right) N = \left(1 - \frac{\delta}{2\,\eta\, T_\mathrm{c}} + \frac{\tau_\epsilon}{\eta\, T_\mathrm{c}}\right) N \,. \end{aligned} \tag{3.94}$$

The factor η is a correction factor to model the correlation peaks for BPSK and BOC(1, 1) modulation. As can be seen in Fig. 3.16, the correlation peak for BOC(1, 1) modulation is steeper. It is modelled with $\eta = 1/3$ in (3.93) and (3.94), while $\eta = 1$ corresponds to BPSK modulation. This leads to

$$R^2(\tau - \widehat{\tau}_\mathrm{E}) - R^2(\tau - \widehat{\tau}_\mathrm{L}) = -4\left(1 - \frac{\delta}{2\,\eta\,T_\mathrm{c}}\right) N^2\,\frac{\tau_\epsilon}{\eta\,T_\mathrm{c}} = -4\,R\!\left(\frac{\delta}{2}\right)\frac{N\,\tau_\epsilon}{\eta\,T_\mathrm{c}} \tag{3.95}$$

and

$$\begin{aligned} R^4(\tau - \widehat{\tau}_\mathrm{E}) - R^4(\tau - \widehat{\tau}_\mathrm{L}) &= -8\left(1 - \frac{\delta}{2\,\eta\,T_\mathrm{c}}\right)^3 N^4\,\frac{\tau_\epsilon}{\eta\,T_\mathrm{c}} - 8\left(1 - \frac{\delta}{2\,\eta\,T_\mathrm{c}}\right) N^4\,\frac{\tau_\epsilon^3}{\eta^3\,T_\mathrm{c}^3} \\ &= -8\,R^3\!\left(\frac{\delta}{2}\right)\frac{N\,\tau_\epsilon}{\eta\,T_\mathrm{c}} - 8\,R\!\left(\frac{\delta}{2}\right)\frac{N^3\,\tau_\epsilon^3}{\eta^3\,T_\mathrm{c}^3}\;. \end{aligned} \tag{3.96}$$

Inserting (3.95) and (3.96) into (3.84) yields

$$\begin{aligned} m_\Delta = &-16\,(M-1)\,\sigma_w^2\,C\,R\!\left(\frac{\delta}{2}\right)\frac{N\,\tau_\epsilon}{\eta\,T_\mathrm{c}}\,\mathrm{sinc}^2(f_\mathrm{d}\,N\,T_\mathrm{s}) \\ &- 32\,(M-1)^2\,C^2\,R^3\!\left(\frac{\delta}{2}\right)\frac{N\,\tau_\epsilon}{\eta\,T_\mathrm{c}}\,\mathrm{sinc}^4(f_\mathrm{d}\,N\,T_\mathrm{s}) \\ &- 32\,(M-1)^2\,C^2\,R\!\left(\frac{\delta}{2}\right)\frac{N^3\,\tau_\epsilon^3}{\eta^3\,T_\mathrm{c}^3}\,\mathrm{sinc}^4(f_\mathrm{d}\,N\,T_\mathrm{s})\;. \end{aligned} \tag{3.97}$$

Consequently, the slope of τ_ϵ in the origin as illustrated in Fig. 3.16(b) is

$$\boxed{\begin{aligned} \left.\frac{\partial m_\Delta}{\partial \tau_\epsilon}\right|_{\tau_\epsilon=0} = &-16\,(M-1)\,\sigma_w^2\,C\,R\!\left(\frac{\delta}{2}\right)\frac{N}{\eta\,T_\mathrm{c}}\,\mathrm{sinc}^2(f_\mathrm{d}\,N\,T_\mathrm{s}) \\ &- 32\,(M-1)^2\,C^2\,R^3\!\left(\frac{\delta}{2}\right)\frac{N}{\eta\,T_\mathrm{c}}\,\mathrm{sinc}^4(f_\mathrm{d}\,N\,T_\mathrm{s}) \end{aligned}}\;. \tag{3.98}$$

The other required term for the calculation of $\sigma_{\widehat{\tau}}^2$ is the variance of the discrimination function

$$\begin{aligned} \sigma_\Delta^2 &= \mathrm{E}\big\{(\Delta - m_\Delta)^2\big\} = \mathrm{E}\Big\{\big(|\Psi_\mathrm{E}|^2 - |\Psi_\mathrm{L}|^2 - m_\Delta\big)^2\Big\} \\ &= \mathrm{E}\big\{|\Psi_\mathrm{E}|^4 + |\Psi_\mathrm{L}|^4 + m_\Delta^2 - 2\,|\Psi_\mathrm{E}|^2\,|\Psi_\mathrm{L}|^2 - 2\,|\Psi_\mathrm{E}|^2\,m_\Delta + 2\,|\Psi_\mathrm{L}|^2\,m_\Delta\big\}\;. \end{aligned} \tag{3.99}$$

The fourth moment of a complex-valued Gaussian variable with statistically independent real and imaginary components results in [28, 53]

$$\mathrm{E}\big\{|\Psi|^4\big\} = \sigma_\Psi^4 + 2\,\sigma_\Psi^2\,|m_\Psi|^2 + \big(\sigma_\Psi^2 + |m_\Psi|^2\big)^2\;. \tag{3.100}$$

The squared discrimination mean is

$$m_\Delta^2 = \big(\sigma_{\Psi,\mathrm{E}}^2 + |m_{\Psi,\mathrm{E}}|^2\big)^2 - 2\,\big(\sigma_{\Psi,\mathrm{E}}^2 + |m_{\Psi,\mathrm{E}}|^2\big)\,\big(\sigma_{\Psi,\mathrm{L}}^2 + |m_{\Psi,\mathrm{L}}|^2\big) + \big(\sigma_{\Psi,\mathrm{L}}^2 + |m_{\Psi,\mathrm{L}}|^2\big)^2\;. \tag{3.101}$$

The correlation factor between the early and late predetection noise $w_{\mu,\mathrm{E}}$ and $w_{\mu,\mathrm{L}}$ can be derived from (3.16), (3.28), (3.36), and (3.37) as

$$\begin{aligned}
&\mathrm{E}\big\{ w_{\mu,\mathrm{E}}\, w_{\mu,\mathrm{L}}^{*} \big\} \\
&= \mathrm{E}\left\{ \left(\sum_{\nu=\mu\,N}^{(\mu+1)\,N-1} n_\nu\, c_{\lfloor(\nu\,T_\mathrm{s}+\widehat{\tau}_\mathrm{E})/T_\mathrm{c}\rfloor}\, q_{\lfloor(\nu\,T_\mathrm{s}+\widehat{\tau}_\mathrm{E})/T_\mathrm{c}\rfloor} \right) \left(\sum_{\nu=\mu\,N}^{(\mu+1)\,N-1} n_\nu\, c_{\lfloor(\nu\,T_\mathrm{s}+\widehat{\tau}_\mathrm{L})/T_\mathrm{c}\rfloor}\, q_{\lfloor(\nu\,T_\mathrm{s}+\widehat{\tau}_\mathrm{L})/T_\mathrm{c}\rfloor} \right)^{*} \right\} \\
&= \sum_{\nu=\mu\,N}^{(\mu+1)\,N-1} \mathrm{E}\big\{ \big(n_\nu\, c_{\lfloor(\nu\,T_\mathrm{s}+\widehat{\tau}_\mathrm{E})/T_\mathrm{c}\rfloor}\, q_{\lfloor(\nu\,T_\mathrm{s}+\widehat{\tau}_\mathrm{E})/T_\mathrm{c}\rfloor} \big) \big(n_\nu\, c_{\lfloor(\nu\,T_\mathrm{s}+\widehat{\tau}_\mathrm{L})/T_\mathrm{c}\rfloor}\, q_{\lfloor(\nu\,T_\mathrm{s}+\widehat{\tau}_\mathrm{L})/T_\mathrm{c}\rfloor} \big)^{*} \big\} \\
&= \mathrm{E}\{ n_\nu\, n_\nu^{*} \} \sum_{\nu=\mu\,N}^{(\mu+1)\,N-1} c_{\lfloor(\nu\,T_\mathrm{s}+\widehat{\tau}_\mathrm{E})/T_\mathrm{c}\rfloor}\, q_{\lfloor(\nu\,T_\mathrm{s}+\widehat{\tau}_\mathrm{E})/T_\mathrm{c}\rfloor}\, c_{\lfloor(\nu\,T_\mathrm{s}+\widehat{\tau}_\mathrm{L})/T_\mathrm{c}\rfloor}\, q_{\lfloor(\nu\,T_\mathrm{s}+\widehat{\tau}_\mathrm{L})/T_\mathrm{c}\rfloor} \\
&= \mathrm{E}\big\{ |n_\nu|^2 \big\}\, R(\widehat{\tau}_\mathrm{E}-\widehat{\tau}_\mathrm{L}) = \frac{R(\widehat{\tau}_\mathrm{E}-\widehat{\tau}_\mathrm{L})}{N}\,\sigma_w^2 = \left(1-\frac{\delta}{\eta\,T_\mathrm{c}}\right)\sigma_w^2 = \frac{R(\delta)}{N}\,\sigma_w^2 \,.
\end{aligned} \tag{3.102}$$

The expectation value of the *product* of two statistically dependent central CHI-SQUARED distributed variables can be found with help of the *sum* of two statistically dependent central CHI-SQUARED distributed variables

$$\mathrm{E}\big\{ |w_{\mu,\mathrm{E}}|^2\; |w_{\mu,\mathrm{L}}|^2 \big\} = \frac{1}{2}\,\mathrm{E}\Big\{ \big(|w_{\mu,\mathrm{E}}|^2 + |w_{\mu,\mathrm{L}}|^2 \big)^2 - |w_{\mu,\mathrm{E}}|^4 - |w_{\mu,\mathrm{L}}|^4 \Big\} \,. \tag{3.103}$$

The characteristic function of the *sum* of two statistically dependent central CHI-SQUARED distributed variables with two degrees of freedom and the correlation factor $R(\delta)/N$ is [56]

$$\Phi(\mathrm{j}\,\omega) = \frac{1-\frac{\mathrm{R}^2(\delta)}{\mathrm{N}^2}}{\left[1-\mathrm{j}\,\omega\left(1-\frac{\mathrm{R}^2(\delta)}{\mathrm{N}^2}\right)\sigma_\mathrm{w}^2\right]^2-\frac{\mathrm{R}^2(\delta)}{\mathrm{N}^2}} \,. \tag{3.104}$$

The second derivative of (3.104) yields the second moment

$$\mathrm{E}\Big\{ \big(|w_{\mu,\mathrm{E}}|^2 + |w_{\mu,\mathrm{L}}|^2 \big)^2 \Big\} = (-\mathrm{j})^2\, \frac{\partial^2 \Phi(\mathrm{j}\,\omega)}{\partial \omega^2}\bigg|_{\omega=0} = 6\,\sigma_w^4 + 2\,\frac{R^2(\delta)}{N^2}\,\sigma_w^4 \,. \tag{3.105}$$

Inserting (3.105) into (3.103) gives

$$\mathrm{E}\big\{ |w_{\mu,\mathrm{E}}|^2\; |w_{\mu,\mathrm{L}}|^2 \big\} = \left(1+\frac{R^2(\delta)}{N^2}\right)\sigma_w^4 \,. \tag{3.106}$$

From (3.39), (3.51), and (3.106) follows

$$\begin{aligned}
\mathrm{E}\big\{ |\Psi_\mathrm{E}|^2\; |\Psi_\mathrm{L}|^2 \big\} = {} & \big(\sigma_{\Psi,\mathrm{E}}^2 + |m_{\Psi,\mathrm{E}}|^2 \big) \big(\sigma_{\Psi,\mathrm{L}}^2 + |m_{\Psi,\mathrm{L}}|^2 \big) \\
& + \frac{R^2(\delta)}{N^2}\,\sigma_{\Psi,\mathrm{E}}^2\,\sigma_{\Psi,\mathrm{L}}^2 + 2\,\frac{R(\delta)}{N}\,\sigma_{\Psi,\mathrm{E}}\,\sigma_{\Psi,\mathrm{L}}\,|m_{\Psi,\mathrm{E}}|\,|m_{\Psi,\mathrm{L}}| \,.
\end{aligned} \tag{3.107}$$

Inserting (3.97), (3.100), (3.101), and (3.107) into (3.99) yields the discrimination variance

$$\boxed{\begin{aligned}
\sigma_\Delta^2 = {} & \sigma_{\Psi,\mathrm{E}}^4 + \sigma_{\Psi,\mathrm{L}}^4 + 2\,\sigma_{\Psi,\mathrm{E}}^2\,|m_{\Psi,\mathrm{E}}|^2 + 2\,\sigma_{\Psi,\mathrm{L}}^2\,|m_{\Psi,\mathrm{L}}|^2 \\
& - 2\,\frac{R^2(\delta)}{N^2}\,\sigma_{\Psi,\mathrm{E}}^2\,\sigma_{\Psi,\mathrm{L}}^2 - 4\,\frac{R(\delta)}{N}\,\sigma_{\Psi,\mathrm{E}}\,\sigma_{\Psi,\mathrm{L}}\,|m_{\Psi,\mathrm{E}}|\,|m_{\Psi,\mathrm{L}}|
\end{aligned}} \,. \tag{3.108}$$

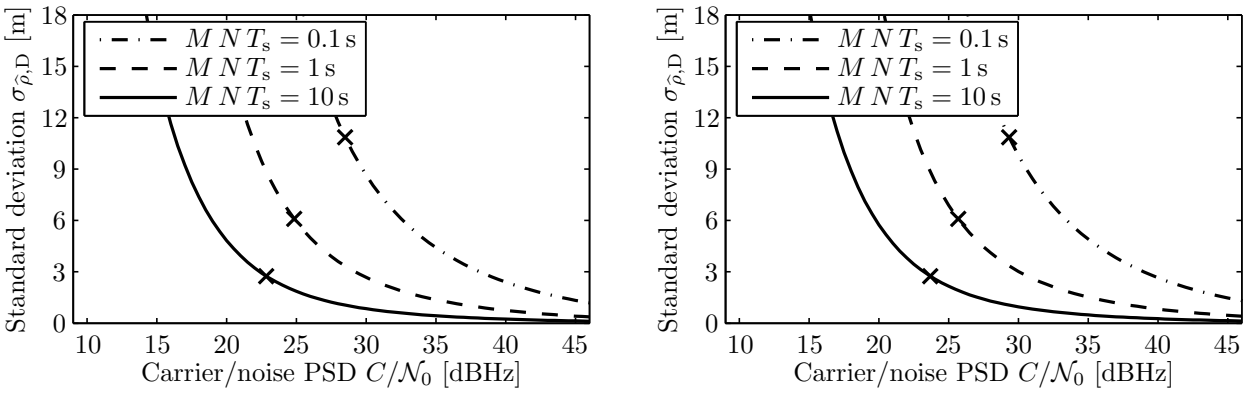

(a) GPS L1-C/A with $f_\mathrm{d} = 0$. (b) GPS L1-C/A with $f_\mathrm{d} = 60\,\mathrm{Hz}$.

Figure 3.18: Range estimation with the differential correlation technique for $T_0 = 290\,\mathrm{K}$, $F = 3\,\mathrm{dB}$, $N\,T_\mathrm{s} = 4\,\mathrm{ms}$, $B = 4.092\,\mathrm{MHz}$, and $\delta = 1/B$.

The code phase estimation variance $\sigma_{\widehat{\tau}}^2$ is thus obtained by inserting $(\partial m_\Delta/\partial\tau_\epsilon)|_{\tau_\epsilon=0}$ as specified in (3.98) and σ_Δ^2 as specified in (3.108) into (3.91). Multiplying it with the squared speed of light $\mathrm{c} = 299.8 \times 10^6\,\mathrm{m/s}$, yields the variance of the estimated distance between receiver and satellite for the differential correlation

$$\boxed{\sigma_{\widehat{\rho},\mathrm{D}}^2 = \mathrm{c}^2\,\sigma_{\widehat{\tau}}^2 = \frac{\mathrm{c}^2\,\sigma_\Delta^2}{\left(\frac{\partial m_\Delta}{\partial\tau_\epsilon}\Big|_{\tau_\epsilon=0}\right)^2}}\,. \tag{3.109}$$

The variance of the range estimate $\sigma_{\widehat{\rho},\mathrm{D}}^2$ in (3.109) decreases with a decreasing discrimination spacing δ. However, it can be shown that a discrimination spacing below the NYQUIST sampling period

$$\delta = \frac{1}{B} \tag{3.110}$$

does not generate any further ranging accuracy improvements [60, 61]. The narrow correlation technique requires a correspondingly wide filter bandwidth. The discrimination spacing $\delta = 1/B$ is hence subsequently applied.

Fig. 3.18 shows the standard deviation of the range estimation for the differential correlation $\sigma_{\widehat{\rho},\mathrm{D}}$ as a function of the carrier-to-noise PSD $C/\mathcal{N}_0$. The accuracy is good for sufficiently high signal-to-noise ratios. If Fig. 3.18 is viewed together with Fig. 3.9 it becomes apparent that the very low signal-to-noise ratios do not even permit signal acquisition and are thus irrelevant. The cross marks in Fig. 3.18 indicate the accuracy obtained for the sensitivity limit, where the $C/\mathcal{N}_0$ values yield $P_\mathrm{d} = 90\,\%$, as shown in Fig. 3.9.

Fig. 3.19 shows the standard deviation of the range estimates $\sigma_{\widehat{\rho},\mathrm{D}}$ as a function of the observation time $M\,N\,T_\mathrm{s}$. It follows the presentation of the reception sensitivity as a function of $M\,N\,T_\mathrm{s}$ in Fig. 3.10 and 3.14. The receiver parameters $T_0 = 290\,\mathrm{K}$, $F = 3\,\mathrm{dB}$ are elaborated in Section 3.7. For mass market receivers, the front-end filter bandwidth B is typically set to around the zero-to-zero bandwidth of the satellite signal, which is $B = 4.092\,\mathrm{MHz}$ for Galileo E1-B/C. A higher bandwidth would require a correspondingly higher sampling rate. It would increase the implementation costs of the entire signal processing chain without improving the reception sensitivity. The filter bandwidth, however, does affect the range errors

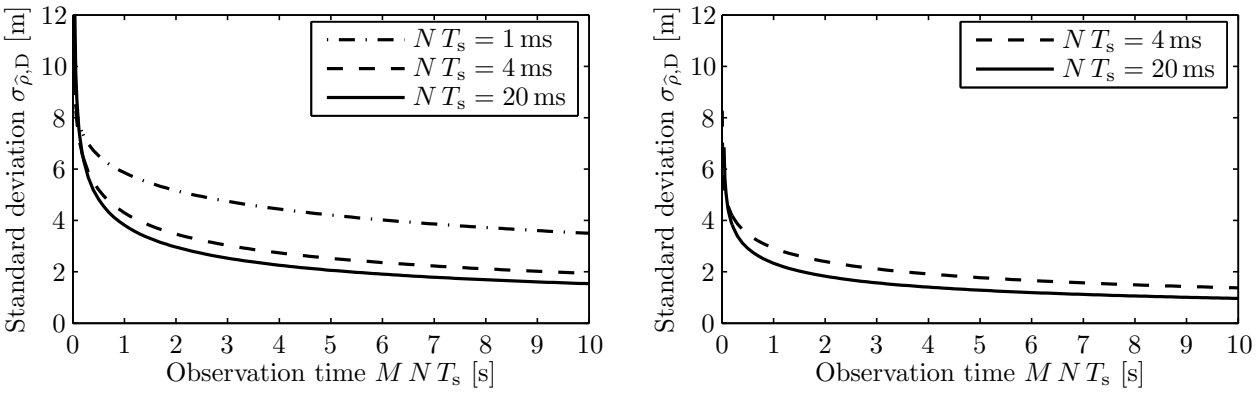

(a) GPS L1-C/A. (b) Galileo E1-C (pilot only).

Figure 3.19: Range estimation accuracy at the sensitivity limit with the differential correlation technique for $T_0 = 290\,\mathrm{K}$, $F = 3\,\mathrm{dB}$, $B = 4.092\,\mathrm{MHz}$, and $\delta = 1/B$.

due to thermal noise. To allow for direct comparison, the same bandwidth $B = 4.092\,\mathrm{MHz}$ has been applied to the GPS and Galileo simulations in this thesis. The smaller the distance between the early and late code delay δ, the higher is the range accuracy. It is set to $1/B$, which corresponds to exactly one sample difference for the NYQUIST sampling rate. Any smaller δ would not further improve the positioning accuracy. The aim of Fig. 3.19 is to provide the data to calculate how much the differential correlation can improve the positioning accuracy as compared to the state-of-the-art noncoherent integration. Obviously, the accuracy of the range estimate depends on the carrier-to-noise PSD $C/\mathcal{N}_0$ of the received signal. In order to allow a comparison of the accuracies provided by GPS and Galileo using the differential correlation and the noncoherent integration, their range estimates are calculated for the same $C/\mathcal{N}_0$ values. The weakest reception sensitivity is obtained by the state-of-the-art noncoherent integration for Galileo. All range accuracies are therefore subsequently calculated for the $C_\mathrm{N}/\mathcal{N}_0$ values where the noncoherent integration allows the positioning with $P_\mathrm{d} = 90\,\%$. These $C_\mathrm{N}/\mathcal{N}_0$ values are presented in Fig. 3.14. For $N\,T_\mathrm{s} = 4\,\mathrm{ms}$ and $N\,T_\mathrm{s} = 20\,\mathrm{ms}$, the $C_\mathrm{N}/\mathcal{N}_0$ values for Galileo have been utilized for the accuracy simulations of GPS and Galileo. Since the $C_\mathrm{N}/\mathcal{N}_0$ values in Fig. 3.14 rise for an increasing frequency deviation f_d, the range accuracies in Fig. 3.19 turn out to be independent of f_d. Since the probability of detection is kept constant at $P_\mathrm{d} = 90\,\%$, the degrading effect of the frequency deviation is compensated with a higher $C_\mathrm{N}/\mathcal{N}_0$, such that $\sigma_{\hat{\rho},\mathrm{D}}$ becomes independent of f_d.

The range estimation accuracy in Fig. 3.19 shows better values for Galileo E1-C than for GPS L1-C/A, since the Galileo signal is BOC(1, 1)-modulated and hence has a steeper correlation peak. The correlation peaks, as well as the resulting discrimination functions for GPS and Galileo are illustrated in Fig. 3.16. The steeper correlation peak yields a larger slope of the discrimination function for the BOC-modulated Galileo signals, which translates in a a higher range accuracy. However, since Fig. 3.19 is mainly provided as a reference to compare the accuracies of differential correlation and nocoherent integration, the actual values are less significant than their ratio. The presented range estimation accuracies are relatively high, since multipath errors are not considered. The estimation errors hence result from the additive white GAUSSIAN noise and are still larger than the CRAMER-RAO lower bound [29].

3.15 Noncoherent Integration Accuracy

In this section, the ranging accuracy is derived for the state-of-the-art noncoherent integration method as described in Sections 2.4 and 3.10. The early decision statistic for noncoherent integration has the mean [28, 53]

$$m_{\Lambda,\mathrm{E}} = \mathrm{E}\left\{\Lambda_\mathrm{E}\right\} = \mathrm{E}\left\{\sum_{\mu=0}^{M-1} |y_{\mu,\mathrm{E}} + w_{\mu,\mathrm{E}}|^2\right\} = M\left(\sigma_w^2 + |y_{\mu,\mathrm{E}}|^2\right) \ , \tag{3.111}$$

with

$$y_{\mu,\mathrm{E}} = y_\mu\big|_{R(\tau-\widehat{\tau})=R(\tau-\widehat{\tau}_\mathrm{E})} \ . \tag{3.112}$$

The late decision statistic has correspondingly the mean

$$m_{\Lambda,\mathrm{L}} = \mathrm{E}\left\{\Lambda_\mathrm{E}\right\} = \mathrm{E}\left\{\sum_{\mu=0}^{M-1} |y_{\mu,\mathrm{L}} + w_{\mu,\mathrm{L}}|^2\right\} = M\left(\sigma_w^2 + |y_{\mu,\mathrm{L}}|^2\right) \ , \tag{3.113}$$

with

$$y_{\mu,\mathrm{L}} = y_\mu\big|_{R(\tau-\widehat{\tau})=R(\tau-\widehat{\tau}_\mathrm{L})} \ . \tag{3.114}$$

The code discrimination function

$$\Delta = \Lambda_\mathrm{E} - \Lambda_\mathrm{L} \tag{3.115}$$

therefore has the expectation value

$$\begin{aligned} m_\Delta &= \mathrm{E}\{\Delta\} = \mathrm{E}\{\Lambda_\mathrm{E} - \Lambda_\mathrm{L}\} = M\left(|y_{\mu,\mathrm{E}}|^2 - |y_{\mu,\mathrm{L}}|^2\right) \\ &= 2\,M\,C\left[R^2(\tau-\widehat{\tau}_\mathrm{E}) - R^2(\tau-\widehat{\tau}_\mathrm{L})\right]\mathrm{sinc}^2(f_\mathrm{d}\,N\,T_\mathrm{s}) \\ &= -8\,M\,C\,R\!\left(\frac{\delta}{2}\right)\frac{N\,\tau_\epsilon}{\eta\,T_\mathrm{c}}\,\mathrm{sinc}^2(f_\mathrm{d}\,N\,T_\mathrm{s}) \ . \end{aligned} \tag{3.116}$$

The derivative with respect to τ_ϵ yields

$$\boxed{\frac{\partial m_\Delta}{\partial \tau_\epsilon} = -8\,M\,C\,R\!\left(\frac{\delta}{2}\right)\frac{N}{\eta\,T_\mathrm{c}}\,\mathrm{sinc}^2(f_\mathrm{d}\,N\,T_\mathrm{s})} \ . \tag{3.117}$$

The variance of the discrimination function is

$$\begin{aligned} \sigma_\Delta^2 &= \mathrm{E}\big\{(\Delta - m_\Delta)^2\big\} = \mathrm{E}\big\{(\Lambda_\mathrm{E} - \Lambda_\mathrm{L} - m_\Delta)^2\big\} \\ &= \mathrm{E}\big\{\Lambda_\mathrm{E}^2 + \Lambda_\mathrm{L}^2 + m_\Delta^2 - 2\,\Lambda_\mathrm{E}\,\Lambda_\mathrm{L} - 2\,\Lambda_\mathrm{E}\,m_\Delta + 2\,\Lambda_\mathrm{L}\,m_\Delta\big\} \ . \end{aligned} \tag{3.118}$$

The second moment of a noncentral Chi-squared distributed variable is [28, 53]

$$\mathrm{E}\big\{\Lambda^2\big\} = M\,\sigma_w^4 + 2\,M\,\sigma_w^2\,|y_\mu|^2 + M^2\left(\sigma_w^2 + |y_\mu|^2\right)^2 . \tag{3.119}$$

With (3.103) and (3.107), the expectation value of the product of the two statistically dependent noncentral Chi-squared distributed decision statistics Λ_E and Λ_L results in

$$\begin{aligned} \mathrm{E}\{\Lambda_\mathrm{E}\,\Lambda_\mathrm{L}\} &= \mathrm{E}\left\{\left(\sum_{\mu=0}^{M-1} |y_{\mu,\mathrm{E}} + w_{\mu,\mathrm{E}}|^2\right)\left(\sum_{\mu=0}^{M-1} |y_{\mu,\mathrm{L}} + w_{\mu,\mathrm{L}}|^2\right)\right\} \\ &= M^2\left(\sigma_w^2 + |y_{\mu,\mathrm{E}}|^2\right)\left(\sigma_w^2 + |y_{\mu,\mathrm{L}}|^2\right) + M\,\frac{R^2(\delta)}{N^2}\,\sigma_w^4 + 2\,M\,\frac{R(\delta)}{N}\,\sigma_w^2\,|y_{\mu,\mathrm{E}}|\,|y_{\mu,\mathrm{L}}| \ . \end{aligned} \tag{3.120}$$

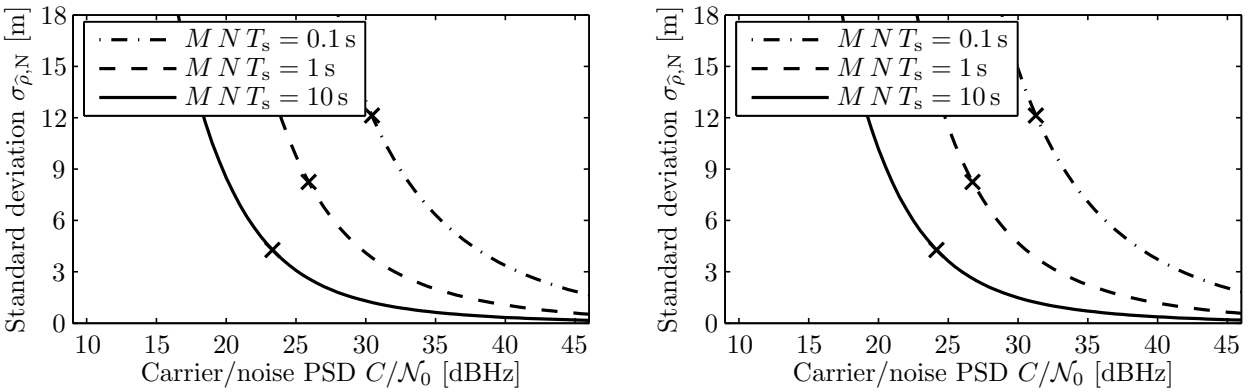

(a) GPS L1-C/A with $f_\mathrm{d} = 0$. (b) GPS L1-C/A with $f_\mathrm{d} = 60\,\mathrm{Hz}$.

Figure 3.20: Range estimation with the noncoherent integration method for $T_0 = 290\,\mathrm{K}$, $F = 3\,\mathrm{dB}$, $N\,T_\mathrm{s} = 4\,\mathrm{ms}$, $B = 4.092\,\mathrm{MHz}$, and $\delta = 1/B$.

Inserting (3.116), (3.119), and (3.120) into (3.118) finally yields the variance of the discrimination function

$$\boxed{\sigma_\Delta^2 = 2\,M\left(1 - \frac{R^2(\delta)}{N^2}\right)\sigma_w^4 + 2\,M\,\sigma_w^2\left(|y_{\mu,\mathrm{E}}|^2 + |y_{\mu,\mathrm{L}}|^2 - 2\,\frac{R(\delta)}{N}\,|y_{\mu,\mathrm{E}}|\,|y_{\mu,\mathrm{L}}|\right)}\,. \tag{3.121}$$

The variance of the range estimation is hence

$$\boxed{\sigma_{\widehat{\rho},\mathrm{N}}^2 = \frac{\mathrm{c}^2\,\sigma_\Delta^2}{\left(\frac{\partial m_\Delta}{\partial \tau_\epsilon}\right)^2}}\,, \tag{3.122}$$

where $\partial m_\Delta/\partial\tau_\epsilon$ and σ_Δ^2 are defined in (3.117) and (3.121).

Fig. 3.20 shows the ranging accuracy of the noncoherent integration method as a function of the carrier-to-noise PSD $C/\mathcal{N}_0$. The higher ranging inaccuracies for very low $C/\mathcal{N}_0$ values are irrelevant, since these signal-to-noise ratios do not even permit the signal acquisition, as illustrated in Fig. 3.13. The cross marks in Fig. 3.20 denote the sensitivity limit with $P_\mathrm{d} = 90\,\%$ in Fig. 3.13.

Fig. 3.21 shows the standard deviation of the range estimates $\sigma_{\widehat{\rho},\mathrm{N}}$ for the noncoherent integration approach with equal carrier-to-noise PSD $C_\mathrm{N}/\mathcal{N}_0$ as applied for the accuracy of the differential correlation in Fig. 3.19. The two figures are therefore directly comparable, as the same receiver parameters are applied for both. The accuracy gain of the differential correlation is provided in the next section based on the ratio of the values in the two figures. The applied $C_\mathrm{N}/\mathcal{N}_0$ values are the ones where the noncoherent integration allows positioning with $P_\mathrm{d} = 90\,\%$, as shown in Fig. 3.14. Except for $N\,T_\mathrm{s} = 1\,\mathrm{ms}$, the Galileo $C_\mathrm{N}/\mathcal{N}_0$ values have been applied for the accuracy simulation of GPS and Galileo. Since the $C_\mathrm{N}/\mathcal{N}_0$ values in Fig. 3.14 rise for an increasing frequency deviation f_d, such that the probability of detection is constant, the range accuracies in Fig. 3.21 are independent of f_d. The accuracy for Galileo is higher in Fig. 3.21 for the same reasons as stated in the previous section for the differential correlation in Fig. 3.19.

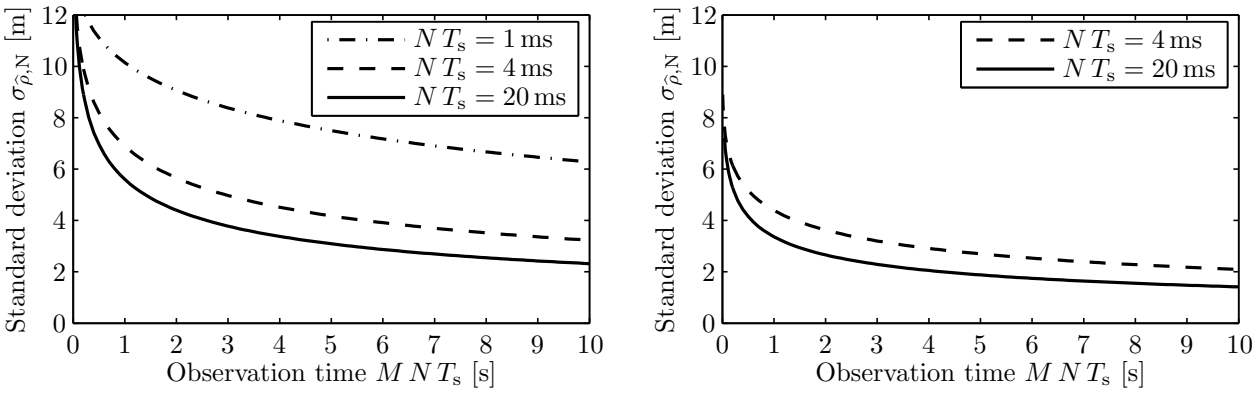

(a) GPS L1-C/A. (b) Galileo E1-C (pilot only).

Figure 3.21: Range estimation accuracy at the sensitivity limit with the noncoherent integration method for $T_0 = 290\,\mathrm{K}$, $F = 3\,\mathrm{dB}$, $B = 4.092\,\mathrm{MHz}$, and $\delta = 1/B$.

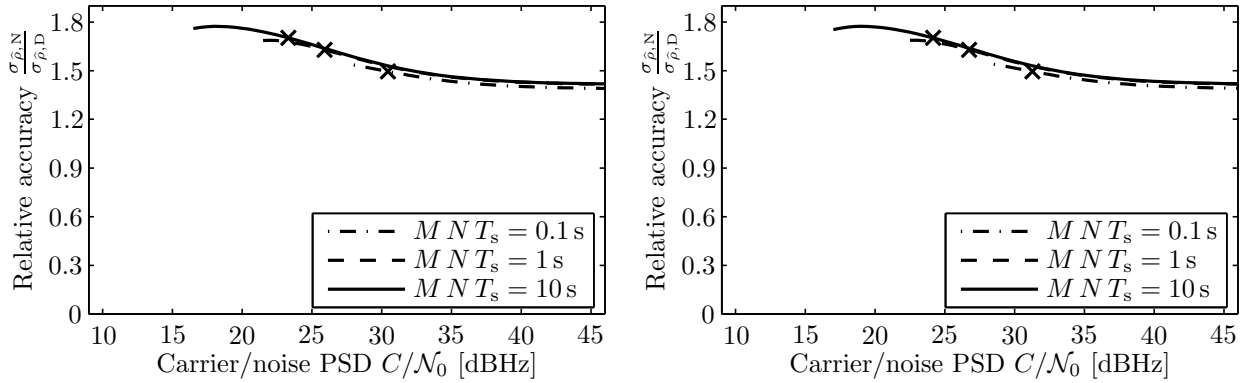

(a) GPS L1-C/A with $f_\mathrm{d} = 0$. (b) GPS L1-C/A with $f_\mathrm{d} = 60\,\mathrm{Hz}$.

Figure 3.22: Relative accuracy of the differential correlation technique for $T_0 = 290\,\mathrm{K}$, $F = 3\,\mathrm{dB}$, $N\,T_\mathrm{s} = 4\,\mathrm{ms}$, $B = 4.092\,\mathrm{MHz}$, and $\delta = 1/B$.

3.16 Accuracy Improvement

Fig. 3.22 compares the ranging accuracies of the differential correlation and the noncoherent integration procedures. It shows the ratio of the range standard deviations of the noncoherent integration method $\sigma_{\widehat{\rho},\mathrm{N}}$ and the differential correlation technique $\sigma_{\widehat{\rho},\mathrm{D}}$. The relative accuracy in Fig. 3.22 is obtained from the ratio of the values in Fig. 3.18 and 3.20. The range accuracy of the differential correlation is 39 % to 77 % more accurate than range accuracy of the noncoherent integration method.

Fig. 3.23 compares the ranging accuracies for the carrier-to-noise PSD $C_\mathrm{N}/\mathcal{N}_0$ which yields the detection probability $P_\mathrm{D} = 90\,\%$ for the state-of-the-art noncoherent integration. The relative accuracy in Fig. 3.23 is obtained from the ratio of the values in Fig. 3.19 and 3.21. It shows the accuracies for the same receiver parameters as used in Fig. 3.10 and 3.14. The carrier-to-noise PSD $C_\mathrm{N}/\mathcal{N}_0$ which permits the detection probability $P_\mathrm{d} = 90\,\%$ can be retrieved from Fig. 3.14 for various observation times $M\,N\,T_\mathrm{s}$. The range accuracy of the differential correlation technique becomes as much as 47 % to 80 % better than the range accuracy of the noncoherent integration method. It is slightly larger for shorter coherent integration periods and remains fairly constant over the range of observation periods $M\,N, T_\mathrm{s}$.

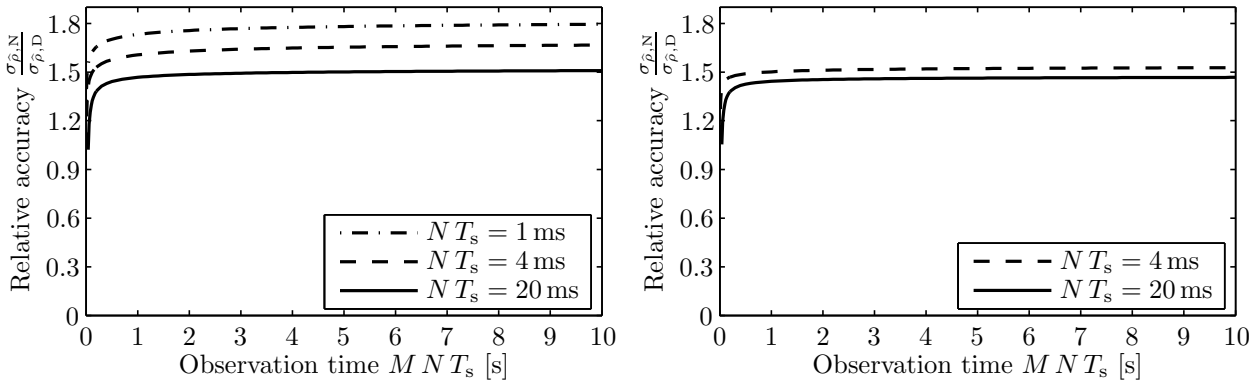

(a) GPS L1-C/A. (b) Galileo E1-C (pilot only).

Figure 3.23: Accuracy improvement of the differential correlation technique for $T_0 = 290\,\mathrm{K}$, $F = 3\,\mathrm{dB}$, $B = 4.092\,\mathrm{MHz}$, and $\delta = 1/B$.

3.17 Conclusion

Differential correlation is an attractive alternative to the state-of-the-art *noncoherent integration* method. The noncoherent integration procedure accumulates the squared magnitude of the coherently integrated predetection samples and thereby suffers from a squaring loss. The differential correlation approach on the other hand multiplies each predetection sample with the complex conjugate of its predecessor and accumulates these products. Since successive predetection samples are uncorrelated, the differential correlation technique yields a better reception sensitivity than the noncoherent integration routine. The product of two uncorrelated Gaussian variables has a lower variance than the product of two identical Gaussian variables. The sensitivity gain of the differential correlation method starts off with up to 2.7 dB for very short observation periods, but decreases substantially for very long observation periods. The sensitivity gain is independent of frequency deviations. Unlike the long coherent integration method, the differential correlation technique does not increase the number of frequency search bins over that of the noncoherent integration method. Since the decision statistics obtained from the differential correlation method have a lower variance, the code discrimination function for the differential correlation result has a lower variance, too. This effect improves the positioning accuracy. The differential correlation technique increases the accuracy of the estimated receiver-satellite distance to between 47 % and 80 % of the noncoherent integration results.

The decrease in sensitivity gain for very long observation periods is due to the asymptotic reception sensitivity characteristic of differential correlation and noncoherent integration. While both reception sensitivities converge, their slope reduces and their difference decreases. The adaptation of the detection threshold, which will be introduced in the next chapter, reduces the asymptotic effect. It not only enhances the reception sensitivity, but also leads to a sustained gain of the differential correlation technique over the noncoherent integration, also for very long observation periods.

Chapter 4

Adaptive Detection Threshold

The last chapter has shown that the reception sensitivity of both, the *differential correlation* and the state-of-the-art *noncoherent integration*, exhibit an asymptotic characteristic. Although the differential correlation yields a higher reception sensitivity than the noncoherent integration, both have problems with highly attenuated signals. The sensitivity improvement of extended observation periods decreases with increasing observation periods. The reason for this effect lies in out-of-phase autocorrelation values.

Fig. 4.1 shows examples of GPS correlation functions plus added thermal noise for different carrier-to-noise PSD values $C/\mathcal{N}_0$. The graph to the left displays the case of line-of-sight propagation. The line-of-sight correlation peak is out of the display range at $2.02 \times 10^6\,\sigma_w^4$. The adaptive detection threshold λ is drawn such that the out-of-phase autocorrelation values plus the thermal noise do not exceed λ with a probability greater than $P_\mathrm{f} = 10^{-5}$. The graph to the right displays the case of a moderate indoor signal with a carrier-to-noise PSD $C/\mathcal{N}_0 = 25\,\mathrm{dBHz}$. It can be observed that both, the correlation peak and the out-of-phase autocorrelation values are reduced. The correlation peak is reduced to an extent that it cannot be detected any more with the previous detection threshold λ. However, if the detection threshold is lowered for the lower signal power, the correlation peak can still be detected without violating the probability of false detection $P_\mathrm{f} = 10^{-5}$. The reason is

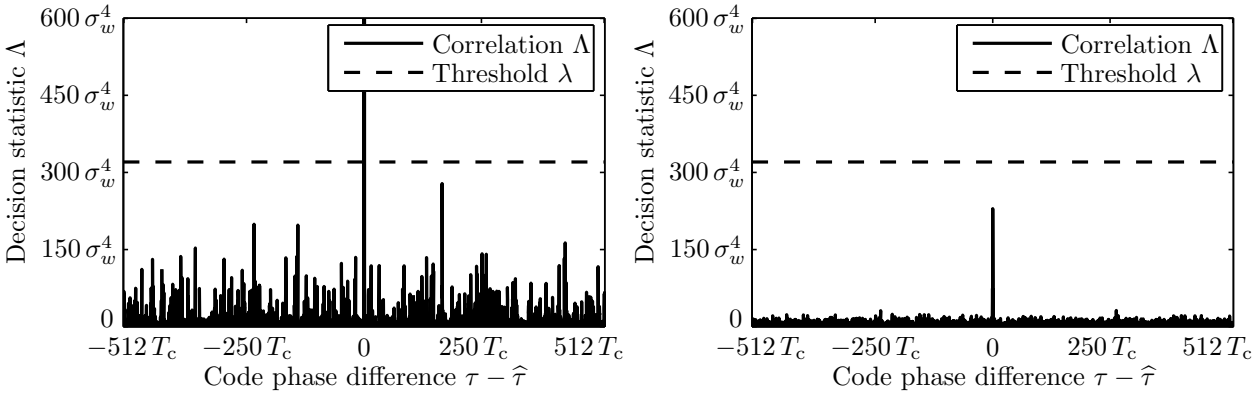

(a) GPS L1-C/A with $C/\mathcal{N}_0 = 45.5\,\mathrm{dBHz}$. (b) GPS L1-C/A with $C/\mathcal{N}_0 = 25\,\mathrm{dBHz}$.

Figure 4.1: Correlation functions with additive thermal noise and detection threshold λ for $T_0 = 290\,\mathrm{K}$, $F = 3\,\mathrm{dB}$, $N\,T_\mathrm{s} = 20\,\mathrm{ms}$, $M\,N\,T_\mathrm{s} = 0.1\,\mathrm{s}$, and $P_\mathrm{f} = 10^{-5}$.

the concurrent reduction of both, the correlation peak and the out-of-phase autocorrelation values.

The reception sensitivity can hence be improved if the receiver first estimates the received signal power and then correspondingly adjusts the detection threshold. The *adaptive detection threshold* substantially improves the reception sensitivities of the differential correlation technique and the noncoherent integration method.

4.1 Attenuation Mitigation

As introduced in Section 3.7, GPS receivers typically employ the Neyman-Pearson criterion, where the false detection probability P_f must not exceed a fixed number. The probability of detection P_d is maximized by choosing the lowest detection threshold λ without exceeding the maximum false detection probability. False detection is caused by out-of-phase autocorrelation, cross-correlation, and additive noise.

If the received signal strength decreases due to attenuation, the correlation peak and the out-of-phase autocorrelation values also decrease. If the line-of-sight detection threshold is used, then the probability of detection declines. However, the false detection probability also declines due to lower out-of-phase autocorrelation values. The detection threshold can be lowered for weaker signals in order to make full use of the maximum acceptable false detection probability. This increases the probability of detection for the correlation peak and therefore the reception sensitivity.

In order to optimally adjust the detection threshold, knowledge of the probability distribution of the received signal is required. If its correlation function, specified in (3.28) as

$$\begin{aligned} R(\tau-\widehat{\tau}) &= \sum_{\nu=0}^{N-1} c_{\lfloor(\nu\,T_\mathrm{s}+\tau)/T_\mathrm{c}\rfloor}\, q_{\lfloor(\nu\,T_\mathrm{s}+\tau)/T_\mathrm{c}\rfloor}\, c_{\lfloor(\nu\,T_\mathrm{s}+\widehat{\tau})/T_\mathrm{c}\rfloor}\, q_{\lfloor(\nu\,T_\mathrm{s}+\widehat{\tau})/T_\mathrm{c}\rfloor} \\ &\simeq \frac{1}{T_\mathrm{s}} \int_0^{N\,T_\mathrm{s}} c(t+\tau)\, q(t+\tau)\, c(t+\widehat{\tau})\, q(t+\widehat{\tau})\; dt\;, \end{aligned} \tag{4.1}$$

was assumed to be ideal, its out-of-phase autocorrelation and cross-correlation values would all be zero. In this case, the differential correlation mean, given in (3.39) as

$$m_\Psi = 2\,(M-1)\,C\,R^2(\tau-\widehat{\tau})\,\mathrm{sinc}^2(f_\mathrm{d}\,N\,T_\mathrm{s})\,\mathrm{e}^{\mathrm{j}\,2\,\pi\,f_\mathrm{d}\,N\,T_\mathrm{s}} \tag{4.2}$$

would be zero for hypothesis H_0. The cumulative probability density function of the decision statistic Λ, defined in (3.61) as

$$P_\Lambda(\Lambda) \simeq 1 - \mathrm{Q}_1\left(\sqrt{\frac{2\,|m_\Psi|^2}{\sigma_\Psi^2}},\, \sqrt{\frac{2\Lambda}{\sigma_\Psi^2}}\right) \tag{4.3}$$

would thus transform from a noncentral Chi-Squared to a central Chi-Squared distribution. The differential correlation variance in (3.51)

$$\sigma_\Psi^2 = (M-1)\,\sigma_w^4 + 4\,(M-1)\,\sigma_w^2\,C\,R^2(\tau-\widehat{\tau})\,\mathrm{sinc}^2(f_\mathrm{d}\,N\,T_\mathrm{s}) \tag{4.4}$$

would be reduced to $(M-1)\,\sigma_w^4$ for hypothesis H_0. Thus, the detection threshold, which is defined in (3.65) by

$$\lambda = P^{-1}_{\Lambda|\mathrm{H}_0}(1-P_\mathrm{f}) = \frac{\sigma^2_{\Psi,\mathrm{H}_0}}{2}\left[\mathrm{Q}^{-1}_{1,\beta}\left(\sqrt{\frac{2\,|m_{\Psi,\mathrm{H}_0}|^2}{\sigma^2_{\Psi,\mathrm{H}_0}}},\, P_\mathrm{f}\right)\right]^2 \tag{4.5}$$

with

$$m_{\Psi,\mathrm{H}_0} = m_\Psi\big|_{R^2(\tau-\widehat{\tau})=R^2_\mathrm{m}}\,, \quad \sigma^2_{\Psi,\mathrm{H}_0} = \sigma^2_\Psi\big|_{R^2(\tau-\widehat{\tau})=R^2_\mathrm{m}} \tag{4.6}$$

would be lowered significantly. The lowered detection threshold λ would obviously lead to a higher detection probability P_d. The assumption of an idealized correlation function $R(\tau-\widehat{\tau})$ would hence produce substantially higher reception sensitivities.

4.2 Detection Threshold Adjustment

The Welch, Sidelnikov, and Sarwate bounds provide lower bounds for the minimum possible value of the *maximum nontrivial correlation value* [62]. The maximum nontrivial correlation value is the maximum of the out-of-phase autocorrelation and the cross-correlation values. There are spreading codes with very good autocorrelation properties but poor cross-correlation properties and vice versa. Both have to be optimized for the code division multiple access scheme of GPS and Galileo. Low nontrivial correlation values reduce the probability of false acquisition. The Gold code of the GPS L1-C/A signal has equal maximum out-of-phase autocorrelation and cross-correlation values, which are close to the lower bounds [52, 62]. The spreading codes for the Galileo signals are memory-mapped pure random codes that have been chosen by computer simulation for further improved correlation properties.

The false detection probability is given in (3.63) as

$$P_\mathrm{f} = \Pr\{\Lambda \geqslant \lambda|\mathrm{H}_0\} = 1 - P_{\Lambda|\mathrm{H}_0}(\lambda) = \mathrm{Q}_1\left(\sqrt{\frac{2\,|m_{\Psi,\mathrm{H}_0}|^2}{\sigma^2_{\Psi,\mathrm{H}_0}}},\, \sqrt{\frac{2\,\lambda}{\sigma^2_{\Psi,\mathrm{H}_0}}}\right)\,. \tag{4.7}$$

If an idealized correlation function $R(\tau-\widehat{\tau})$ with $R_\mathrm{m}=0$ was assumed, the detection threshold λ would be calculated based on the central Chi-Squared distribution. However, the lowered detection threshold would lead to a violation of the maximum permissable false detection probability, if the actual correlation function with $R_\mathrm{m}\neq 0$ is applied in (4.7). Fig. 4.2.a and 4.2.b show P_f for the case where the threshold λ is calculated for an idealized correlation function with $R_\mathrm{m}=0$, but the received signal has the actual correlation function with $R_\mathrm{m}=65\,N/1023$ for GPS L1-C/A and $R_\mathrm{m}=0.094\,N$ for Galileo E1-C [5, 29]. It can be observed that P_f increases to 100 % with an increasing carrier-to-noise PSD $C/\mathcal{N}_0$. The nominal false detection probability $P_\mathrm{f}=10^{-5}$ is only met for the carrier power $C=0$. The threshold is much too low for signals from around $C/\mathcal{N}_0 = 25\,\mathrm{dBHz}$ onwards. The reason are the out-of-phase correlation values that increase above the threshold and cause frequent false detections.

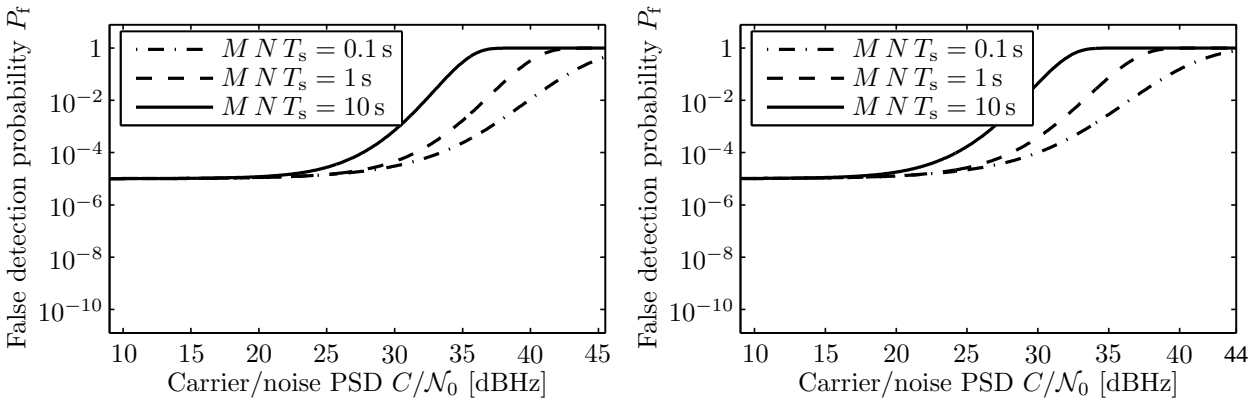

(a) GPS L1-C/A with $R_m = 0$. (b) Galileo E1-C with $R_m = 0$.

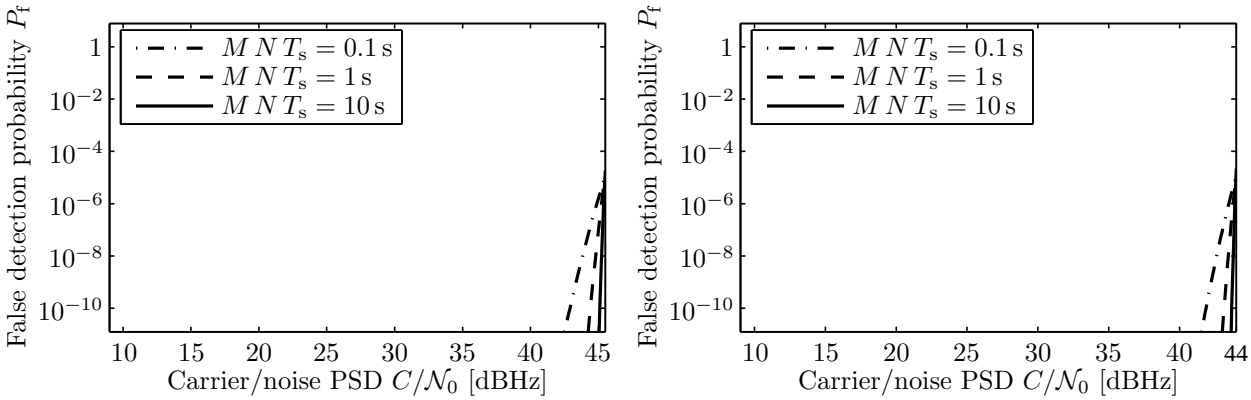

(c) GPS L1-C/A with $R_m = 65\,N/1023$. (d) Galileo E1-C with $R_m = 0.094\,N$.

Figure 4.2: Probability of false detection P_f for different detection thresholds λ with $T_0 = 290\,K$, $F = 3\,dB$, and $N\,T_s = 20\,ms$.

Fig. 4.2.c and 4.2.d show P_f for the case where the threshold λ is calculated for the nominal signal power and the real correlation function with $R_m = 65\,N/1023$ for GPS L1-C/A and $R_m = 0.094\,N$ for Galileo E1-C [62]. It can be observed that P_f has the nominal value for the line-of-sight carrier power, but decreases very fast for lower $C/\mathcal{N}_0$ values. The reason for this effect is that the mean m_Ψ in (4.2) and the variance σ_Ψ^2 in (4.4) are functions of the carrier power C. The threshold λ in Fig. 4.2.c and 4.2.d, however, is calculated for the line-of-sight carrier power C as specified in Table 3.1. This threshold is unnecessarily high for weak signals.

If the maximum permissable false detection probability P_f in (4.7) is to be fully utilized, the detection threshold λ has to be calculated with (4.5) for the actual received signal properties. It is required to calculate the mean m_Ψ in (4.2) for $R^2(\tau - \widehat{\tau}) = R_m^2$ as a function of the received carrier power C and frequency deviation f_d. The variance σ_Ψ^2 in (4.4) has to be calculated as a function of the received carrier power C, frequency deviation f_d, and noise temperature T_0 using $R^2(\tau - \widehat{\tau}) = R_m^2$. The detection threshold λ can be lowered for a decreasing C. It is always set as low as possible without violating the maximum permissable false detection probability P_f in (4.7). This technique substantially improves the probability of detection P_d. Fig. 4.3 shows the adaptive detection threshold λ as a function of $C/\mathcal{N}_0$. The value converges for very low $C/\mathcal{N}_0$ values, since the out-of-phase correlation values become insignificant compared to the additive noise component.

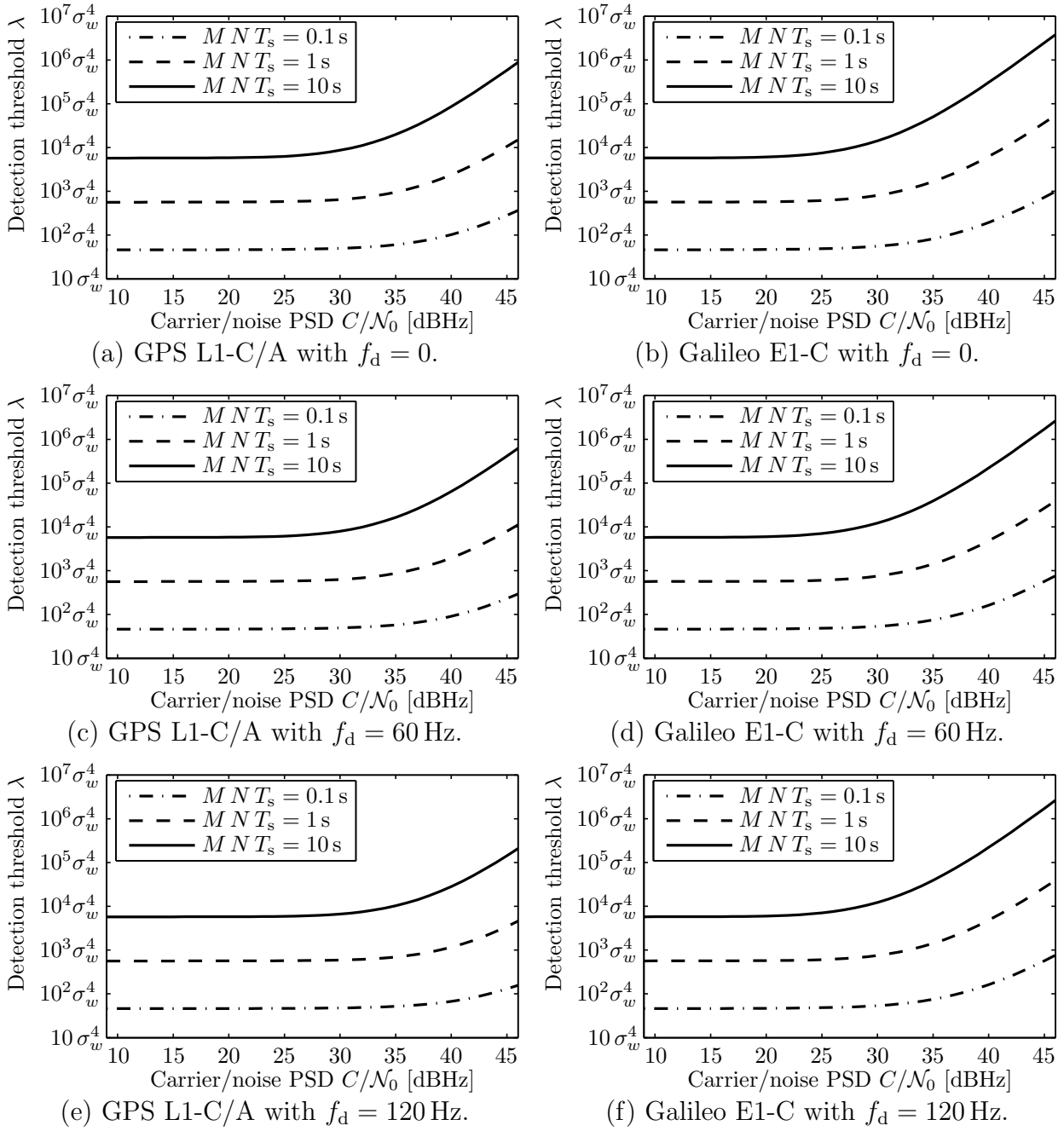

(a) GPS L1-C/A with $f_\mathrm{d} = 0$.

(b) Galileo E1-C with $f_\mathrm{d} = 0$.

(c) GPS L1-C/A with $f_\mathrm{d} = 60\,\mathrm{Hz}$.

(d) Galileo E1-C with $f_\mathrm{d} = 60\,\mathrm{Hz}$.

(e) GPS L1-C/A with $f_\mathrm{d} = 120\,\mathrm{Hz}$.

(f) Galileo E1-C with $f_\mathrm{d} = 120\,\mathrm{Hz}$.

Figure 4.3: Adaptive detection threshold λ for $T_0 = 290\,\mathrm{K}$, $F = 3\,\mathrm{dB}$, $N\,T_\mathrm{s} = 20\,\mathrm{ms}$, and $B = 4.092\,\mathrm{MHz}$.

4.3 Cross-Correlation Mitigation

An important aspect that has to be considered when lowering the detection threshold is the cross-correlation between the signals. The maximum cross-correlation value of the Gold code for GPS L1-C/A is 65/1023, which corresponds to an attenuation of 24 dB [29, 63]. If two signals are received with the same Doppler frequency shift and have a power difference of 24 dB, then the stronger signal introduces cross-correlation of equal power as the autocorrelation peak of the weak signal. The cross-correlation is significantly reduced if the two signals have a different Doppler shift. With a coherent integration of $N\,T_\mathrm{s} = 20\,\mathrm{ms}$ and a Doppler shift difference of just 45 Hz, a GPS L1-C/A signal already has to be 43 dB

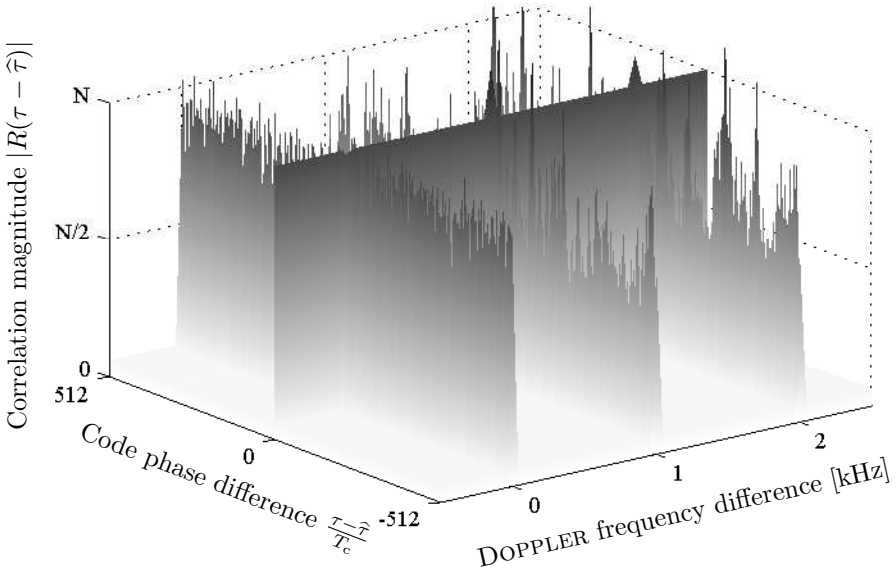

Figure 4.4: Correlation function of a weak GPS L1-C/A signal with $N\,T_\mathrm{s} = 20\,\mathrm{ms}$ in presence of a 24 dB stronger GPS L1-C/A signal with varying Doppler frequency difference.

stronger than another signal to have its cross-correlation reach the same level as the auto-correlation peak of the weak signal. The cross-correlation reoccurs for GPS L1-C/A if the Doppler shift difference is an integer multiple of 1 kHz [29, 63].

Fig. 4.4 illustrates the case where a weak GPS L1-C/A signal is correlated with its correct local spreading code. At the same time a 24 dB stronger GPS L1-C/A signal with a different spreading code causes interference. The Y-axis represents the code phase difference $\tau - \widehat{\tau}$. The correct autocorrelation peak can be found for $\tau - \widehat{\tau} = 0$, independent of the Doppler frequencies. The X-axis denotes the Doppler frequency difference between the strong and weak signal. If both have equal Doppler frequencies, such that the difference is zero, one can observe severe cross-correlation. As soon as there is a little Doppler frequency difference, the cross-correlation vanishes, leaving only the correct autocorrelation peak behind. However, the cross-correlation reoccurs at integer multiples of 1 kHz, which can be explained with the combined correlation function

$$R(\tau-\widehat{\tau}) = \sum_{\nu=0}^{N-1} c^{(1)}_{\lfloor(\nu\,T_\mathrm{s}+\widehat{\tau})/T_\mathrm{c}\rfloor}\left[\sqrt{2\,C^{(1)}}\,c^{(1)}_{\lfloor(\nu\,T_\mathrm{s}+\tau)/T_\mathrm{c}\rfloor} + \sqrt{2\,C^{(2)}}\,c^{(2)}_{\lfloor(\nu\,T_\mathrm{s}+\tau)/T_\mathrm{c}\rfloor}\,\mathrm{e}^{\mathrm{j}\,2\,\pi\,f_\mathrm{d}\,(\nu\,T_\mathrm{s}+\tau)}\right]. \tag{4.8}$$

The weak signal with carrier power $C^{(1)}$ and spreading code $c^{(1)}_{\lfloor(\nu\,T_\mathrm{s}+\tau)/T_\mathrm{c}\rfloor}$ is being despread with the correct local code $c^{(1)}_{\lfloor(\nu\,T_\mathrm{s}+\widehat{\tau})/T_\mathrm{c}\rfloor}$. The strong interfering signal with carrier power $C^{(2)}$ has a different spreading code $c^{(2)}_{\lfloor(\nu\,T_\mathrm{s}+\tau)/T_\mathrm{c}\rfloor}$ and a frequency offset f_d. Every 1 ms interval produces a correlation function with the autocorrelation peak in the middle and cross-correlation on the side. In the case of zero frequency deviation, the Gold code of GPS L1-C/A has around 24 dB isolation between the autocorrelation peak and the cross-correlation values. Just like the autocorrelation function, the cross-correlation function is also three-valued, where the correlation values $R(\tau-\widehat{\tau})|_{\tau-\widehat{\tau}=\nu\,T_\mathrm{c}} = -65\,N/1023$ and $R(\tau-\widehat{\tau})|_{\tau-\widehat{\tau}=\nu\,T_\mathrm{c}} = 63\,N/1023$ each have a 12.5 % occurrence rate [29, 52].

In the case of non-zero frequency deviation, the cross-correlation function becomes more erratic, with the maximum cross-correlation values only 21 dB below the correlation peak. This, however, is only true for 0.1 % of the cross-correlation values, while 98 % of the cross-correlation values have more than 24 dB isolation [63]. If $N\,T_\mathrm{s} > 1\,\mathrm{ms}$, then multiples of these cross-correlation functions with the correlation peak in the middle are accumulated. When the frequency deviation f_d is not an integer multiple of 1 kHz, then the phase $\mathrm{e}^{\mathrm{j}\,2\,\pi\,f_\mathrm{d}\,(\nu\,T_\mathrm{s}+\tau)}$ in (4.8) has a different value after each 1 ms interval. As a result the cross-correlation function of each 1 ms interval looks different. The cross-correlation values for each code delay vary between positive and negative values for each 1 ms period. When multiple cross-correlation functions are coherently accumulated, the cross-correlation values partially cancel out each other. The isolation between the autocorrelation peak and the cross-correlation values becomes much larger than for zero frequency deviation.

However, if the frequency deviation f_d in (4.8) is an integer multiple of 1 kHz, the phase $\mathrm{e}^{\mathrm{j}\,2\,\pi\,f_\mathrm{d}\,(\nu\,T_\mathrm{s}+\tau)}$ has exactly the same value after each 1 ms interval. As a result, the cross-correlation functions of each 1 ms period are identical. When they are coherently accumulated multiple times, each code delay always yields the same correlation values. No positive and negative values cancel out each other. The same cross-correlation is simply scaled by $N\,T_\mathrm{s}/(1\,\mathrm{ms})$. At integer multiples of 1 kHz, the isolation between the autocorrelation peak and the cross-correlation is therefore suddenly reduced to around 21–24 dB. Since the interfering signal in Fig. 4.4 has 24 dB more signal power than the wanted signal, the maximum cross-correlation values at integer multiples of 1 kHz slightly exceed the autocorrelation peak.

The simplest way to prevent false detection due to cross-correlation is to utilize the strongest signal in each frequency bin to calculate the detection threshold in this frequency bin and the bins apart by an integer multiple of 1 kHz. In result, the weakest signal that can be detected in the respective frequency bins must be less than 24 dB weaker than the strongest signal in these bins. Fortunately, the frequency bins become rather narrow with an increasing coherent integration period. A typical bin size is 30–50 Hz for $N\,T_\mathrm{s} = 20\,\mathrm{ms}$. The likelihood of this interference scenario is rather low. This could be the most cost-effective solution for many mass market products, since the resulting availability degradation might be negligible. However, the cross-correlation problem can also be resolved for two signals in the same frequency bin by a variety of different cross-correlation mitigation techniques [64, 65, 66]. One possible method relies on multiple correlations separated by more than 1.54 s. It utilizes the effect that the cross-correlation pattern moves by one chip each 1.54 s for a frequency difference of 1 kHz [29].

While the maximum cross-correlation for the Galileo E1-C primary codes is of similar magnitude as for GPS L1-C/A, the secondary spreading codes of Galileo E1-C can resolve the problem. For example, if the secondary codes of two signals differ by half the chips within the observation period, then the cross-correlation effect fully vanishes. A method to prevent cross-correlation for Galileo L1-C is hence to correlate the signals at the time instances when their secondary codes suppress the cross-correlation. The respective timing information could be provided by assistance data. If the correlation period extends over a sufficient number of secondary code chips, the cross-correlation will also be strongly suppressed when the correlation starts at an arbitrary time. Furthermore, it would even be possible to utilize the

data bits of the GPS L1-C/A signal to suppress cross-correlation. A reference receiver would have to track interfering signals and predict some data bits. It could then provide assistance data to schedule the correlation process of the mobile receiver such that the data bits of the interfering signals have different values around half the time.

4.4 Attenuation Estimation

The adaptive detection threshold λ requires knowledge of the actual received differential correlation variance $\sigma^2_{\Psi,\mathrm{H}_0}$ and magnitude of the mean $|m_{\Psi,\mathrm{H}_0}|$. The decision statistic Λ is the squared magnitude of the GAUSSIAN distributed differential correlation result Ψ. The combination of its first moment

$$\mathrm{E}\{\Lambda\} = \mathrm{E}\{|\Psi|^2\} = |m_\Psi|^2 + \sigma^2_\Psi \tag{4.9}$$

with its second moment

$$\mathrm{E}\{\Lambda^2\} = \mathrm{E}\{|\Psi|^4\} = \sigma^4_\Psi + 2\,\sigma^2_\Psi\,|m_\Psi|^2 + \left(\sigma^2_\Psi + |m_\Psi|^2\right)^2 \tag{4.10}$$

yields the relationships

$$|m_\Psi|^2 = \sqrt{2\,\left(\mathrm{E}\{\Lambda\}\right)^2 - \mathrm{E}\{\Lambda^2\}} \tag{4.11}$$

and

$$\sigma^2_\Psi = \mathrm{E}\{\Lambda\} - |m_\Psi|^2\,. \tag{4.12}$$

This can be utilized to estimate the parameters $|m_{\Psi,\mathrm{H}_0}|$ and $\sigma^2_{\Psi,\mathrm{H}_0}$. Since both parameters should be estimated for hypothesis H_0, the first step is to exclude the correlation peak. The different decision statistics within one frequency search bin are denoted as Λ_ι. The different code phase search bins are thereby indexed with ι. First, the index $\hat{\iota}$, which originates most likely from the correlation peak is selected by one of the methods described in Section 3.12.

The interval of the correlation peak is excluded in the following estimation algorithm, such that only the out-of-phase correlation values for are used. The variable D is introduced in Section 2.3 as the number of code phase search bins. The first moment is hence estimated by

$$\boxed{\mathcal{M}_1 = \frac{1}{D - 2\,\lceil T_\mathrm{c}/T_\mathrm{s}\rceil + 1}\left[\sum_{\nu=1}^{\hat{\iota}-\lceil T_\mathrm{c}/T_\mathrm{s}\rceil}\Lambda_\nu + \sum_{\nu=\hat{\iota}+\lceil T_\mathrm{c}/T_\mathrm{s}\rceil}^{D}\Lambda_\nu\right] \simeq \mathrm{E}\{\Lambda\}\,\big|_{\tau\neq\hat{\tau}}} \tag{4.13}$$

and the second moment is estimated by

$$\boxed{\mathcal{M}_2 = \frac{1}{D - 2\,\lceil T_\mathrm{c}/T_\mathrm{s}\rceil + 1}\left[\sum_{\nu=1}^{\hat{\iota}-\lceil T_\mathrm{c}/T_\mathrm{s}\rceil}\Lambda^2_\nu + \sum_{\nu=\hat{\iota}+\lceil T_\mathrm{c}/T_\mathrm{s}\rceil}^{D}\Lambda^2_\nu\right] \simeq \mathrm{E}\{\Lambda^2\}\,\big|_{\tau\neq\hat{\tau}}}\,, \tag{4.14}$$

where $\lceil\,\cdot\,\rceil$ is the ceiling function for rounding to the nearest integer more or equal.

The GPS L1-C/A out-of-phase correlation values plus noise can be seen in Fig. 4.1 on both sides of the correlation peak. The GPS L1-C/A signals utilize GOLD codes of length

1023, which have the three different out-of-phase autocorrelation values 63, -1, -65 [52]. The average magnitude of the out-of-phase autocorrelation values $\mathrm{E}\{|R(\tau - \widehat{\tau})|\}|_{\tau \neq \widehat{\tau}}$ lies below the maximum magnitude of the out-of-phase autocorrelation values R_m. When analyzing the correlation functions, it can be observed that the relationship $\mathrm{E}\{|R(\tau - \widehat{\tau})|\}|_{\tau \neq \widehat{\tau}} = \vartheta\, R_\mathrm{m}$ is different for all space vehicles and the conversion factor ϑ lies in the range $\vartheta \in [0.21,\, 0.32]$ for GPS L1-C/A. For Galileo E1-B and E1-C it is a bit lower in the range $\vartheta \in [0.18,\, 0.25]$. The detection threshold λ has to be calculated with the factor ϑ of the particular space vehicle using the relationship $\mathrm{E}\{|m_\Psi|\}|_{\tau \neq \widehat{\tau}} = \vartheta^2\, |m_{\Psi,\mathrm{H}_0}|$.

With (4.11), the squared magnitude of the differential correlation mean for hypothesis H_0 can therefore be estimated as

$$\boxed{|\widehat{m}_{\Psi,\mathrm{H}_0}|^2 = \frac{1}{\vartheta^4}\sqrt{2\,\mathcal{M}_1^2 - \mathcal{M}_2}}\,. \tag{4.15}$$

With (3.39) and (3.51), the differential correlation variance can be expressed as

$$\sigma_\Psi^2 = (M-1)\,\sigma_w^4 + 2\,\sigma_w^2\,|m_\Psi|\,. \tag{4.16}$$

The variable σ_w^2 can be calculated with

$$0 = \sigma_w^4 + \frac{2\,|m_\Psi|}{M-1}\sigma_w^2 - \frac{\sigma_\Psi^2}{M-1} \tag{4.17}$$

as

$$\sigma_w^2 = -\frac{|m_\Psi|}{M-1} + \sqrt{\frac{|m_\Psi|^2}{(M-1)^2} + \frac{\sigma_\Psi^2}{M-1}}\,. \tag{4.18}$$

With (4.12) it is estimated as

$$\widehat{\sigma}_w^2 = -\frac{\vartheta^2\,|\widehat{m}_{\Psi,\mathrm{H}_0}|}{M-1} + \sqrt{\frac{\vartheta^4\,|\widehat{m}_{\Psi,\mathrm{H}_0}|^2}{(M-1)^2} + \frac{\mathcal{M}_1 - \vartheta^4\,|\widehat{m}_{\Psi,\mathrm{H}_0}|^2}{(M-1)}}\,. \tag{4.19}$$

The differential correlation variance for hypothesis H_0 can hence be estimated as

$$\boxed{\widehat{\sigma}_{\Psi,\mathrm{H}_0}^2 = (M-1)\,\widehat{\sigma}_w^4 + 2\,\widehat{\sigma}_w^2\,|\widehat{m}_{\Psi,\mathrm{H}_0}|}\,. \tag{4.20}$$

Incorporating the previous results, the adaptive detection threshold is

$$\boxed{\widehat{\lambda} = P_{\Lambda|\mathrm{H}_0}^{-1}(1-P_\mathrm{f}) = \frac{\widehat{\sigma}_{\Psi,\mathrm{H}_0}^2}{2}\left[\mathrm{Q}_{1,\beta}^{-1}\left(\sqrt{\frac{2\,|\widehat{m}_{\Psi,\mathrm{H}_0}|^2}{\widehat{\sigma}_{\Psi,\mathrm{H}_0}^2}},\, P_\mathrm{f}\right)\right]^2}\,. \tag{4.21}$$

Fig. 4.5 compares a simulation of the estimated detection threshold $\widehat{\lambda}$ versus the optimal detection threshold λ. Due to the applied sample rate of four samples per chip, a total number of 1021×4 code phase bins have been evaluated for the GPS L1-C/A simulations and 4090×4 code phase bins for the Galileo E1-C simulations. Both corresponds to a full-epoch search excluding the correlation peak. No relevant estimation errors can be observed in the simulations. The estimation method presented here shows a high level of reliability.

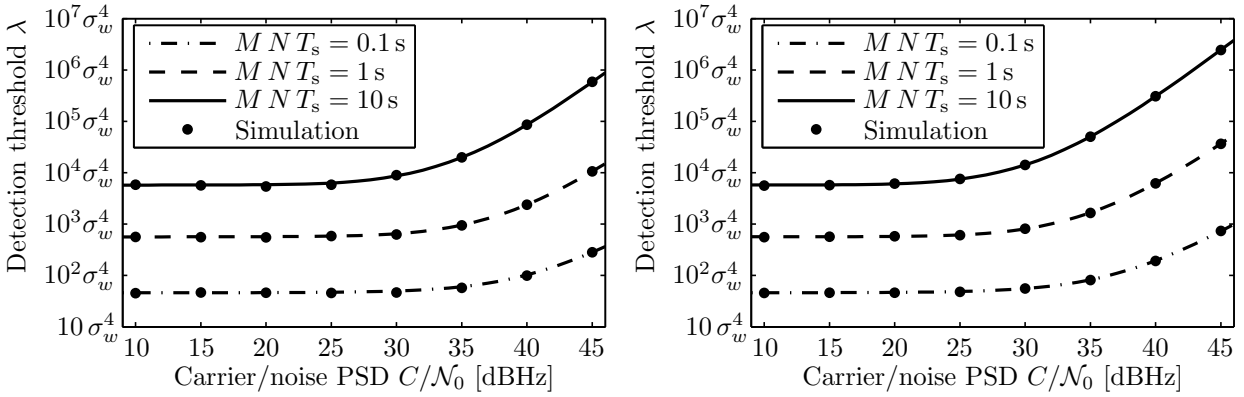

(a) GPS L1-C/A with $f_\mathrm{d} = 0$.

(b) Galileo E1-C with $f_\mathrm{d} = 0$.

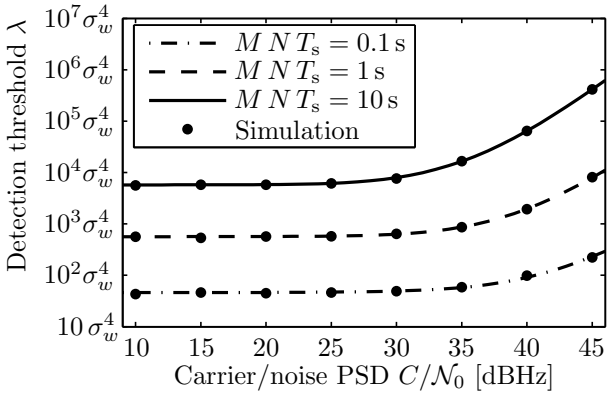

(c) GPS L1-C/A with $f_\mathrm{d} = 60\,\mathrm{Hz}$.

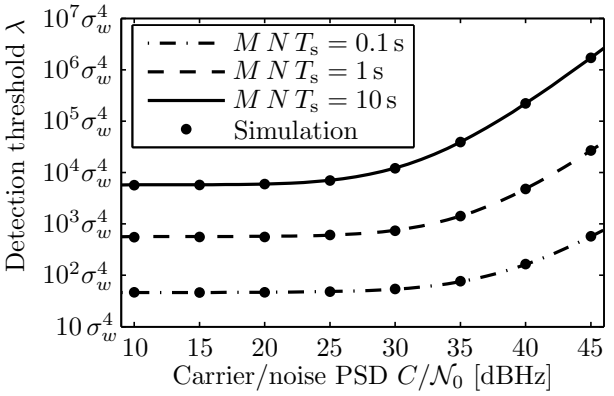

(d) Galileo E1-C with $f_\mathrm{d} = 60\,\mathrm{Hz}$.

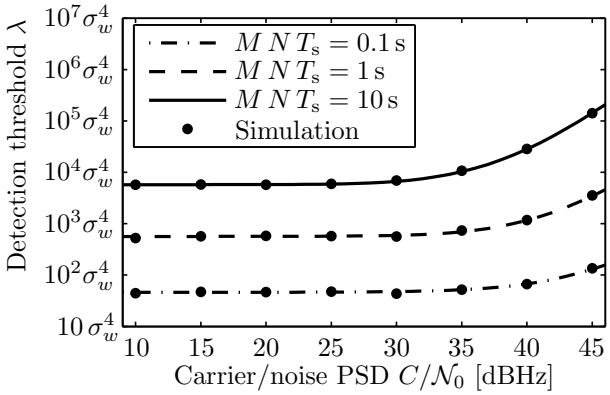

(e) GPS L1-C/A with $f_\mathrm{d} = 120\,\mathrm{Hz}$.

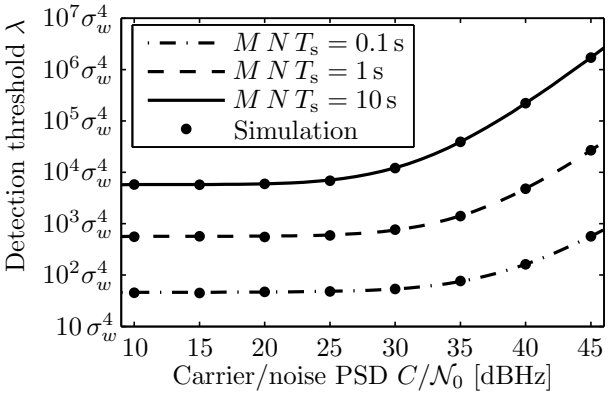

(f) Galileo E1-C with $f_\mathrm{d} = 120\,\mathrm{Hz}$.

Figure 4.5: Comparison of the estimated detection threshold $\widehat{\lambda}$ versus the simulated optimal detection threshold λ for $T_0 = 290\,\mathrm{K}$, $F = 3\,\mathrm{dB}$, $N\,T_\mathrm{s} = 20\,\mathrm{ms}$, and $B = 4.092\,\mathrm{MHz}$.

4.5 Differential Correlation Sensitivity

The probability of detection is calculated with

$$\boxed{P_\mathrm{d} = \Pr\{\Lambda \geqslant \lambda | \mathrm{H}_1\} = 1 - P_{\Lambda|\mathrm{H}_1}(\lambda) = \mathrm{Q}_1\left(\sqrt{\frac{2\,|m_{\Psi,\mathrm{H}_1}|^2}{\sigma^2_{\Psi,\mathrm{H}_1}}}, \sqrt{\frac{2\,\lambda}{\sigma^2_{\Psi,\mathrm{H}_1}}}\right)} \tag{4.22}$$

as specified in (3.66) by applying

$$m_{\Psi,\mathrm{H}_1} = m_\Psi\big|_{R^2(\tau-\widehat{\tau})=N^2}\,, \quad \sigma^2_{\Psi,\mathrm{H}_1} = \sigma^2_\Psi\big|_{R^2(\tau-\widehat{\tau})=N^2}\,. \tag{4.23}$$

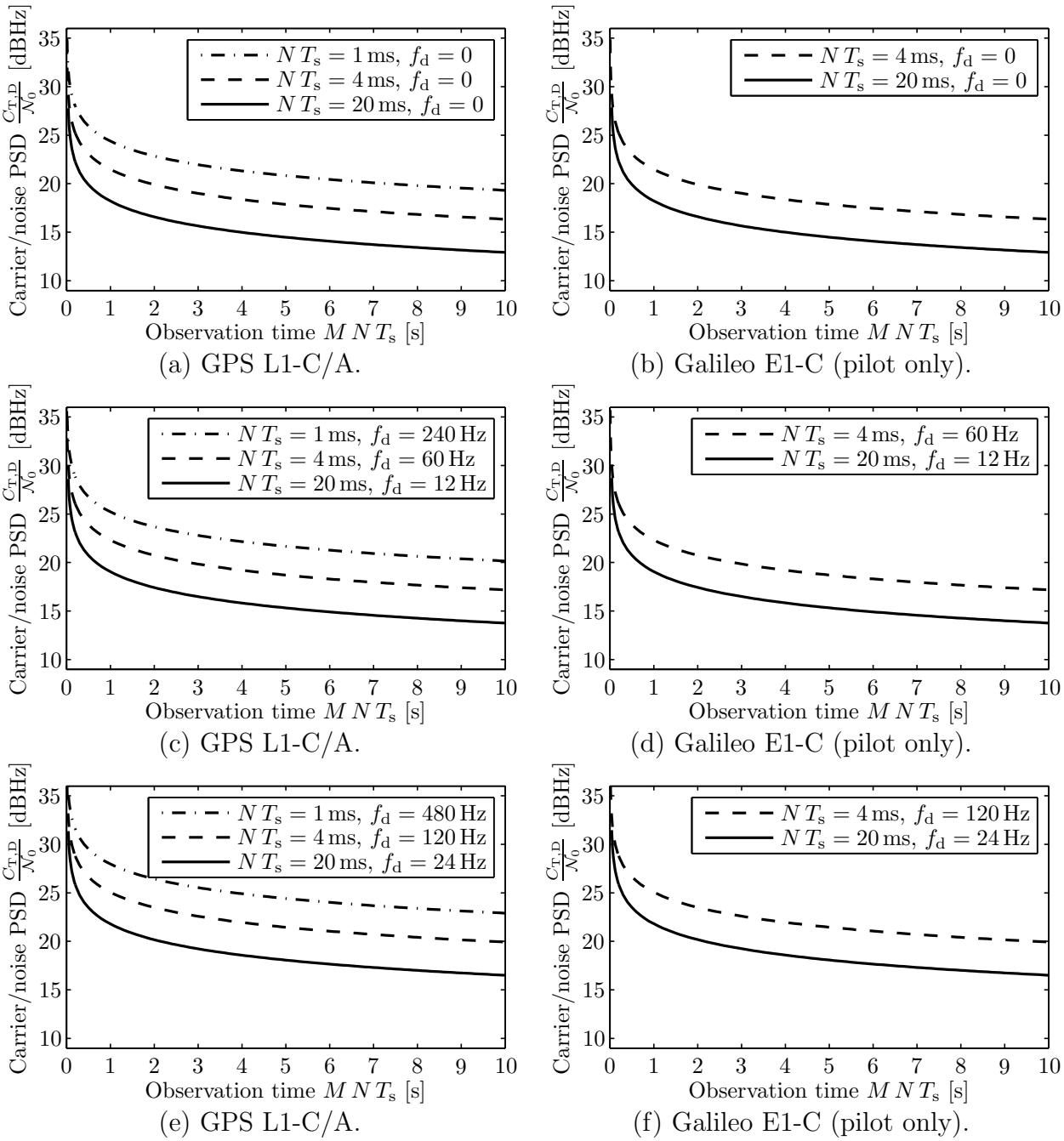

(a) GPS L1-C/A. (b) Galileo E1-C (pilot only).

(c) GPS L1-C/A. (d) Galileo E1-C (pilot only).

(e) GPS L1-C/A. (f) Galileo E1-C (pilot only).

Figure 4.6: Reception sensitivity with the adaptive detection threshold technique for the differential correlation with $T_0 = 290\,\text{K}$, $F = 3\,\text{dB}$, $P_f = 10^{-5}$, and $P_d = 90\,\%$.

Fig. 4.6 illustrates the carrier-to-noise PSD values $C_{T,D}/\mathcal{N}_0$ for the probability of detection $P_d = 90\,\%$, when the adaptive detection threshold of Fig. 4.3 is used in combination with differential correlation. The choice of the receiver parameters $T_0 = 290\,\text{K}$, $F = 3\,\text{dB}$, $P_f = 10^{-5}$, and $P_d = 90\,\%$ has been discussed in Section 3.7. When compared to the reception sensitivity presented in Fig. 3.10, it becomes apparent that the adaptive detection threshold method yields a very high improvement. Furthermore, with the static detection threshold in Fig. 3.10, the sensitivity for GPS L1-C/A has been slightly higher than for Galileo E1-C. This has been due to the slightly higher maximum out-of-phase autocorrelation value of Galileo E1-C, since it is transmitted in phase with the Galileo E1-B signal. This effect has virtually vanished in Fig. 4.3 when the detection threshold is dynamically

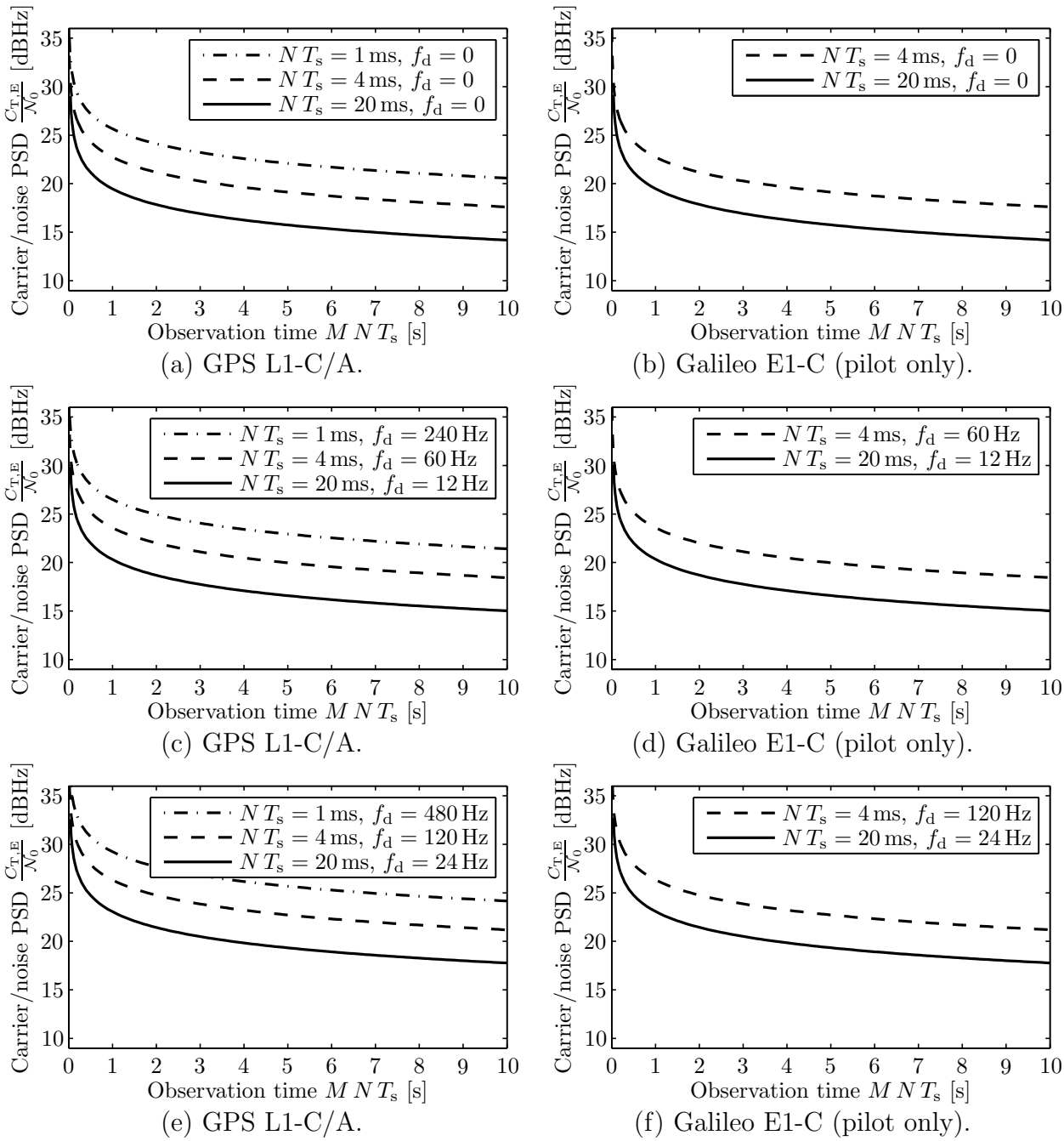

(a) GPS L1-C/A. (b) Galileo E1-C (pilot only).

(c) GPS L1-C/A. (d) Galileo E1-C (pilot only).

(e) GPS L1-C/A. (f) Galileo E1-C (pilot only).

Figure 4.7: Reception sensitivity with the adaptive detection threshold technique for a detection threshold estimation error of factor 2 with $T_0 = 290\,\text{K}$, $F = 3\,\text{dB}$, $P_\text{f} = 10^{-5}$, and $P_\text{d} = 90\,\%$.

adjusted. The sensitivity for Galileo E1-C has reached the one for GPS L1-C/A.

The sensitivity gain of the adaptive detection threshold technique is furthermore fairly insensitive to reasonable estimation errors. Fig. 4.7 shows the reception sensitivity $C_{\text{T,E}}/\mathcal{N}_0$ for $\widehat{\lambda} = 2\,\lambda$. Fig. 4.8 shows the loss $C_{\text{T,E}}/C_{\text{T,D}}$ that is introduced by this estimation error of factor 2. In dB, it is calculated as the difference between the curves in Fig. 4.7 and 4.6. Since the estimation error degrades the reception in the same way for an increasing frequency deviation f_d, the sensitivity loss becomes independent of f_d and Fig. 4.8 is not parameterized by f_d. It applies to any f_d within the frequency search bin. The sensitivity introduced by the severe estimation error of $\widehat{\lambda} = 2\,\lambda$ causes only a minor sensitivity loss of 1.3 dB.

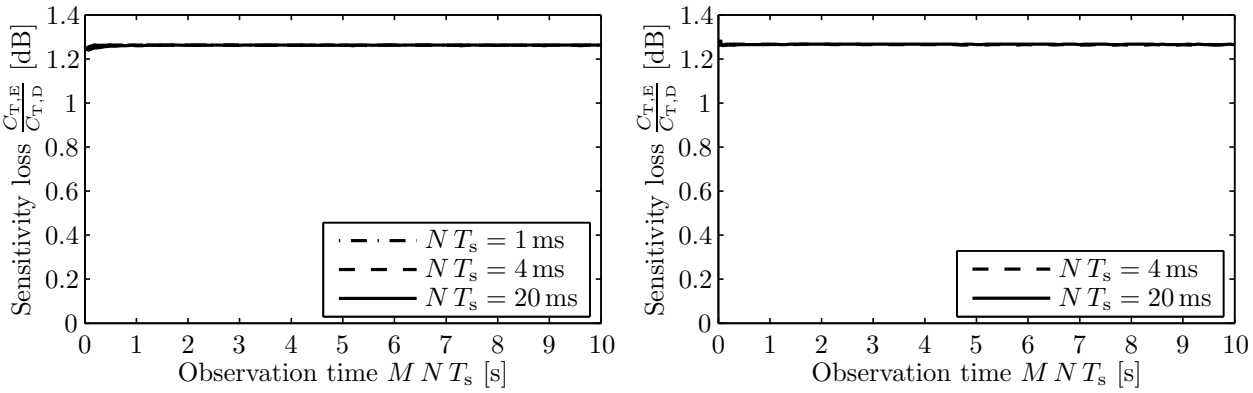

(a) GPS L1-C/A. (b) Galileo E1-C (pilot only).

Figure 4.8: Sensitivity loss caused by a detection threshold estimation error of factor 2 with $T_0 = 290\,\mathrm{K}$, $F = 3\,\mathrm{dB}$, $P_\mathrm{f} = 10^{-5}$, and $P_\mathrm{d} = 90\,\%$.

4.6 Noncoherent Integration Sensitivity

The reception sensitivity of the noncoherent integration method can also be substantially improved with an adaptive detection threshold procedure. The detection threshold for the noncoherent integration approach is given in (3.76) as

$$\lambda = \frac{\sigma_w^2}{2}\left[\mathrm{Q}_{M,\beta}^{-1}\left(\sqrt{\frac{2\,M\,|y_{\mu,\mathrm{H_0}}|^2}{\sigma_w^2}},\,P_\mathrm{f}\right)\right]^2. \tag{4.24}$$

It is a function of the deterministic predetection component

$$y_\mu \simeq \sqrt{2\,C}\,d_{\mathrm{s},\mu}\,R(\tau-\widehat{\tau})\,\mathrm{sinc}(f_\mathrm{d}\,N\,T_\mathrm{s})\,\mathrm{e}^{\mathrm{j}\,[(2\,\mu+1)\,\pi\,f_\mathrm{d}\,N\,T_\mathrm{s}+\varphi_\mathrm{c}]} \tag{4.25}$$

as defined in (3.31) and the predetection noise variance

$$\sigma_w^2 = 2\,Nk\,T_0\,B\,F \tag{4.26}$$

given in (3.19).

Fig. 4.9 shows the reception sensitivity $C_{\mathrm{T,N}}/\mathcal{N}_0$ for the noncoherent integration method with the adaptive detection threshold, which is given by inserting the actual carrier power C, frequency deviation f_d, and noise temperature T_0 into (4.25) and (4.26). The estimation of the two parameters $|y_{\mu,\mathrm{H_0}}|^2$ and σ_w^2 can be performed in a similar fashion as described in Section 4.4 or with conventional signal-to-noise ratio estimation techniques [67, 68, 69].

4.7 Sensitivity Gain

This section illustrates the sensitivity gain that can be obtained by the adaptive selection of the detection threshold. The sensitivity gain $C_\mathrm{D}/C_{\mathrm{T,D}}$ obtained by applying the adaptive detection threshold method to the differential correlation technique is the difference between the values in dB of Fig. 3.10 and 4.6. It can be observed that the maximum reception sensitivity in Fig. 3.10 is bound, while Fig. 4.6 presents far better sensitivity. The gain of the

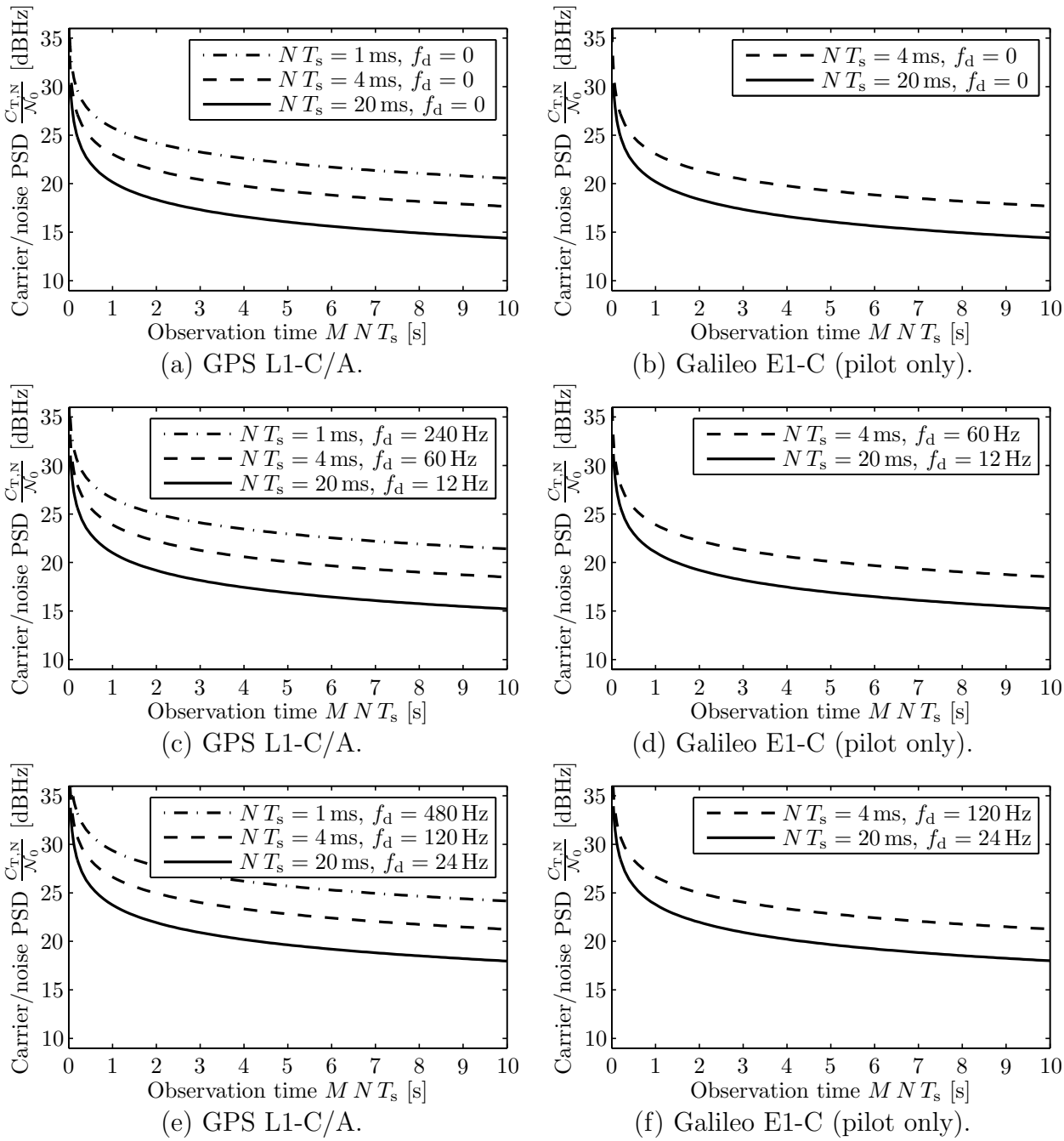

(a) GPS L1-C/A. (b) Galileo E1-C (pilot only).

(c) GPS L1-C/A. (d) Galileo E1-C (pilot only).

(e) GPS L1-C/A. (f) Galileo E1-C (pilot only).

Figure 4.9: Reception sensitivity with the adaptive detection threshold technique for the noncoherent integration with $T_0 = 290\,\text{K}$, $F = 3\,\text{dB}$, $P_\text{f} = 10^{-5}$, and $P_\text{d} = 90\,\%$.

presented method is therefore very large. The gain of the adaptive detection threshold when applied to the differential correlation is displayed in Fig. 4.10 and reaches up to 9.6 dB for GPS and 11.3 dB for Galileo. The reception sensitivity of differential correlation with and without adaptive detection threshold degrades the same amount for an increasing frequency deviation f_d. The difference remains independent of f_d. Fig. 4.10 is therefore not parameterized by f_d and its values are generally applicable to an arbitrary f_d. The gain is higher for longer coherent integration periods, since the out-of-phase autocorrelation values become more significant for long integration. It also increases for longer observation periods, because this yields higher reception sensitivity where the nontrivial correlation values have a stronger impact. The Galileo E1-B (data) and E1-C (pilot) signals are transmitted jointly on the in-

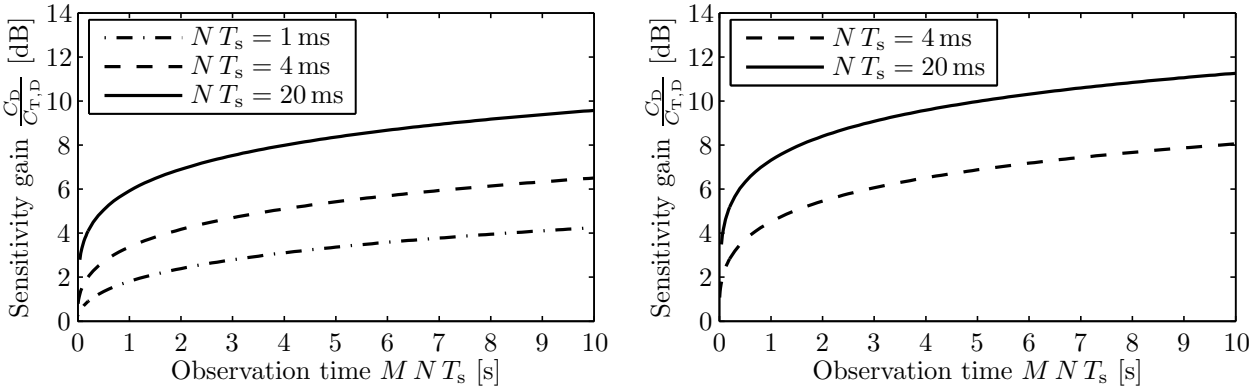

(a) GPS L1-C/A. (b) Galileo E1-C (pilot only).

Figure 4.10: Sensitivity gain of the adaptive detection threshold technique for the differential correlation with $T_0 = 290\,\text{K}$, $F = 3\,\text{dB}$, $P_\text{f} = 10^{-5}$, and $P_\text{d} = 90\,\%$.

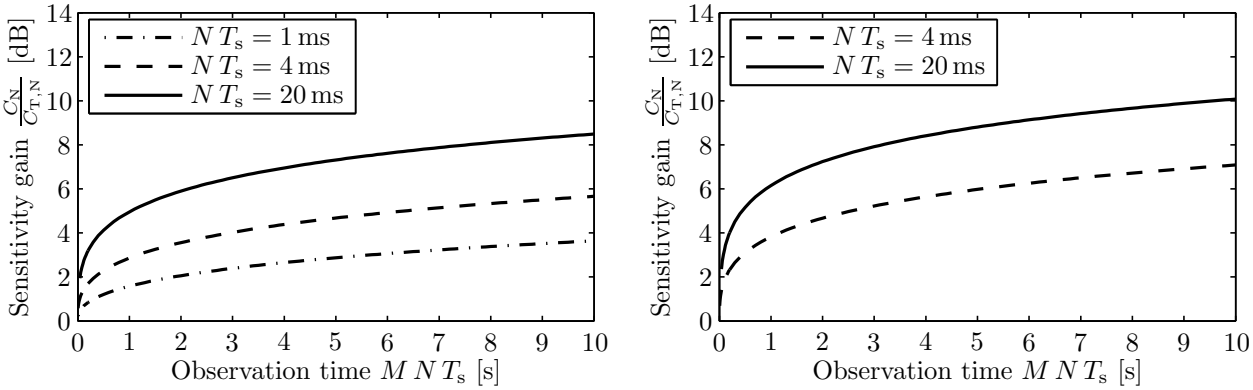

(a) GPS L1-C/A. (b) Galileo E1-C (pilot only).

Figure 4.11: Sensitivity gain of the adaptive detection threshold technique for the noncoherent integration method with $T_0 = 290\,\text{K}$, $F = 3\,\text{dB}$, $P_\text{f} = 10^{-5}$, and $P_\text{d} = 90\,\%$.

phase component of a single carrier, which causes a small degree of cross-correlation between the Galileo E1-B and E1-C signals. The maximum out-of-phase autocorrelation value for despreading the Galileo E1-B/C signals with the Galileo E1-B or the Galileo E1-C codes is therefore slightly larger than for GPS L1-C/A. The slightly higher nontrivial correlation values in turn lead to a slightly larger sensitivity gain of the adaptive detection threshold for Galileo E1-C.

The sensitivity gain $C_\text{N}/C_\text{T,N}$ of the adaptive detection threshold for the noncoherent integration is calculated as the difference between the values in dB of Fig. 3.14 and 4.9. It is presented in Fig. 4.11 and reaches 8.5 dB for GPS and 10.1 dB for Galileo. As previously, the gain is independent of f_d and therefore also not parameterized by f_d. The gain characteristics are the same as for differential correlation, just on a lower level.

Fig. 4.12 shows the cumulative sensitivity gain $C_\text{N}/C_\text{T,D}$ obtained by the differential correlation with the adaptive detection threshold versus the state-of-the-art noncoherent integration. When calculated in dB, it is the difference between the values of Fig. 3.14 and Fig. 4.6. The cumulative gain of the differential correlation technique with the adaptive detection threshold in Fig. 4.12 is also independent of f_d and reaches up to 10 dB for GPS and 11.6 dB for Galileo.

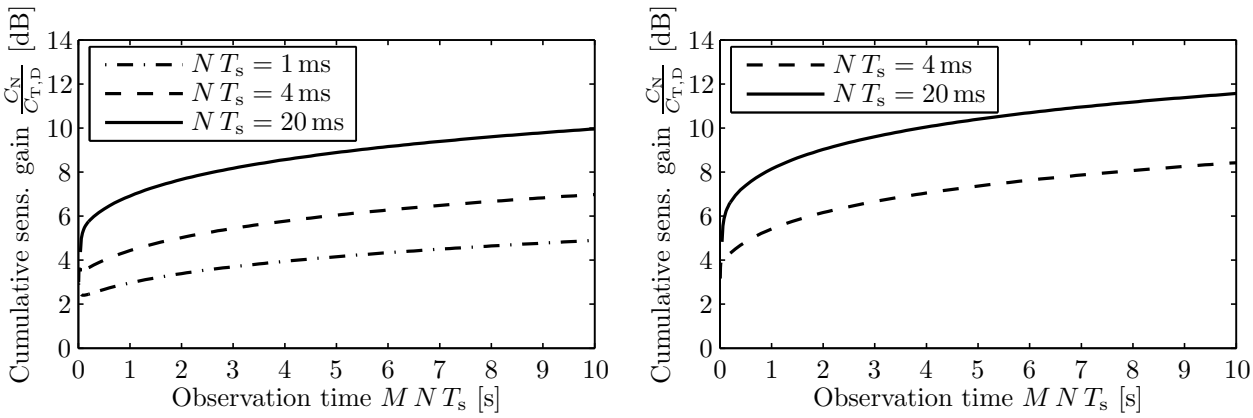

(a) GPS L1-C/A. (b) Galileo E1-C (pilot only).

Figure 4.12: Cumulative sensitivity gain of the differential correlation with adaptive detection threshold versus the state-of-the-art noncoherent integration without adaptation of the threshold for $T_0 = 290\,\mathrm{K}$, $F = 3\,\mathrm{dB}$, $P_\mathrm{f} = 10^{-5}$, and $P_\mathrm{d} = 90\,\%$.

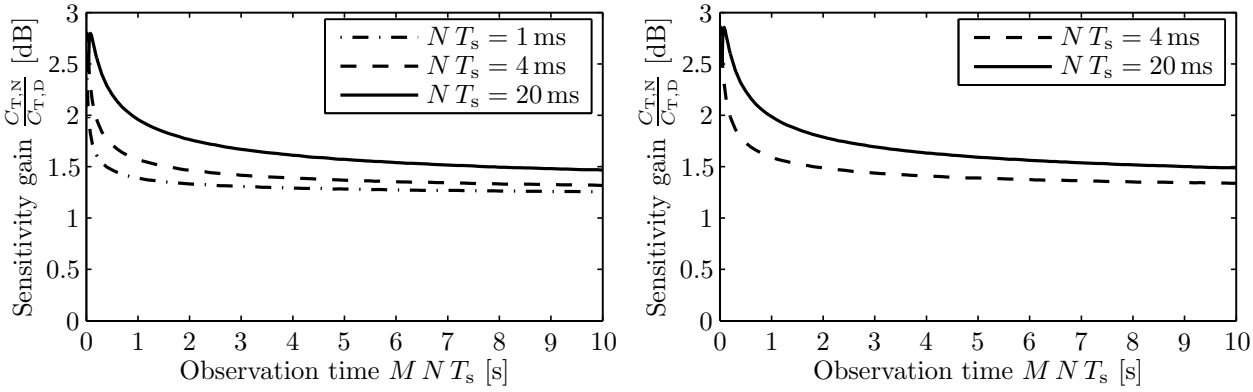

(a) GPS L1-C/A. (b) Galileo E1-C (pilot only).

Figure 4.13: Sensitivity gain of the differential correlation versus the noncoherent integration when both utilize the adaptive detection threshold technique for $T_0 = 290\,\mathrm{K}$, $F = 3\,\mathrm{dB}$, $P_\mathrm{f} = 10^{-5}$, and $P_\mathrm{d} = 90\,\%$.

Even when compared to the noncoherent integration with adaptive detection threshold, the differential correlation with adaptive detection threshold offers a significant sensitivity gain. As shown in Fig. 4.13, the gain $C_{\mathrm{T,N}}/C_{\mathrm{T,D}}$ ranges from 1.5 dB to 2.9 dB, where it is calculated as the difference in dB between Fig. 4.9 and Fig. 4.6. Since differential correlation and noncoherent integration are affected in the same way by the residual frequency deviation f_d, the gain in Fig. 4.13 is independent of f_d. The sensitivity gain of the differential correlation technique origins from it multiplying successive predetection results, while the noncoherent integration squares the predetection results. Successive predetection samples are statistically independent such that the resulting noise power is less than when squaring the predetection samples.

4.8 Conclusion

A method to estimate the variance of the correlation result σ_Ψ^2 and its mean magnitude $|m_\Psi|$ under hypothesis H_0 is provided. With the help of these two parameters, the optimum

detection threshold λ can be calculated as a function of the received carrier power C, frequency deviation f_d, and noise temperature T_0. The optimum detection threshold is higher for line-of-sight signals than for attenuated signals. The continuous adjustment of the threshold yields a constant false detection probability, which maximizes the probability of correct detection. The *adaptive detection threshold* therefore substantially improves the reception sensitivity by up to 11.6 dB for the presented receiver configurations. The remote chance of harmful cross-correlation between strong and weak signals with unfortunate DOPPLER frequencies can be circumvented with the presented techniques. Since the adaptive detection threshold has no impact on the positioning accuracy for a given carrier-to-noise PSD, the analysis of the positioning accuracy in Chapter 3 is also applicable to this chapter. If both, the differential correlation and the noncoherent integration are enhanced with the adaptive detection threshold, the differential correlation still provides a sensitivity gain of 1.5–2.9 dB.

Chapter 5

Frequency Offset Correction

Depending on the location of the satellites, the Galileo/GPS signals can have a DOPPLER frequency shift of up to ±6 kHz. With knowledge of the approximate receiver location, the approximate time, and the expected satellite constellation, this DOPPLER search space can be narrowed down. However, the exact receiver location, the exact receiver motion, and the exact local oscillator frequency remain unknown. This limits the accuracy of the estimated frequency shift before the single shot positioning starts. A residual frequency deviation between the down-conversion frequency and the received signal frequency generally remains. The previous chapters have shown how the residual frequency deviation degrades the reception sensitivity. The longer the coherent integration period is, the smaller the tolerable frequency deviation. The phase of the differential correlation result has been derived in Chapter 3 to be directly proportional to the frequency deviation. This chapter exploits this characteristic for a *frequency offset correction* technique.

The new technique partitions the observation period into intermediate differential correlation intervals. The residual frequency deviation is estimated based on the phase of each intermediate differential correlation result. This information is fed back to the down-conversion stage, which corrects the down-conversion frequency of the following intermediate differential correlation interval. The result is an increased signal-to-noise ratio of the final differential correlation result, which increases reception sensitivity, as well as positioning accuracy. The reduced frequency deviation furthermore allows longer coherent integration, which improves reception sensitivity and positioning accuracy even more.

5.1 Frequency Deviation Feedback

Fig. 5.1 shows the signal processing steps of one channel of the frequency offset correction method. When compared to the previous signal processing chain of the differential correlation in Fig. 3.3, the main difference is the feedback path for the estimated frequency deviation. The expectation value of the intermediate differential correlation result

$$\boxed{\Psi_\kappa = \sum_{\mu=\kappa M+1}^{(\kappa+1) M-1} s_\mu \, s^*_{\mu-1}} \tag{5.1}$$

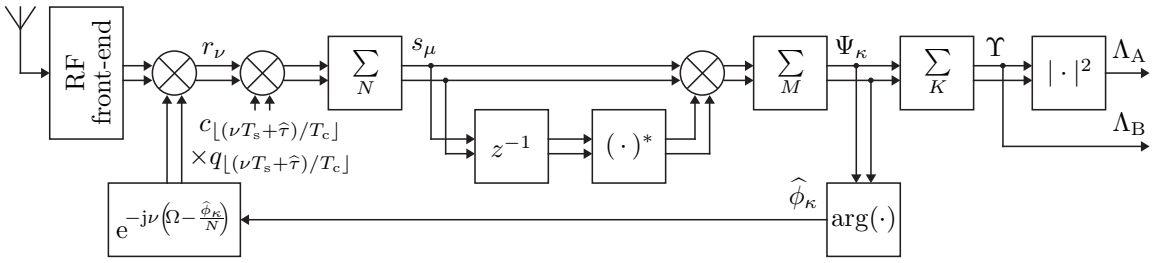

Figure 5.1: Receiver channel with the frequency offset correction technique.

is given in (3.39) as

$$m_{\Psi_\kappa} = \mathrm{E}\{\Psi_\kappa\} = 2\,(M-1)\,C\,R^2(\tau-\widehat{\tau})\,\mathrm{sinc}^2(f_{\mathrm{d},\kappa}\,N\,T_\mathrm{s})\,\mathrm{e}^{\mathrm{j}\,2\,\pi\,f_{\mathrm{d},\kappa}\,N\,T_\mathrm{s}}\,, \tag{5.2}$$

where $f_{\mathrm{d},\kappa}$ is the frequency deviation during the intermediate differential correlation interval κ. It can be observed in (5.2) that the phase of $\mathrm{E}\{\Psi_\kappa\}$ is a function of the frequency deviation $f_{\mathrm{d},\kappa}$ with

$$\mathrm{E}\{\Psi_\kappa\} = |\mathrm{E}\{\Psi_\kappa\}|\;\mathrm{e}^{\mathrm{j}\,2\,\pi\,f_{\mathrm{d},\kappa}\,N\,T_\mathrm{s}}\,. \tag{5.3}$$

Within the range $f_{\mathrm{d},\kappa} \in [-1/(2\,N\,T_\mathrm{s}),\, 1/(2\,N\,T_\mathrm{s})]$, the residual frequency deviation can therefore be estimated by

$$\boxed{\widehat{f}_{\mathrm{d},\kappa} = \frac{\arg(\Psi_\kappa)}{2\,\pi\,N\,T_\mathrm{s}} = \frac{\arg\left(\sum\limits_{\mu=\kappa\,M+1}^{(\kappa+1)\,M-1} s_\mu\,s_{\mu-1}^*\right)}{2\,\pi\,N\,T_\mathrm{s}}}\,. \tag{5.4}$$

The frequency estimation method in (5.4) has two advantages over alternative methods [70, 71, 72]. The first one is very low additional implementation complexity as it reuses the differential correlation processing of Chapter 3. If Fig. 5.1 is compared to the illustration of the differential correlation in Fig. 3.3, the low overhead becomes apparent. The additionally required steps are just to calculate the argument of the differential correlation result and feed it back to the down-conversion unit. The second advantage is that the averaging functionality of the existing differential correlation procedure is utilized to reduce the probability of phase jumps that occur when the real or imaginary parts of the products $s_\mu\,s_{\mu-1}^*$ introduce sign changes due to the added noise [73].

5.2 Open Loop Frequency Estimation Accuracy

The accuracy of the frequency estimation method can be determined by deriving the probability density function of the estimated frequency deviation $\widehat{f}_{\mathrm{d},\kappa}$. In Section 3.5, the differential correlation result Ψ_κ is derived to be GAUSSIAN distributed. From (3.52), its inphase variance can be derived as

$$\begin{aligned}\sigma^2_{\Psi_\kappa,\mathrm{I}} &= \mathrm{E}\big\{\Re\{\Psi_\kappa - \mathrm{E}\{\Psi_\kappa\}\}^2\big\} \\ &= \frac{(M-1)\,\sigma_w^4}{2} + 2\,\sigma_w^2\,C\,R^2(\tau-\widehat{\tau})\,\mathrm{sinc}^2(f_{\mathrm{d},\kappa}\,N\,T_\mathrm{s})\left[1+2\,(M-2)\,\cos^2(2\,\pi\,f_{\mathrm{d},\kappa}\,N\,T_\mathrm{s})\right],\end{aligned} \tag{5.5}$$

and with (3.53) its quadrature variance results in

$$\begin{aligned}\sigma^2_{\Psi_\kappa,\mathrm{Q}} &= \mathrm{E}\big\{\Im\{\Psi_\kappa - \mathrm{E}\{\Psi_\kappa\}\}^2\big\} \\ &= \frac{(M-1)\,\sigma_w^4}{2} + 2\,\sigma_w^2\,C\,R^2(\tau-\widehat{\tau})\,\mathrm{sinc}^2(f_{\mathrm{d},\kappa}\,N\,T_\mathrm{s})\,\big[1+2\,(M-2)\,\sin^2(2\,\pi\,f_{\mathrm{d},\kappa}\,N\,T_\mathrm{s})\big]\,.\end{aligned} \tag{5.6}$$

Using the estimated correlation magnitude

$$\widehat{a}_\kappa = |\Psi_\kappa|\,, \tag{5.7}$$

the estimated correlation phase

$$\widehat{\phi}_\kappa = \arg(\Psi_\kappa)\,, \tag{5.8}$$

and the JACOBIAN determinant

$$\mathrm{J}_\kappa = \begin{vmatrix} \frac{\partial\Re\{\Psi_\kappa\}}{\widehat{a}_\kappa} & \frac{\partial\Re\{\Psi_\kappa\}}{\widehat{\phi}_\kappa} \\ \frac{\partial\Im\{\Psi_\kappa\}}{\widehat{a}_\kappa} & \frac{\partial\Im\{\Psi_\kappa\}}{\widehat{\phi}_\kappa} \end{vmatrix} = \begin{vmatrix} \cos\big(\widehat{\phi}_\kappa\big) & -\widehat{a}_\kappa\,\sin\big(\widehat{\phi}_\kappa\big) \\ \sin\big(\widehat{\phi}_\kappa\big) & \widehat{a}_\kappa\,\cos\big(\widehat{\phi}_\kappa\big) \end{vmatrix} = \widehat{\mathrm{a}}_\kappa\,, \tag{5.9}$$

the probability density function of Ψ_κ can be transformed into polar coordinates as

$$p_{\Psi_\kappa}\big(\widehat{a}_\kappa,\,\widehat{\phi}_\kappa\big) = \frac{\widehat{a}_\kappa}{2\,\pi\,\sigma_{\Psi_\kappa,\mathrm{I}}\,\sigma_{\Psi_\kappa,\mathrm{Q}}}\,\exp\left(-\frac{\Big[\widehat{a}_\kappa\,\cos\big(\widehat{\phi}_\kappa\big) - \Re\{m_{\Psi_\kappa}\}\Big]^2}{2\,\sigma^2_{\Psi_\kappa,\mathrm{I}}} - \frac{\Big[\widehat{a}_\kappa\,\sin\big(\widehat{\phi}_\kappa\big) - \Im\{m_{\Psi_\kappa}\}\Big]^2}{2\,\sigma^2_{\Psi_\kappa,\mathrm{Q}}}\right). \tag{5.10}$$

By substituting

$$g_\kappa = \sqrt{\frac{\cos^2\big(\widehat{\phi}_\kappa\big)}{2\,\sigma^2_{\Psi_\kappa,\mathrm{I}}} + \frac{\sin^2\big(\widehat{\phi}_\kappa\big)}{2\,\sigma^2_{\Psi_\kappa,\mathrm{Q}}}}\,, \tag{5.11}$$

$$h_\kappa = \frac{\Re\{m_{\Psi_\kappa}\}\cos\big(\widehat{\phi}_\kappa\big)}{\sigma^2_{\Psi_\kappa,\mathrm{I}}} + \frac{\Im\{m_{\Psi_\kappa}\}\sin\big(\widehat{\phi}_\kappa\big)}{\sigma^2_{\Psi_\kappa,\mathrm{Q}}}\,, \tag{5.12}$$

and

$$l_\kappa = \frac{\exp\Big(-\frac{\Re\{m_{\Psi_\kappa}\}^2}{2\,\sigma^2_{\Psi_\kappa,\mathrm{I}}} - \frac{\Im\{m_{\Psi_\kappa}\}^2}{2\,\sigma^2_{\Psi,\mathrm{Q}}}\Big)}{2\,\pi\,\sigma_{\Psi_\kappa,\mathrm{I}}\,\sigma_{\Psi_\kappa,\mathrm{Q}}}\,, \tag{5.13}$$

the probability density in (5.10) can be rewritten as

$$p_{\Psi_\kappa}\big(\widehat{a}_\kappa,\,\widehat{\phi}_\kappa\big) = l_\kappa\,\widehat{a}_\kappa\,\exp\big(-\widehat{a}_\kappa^2\,g_\kappa^2 + \widehat{a}_\kappa\,h_\kappa\big)\,. \tag{5.14}$$

Integration over $\widehat{a}_\kappa$ yields the probability density of $\widehat{\phi}_\kappa$

$$p_{\widehat{\phi}_\kappa}\big(\widehat{\phi}_\kappa\big) = \int_0^\infty p_{\Psi_\kappa}\big(\widehat{a}_\kappa,\,\widehat{\phi}_\kappa\big)\,d\widehat{a}_\kappa = l_\kappa\int_0^\infty \widehat{a}_\kappa\,\exp\big(-\widehat{a}_\kappa^2\,g_\kappa^2 + \widehat{a}_\kappa\,h_\kappa\big)\;d\widehat{a}_\kappa\,. \tag{5.15}$$

By substituting

$$b_\kappa = \widehat{a}_\kappa\,g_\kappa - \frac{h_\kappa}{2\,g_\kappa}\,, \tag{5.16}$$

the integral in (5.15) can be solved as

$$\begin{aligned} p_{\widehat{\phi}_\kappa}\big(\widehat{\phi}_\kappa\big) &= l_\kappa \int_{-\frac{h_\kappa}{2\,g_\kappa}}^{\infty} \left[\frac{b_\kappa}{g_\kappa} + \frac{h_\kappa}{2\,g_\kappa^2}\right] \frac{1}{g_\kappa} \exp\!\left(-b_\kappa^2 + \frac{h_\kappa^2}{4\,g_\kappa^2}\right)\, db_\kappa \\ &= \frac{l_\kappa}{g_\kappa^2} \exp\!\left(\frac{h_\kappa^2}{4\,g_\kappa^2}\right) \left[\int_{-\frac{h_\kappa}{2\,g_\kappa}}^{\infty} b_\kappa \exp\!\big(-b_\kappa^2\big)\, db_\kappa + \frac{h_\kappa}{2\,g_\kappa} \int_{-\frac{h_\kappa}{2\,g_\kappa}}^{\infty} \exp\!\big(-b_\kappa^2\big)\, db_\kappa\right] \\ &= \frac{l_\kappa}{g_\kappa^2} \exp\!\left(\frac{h_\kappa^2}{4\,g_\kappa^2}\right) \left[\frac{1}{2} \exp\!\left(-\frac{h_\kappa^2}{4\,g_\kappa^2}\right) + \frac{\sqrt{\pi}\,h_\kappa}{4\,g_\kappa} \operatorname{erfc}\!\left(-\frac{h_\kappa}{2\,g_\kappa}\right)\right] \\ &= \frac{l_\kappa}{2\,g_\kappa^2} + \frac{\sqrt{\pi}\,l_\kappa\,h_\kappa}{4\,g_\kappa^2} \exp\!\left(\frac{h_\kappa^2}{4\,g_\kappa^2}\right) \operatorname{erfc}\!\left(-\frac{h_\kappa}{2\,g_\kappa}\right) \end{aligned} \tag{5.17}$$

with $\operatorname{erfc}(\,\cdot\,)$ denoting the complementary error function. Replacing the phase $\widehat{\phi}_\kappa$ by the estimated frequency deviation

$$\widehat{f}_{\mathrm{d},\kappa} = \frac{\widehat{\phi}_\kappa}{2\,\pi\,N\,T_\mathrm{s}} \tag{5.18}$$

as specified in (5.4) yields the probability density function of the estimated frequency deviation

$$p_{\widehat{f}_{\mathrm{d},\kappa}}\big(\widehat{f}_{\mathrm{d},\kappa}\big) = \frac{2\,\pi\,l_\kappa\,N\,T_\mathrm{s}}{2\,u_\kappa^2} + \frac{2\,\pi^{\frac{3}{2}}\,l_\kappa\,N\,T_\mathrm{s}\,v_\kappa}{4\,u_\kappa^2} \exp\!\left(\frac{v_\kappa^2}{4\,u_\kappa^2}\right) \operatorname{erfc}\!\left(-\frac{v_\kappa}{2\,u_\kappa}\right) \tag{5.19}$$

with

$$u_\kappa = \sqrt{\frac{\cos^2\!\big(2\,\pi\,N\,T_\mathrm{s}\,\widehat{f}_{\mathrm{d},\kappa}\big)}{2\,\sigma_{\Psi_\kappa,\mathrm{I}}^2} + \frac{\sin^2\!\big(2\,\pi\,N\,T_\mathrm{s}\,\widehat{f}_{\mathrm{d},\kappa}\big)}{2\,\sigma_{\Psi_\kappa,\mathrm{Q}}^2}} \tag{5.20}$$

and

$$v_\kappa = \frac{\Re\{m_{\Psi_\kappa}\}\,\cos\!\big(2\,\pi\,N\,T_\mathrm{s}\,\widehat{f}_{\mathrm{d},\kappa}\big)}{\sigma_{\Psi_\kappa,\mathrm{I}}^2} + \frac{\Im\{m_{\Psi_\kappa}\}\,\sin\!\big(2\,\pi\,N\,T_\mathrm{s}\,\widehat{f}_{\mathrm{d},\kappa}\big)}{\sigma_{\Psi_\kappa,\mathrm{Q}}^2}\,. \tag{5.21}$$

Fig. 5.2.a, 5.2.c, and 5.2.e show the expectation value of the estimated frequency deviation

$$m_{\widehat{f}_{\mathrm{d},\kappa}} = \mathrm{E}\Big\{\widehat{f}_{\mathrm{d},\kappa}\Big\} \tag{5.22}$$

as a function of the observation period $M\,N\,T_\mathrm{s}$. The results in Fig. 5.2 have been determined by numerical integration with the adaptive SIMPSON quadrature method [74]. It can be observed that the expectation value of the frequency estimation converges quickly for sufficiently long observation periods. Fig. 5.2.b, 5.2.d, and 5.2.f show the standard deviation of the estimated frequency deviation

$$\sigma_{\widehat{f}_{\mathrm{d},\kappa}} = \sqrt{\mathrm{E}\left\{\left(\widehat{f}_{\mathrm{d},\kappa} - \mathrm{E}\Big\{\widehat{f}_{\mathrm{d},\kappa}\Big\}\right)^2\right\}}\,. \tag{5.23}$$

The standard deviation $\sigma_{\widehat{f}_{\mathrm{d},\kappa}}$ decreases exponentially with increasing observation periods. The presented method can estimate the residual frequency deviation $f_{\mathrm{d},\kappa}$ even for low carrier-to-noise PSD values $C/\mathcal{N}_0$.

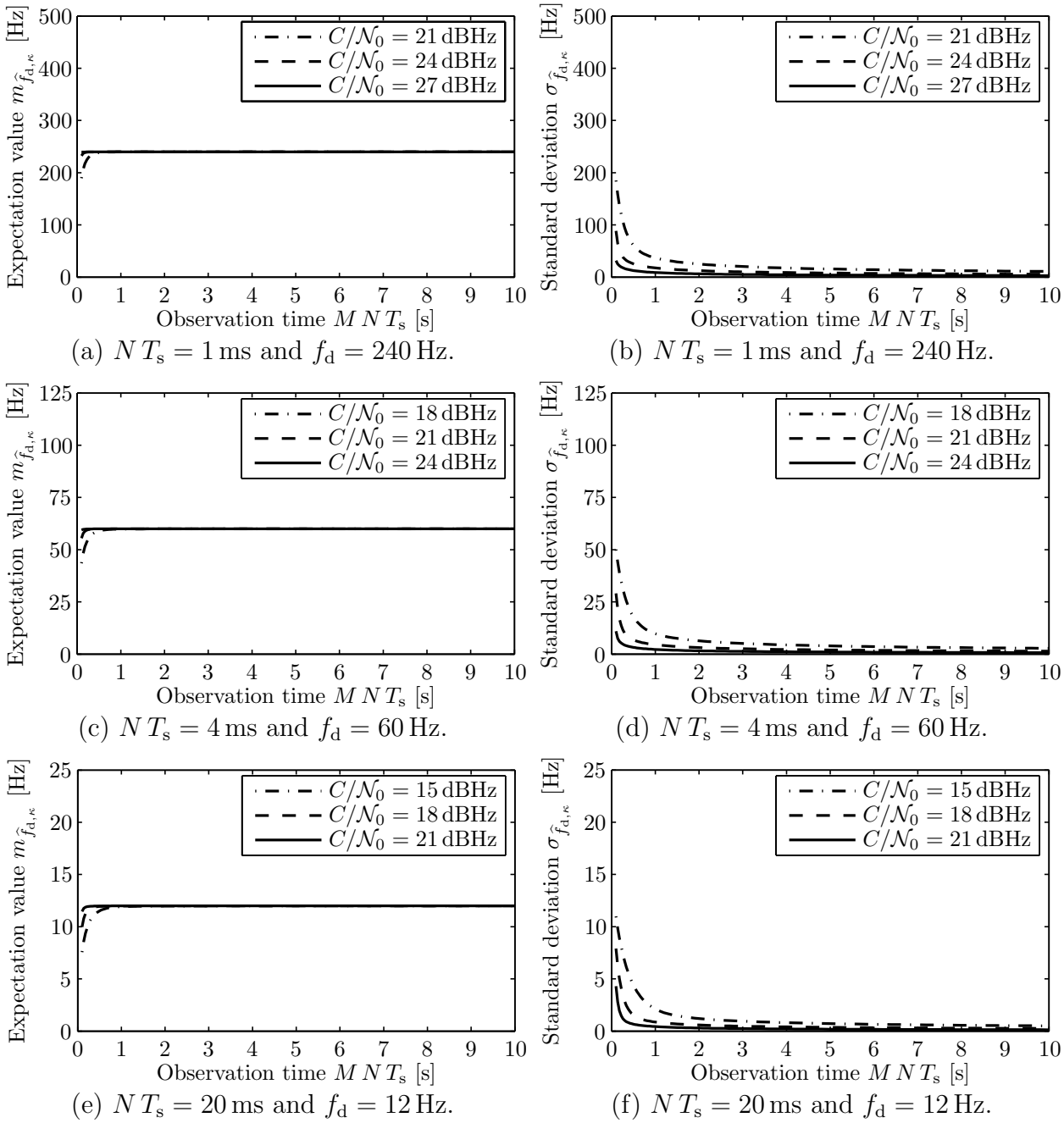

(a) $N\,T_\mathrm{s} = 1\,\mathrm{ms}$ and $f_\mathrm{d} = 240\,\mathrm{Hz}$.
(b) $N\,T_\mathrm{s} = 1\,\mathrm{ms}$ and $f_\mathrm{d} = 240\,\mathrm{Hz}$.
(c) $N\,T_\mathrm{s} = 4\,\mathrm{ms}$ and $f_\mathrm{d} = 60\,\mathrm{Hz}$.
(d) $N\,T_\mathrm{s} = 4\,\mathrm{ms}$ and $f_\mathrm{d} = 60\,\mathrm{Hz}$.
(e) $N\,T_\mathrm{s} = 20\,\mathrm{ms}$ and $f_\mathrm{d} = 12\,\mathrm{Hz}$.
(f) $N\,T_\mathrm{s} = 20\,\mathrm{ms}$ and $f_\mathrm{d} = 12\,\mathrm{Hz}$.

Figure 5.2: Expectation value and standard deviation of the frequency offset estimation for GPS L1-C/A and Galileo E1-C.

5.3 Feedback Loop

The frequency deviation

$$f_{\mathrm{d},\kappa} = f_\mathrm{IF} + f_\mathrm{D} - f_{\mathrm{LO},\kappa} \tag{5.24}$$

is a function of the intermediate frequency f_IF, the Doppler frequency shift, and the time-variant digital down-conversion frequency $f_{\mathrm{LO},\kappa}$. The simulations in this chapter utilize a channel model with a constant Doppler shift f_D. However, the frequency correction method also works for a dynamically changing frequency deviation. Once the frequency offset has been estimated, a frequency correction loop can feed the frequency deviation back

and subtract it from the current down-conversion frequency to calculate the next down-conversion frequency as

$$\boxed{f_{\mathrm{LO},\kappa+1} = f_{\mathrm{LO},\kappa} - f_{\mathrm{d},\kappa} = f_{\mathrm{LO},\kappa} - \frac{\arg(\Psi_\kappa)}{2\,\pi\,N\,T_\mathrm{s}} = f_{\mathrm{LO},\kappa} - \frac{\arg\left(\sum\limits_{\mu=\kappa\,M+1}^{(\kappa+1)\,M-1} s_\mu\,s_{\mu-1}^*\right)}{2\,\pi\,N\,T_\mathrm{s}}}\,. \tag{5.25}$$

The initially selected down-conversion frequency during the first intermediate differential correlation interval is denoted $f_{\mathrm{LO},0}$. After $M\,N$ signal samples are processed, the differential correlation result Ψ_κ is utilized to calculate $\widehat{f}_{\mathrm{d},\kappa}$ as specified in (5.4). The estimated frequency deviation $\widehat{f}_{\mathrm{d},\kappa}$ is fed back to the down-conversion unit for the calculation of the optimized down-conversion frequency $f_{\mathrm{LO},\kappa+1}$, which is used for the following $M\,N$ signal samples. The rotation angle of the down-conversion unit in Fig. 5.1 is calculated as

$$\Omega_\kappa = 2\,\pi\,f_{\mathrm{LO},\kappa}\,T_\mathrm{s}\,. \tag{5.26}$$

With (5.4) and (5.25), the sequence of rotation angles can simply be calculated as

$$\Omega_{\kappa+1} = \Omega_\kappa - \frac{\arg(\Psi_\kappa)}{N}\,. \tag{5.27}$$

As illustrated in Fig. 5.1, the final differential correlation result is calculated as

$$\Upsilon = \sum_{\mu=1}^{K\,M-1} s_\mu\,s_{\mu-1}^* = \sum_{\mu=1}^{K\,M-1} (y_\mu + w_\mu)\,(y_{\mu-1} + w_{\mu-1})^*\,. \tag{5.28}$$

From (3.25) and (3.31), the deterministic predetection component for the case of frequency correction results in

$$y_\mu \simeq \sqrt{2\,C}\,R(\tau - \widehat{\tau})\,\mathrm{sinc}(f_{\mathrm{d},\lfloor\mu/M\rfloor}\,N\,T_\mathrm{s})\,\mathrm{e}^{\mathrm{j}\,\varphi_\mu} \tag{5.29}$$

with the phase

$$\varphi_\mu = \varphi_{\mu-1} + \pi\,(f_{\mathrm{d},\lfloor\mu/M\rfloor} + f_{\mathrm{d},\lfloor(\mu-1)/M\rfloor})\,N\,T_\mathrm{s}\,. \tag{5.30}$$

Utilizing (3.38) and (3.39), the expectation value of the final differential correlation result is derived to be

$$\begin{aligned} m_\Upsilon = \mathrm{E}\{\Upsilon\} &= \sum_{\mu=1}^{K\,M-1} y_\mu\,y_{\mu-1}^* \\ &= 2\,C\,R^2(\tau - \widehat{\tau}) \sum_{\mu=1}^{K\,M-1} \mathrm{sinc}(f_{\mathrm{d},\lfloor\mu/M\rfloor}\,N\,T_\mathrm{s})\,\mathrm{sinc}(f_{\mathrm{d},\lfloor(\mu-1)/M\rfloor}\,N\,T_\mathrm{s}) \\ &\qquad \times \mathrm{e}^{\mathrm{j}\,\pi\,(f_{\mathrm{d},\lfloor\mu/M\rfloor} + f_{\mathrm{d},\lfloor(\mu-1)/M\rfloor})\,N\,T_\mathrm{s}} \\ &= 2\,C\,R^2(\tau - \widehat{\tau}) \left[\sum_{\kappa=0}^{K-1} (M-1)\,\mathrm{sinc}^2(f_{\mathrm{d},\kappa}\,N\,T_\mathrm{s})\,\mathrm{e}^{\mathrm{j}\,2\,\pi\,f_{\mathrm{d},\kappa}\,N\,T_\mathrm{s}}\right. \\ &\qquad \left. + \sum_{\kappa=1}^{K-1} \mathrm{sinc}(f_{\mathrm{d},\kappa}\,N\,T_\mathrm{s})\,\mathrm{sinc}(f_{\mathrm{d},\kappa-1}\,N\,T_\mathrm{s})\,\mathrm{e}^{\mathrm{j}\,\pi\,(f_{\mathrm{d},\kappa} + f_{\mathrm{d},\kappa-1})\,N\,T_\mathrm{s}}\right]. \end{aligned} \tag{5.31}$$

It can be observed that the mean m_Υ incrementally converges to a purely real value when the frequency deviation $f_{\mathrm{d},\kappa}$ is incrementally reduced. Furthermore, the term $\mathrm{sinc}(f_{\mathrm{d},\kappa}\,N\,T_\mathrm{s})$ increases towards one as $f_{\mathrm{d},\kappa}$ is reduced. This increase of m_Υ may lead to a larger correlation gain, as will be shown subsequently.

Using (3.42), (3.43), and (3.51) with $y_{-1} = y_{K\,M} = 0$, the combined variance of the inphase and quadrature components results in

$$\begin{aligned}
\sigma_\Upsilon^2 &= \mathrm{E}\big\{|\Upsilon - \mathrm{E}\{\Upsilon\}|^2\big\} = \mathrm{E}\left\{\left|\sum_{\mu=1}^{K\,M-1}(w_\mu\,w_{\mu-1}^* + y_\mu\,w_{\mu-1}^* + w_\mu\,y_{\mu-1}^*)\right|^2\right\} \\
&= (K\,M-1)\,\sigma_w^4 + \frac{\sigma_w^2}{2}\sum_{\mu=0}^{K\,M-1}|y_{\mu+1}+y_{\mu-1}|^2 + \frac{\sigma_w^2}{2}\sum_{\mu=0}^{K\,M-1}|y_{\mu+1}-y_{\mu-1}|^2 \\
&= (K\,M-1)\,\sigma_w^4 + \sigma_w^2\sum_{\mu=1}^{K\,M-1}\big(|y_\mu|^2+|y_{\mu-1}|^2\big) \\
&= (K\,M-1)\,\sigma_w^4 + 2\,\sigma_w^2\,C\,R^2(\tau-\widehat{\tau})\sum_{\mu=1}^{K\,M-1}\Big[\mathrm{sinc}^2(f_{\mathrm{d},\lfloor\mu/M\rfloor}\,N\,T_\mathrm{s}) + \mathrm{sinc}^2(f_{\mathrm{d},\lfloor(\mu-1)/M\rfloor}\,N\,T_\mathrm{s})\Big] \\
&= (K\,M-1)\,\sigma_w^4 + 2\,\sigma_w^2\,C\,R^2(\tau-\widehat{\tau})\Bigg[(2M-1)\left[\mathrm{sinc}^2(f_{\mathrm{d},0}\,N\,T_\mathrm{s}) + \mathrm{sinc}^2(f_{\mathrm{d},\mathrm{K}-1}\,N\,T_\mathrm{s})\right] \\
&\qquad\qquad + \sum_{\kappa=1}^{K-2} 2\,M\,\mathrm{sinc}^2(f_{\mathrm{d},\kappa}\,N\,T_\mathrm{s})\Bigg]
\end{aligned} \tag{5.32}$$

with the predetection noise variance

$$\sigma_w^2 = \mathrm{E}\big\{|w|^2\big\} = 2\,N\,k\,T_0\,B\,F \tag{5.33}$$

as defined in (3.19). The inphase correlation variance is derived from (3.42) and (3.51) to be

$$\begin{aligned}
\sigma_{\Upsilon,\mathrm{I}}^2 &= \mathrm{E}\big\{\Re\{\Upsilon - \mathrm{E}\{\Upsilon\}\}^2\big\} = \mathrm{E}\left\{\Re\left\{\sum_{\mu=1}^{K\,M-1}(w_\mu\,w_{\mu-1}^* + y_\mu\,w_{\mu-1}^* + w_\mu\,y_{\mu-1}^*)\right\}^2\right\} \\
&= \frac{(K\,M-1)\,\sigma_w^4}{2} + \frac{\sigma_w^2}{2}\left[|y_1|^2 + |y_{K\,M-2}|^2 + \sum_{\mu=1}^{K\,M-2}\big(|y_{\mu+1}+y_{\mu-1}|^2\big)\right] \\
&= \frac{(K\,M-1)\,\sigma_w^4}{2} + \sigma_w^2\,C\,R^2(\tau-\widehat{\tau})\Bigg[\mathrm{sinc}^2(f_{\mathrm{d},\lfloor 2/M\rfloor}\,N\,T_\mathrm{s}) + \mathrm{sinc}^2(f_{\mathrm{d},\lfloor(K\,M-2)/M\rfloor}\,N\,T_\mathrm{s}) \\
&\qquad + \sum_{\mu=1}^{K\,M-2}\Big|\mathrm{sinc}^2(f_{\mathrm{d},\lfloor(\mu+1)/M\rfloor}\,N\,T_\mathrm{s}) + \mathrm{sinc}^2(f_{\mathrm{d},\lfloor(\mu-1)/M\rfloor}\,N\,T_\mathrm{s}) \\
&\qquad\qquad \times \mathrm{e}^{\mathrm{j}\,\pi\,(f_{\mathrm{d},\lfloor(\mu+1)/M\rfloor} + 2\,f_{\mathrm{d},\lfloor\mu/M\rfloor} + f_{\mathrm{d},\lfloor(\mu-1)/M\rfloor})\,N\,T_\mathrm{s}}\Big|^2\Bigg]
\end{aligned} \tag{5.34}$$

$$\sigma^2_{\Upsilon,\mathrm{I}} = \frac{(K\,M-1)\,\sigma_w^4}{2} + \sigma_w^2\,C\,R^2(\tau-\widehat{\tau})\Bigg[\mathrm{sinc}^2(f_{\mathrm{d},0}\,N\,T_\mathrm{s}) + \mathrm{sinc}^2(f_{\mathrm{d},K-1}\,N\,T_\mathrm{s}) + \sum_{\kappa=0}^{K-1} 4\,(M-2)\,\mathrm{sinc}^2(f_{\mathrm{d},\kappa}\,N\,T_\mathrm{s})\,\cos^2(2\,\pi\,f_{\mathrm{d},\kappa}\,N\,T_\mathrm{s}) + \sum_{\kappa=0}^{K-2} \left|\mathrm{sinc}(f_{\mathrm{d},\kappa+1}\,N\,T_\mathrm{s}) + \mathrm{sinc}(f_{\mathrm{d},\kappa}\,N\,T_\mathrm{s})\,\mathrm{e}^{\mathrm{j}\,\pi(f_{\mathrm{d},\kappa+1}+3\,f_{\mathrm{d},\kappa})\,N\,T_\mathrm{s}}\right|^2 + \sum_{\kappa=1}^{K-1} \left|\mathrm{sinc}(f_{\mathrm{d},\kappa}\,N\,T_\mathrm{s}) + \mathrm{sinc}(f_{\mathrm{d},\kappa-1}\,N\,T_\mathrm{s})\,\mathrm{e}^{\mathrm{j}\,\pi(3\,f_{\mathrm{d},\kappa}+f_{\mathrm{d},\kappa-1})\,N\,T_\mathrm{s}}\right|^2\Bigg]. \tag{5.35}$$

5.4 Reception Sensitivity

Fig. 5.1 shows two possibilities to calculate the decision statistic Λ. Since the correlation result Υ is complex-valued, the conventional approach is to take the squared magnitude of Υ as the decision statistic

$$\boxed{\Lambda_\mathrm{A} = |\Upsilon|^2 = \left|\sum_{\mu=1}^{K\,M-1} s_\mu\,s_{\mu-1}^*\right|^2}. \tag{5.36}$$

This method utilizes not only the inphase and quadrature correlation power, but it also includes the inphase and quadrature noise power.

The frequency offset correction method decreases the frequency deviation $f_{\mathrm{d},\kappa}$ towards zero. This leads to a reduction in the quadrature correlation power $\Im\{m_\Upsilon\}^2$ as specified in (5.31), while the inphase correlation power $\Re\{m_\Upsilon\}^2$ increases accordingly. Depending on the reception conditions and the receiver settings, it can therefore be advantageous to just evaluate the inphase component of Υ as the decision statistic

$$\boxed{\Lambda_\mathrm{B} = \Re\{\Upsilon\} = \Re\left\{\sum_{\mu=1}^{K\,M-1} s_\mu\,s_{\mu-1}^*\right\}}. \tag{5.37}$$

This method not only rejects the quadrature noise power, but it also rejects the quadrature signal power. Just evaluating the real part of the differential correlation result also reduces the implementation complexity.

The differential correlation result Υ is a GAUSSIAN distributed variable. Since method A utilizes the squared magnitude of Υ as the decision statistic Λ_A, it obeys the noncentral CHI-SQUARED distribution with two degrees of freedom. Its detection threshold λ_A can therefore be derived from the specification in (3.65) as

$$\lambda_\mathrm{A} = P^{-1}_{\Lambda_\mathrm{A}|\mathrm{H}_0}(1-P_\mathrm{f,A}) = \frac{\sigma^2_{\Upsilon,\mathrm{H}_0}}{2}\left[\mathrm{Q}^{-1}_{1,\beta}\left(\sqrt{\frac{2\,|m_{\Upsilon,\mathrm{H}_0}|^2}{\sigma^2_{\Upsilon,\mathrm{H}_0}}},\,P_\mathrm{f,A}\right)\right]^2 \tag{5.38}$$

with

$$m_{\Upsilon,\mathrm{H}_0} = m_\Upsilon\big|_{R^2(\tau-\widehat{\tau})=R_\mathrm{m}^2} \,, \quad \sigma^2_{\Upsilon,\mathrm{H}_0} = \sigma^2_\Upsilon\big|_{R^2(\tau-\widehat{\tau})=R_\mathrm{m}^2} \,. \tag{5.39}$$

To obtain comparable results, the adaptive detection threshold method as described in Chapter 4 is subsequently applied.

The probability of detection for method A is obtained from (3.66) as

$$\boxed{P_{\mathrm{d,A}} = \Pr\{\Lambda_\mathrm{A} \geqslant \lambda_\mathrm{A}|\mathrm{H}_1\} = 1 - P_{\Lambda_\mathrm{A},\mathrm{H}_1}(\lambda_\mathrm{A}) = \mathrm{Q}_1\!\left(\sqrt{\frac{2\,|m_{\Upsilon,\mathrm{H}_0}|^2}{\sigma^2_{\Upsilon,\mathrm{H}_1}}}, \sqrt{\frac{2\,\lambda_\mathrm{A}}{\sigma^2_{\Upsilon,\mathrm{H}_1}}}\right)} \tag{5.40}$$

with

$$m_{\Upsilon,\mathrm{H}_1} = m_\Upsilon\big|_{R^2(\tau-\widehat{\tau})=N^2} \,, \quad \sigma^2_{\Upsilon,\mathrm{H}_1} = \sigma^2_\Upsilon\big|_{R^2(\tau-\widehat{\tau})=N^2} \,. \tag{5.41}$$

Since method B in Fig. 5.1 just uses the real part of Υ as the decision statistic Λ_B, it obeys the GAUSSIAN distribution with the mean $\Re\{m_\Upsilon\}$ and the variance σ^2_Υ. Its probability of false detection is hence

$$P_{\mathrm{f,B}} = \Pr\{\Lambda_\mathrm{B} \geqslant \lambda_\mathrm{B}|\mathrm{H}_0\} = 1 - P_{\Lambda_\mathrm{B},\mathrm{H}_0}(\lambda_\mathrm{B}) = \frac{1}{2}\,\mathrm{erfc}\!\left(\frac{\lambda_\mathrm{B} - \Re\{m_{\Upsilon,\mathrm{H}_0}\}}{\sqrt{2}\,\sigma_{\Upsilon,\mathrm{I},\mathrm{H}_0}}\right) \tag{5.42}$$

with

$$\sigma^2_{\Upsilon,\mathrm{I},\mathrm{H}_0} = \sigma^2_{\Upsilon,\mathrm{I}}\big|_{R^2(\tau-\widehat{\tau})=R_\mathrm{m}^2} \,. \tag{5.43}$$

Its detection threshold λ_B can be calculated as

$$\lambda_\mathrm{B} = P^{-1}_{\Lambda_\mathrm{B}|\mathrm{H}_0}(1 - P_\mathrm{f}) = \sqrt{2}\,\sigma_{\Upsilon,\mathrm{I},\mathrm{H}_0}\,\mathrm{erfc}^{-1}(2\,P_\mathrm{f}) + \Re\{m_{\Upsilon,\mathrm{H}_0}\} \tag{5.44}$$

while the probability of detection for method B is

$$\boxed{P_{\mathrm{d,B}} = \Pr\{\Lambda_\mathrm{B} \geqslant \lambda_\mathrm{B}|\mathrm{H}_1\} = 1 - P_{\Lambda_\mathrm{B},\mathrm{H}_1}(\lambda_\mathrm{B}) = \frac{1}{2}\,\mathrm{erfc}\!\left(\frac{\lambda_\mathrm{B} - \Re\{m_{\Upsilon,\mathrm{H}_1}\}}{\sqrt{2}\,\sigma_{\Upsilon,\mathrm{I},\mathrm{H}_1}}\right)} \tag{5.45}$$

with

$$\sigma^2_{\Upsilon,\mathrm{I},\mathrm{H}_1} = \sigma^2_{\Upsilon,\mathrm{I}}\big|_{R^2(\tau-\widehat{\tau})=N^2} \,. \tag{5.46}$$

Fig. 5.3 shows the reception sensitivity for the probability of detection $P_\mathrm{d} = 90\,\%$ as achieved with the frequency offset correction method. Fig. 5.3.a to 5.3.d illustrate the carrier-to-noise PSD $C_{\mathrm{F,A}}/\mathcal{N}_0$ where method A achieves $P_\mathrm{d} = 90\,\%$, while Fig. 5.3.e to 5.3.h show the carrier-to-noise PSD for method B, $C_{\mathrm{F,B}}/\mathcal{N}_0$. The simulations in this and the following chapters cover small and large frequency deviations. Unlike the last two chapters, the case of zero frequency deviation is not included any more. The figures for reception sensitivity in the last two chapters included six plots showing zero, small, and large frequency deviations for GPS and Galileo. The figures from this point onwards include eight plots showing small and large frequency deviations using methods A and B for GPS and Galileo. The receiver parameters $T_0 = 290\,\mathrm{K}$, $F = 3\,\mathrm{dB}$, $P_\mathrm{f} = 10^{-5}$, and $P_\mathrm{d} = 90\,\%$ in Fig. 5.3 are typical and reasonable values that can also be found in literature to compare different receiver techniques. They are justified and elaborated in detail in Section 3.7. Since the frequency

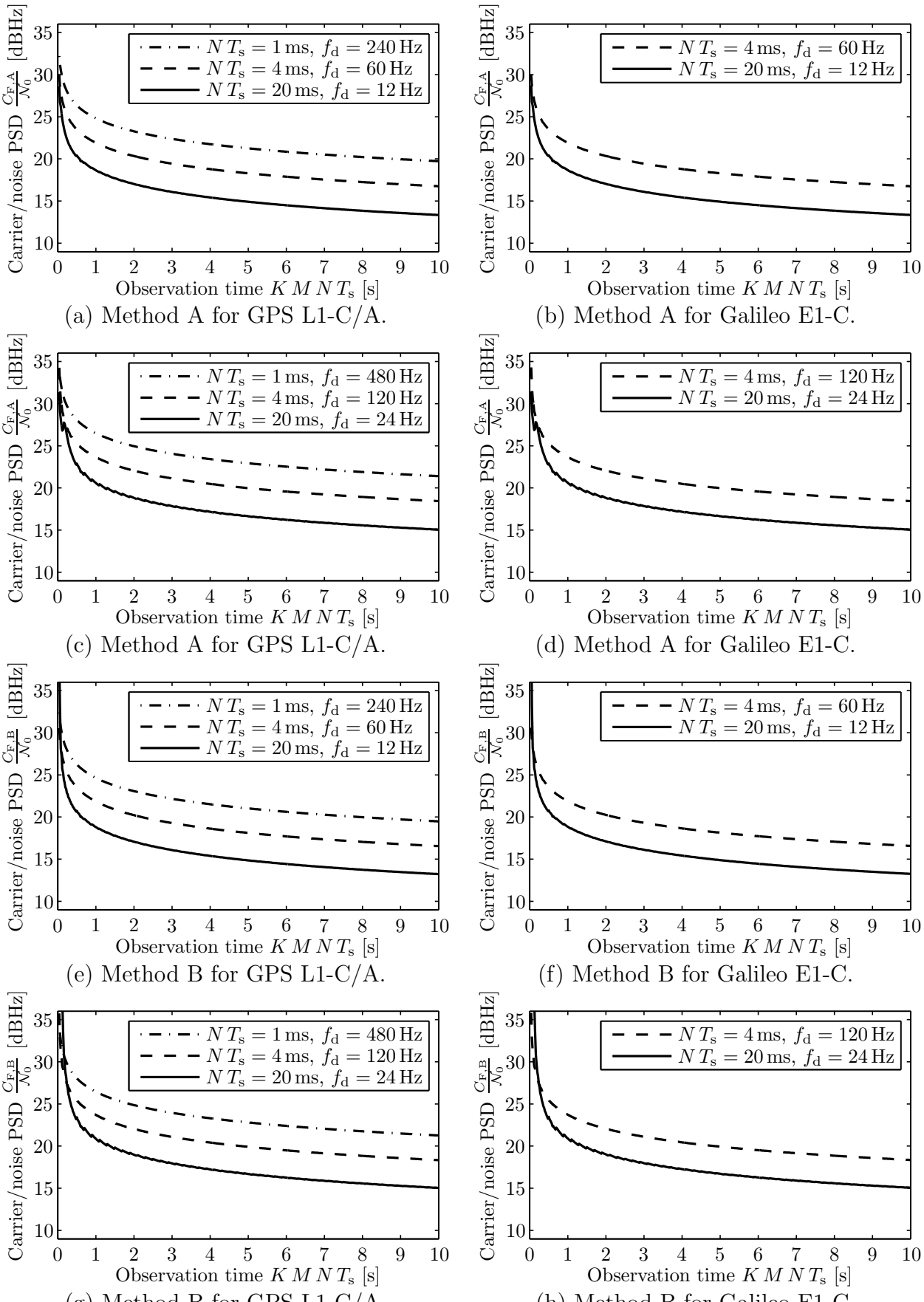

(a) Method A for GPS L1-C/A. (b) Method A for Galileo E1-C.

(c) Method A for GPS L1-C/A. (d) Method A for Galileo E1-C.

(e) Method B for GPS L1-C/A. (f) Method B for Galileo E1-C.

(g) Method B for GPS L1-C/A. (h) Method B for Galileo E1-C.

Figure 5.3: Reception sensitivity with the frequency offset correction technique for $T_0 = 290\,\mathrm{K}$, $F = 3\,\mathrm{dB}$, $K = 10$, $P_\mathrm{f} = 10^{-5}$, and $P_\mathrm{d} = 90\,\%$.

offset estimation error as displayed in Fig. 5.2 has to be minimized, sufficiently long intermediate differential correlation intervals $M\,N\,T_\mathrm{s}$ are desired. The choice of K in Fig. 5.3 is therefore $K = 10$, such that the frequency deviation is estimated only 10 times during the observation period $K\,M\,N\,T_\mathrm{s}$. Performing the estimation more often would reduce the accumulation time $M\,N\,T_\mathrm{s}$ for the estimation, which in turn would degrade the estimation accuracy. With $K = 10$, the values of M in Fig. 5.3 equal the observation period divided by $K\,N\,T_\mathrm{s}$. For example, when $K\,M\,N\,T_\mathrm{s} = 10\,\mathrm{s}$, the frequency deviation is estimated every 1 s. The value $K = 10$ has been found empirically to yield a good trade-off between high frequency estimation accuracy and fast response.

5.5 Sensitivity Gain

The sensitivity gain of the frequency offset correction technique versus the differential correlation with adaptive detection threshold is the difference between the values in dB of Fig. 4.6 and 5.3. The gain for method A, $C_{\mathrm{T,D}}/C_{\mathrm{F,A}}$, and method B, $C_{\mathrm{T,D}}/C_{\mathrm{F,B}}$, is displayed in Fig. 5.4. It can be observed in Fig. 5.4 that the frequency correction requires a little while to converge and delivers its maximum gain for intermediate and long observation periods. Method A converges faster than method B. It can be observed in Fig. 5.3.e to 5.3.h that the frequency offset compensation has not yet settled for method B with the combination of a short observation period and a long coherent integration interval. The loss of the quadrature correlation power causes the inferior initial sensitivity of method B. Once converged, both methods reach around the same reception sensitivity. The gain is approximately the same for the different coherent integration intervals and initial frequency deviations. The reason is that the products $f_\mathrm{d}\,N\,T_\mathrm{s}$ yield the same values of 0.24 and 0.48. The sensitivity gain of the frequency correction depends on the value of $f_\mathrm{d}\,N\,T_\mathrm{s}$, since this is term degrades the reception sensitivity in (5.31) with $\mathrm{sinc}^2(f_{\mathrm{d},\kappa}\,N\,T_\mathrm{s})$. The larger the product $f_\mathrm{d}\,N\,T_\mathrm{s}$, the larger is the sensitivity gain of the frequency correction. The saturated sensitivity gain for the larger frequency deviation is 1.5 dB for method A and 1.6 dB for method B. Both methods hence yield a similar reception sensitivity. Method B thereby introduces a lower implementation complexity, which can reduce application costs. Unfortunately, method B also yields a slightly lower positioning accuracy, as shown in the next chapter. To provide a complete analysis, both methods, A and B, will be presented subsequently.

Fig. 5.5 shows the cumulative sensitivity gain of the frequency offset correction technique versus the state-of-the-art noncoherent integration. Calculated in dB, the gain for methods A and B, $C_\mathrm{N}/C_{\mathrm{F,A}}$ and $C_\mathrm{N}/C_{\mathrm{F,B}}$, is the difference between the values of Fig. 3.14 and 5.3. The cumulative gain is the sum of the sensitivity gain of the differential correlation, the adaptive detection threshold, and the frequency offset correction. The differential correlation contributes around 1.5 dB and the adaptive detection threshold another 10 dB. The differential correlation furthermore enables the frequency correction, which improves the reception sensitivity by an additional 1.5 dB. The cumulative gain therefore reaches 13 dB for the methods A and B.

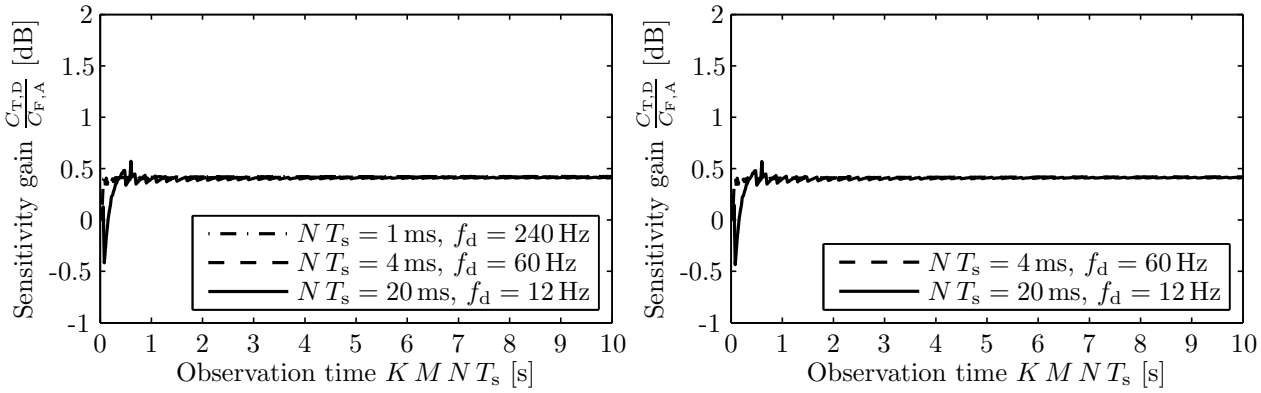

(a) Method A for GPS L1-C/A.

(b) Method A for Galileo E1-C.

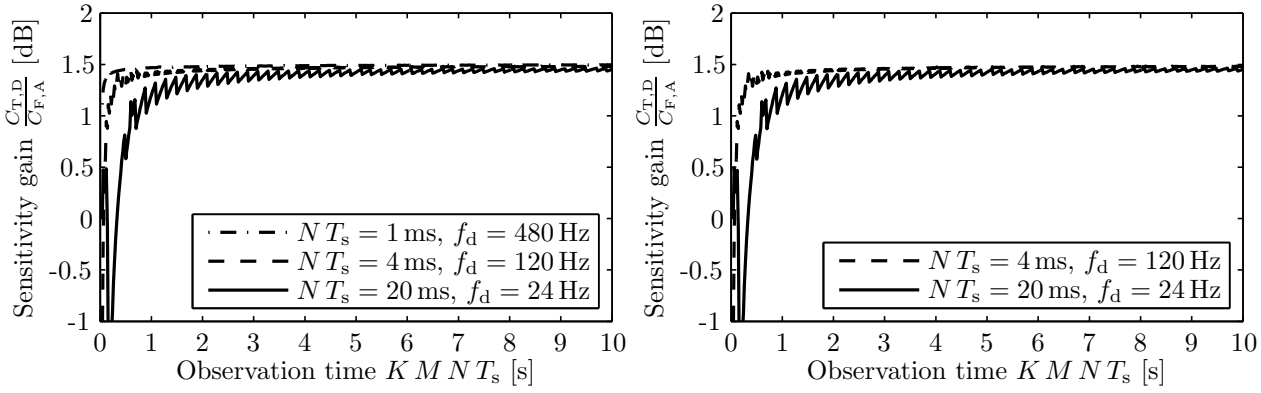

(c) Method A for GPS L1-C/A.

(d) Method A for Galileo E1-C.

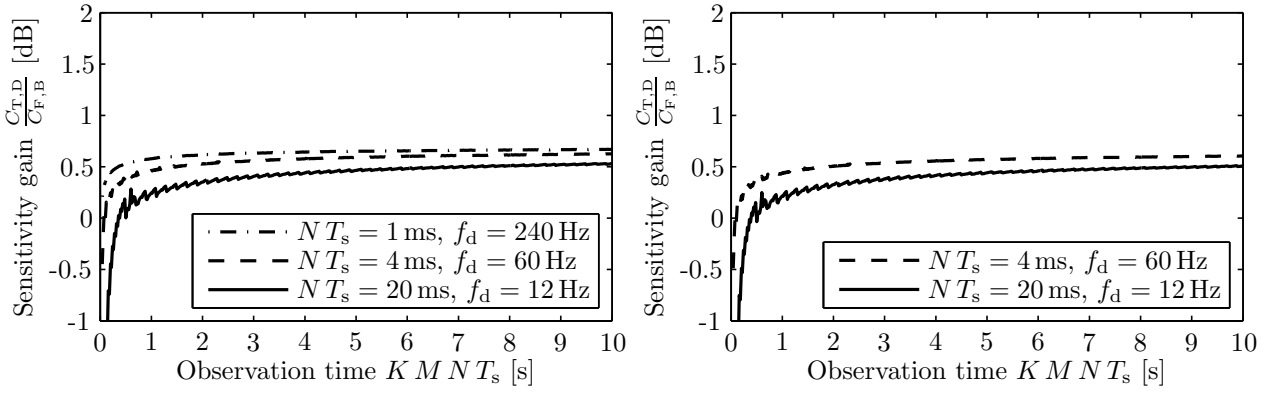

(e) Method B for GPS L1-C/A.

(f) Method B for Galileo E1-C.

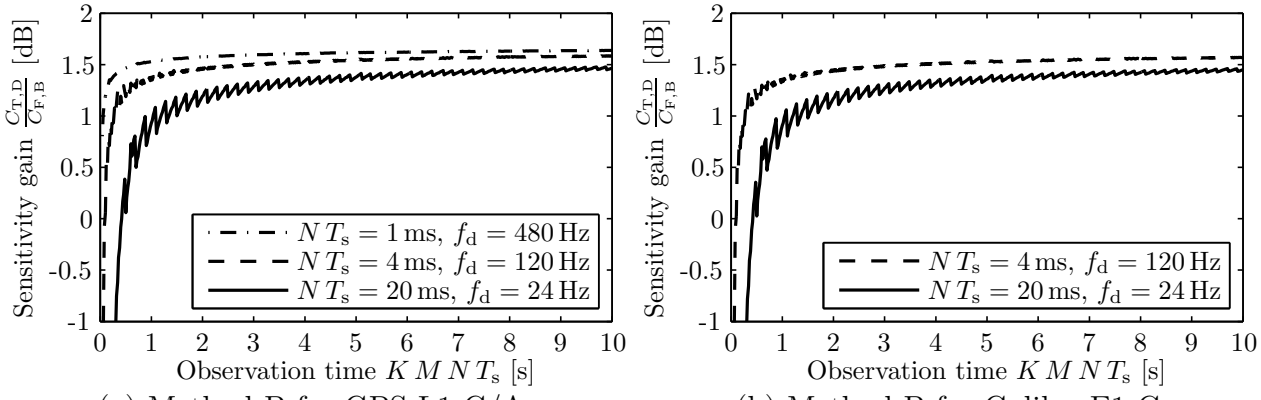

(g) Method B for GPS L1-C/A.

(h) Method B for Galileo E1-C.

Figure 5.4: Sensitivity gain of the frequency offset correction technique for $T_0 = 290\,\mathrm{K}$, $F = 3\,\mathrm{dB}$, $K = 10$, $P_{\mathrm{f}} = 10^{-5}$, and $P_{\mathrm{d}} = 90\,\%$.

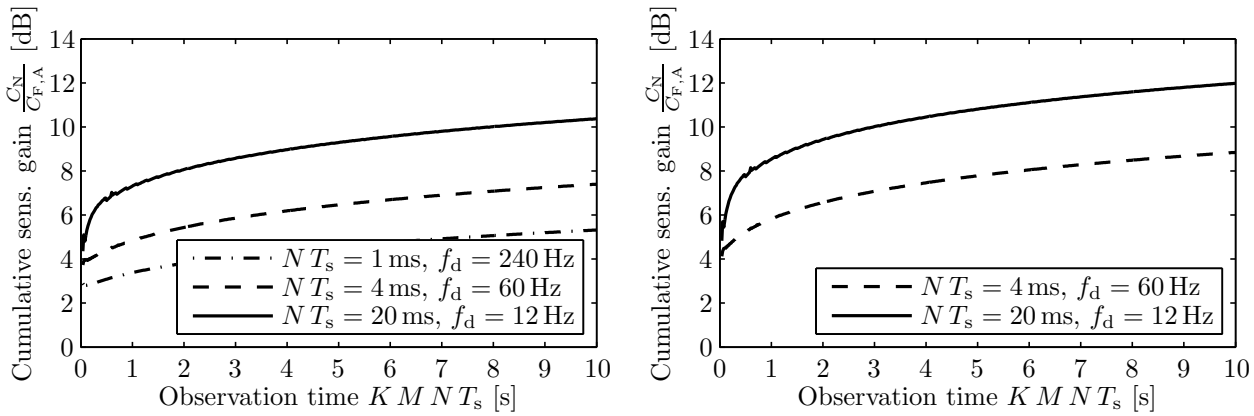

(a) Method A for GPS L1-C/A.

(b) Method A for Galileo E1-C.

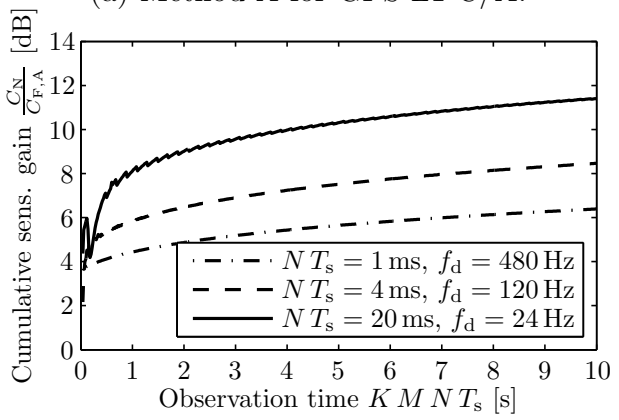

(c) Method A for GPS L1-C/A.

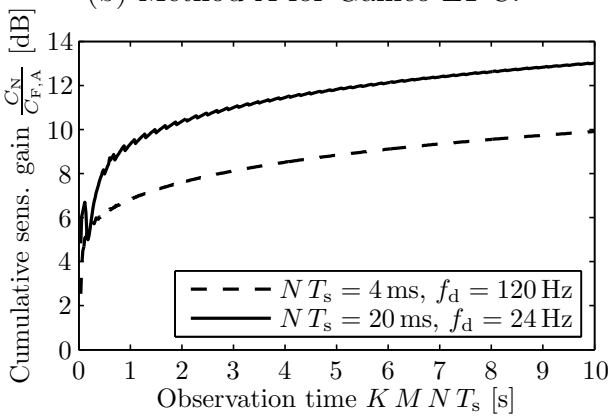

(d) Method A for Galileo E1-C.

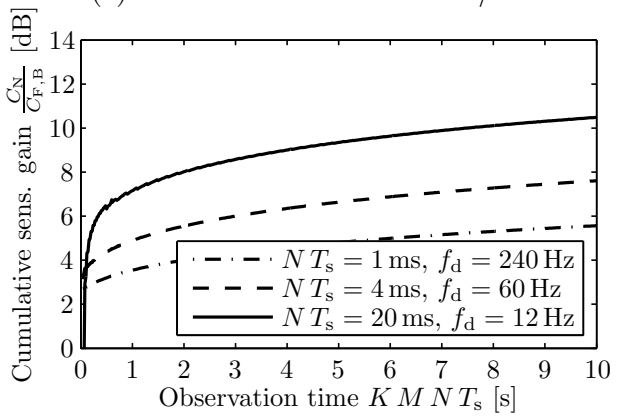

(e) Method B for GPS L1-C/A.

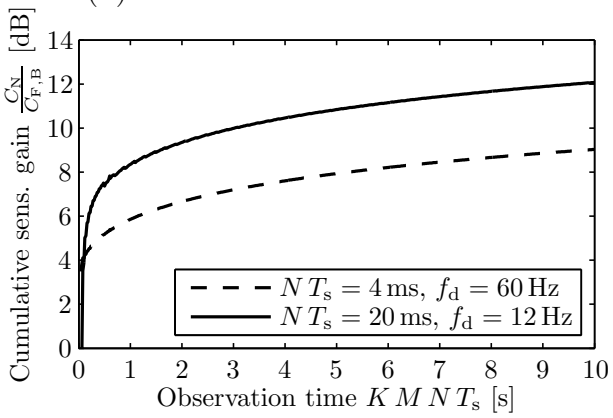

(f) Method B for Galileo E1-C.

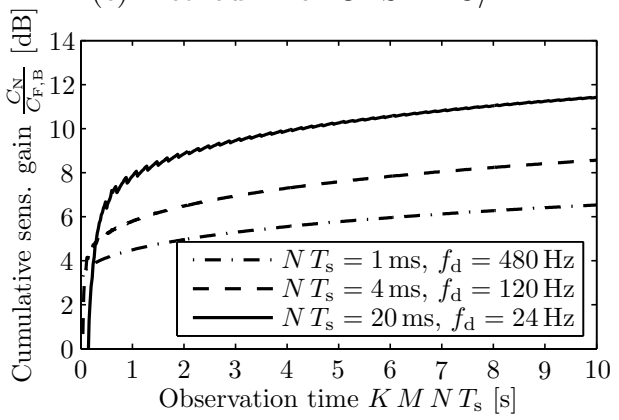

(g) Method B for GPS L1-C/A.

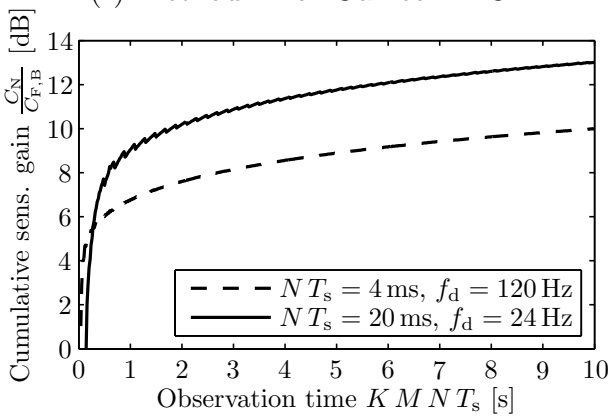

(h) Method B for Galileo E1-C.

Figure 5.5: Cumulative sensitivity gain of the frequency offset correction technique versus the state-of-the-art noncoherent integration for $T_0 = 290\,\text{K}$, $F = 3\,\text{dB}$, $K = 10$, $P_f = 10^{-5}$, and $P_d = 90\,\%$.

5.6 Positioning Accuracy

As described in Section 3.13, the actual correlation peak can be interpolated in between the sampling points with the discrimination function

$$\Delta = \Lambda_{\mathrm{E}} - \Lambda_{\mathrm{L}} = |\Upsilon_{\mathrm{E}}|^2 - |\Upsilon_{\mathrm{L}}|^2 \ . \tag{5.47}$$

The range variance for method A of the frequency correction is defined in (3.109) as

$$\boxed{\sigma^2_{\widehat{\rho},\mathrm{F,A}} = \frac{c^2\,\sigma^2_{\Delta,\mathrm{A}}}{\left(\frac{\partial m_{\Delta,\mathrm{A}}}{\partial \tau_\epsilon}\Big|_{\tau_\epsilon=0}\right)^2}} \ . \tag{5.48}$$

Modifying (3.108) yields the discrimination variance for method A

$$\begin{aligned}\sigma^2_{\Delta,\mathrm{A}} = {}& \sigma^4_{\Upsilon,\mathrm{E}} + \sigma^4_{\Upsilon,\mathrm{L}} + 2\,\sigma^2_{\Upsilon,\mathrm{E}}\,|m_{\Upsilon,\mathrm{E}}|^2 + 2\,\sigma^2_{\Upsilon,\mathrm{L}}\,|m_{\Upsilon,\mathrm{L}}|^2 \\ & - 2\,\frac{R^2(\delta)}{N^2}\,\sigma^2_{\Upsilon,\mathrm{E}}\,\sigma^2_{\Upsilon,\mathrm{L}} - 4\,\frac{R(\delta)}{N}\,\sigma_{\Upsilon,\mathrm{E}}\,\sigma_{\Upsilon,\mathrm{L}}\,|m_{\Upsilon,\mathrm{E}}|\,|m_{\Upsilon,\mathrm{L}}|\end{aligned} \tag{5.49}$$

with the early mean and variance

$$m_{\Upsilon,\mathrm{E}} = m_\Upsilon\big|_{\widehat{\tau}=\widehat{\tau}_{\mathrm{E}}} \ , \quad \sigma^2_{\Upsilon,\mathrm{E}} = \sigma^2_\Upsilon\big|_{\widehat{\tau}=\widehat{\tau}_{\mathrm{E}}} \tag{5.50}$$

and the late mean and variance

$$m_{\Upsilon,\mathrm{L}} = m_\Upsilon\big|_{\widehat{\tau}=\widehat{\tau}_{\mathrm{L}}} \ , \quad \sigma^2_{\Upsilon,\mathrm{L}} = \sigma^2_\Upsilon\big|_{\widehat{\tau}=\widehat{\tau}_{\mathrm{L}}} \ . \tag{5.51}$$

The expectation value of the discrimination function for method A is

$$\begin{aligned} m_{\Delta,\mathrm{A}} &= \mathrm{E}\{\Delta_{\mathrm{A}}\} = \mathrm{E}\big\{|\Upsilon_{\mathrm{E}}|^2 - |\Upsilon_{\mathrm{L}}|^2\big\} = \sigma^2_{\Upsilon,\mathrm{E}} + |m_{\Upsilon,\mathrm{E}}|^2 - \sigma^2_{\Upsilon,\mathrm{L}} - |m_{\Upsilon,\mathrm{L}}|^2 \\ &= 2\,C\,\sigma_w^2\,\big[R^2(\tau-\widehat{\tau}_{\mathrm{E}}) - R^2(\tau-\widehat{\tau}_{\mathrm{L}})\big] \sum_{\mu=1}^{K\,M-1} \big[\mathrm{sinc}^2(f_{\mathrm{d},\lfloor\mu/M\rfloor}\,N\,T_{\mathrm{s}}) + \mathrm{sinc}^2(f_{\mathrm{d},\lfloor(\mu-1)/M\rfloor}\,N\,T_{\mathrm{s}})\big] \\ &\quad +4\,C^2\,\big[R^4(\tau-\widehat{\tau}_{\mathrm{E}}) - R^4(\tau-\widehat{\tau}_{\mathrm{L}})\big] \sum_{\mu=1}^{K\,M-1} \Big|\mathrm{sinc}(f_{\mathrm{d},\lfloor\mu/M\rfloor}\,N\,T_{\mathrm{s}})\,\mathrm{sinc}(f_{\mathrm{d},\lfloor(\mu-1)/M\rfloor}\,N\,T_{\mathrm{s}}) \\ &\qquad\qquad \times \mathrm{e}^{\mathrm{j}\,\pi\,(f_{\mathrm{d},\lfloor\mu/M\rfloor}+f_{\mathrm{d},\lfloor(\mu-1)/M\rfloor})\,N\,T_{\mathrm{s}}}\Big|^2 . \end{aligned} \tag{5.52}$$

With (3.95) and (3.96), it can be simplified to

$$\begin{aligned} m_{\Delta,\mathrm{A}} = {}& -8\,C\,\sigma_w^2\,R\Big(\frac{\delta}{2}\Big)\,\frac{N\,\tau_\epsilon}{\eta\,T_{\mathrm{c}}} \sum_{\mu=1}^{K\,M-1} \big[\mathrm{sinc}^2(f_{\mathrm{d},\lfloor\mu/M\rfloor}\,N\,T_{\mathrm{s}}) + \mathrm{sinc}^2(f_{\mathrm{d},\lfloor(\mu-1)/M\rfloor}\,N\,T_{\mathrm{s}})\big] \\ & - 32\,C^2\,\left[R^3\Big(\frac{\delta}{2}\Big)\,\frac{N\,\tau_\epsilon}{\eta\,T_{\mathrm{c}}} + R\Big(\frac{\delta}{2}\Big)\,\frac{N^3\,\tau_\epsilon^3}{\eta^3\,T_{\mathrm{c}}^3}\right] \Bigg| \sum_{\mu=1}^{K\,M-1} \mathrm{sinc}(f_{\mathrm{d},\lfloor\mu/M\rfloor}\,N\,T_{\mathrm{s}}) \\ & \times \mathrm{sinc}(f_{\mathrm{d},\lfloor(\mu-1)/M\rfloor}\,N\,T_{\mathrm{s}})\,\mathrm{e}^{\mathrm{j}\,\pi\,(f_{\mathrm{d},\lfloor\mu/M\rfloor}+f_{\mathrm{d},\lfloor(\mu-1)/M\rfloor})\,N\,T_{\mathrm{s}}}\Bigg|^2 , \end{aligned} \tag{5.53}$$

where δ is the discrimination spacing and τ_ϵ the initial mean code phase estimation error. The derivative with respect to τ_ϵ is therefore

$$\begin{aligned}
\left.\frac{\partial m_{\Delta,\mathrm{A}}}{\partial \tau_\epsilon}\right|_{\tau_\epsilon=0} &= -8\,C\,\sigma_w^2\,R\!\left(\frac{\delta}{2}\right)\frac{N}{\eta\,T_\mathrm{c}}\sum_{\mu=1}^{K\,M-1}\left[\operatorname{sinc}^2\!(f_{\mathrm{d},\lfloor\mu/M\rfloor}\,N\,T_\mathrm{s})+\operatorname{sinc}^2\!(f_{\mathrm{d},\lfloor(\mu-1)/M\rfloor}\,N\,T_\mathrm{s})\right]\\
&\quad -32\,C^2\,R^3\!\left(\frac{\delta}{2}\right)\frac{N}{\eta\,T_\mathrm{c}}\left|\sum_{\mu=1}^{K\,M-1}\operatorname{sinc}(f_{\mathrm{d},\lfloor\mu/M\rfloor}\,N\,T_\mathrm{s})\operatorname{sinc}(f_{\mathrm{d},\lfloor(\mu-1)/M\rfloor}\,N\,T_\mathrm{s})\right.\\
&\qquad\qquad \left.\times\,\mathrm{e}^{\mathrm{j}\,\pi\,(f_{\mathrm{d},\lfloor\mu/M\rfloor}+f_{\mathrm{d},\lfloor(\mu-1)/M\rfloor})\,N\,T_\mathrm{s}}\right|^2\\
&= -8\,C\,\sigma_w^2\,R\!\left(\frac{\delta}{2}\right)\frac{N}{\eta\,T_\mathrm{c}}\left[(2M-1)\left[\operatorname{sinc}^2\!(f_{\mathrm{d},0}\,N\,T_\mathrm{s})+\operatorname{sinc}^2\!(f_{\mathrm{d},\mathrm{K}-1}\,N\,T_\mathrm{s})\right]\right.\\
&\qquad\qquad \left.+\sum_{\kappa=1}^{K-2}2\,M\operatorname{sinc}^2\!(f_{\mathrm{d},\kappa}\,N\,T_\mathrm{s})\right]\\
&\quad -32\,C^2\,R^3\!\left(\frac{\delta}{2}\right)\frac{N}{\eta\,T_\mathrm{c}}\left|\sum_{\kappa=1}^{K-1}\operatorname{sinc}(f_{\mathrm{d},\kappa}\,N\,T_\mathrm{s})\operatorname{sinc}(f_{\mathrm{d},\kappa-1}\,N\,T_\mathrm{s})\,\mathrm{e}^{\mathrm{j}\,\pi\,(f_{\mathrm{d},\kappa}+f_{\mathrm{d},\kappa-1})\,N\,T_\mathrm{s}}\right.\\
&\qquad\qquad \left.+\sum_{\kappa=0}^{K-1}(M-1)\operatorname{sinc}^2\!(f_{\mathrm{d},\kappa}\,N\,T_\mathrm{s})\,\mathrm{e}^{\mathrm{j}\,2\,\pi\,f_{\mathrm{d},\kappa}\,N\,T_\mathrm{s}}\right|^2.
\end{aligned}\tag{5.54}$$

The variance of the range for method B of the frequency correction is

$$\boxed{\sigma^2_{\widehat{\rho},\mathrm{F,B}}=\frac{c^2\,\sigma^2_{\Delta,\mathrm{B}}}{\left(\frac{\partial m_{\Delta,\mathrm{B}}}{\partial\tau_\epsilon}\right)^2}}\,.\tag{5.55}$$

The discrimination variance for method B results in

$$\sigma^2_{\Delta,\mathrm{B}}=\mathrm{E}\{(\Delta_\mathrm{B}-m_{\Delta,\mathrm{B}})^2\}=\mathrm{E}\{\Re\{\Upsilon_\mathrm{E}-m_{\Upsilon,\mathrm{E}}-\Upsilon_\mathrm{L}+m_{\Upsilon,\mathrm{L}}\}^2\}=\sigma^2_{\Upsilon,\mathrm{I,E}}+\sigma^2_{\Upsilon,\mathrm{I,L}}\tag{5.56}$$

with the early and late inphase variances

$$\sigma^2_{\Upsilon,\mathrm{I,E}}=\sigma^2_{\Upsilon,\mathrm{I}}\Big|_{\widehat{\tau}=\widehat{\tau}_\mathrm{E}}\,,\quad \sigma^2_{\Upsilon,\mathrm{I,L}}=\sigma^2_{\Upsilon,\mathrm{I}}\Big|_{\widehat{\tau}=\widehat{\tau}_\mathrm{L}}\,.\tag{5.57}$$

Since Λ_B is Gaussian distributed, the expectation value of the discrimination function is

$$\begin{aligned}
m_{\Delta,\mathrm{B}} &= \mathrm{E}\{\Delta_\mathrm{B}\}=\mathrm{E}\{\Re\{\Upsilon_\mathrm{E}\}-\Re\{\Upsilon_\mathrm{L}\}\}=\Re\{m_{\Upsilon,\mathrm{E}}\}-\Re\{m_{\Upsilon,\mathrm{L}}\}\\
&= 2\,C\left[R^2(\tau-\widehat{\tau}_\mathrm{E})-R^2(\tau-\widehat{\tau}_\mathrm{L})\right]\sum_{\mu=1}^{K\,M-1}\left[\operatorname{sinc}(f_{\mathrm{d},\lfloor\mu/M\rfloor}\,N\,T_\mathrm{s})\operatorname{sinc}(f_{\mathrm{d},\lfloor(\mu-1)/M\rfloor}\,N\,T_\mathrm{s})\right.\\
&\qquad\qquad \left.\times\cos\!\big(\pi\,(f_{\mathrm{d},\lfloor\mu/M\rfloor}+f_{\mathrm{d},\lfloor(\mu-1)/M\rfloor})\,N\,T_\mathrm{s}\big)\right]\\
&= -8\,C\,R\!\left(\frac{\delta}{2}\right)\frac{N\,\tau_\epsilon}{\eta\,T_\mathrm{c}}\sum_{\mu=1}^{K\,M-1}\left[\operatorname{sinc}(f_{\mathrm{d},\lfloor\mu/M\rfloor}\,N\,T_\mathrm{s})\operatorname{sinc}(f_{\mathrm{d},\lfloor(\mu-1)/M\rfloor}\,N\,T_\mathrm{s})\right.\\
&\qquad\qquad \left.\times\cos\!\big(\pi\,(f_{\mathrm{d},\lfloor\mu/M\rfloor}+f_{\mathrm{d},\lfloor(\mu-1)/M\rfloor})\,N\,T_\mathrm{s}\big)\right],
\end{aligned}\tag{5.58}$$

while the derivative with respect to τ_ϵ is

$$\begin{aligned}\frac{\partial m_{\Delta,\mathrm{B}}}{\partial \tau_\epsilon} &= -8\,C\,R\!\left(\frac{\delta}{2}\right)\,\frac{N}{\eta\,T_\mathrm{c}}\sum_{\mu=1}^{K\,M-1}\Big[\mathrm{sinc}(f_{\mathrm{d},\lfloor\mu/M\rfloor}\,N\,T_\mathrm{s})\,\mathrm{sinc}(f_{\mathrm{d},\lfloor(\mu-1)/M\rfloor}\,N\,T_\mathrm{s}) \\ &\qquad\qquad \times\cos\!\big(\pi\,(f_{\mathrm{d},\lfloor\mu/M\rfloor}+f_{\mathrm{d},\lfloor(\mu-1)/M\rfloor})\,N\,T_\mathrm{s}\big)\Big] \\ &= -\,8\,C\,R\!\left(\frac{\delta}{2}\right)\,\frac{N}{\eta\,T_\mathrm{c}}\Bigg[\sum_{\kappa=0}^{K-1}(M-1)\,\mathrm{sinc}^2(f_{\mathrm{d},\kappa}\,N\,T_\mathrm{s})\,\cos(2\,\pi\,f_{\mathrm{d},\kappa}\,N\,T_\mathrm{s}) \\ &\quad+\sum_{\kappa=1}^{K-1}\mathrm{sinc}(f_{\mathrm{d},\kappa}\,N\,T_\mathrm{s})\,\mathrm{sinc}(f_{\mathrm{d},\kappa-1}\,N\,T_\mathrm{s})\,\cos(\pi\,(f_{\mathrm{d},\kappa}+f_{\mathrm{d},\kappa-1})\,N\,T_\mathrm{s})\Bigg].\end{aligned} \tag{5.59}$$

Fig. 5.6 shows the standard deviation of the estimated range for method A, $\sigma_{\widehat{\rho},\mathrm{F,A}}$, as specified in (5.48) by inserting (5.49) and (5.54), as well as the standard deviation of the estimated range for method B, $\sigma_{\widehat{\rho},\mathrm{F,B}}$, as specified in (5.55) by inserting (5.59) and (5.56). The choice of the parameters $T_0 = 290\,\mathrm{K}$, and $F = 3\,\mathrm{dB}$ has been introduced in Section 3.7, the choice of $K = 10$ in Section 5.4, and the choice of $\delta = 1/B$ and $B = 4.092\,\mathrm{MHz}$ in Section 3.14. Fig. 5.6.a to 5.6.d illustrate the result of method A for GPS and Galileo, while Fig. 5.6.e to 5.6.h present method B. To allow a comparison with the previous results of Chapter 3, the same underlying $C_\mathrm{N}/\mathcal{N}_0$ values have been applied. The $C_\mathrm{N}/\mathcal{N}_0$ values are presented in Fig. 3.14 and yield $P_\mathrm{d} = 90\,\%$ for the state-of-the-art noncoherent integration. By using these common $C_\mathrm{N}/\mathcal{N}_0$ values, it can be shown how much the frequency offset correction technique can improve the positioning accuracy. The carrier-to-noise PSD of Fig. 3.14 has been selected, because the state-of-the-art noncoherent integration delivers the weakest reception sensitivity and would not even permit reliable positioning at lower $C/\mathcal{N}_0$ values.

5.7 Accuracy Improvement

The frequency offset correction influences the mean and variance of the differential correlation results. This leads to a different positioning accuracy than previously. The difference of the range estimation accuracies of the frequency offset correction and the differential correlation is displayed in Fig. 5.7. The relative accuracies $\sigma_{\widehat{\rho},\mathrm{D}}/\sigma_{\widehat{\rho},\mathrm{F,A}}$ and $\sigma_{\widehat{\rho},\mathrm{D}}/\sigma_{\widehat{\rho},\mathrm{F,B}}$ are calculated as the ratios of the values in Fig. 3.19 and 5.6. It can be observed that range accuracy degrades for the combination of a large frequency deviation, a long coherent integration interval, and a very short observation period. This is because the value of K is actually less than 10 for all observation periods below 200 ms for $N\,T_\mathrm{s} = 20\,\mathrm{ms}$. This low number of iterations does not allow the frequency deviation to converge sufficiently. Instead, the degrading effect of a changing phase of the intermediate differential correlation results is still present and not being outweighed by the reduced frequency deviation. This issue of changing signal phases will be addressed in detail in the next chapter. Furthermore, it can be observed that method B yields a range accuracy that is 8–39 % lower than that of method A. This is a result of only using the inphase component of the correlation function. Method A of the frequency offset correction technique can increase the accuracy of the range estimate up to 62 %. As

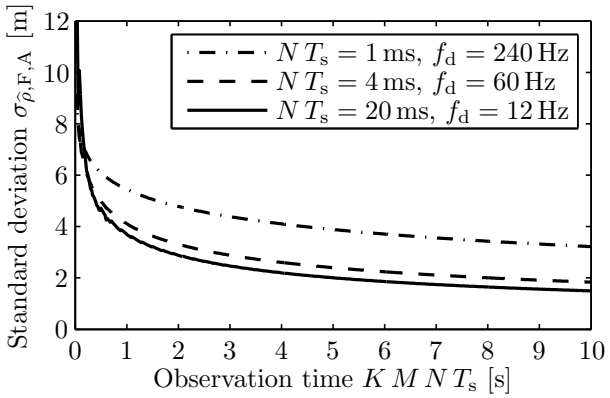

(a) Method A for GPS L1-C/A.

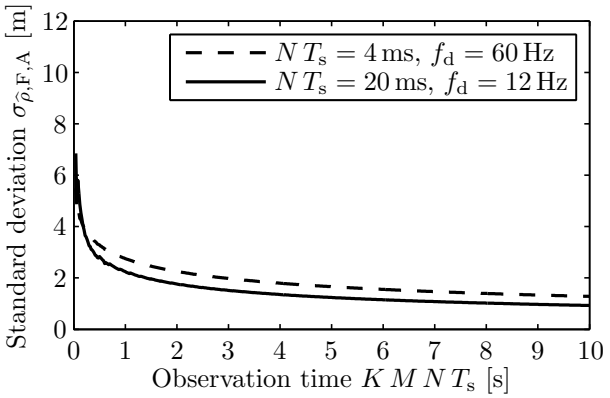

(b) Method A for Galileo E1-C.

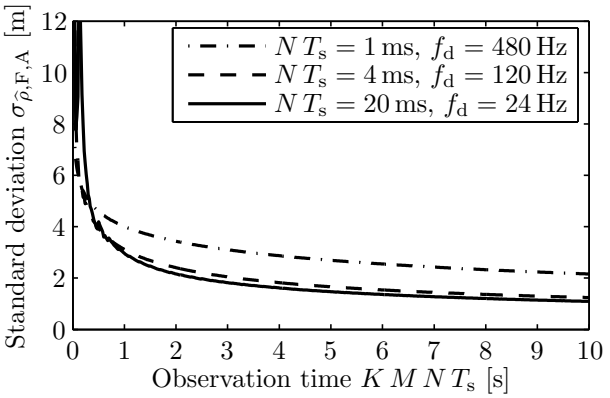

(c) Method A for GPS L1-C/A.

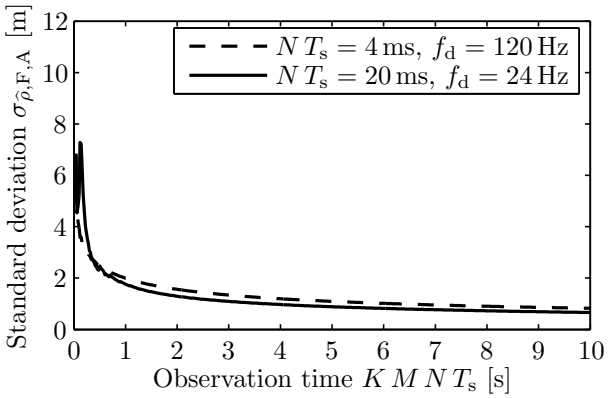

(d) Method A for Galileo E1-C.

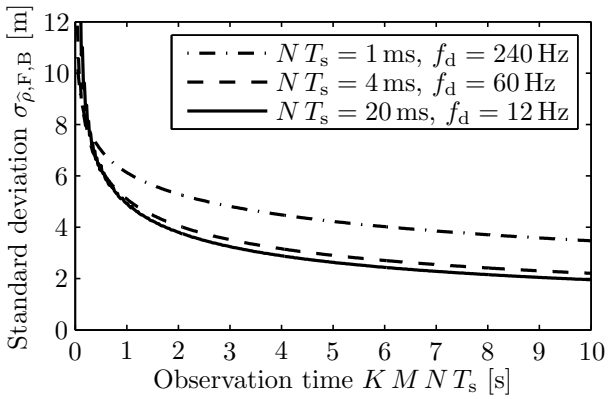

(e) Method B for GPS L1-C/A.

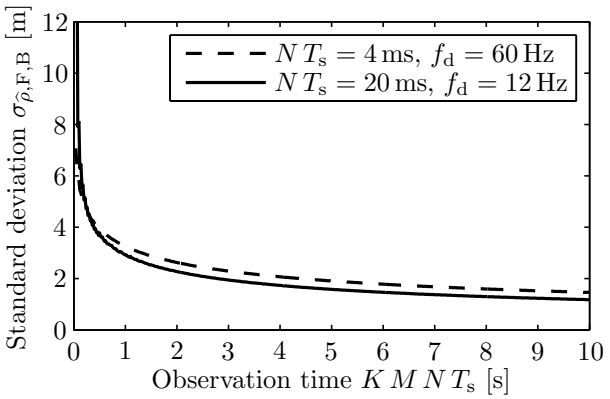

(f) Method B for Galileo E1-C.

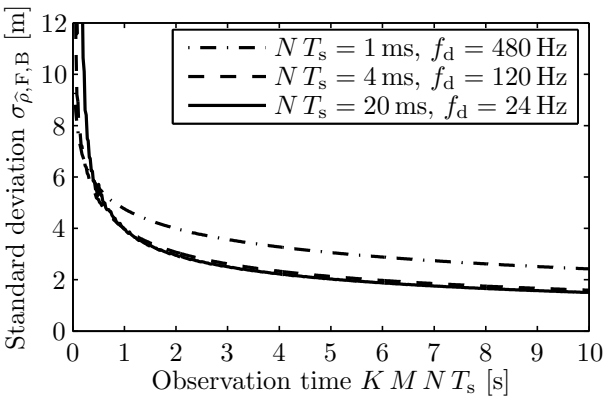

(g) Method B for GPS L1-C/A.

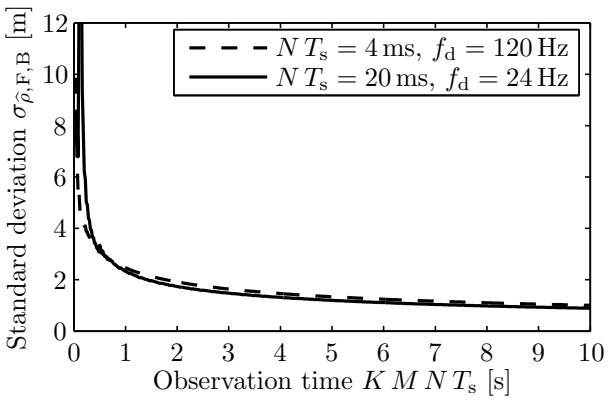

(h) Method B for Galileo E1-C.

Figure 5.6: Range estimation accuracy with the frequency offset correction technique for $T_0 = 290\,\mathrm{K}$, $F = 3\,\mathrm{dB}$, $K = 10$, $\delta = 1/B$, and $B = 4.092\,\mathrm{MHz}$.

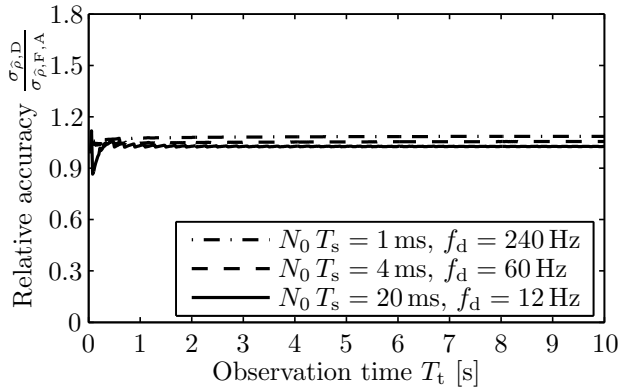

(a) Method A for GPS L1-C/A.

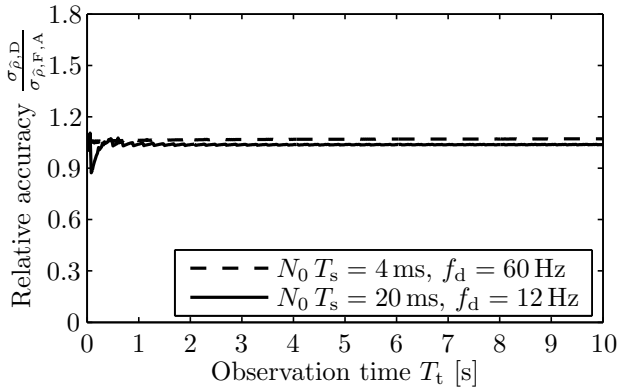

(b) Method A for Galileo E1-C.

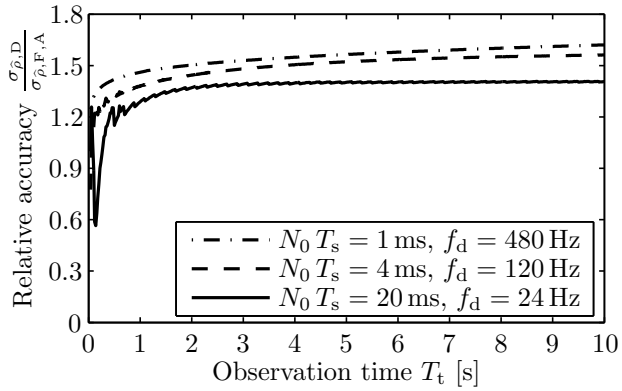

(c) Method A for GPS L1-C/A.

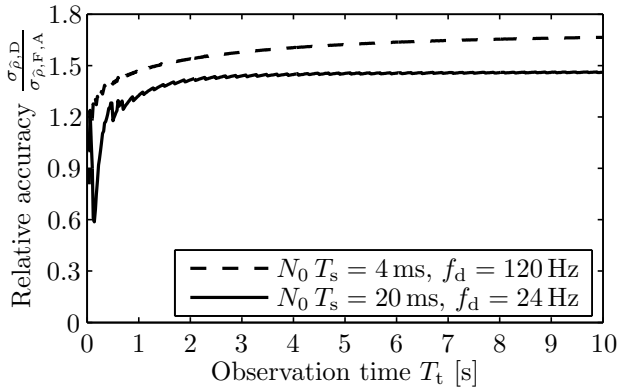

(d) Method A for Galileo E1-C.

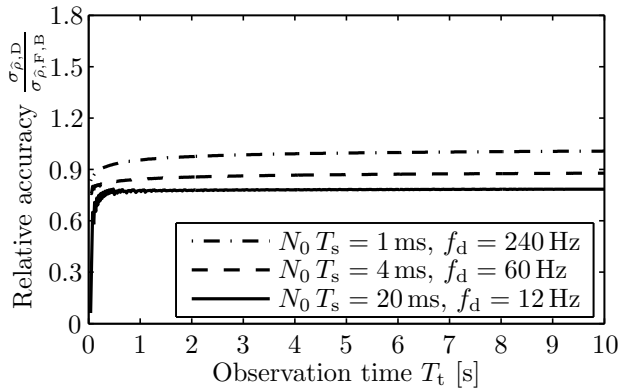

(e) Method B for GPS L1-C/A.

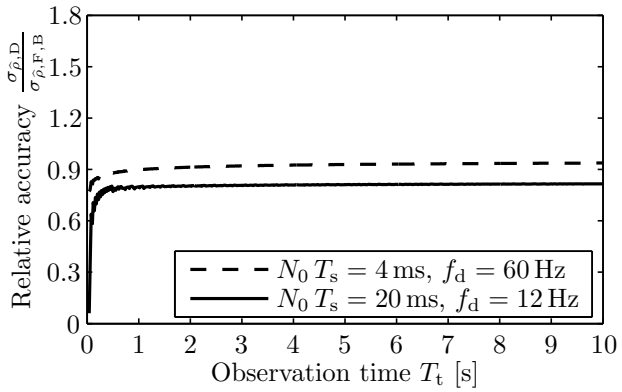

(f) Method B for Galileo E1-C.

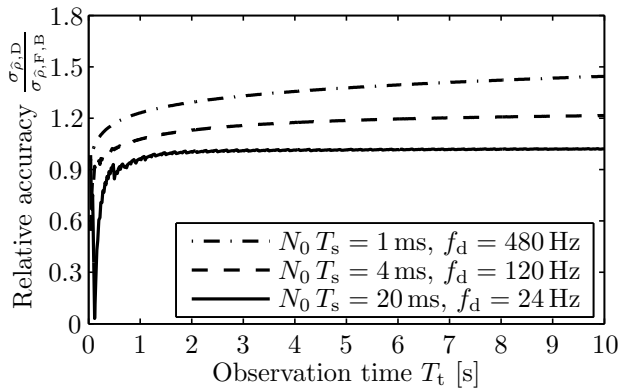

(g) Method B for GPS L1-C/A.

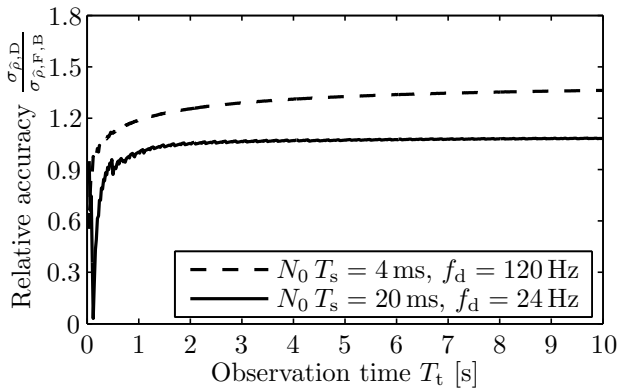

(h) Method B for Galileo E1-C.

Figure 5.7: Accuracy improvement of the frequency offset correction technique for $T_0 = 290\,\mathrm{K}$, $F = 3\,\mathrm{dB}$, $K = 10$, $\delta = 1/B$, and $B = 4.092\,\mathrm{MHz}$.

can be seen in Fig. 5.7, method B can achieve an improvement of 44 % for large frequency deviations, while it slightly worsens the accuracy for low frequency deviations.

The cumulative relative accuracy of the frequency offset correction versus the state-of-the-art noncoherent integration is shown in Fig. 5.8. The cumulative relative accuracies $\sigma_{\hat{\rho},\mathrm{N}}/\sigma_{\hat{\rho},\mathrm{F,A}}$ and $\sigma_{\hat{\rho},\mathrm{N}}/\sigma_{\hat{\rho},\mathrm{F,B}}$ are calculated as the ratios of the values in Fig. 3.21 and 5.6. The accuracy of the estimated distance between receiver and satellite is increased by the frequency offset correction by as much as 191 % more than the state-of-the-art noncoherent integration. Method B improves the accuracy of the range measurements by 159 %. The contributors to this improvement are the differential correlation with 80 %, method A of the frequency offset correction with 62 %, and method B of the frequency offset correction 44 %. The cumulative accuracy enhancement is obtained as $1.8 \times 1.62 - 1$ for method A and $1.8 \times 1.44 - 1$ for method B.

5.8 Conclusion

This chapter presents a technique to estimate the frequency deviation f_d based on the differential correlation result. It allows the iterative compensation of the frequency deviation with the presented feedback loop. The reduction of the frequency deviation yields a higher correlation gain. The *frequency offset correction* technique therefore increases the reception sensitivity by up to 1.5 dB for the presented receiver configuration. This adds up to a cumulative sensitivity gain versus the state-of-the-art noncoherent integration of 13 dB. The additional gain of the frequency correction method is obviously bound by the sensitivity for zero DOPPLER frequency shift. The improved signal-to-noise ratio furthermore leads to a lower variance of the correlation peak estimation. This results in an improved positioning accuracy. The accuracy of the estimated distance between receiver and satellite is increased by as much as 67 %. The cumulative relative accuracy for the frequency offset correction versus the state-of-the-art noncoherent integration is therefore improved by up to 191%. Since the frequency deviation converges towards zero, the differential correlation result converges to a real-valued result. It is therefore also possible to evaluate just the inphase component of the differential correlation result. This not only reduces the implementation complexity, power consumption, and manufacturing costs, but also improves the reception sensitivity by up to 1.6 dB and enhances the accuracy of the range estimates by 44 %. When compared to the state-of-the-art noncoherent integration, the inphase component of the frequency offset correction, enhances the reception sensitivity by 11.4 dB for GPS and 13 dB for Galileo. It improves the range accuracy by a maximum of 159 % for GPS and 108 % for Galileo.

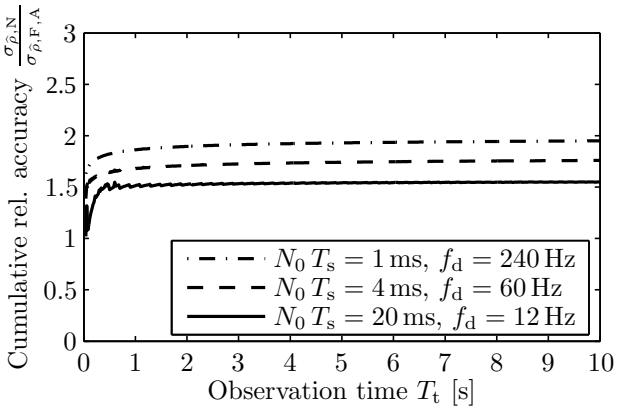

(a) Method A for GPS L1-C/A.

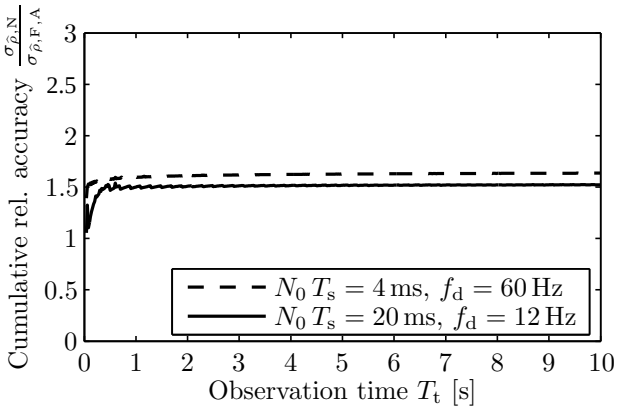

(b) Method A for Galileo E1-C.

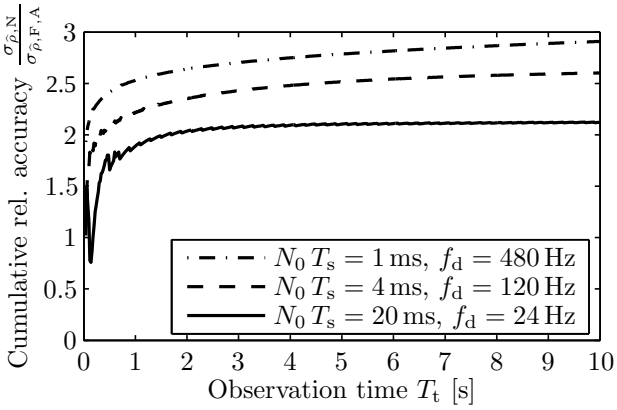

(c) Method A for GPS L1-C/A.

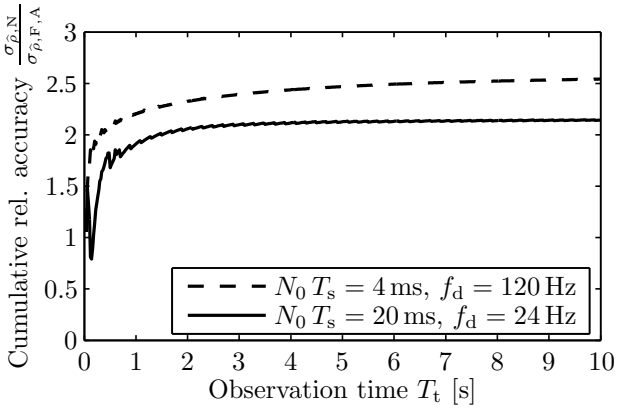

(d) Method A for Galileo E1-C.

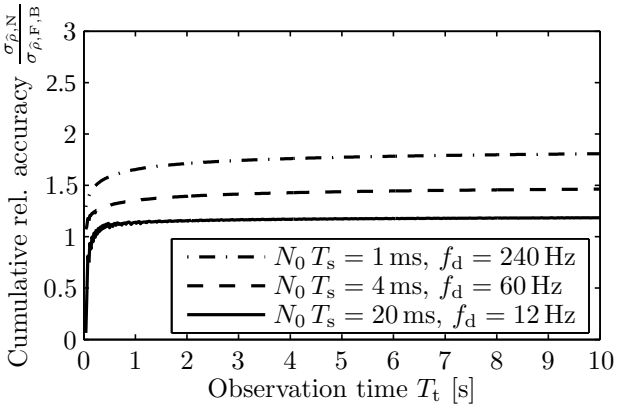

(e) Method B for GPS L1-C/A.

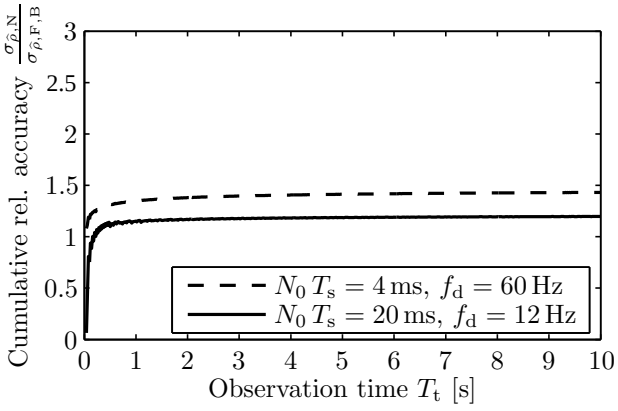

(f) Method B for Galileo E1-C.

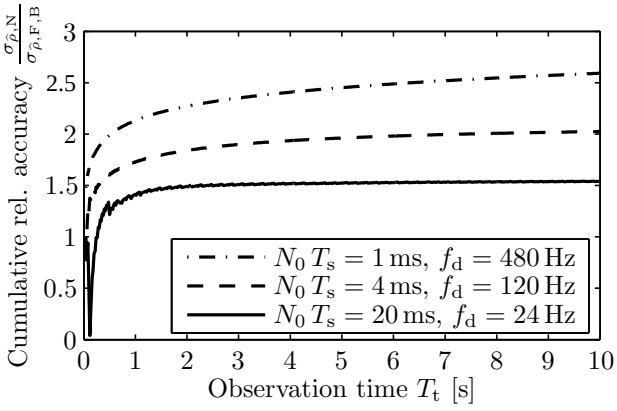

(g) Method B for GPS L1-C/A.

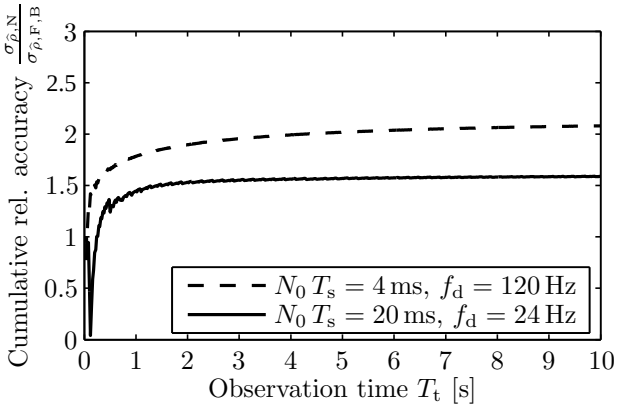

(h) Method B for Galileo E1-C.

Figure 5.8: Cumulative accuracy improvement of the frequency offset correction technique versus the state-of-the-art noncoherent integration for $T_0 = 290\,\mathrm{K}$, $F = 3\,\mathrm{dB}$, $K = 10$, $\delta = 1/B$, and $B = 4.092\,\mathrm{MHz}$.

Chapter 6

Phase Mismatch Correction

The frequency offset correction technique of Chapter 5 leads to phase fluctuations of the intermediate differential correlation results. Excessive phase fluctuations may degrade the combined accumulated correlation power. This chapter therefore introduces a *phase mismatch correction* technique, which rotates the intermediate differential correlation results towards the inphase component before further accumulating them.

This phase mismatch correction compensates sudden phase changes early in the observation period, when the frequency correction technique introduces strong fluctuations of the frequency deviation. It therefore achieves the same correlation gain within a shorter integration interval, which leads to lower energy consumption. Another benefit is that more correlation power accumulates in the inphase path. This allows to only evaluate the inphase component of the differential correlation instead of its magnitude. While a minor quadrature correlation component may be neglected this way, the quadrature noise component is also rejected. Just evaluating the inphase component simplifies the hardware and software implementation. The third accumulator can be simplified from complex-valued to real-valued and the calculation of the squared magnitude can be omitted. This reduces not only implementation expenses, but also power consumption.

6.1 Signal Rotation

It can be observed in (5.31) that the phase of each intermediate differential correlation result $\widehat{\phi}_\kappa$ is proportional to the frequency deviation f_d. The frequency offset correction therefore reduces the phase, which lowers the achievable final differential correlation value Υ. The frequency offset estimation method of Chapter 5 already includes the required signal processing units to calculate the argument of the intermediate differential correlation results Ψ_κ. As shown in Fig. 6.1, the new technique only introduces an additional block to rotate the samples Ψ_κ. This becomes apparent when compared to Fig. 5.1.

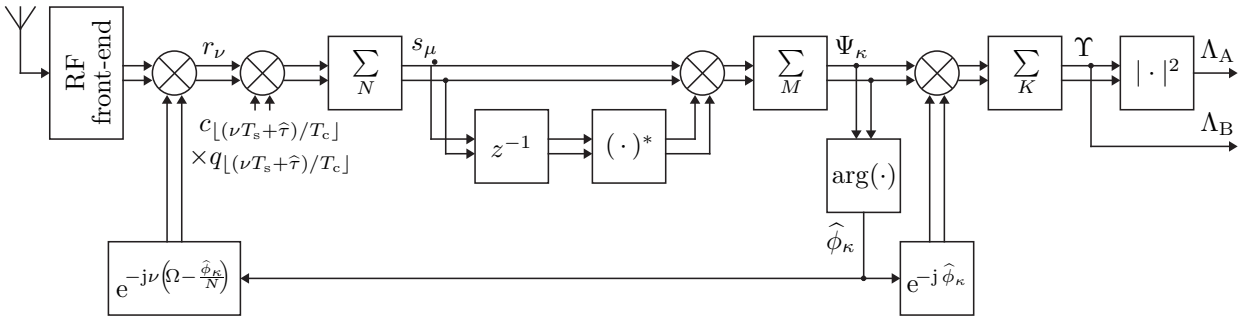

Figure 6.1: Receiver channel with the phase mismatch correction technique.

The correlation phase is estimated as

$$\boxed{\widehat{\phi}_\kappa = \arg(\Psi_\kappa) = \arg\left(\sum_{\mu=\kappa\,M+1}^{(\kappa+1)\,M-1} s_\mu\, s_{\mu-1}^*\right)} \tag{6.1}$$

and the final differential correlation result is thus calculated as

$$\boxed{\Upsilon = \sum_{\kappa=0}^{K-1}\sum_{\mu=\kappa\,M}^{(\kappa+1)\,M-1} s_\mu\, s_{\mu-1}^*\,\mathrm{e}^{-\mathrm{j}\,\widehat{\phi}_\kappa}} \tag{6.2}$$

with $s_{-1} = 0$. From (5.31), the resulting expectation value of the final differential correlation result Υ is derived as

$$\begin{aligned} m_\Upsilon &= \mathrm{E}\{\Upsilon\} \\ &= 2\,C\,R^2(\tau-\widehat{\tau})\left[\sum_{\kappa=0}^{K-1}(M-1)\,\mathrm{sinc}^2(f_{\mathrm{d},\kappa}\,N\,T_\mathrm{s})\,\mathrm{e}^{\mathrm{j}\,2\,\pi\,f_{\mathrm{d},\kappa}\,N\,T_\mathrm{s}-\mathrm{j}\,\widehat{\phi}_\kappa}\right. \\ &\quad \left. + \sum_{\kappa=1}^{K-1}\mathrm{sinc}(f_{\mathrm{d},\kappa}\,N\,T_\mathrm{s})\,\mathrm{sinc}(f_{\mathrm{d},\kappa-1}\,N\,T_\mathrm{s})\,\mathrm{e}^{\mathrm{j}\,\pi\,(f_{\mathrm{d},\kappa}+f_{\mathrm{d},\kappa-1})\,N\,T_\mathrm{s}-\mathrm{j}\,\widehat{\phi}_\kappa}\right]. \end{aligned} \tag{6.3}$$

The combined variance of the inphase and quadrature components of the differential correlation noise remains unchanged since it does not depend on $\widehat{\phi}_\kappa$ and is given in (5.32). If only the inphase path is to be evaluated, a modification of (5.35) yields the variance of the inphase component of the differential correlation noise

$$\begin{aligned} \sigma_{\Upsilon,\mathrm{I}}^2 = \frac{(K\,M-1)\,\sigma_w^4}{2} + \sigma_w^2\,C\,R^2(\tau-\widehat{\tau})\Bigg[&\mathrm{sinc}^2(f_{\mathrm{d},0}\,N\,T_\mathrm{s}) + \mathrm{sinc}^2(f_{\mathrm{d},K-1}\,N\,T_\mathrm{s}) \\ &+ \sum_{\kappa=0}^{K-1} 4\,(M-2)\,\mathrm{sinc}^2(f_{\mathrm{d},\kappa}\,N\,T_\mathrm{s})\,\cos^2(2\,\pi\,f_{\mathrm{d},\kappa}\,N\,T_\mathrm{s}-\widehat{\phi}_\kappa) \\ &+ \sum_{\kappa=0}^{K-2}\left|\mathrm{sinc}(f_{\mathrm{d},\kappa+1}\,N\,T_\mathrm{s}) + \mathrm{sinc}(f_{\mathrm{d},\kappa}\,N\,T_\mathrm{s})\,\mathrm{e}^{\mathrm{j}\,\pi(f_{\mathrm{d},\kappa+1}+3\,f_{\mathrm{d},\kappa})\,N\,T_\mathrm{s}-\mathrm{j}\,\widehat{\phi}_\kappa}\right|^2 \\ &+ \sum_{\kappa=1}^{K-1}\left|\mathrm{sinc}(f_{\mathrm{d},\kappa}\,N\,T_\mathrm{s}) + \mathrm{sinc}(f_{\mathrm{d},\kappa-1}\,N\,T_\mathrm{s})\,\mathrm{e}^{\mathrm{j}\,\pi(3\,f_{\mathrm{d},\kappa}+f_{\mathrm{d},\kappa-1})\,N\,T_\mathrm{s}-\mathrm{j}\,\widehat{\phi}_\kappa}\right|^2\Bigg]. \end{aligned} \tag{6.4}$$

6.2 Phase Estimation Accuracy

The sensitivity gain of the phase mismatch correction method is subject to the accuracy of the signal phase estimation. The probability density function of $\widehat{\phi}_\kappa$ has already been derived in (5.17). Fig. 6.2 shows the expectation value of the estimated phase

$$m_{\widehat{\phi}_\kappa} = \mathrm{E}\Big\{\widehat{\phi}_\kappa\Big\} \tag{6.5}$$

and the standard deviation of the estimated phase

$$\sigma_{\widehat{\phi}_\kappa} = \sqrt{\mathrm{E}\Big\{\Big(\widehat{\phi}_\kappa - \mathrm{E}\Big\{\widehat{\phi}_\kappa\Big\}\Big)^2\Big\}} \tag{6.6}$$

as a function of the observation period $M\,N\,T_\mathrm{s}$. They are obtained by numerical integration with the adaptive SIMPSON quadrature method [74]. As can be observed in Fig. 6.2, the estimated phase converges quickly to the correct value for sufficiently long observation periods. The standard deviation $\sigma_{\widehat{\phi}_\kappa}$ decreases exponentially with increasing observation periods. Even for very low carrier-to-noise PSD values $C/\mathcal{N}_0$, the presented estimation method can substantially reduce the phase mismatch.

6.3 Reception Sensitivity

The phase mismatch correction enables two different decision statistics. The conventional squared magnitude

$$\boxed{\Lambda_\mathrm{A} = |\Upsilon|^2 = \left|\sum_{\kappa=0}^{K-1}\sum_{\mu=\kappa\,M}^{(\kappa+1)\,M-1} s_\mu\, s_{\mu-1}^*\, \mathrm{e}^{-\mathrm{j}\,\widehat{\phi}_\kappa}\right|^2} \tag{6.7}$$

is used for method A and the inphase component

$$\boxed{\Lambda_\mathrm{B} = \Re\{\Upsilon\} = \Re\left\{\sum_{\kappa=0}^{K-1}\sum_{\mu=\kappa\,M}^{(\kappa+1)\,M-1} s_\mu\, s_{\mu-1}^*\, \mathrm{e}^{-\mathrm{j}\,\widehat{\phi}_\kappa}\right\}} \tag{6.8}$$

is used for method B, since the phase mismatch correction rotates the correlation power towards the real part of Υ.

The detection threshold for method A, λ_A, is obtained from (5.38) using $m_{\Upsilon,\mathrm{H}_0} = m_\Upsilon|_{R^2(\tau-\widehat{\tau})=R_\mathrm{m}^2}$ and $\sigma^2_{\Upsilon,\mathrm{H}_0} = \sigma^2_\Upsilon|_{R^2(\tau-\widehat{\tau})=R_\mathrm{m}^2}$ as provided in (6.3) and (5.32). The probability of detection $P_\mathrm{d,A}$ is then obtained from (5.40) by inserting $m_{\Upsilon,\mathrm{H}_1} = m_\Upsilon|_{R^2(\tau-\widehat{\tau})=N^2}$ and $\sigma^2_{\Upsilon,\mathrm{H}_1} = \sigma^2_\Upsilon|_{R^2(\tau-\widehat{\tau})=N^2}$. Similarly, the detection threshold for method B, λ_B, is calculated with (5.44), where $\sigma^2_{\Upsilon,\mathrm{I},\mathrm{H}_0} = \sigma^2_{\Upsilon,\mathrm{I}}|_{R^2(\tau-\widehat{\tau})=R_\mathrm{m}^2}$ is provided in (6.4). This yields the probability of detection $P_\mathrm{d,B}$ with (5.45) by inserting $\sigma^2_{\Upsilon,\mathrm{I},\mathrm{H}_1} = \sigma^2_{\Upsilon,\mathrm{I}}|_{R^2(\tau-\widehat{\tau})=N^2}$.

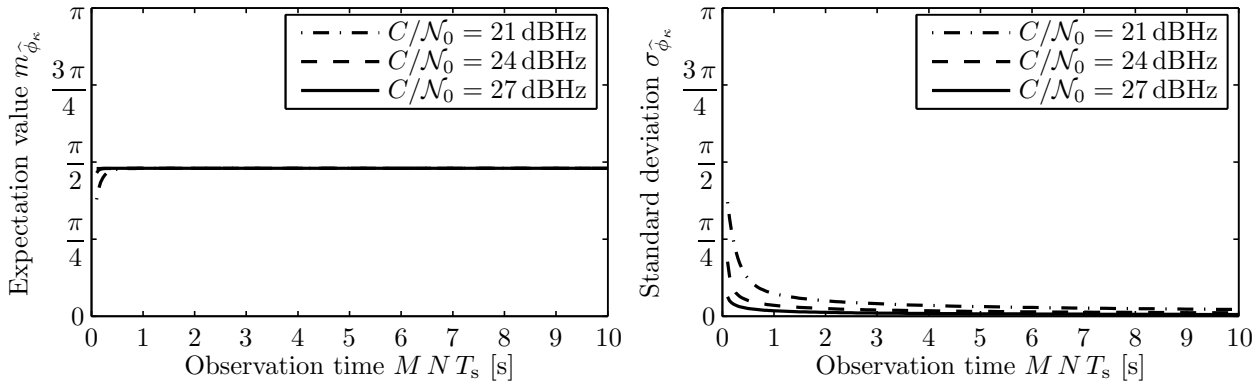

(a) $N\,T_\mathrm{s} = 1\,\mathrm{ms}$ and $f_\mathrm{d} = 240\,\mathrm{Hz}$.

(b) $N\,T_\mathrm{s} = 1\,\mathrm{ms}$ and $f_\mathrm{d} = 240\,\mathrm{Hz}$.

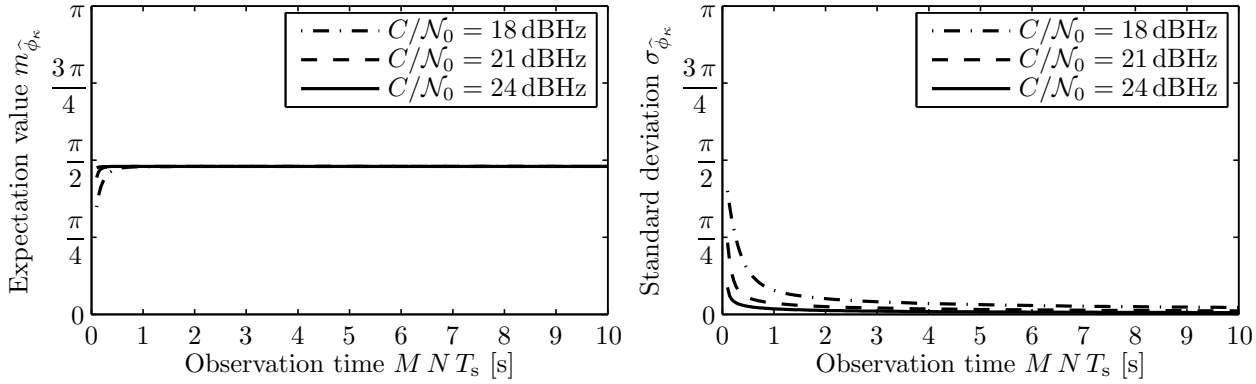

(c) $N\,T_\mathrm{s} = 4\,\mathrm{ms}$ and $f_\mathrm{d} = 60\,\mathrm{Hz}$.

(d) $N\,T_\mathrm{s} = 4\,\mathrm{ms}$ and $f_\mathrm{d} = 60\,\mathrm{Hz}$.

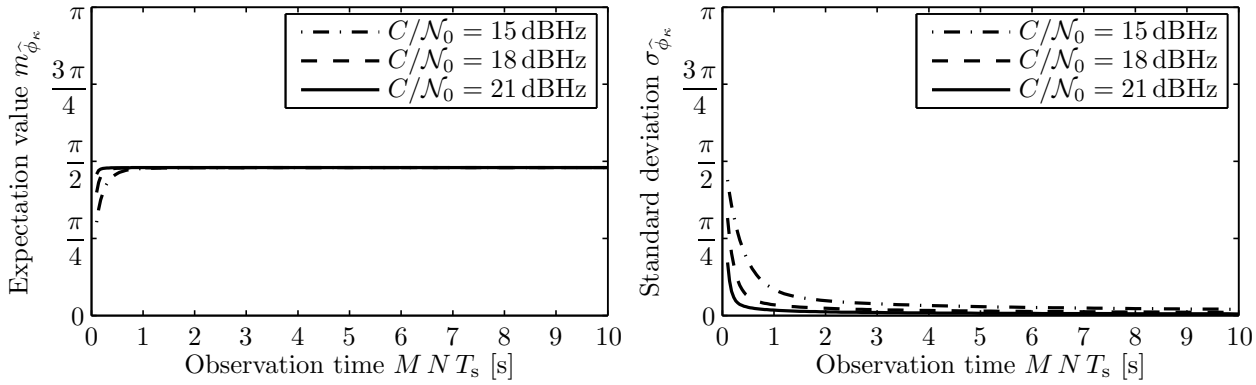

(e) $N\,T_\mathrm{s} = 20\,\mathrm{ms}$ and $f_\mathrm{d} = 12\,\mathrm{Hz}$.

(f) $N\,T_\mathrm{s} = 20\,\mathrm{ms}$ and $f_\mathrm{d} = 12\,\mathrm{Hz}$.

Figure 6.2: Expectation value and standard deviation of the phase mismatch estimation for GPS L1-C/A and Galileo E1-C.

The reception sensitivity achieved by the phase mismatch correction technique is shown in Fig. 6.3. It is presented for GPS and Galileo with $P_\mathrm{d} = 90\,\%$. The minimum carrier-to-noise PSD for methods A and B, $C_{\mathrm{P,A}}/\mathcal{N}_0$ and $C_{\mathrm{P,B}}/\mathcal{N}_0$, are plotted as a function of the observation period. The choice of the receiver parameters $T_0 = 290\,\mathrm{K}$, $F = 3\,\mathrm{dB}$, $P_\mathrm{f} = 10^{-5}$, and $P_\mathrm{d} = 90\,\%$ has been discussed in Section 3.7, while the choice of $K = 10$ has been motivated in Section 5.4. The phase estimation in Fig. 6.2 converges with sufficient accuracy after a certain observation period $M\,N\,T_\mathrm{s}$. The intermediate differential correlation intervals therefore have to be sufficiently long to minimize the impact of the estimation error. The number of phase estimations K in Fig. 6.3 is therefore as previously $K = 10$. The underlying channel model for these simulations introduces a constant frequency deviation

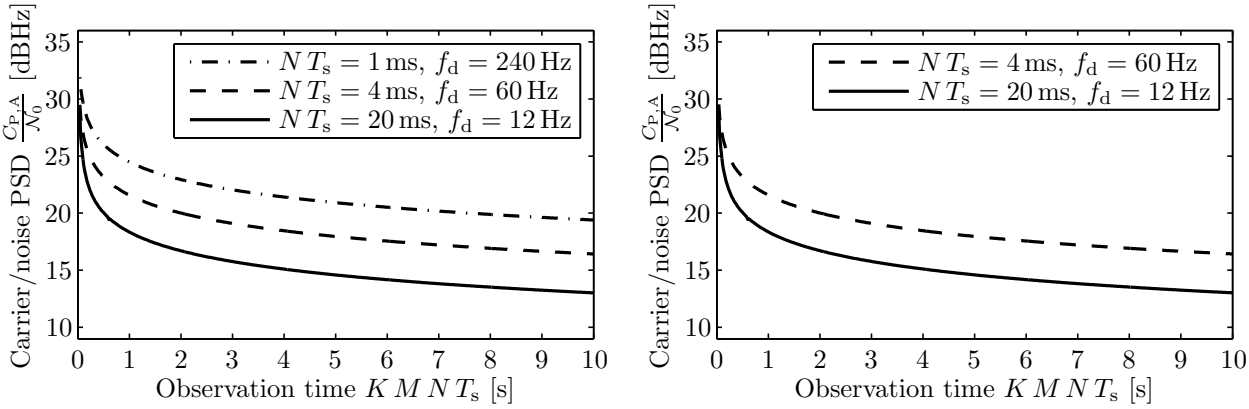

(a) Method A for GPS L1-C/A.

(b) Method A for Galileo E1-C.

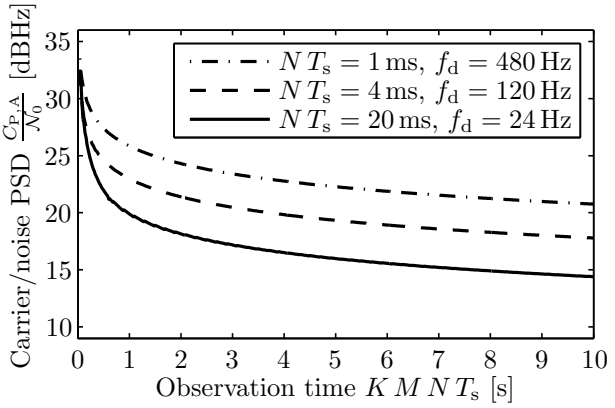

(c) Method A for GPS L1-C/A.

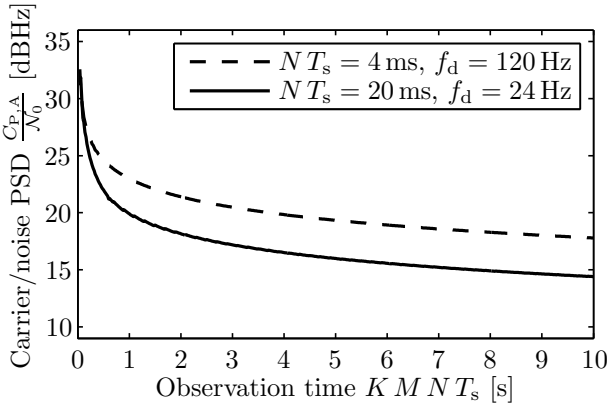

(d) Method A for Galileo E1-C.

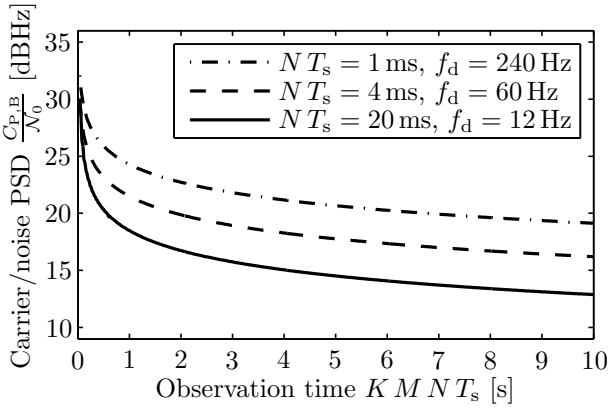

(e) Method B for GPS L1-C/A.

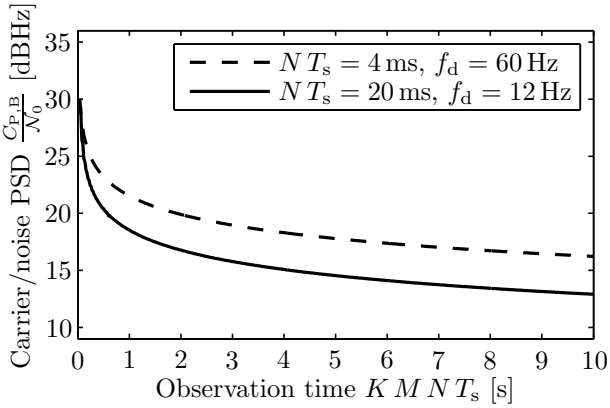

(f) Method B for Galileo E1-C.

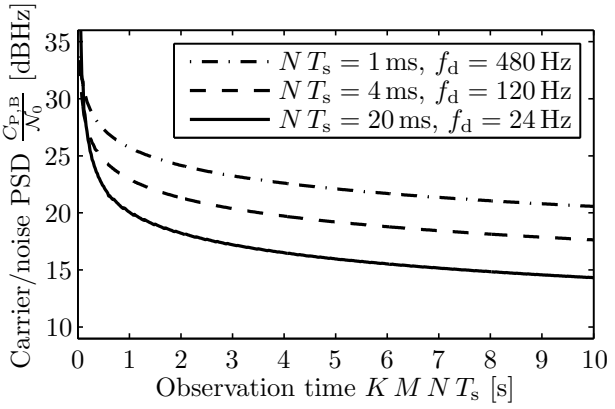

(g) Method B for GPS L1-C/A.

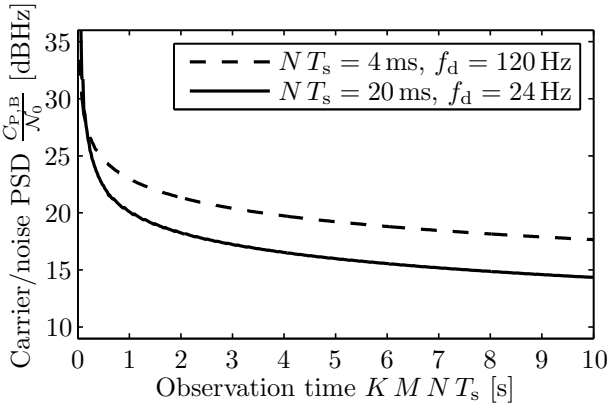

(h) Method B for Galileo E1-C.

Figure 6.3: Reception sensitivity with the phase mismatch correction technique for $T_0 = 290\,\mathrm{K}$, $F = 3\,\mathrm{dB}$, $K = 10$, $P_\mathrm{f} = 10^{-5}$, and $P_\mathrm{d} = 90\,\%$.

f_d. However, the phase mismatch correction technique is also applicable to a dynamically changing frequency offset. If the dynamics are very high, it might be useful to increase the parameter K, in order to partition the observation period into a larger number of phase mismatch correction.

6.4 Sensitivity Gain

The phase mismatch correction method rotates the intermediate differential correlation results towards positive real values, before further accumulating them. This reduces the degradation introduced by the variation of the differential correlation phase. It thus yields a sensitivity gain, which is calculated in this section.

Fig. 6.4 illustrates the sensitivity gain of the phase mismatch correction. The gain for method A, $C_{\mathrm{F,A}}/C_{\mathrm{P,A}}$, and method B, $C_{\mathrm{F,B}}/C_{\mathrm{P,B}}$, is calculated in dB as the difference between the values in Fig. 5.3 and 6.3. It is reduced to 0.7 dB for long observation periods. For short observation periods it can be significantly higher in excess of 1.5 dB, since the frequency correction introduces larger phase fluctuations. For the short observation period of 100 ms, the gain even reaches 8.2 dB with method B. Once the gain has converged it is equal for the different coherent integration intervals. The reason is the same as for the frequency correction in the last chapter. The gain depends on the products $f_\mathrm{d}\,N\,T_\mathrm{s}$ and is higher for larger products. Since these products are equal for the different coherent integration intervals of each plot, the sensitivity gain is also equal. Once converged, the sensitivity gain is furthermore independent of the observation period $K\,M\,N\,T_\mathrm{s}$. The reason for this effect lies in the constant factor K. The simulations in Fig. 6.4 use $K = 10$, which has the effect that the observation period is partitioned into ten intermediate intervals of equal length. The frequency offset and phase mismatch are corrected only after each intermediate interval. The first tenth of the observation period is degraded with the full frequency offset. The cumulative phase correction is the same for all observation periods and each correction acts on equal length intermediate intervals. Since the underlying carrier-to-noise PSD is also lower for longer observation periods, the frequency offset of each subsequent interval is reduced by around the same amount, independent of the length of the total observation period. Hence, the phase fluctuations are around the same and the sensitivity gain is also constant. The reception sensitivity of the phase correction method could be further improved by storing the intermediate differential correlation results and rotating them at the end of the entire observation period with the knowledge of the final accumulated frequency offset estimation.

The cumulative sensitivity gain of the phase mismatch correction technique versus the state-of-the-art noncoherent integration is presented in Fig. 6.5. Subtracting the values in Fig. 6.3 from the values in Fig. 3.14 yields the cumulative gain in dB. The gain for methods A and B, $C_\mathrm{N}/C_{\mathrm{P,A}}$ and $C_\mathrm{N}/C_{\mathrm{P,B}}$, reaches 13.7 dB. This cumulative gain is composed of 1.5 dB from the differential correlation, 10 dB from the adaptive detection threshold, 1.5 dB from the frequency offset correction, and 0.7 dB from the phase mismatch correction.

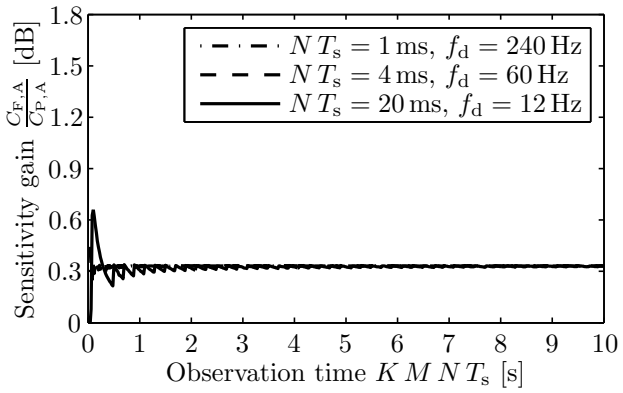

(a) Method A for GPS L1-C/A.

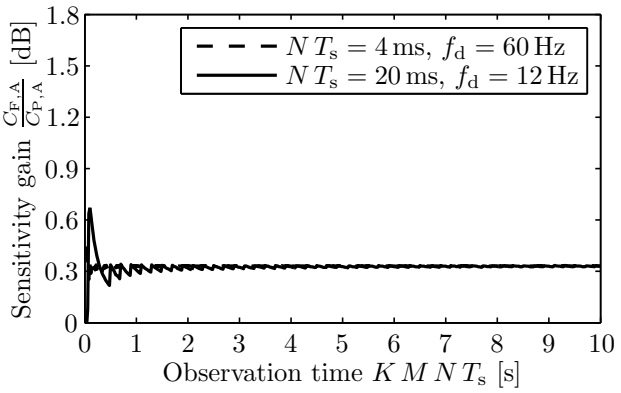

(b) Method A for Galileo E1-C.

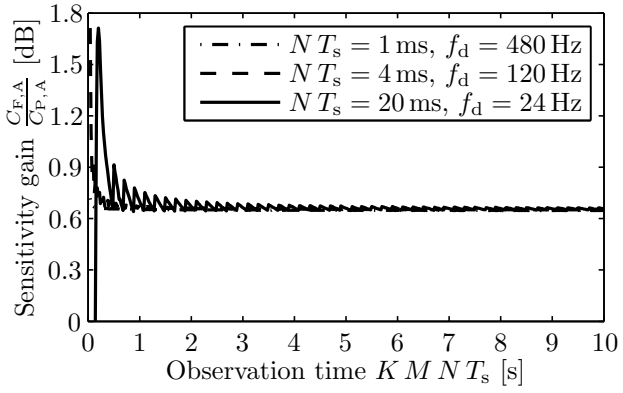

(c) Method A for GPS L1-C/A.

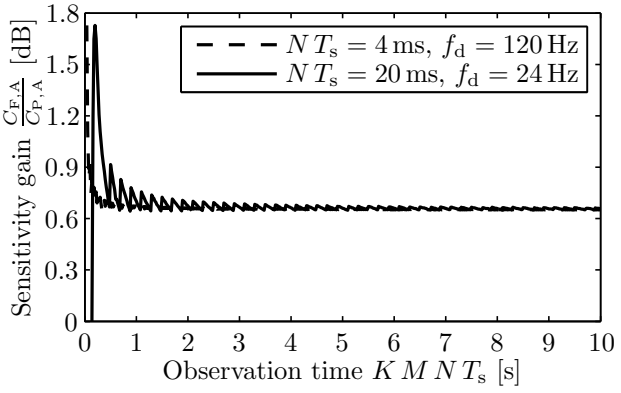

(d) Method A for Galileo E1-C.

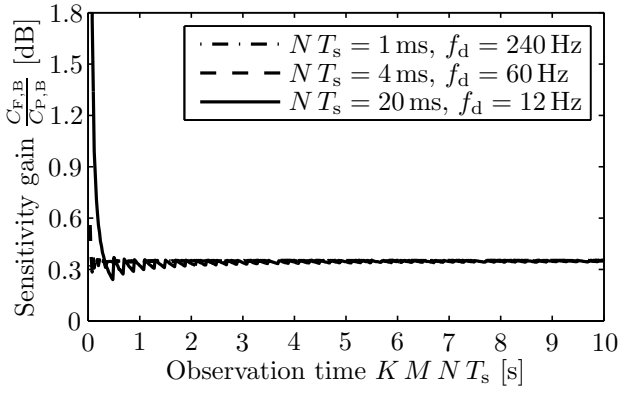

(e) Method B for GPS L1-C/A.

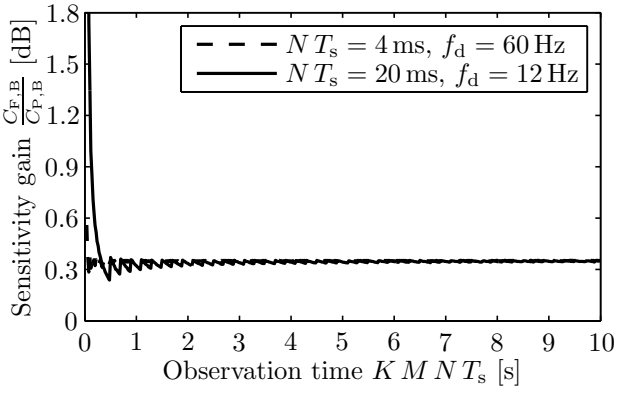

(f) Method B for Galileo E1-C.

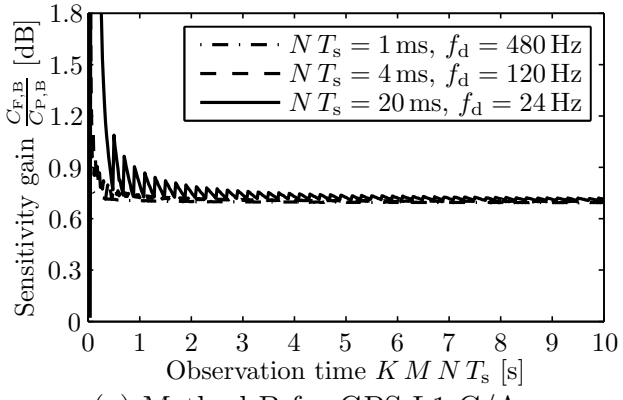

(g) Method B for GPS L1-C/A.

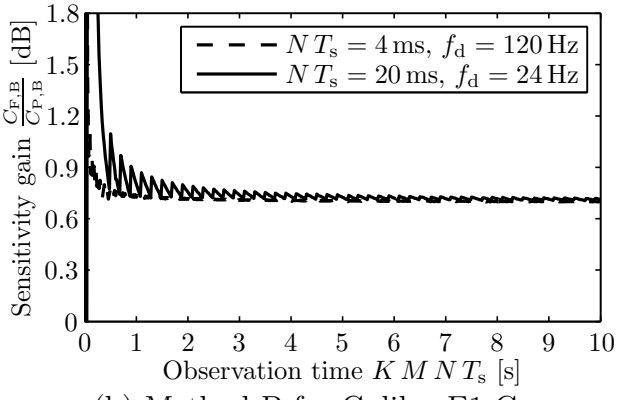

(h) Method B for Galileo E1-C.

Figure 6.4: Sensitivity gain of the phase mismatch correction technique for $T_0 = 290\,\mathrm{K}$, $F = 3\,\mathrm{dB}$, $K = 10$, $P_\mathrm{f} = 10^{-5}$, and $P_\mathrm{d} = 90\,\%$.

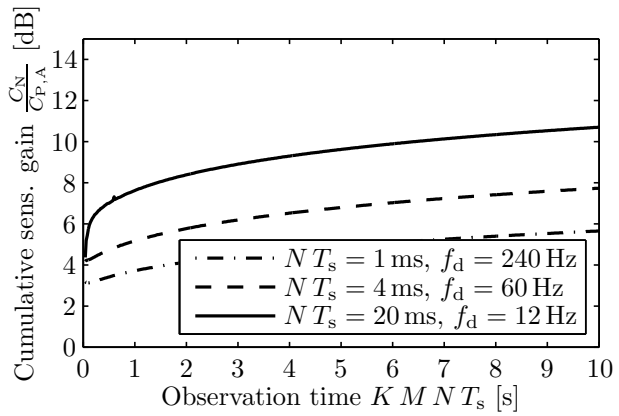

(a) Method A for GPS L1-C/A.

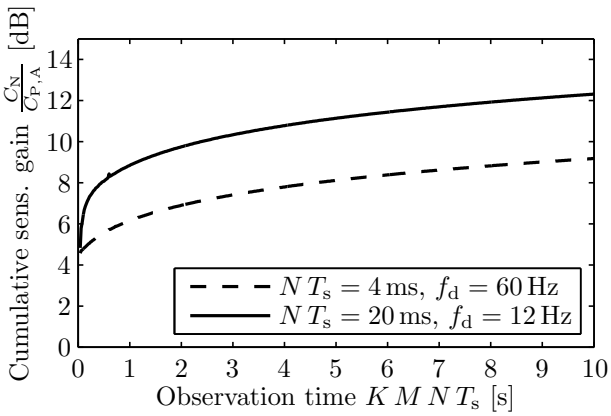

(b) Method A for Galileo E1-C.

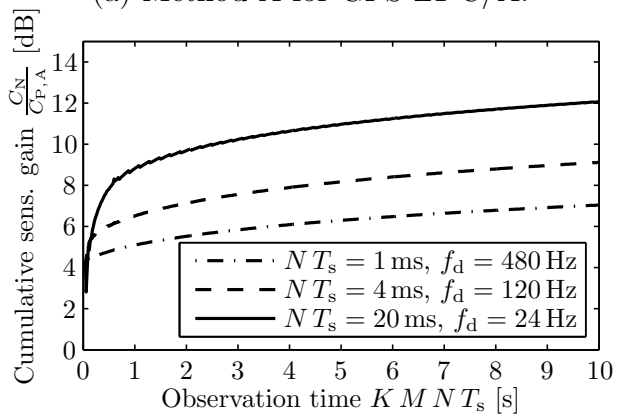

(c) Method A for GPS L1-C/A.

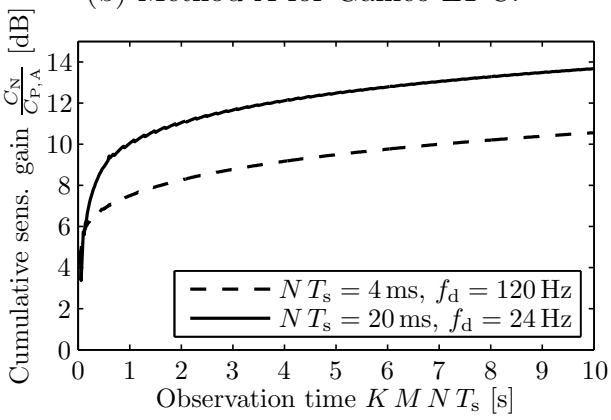

(d) Method A for Galileo E1-C.

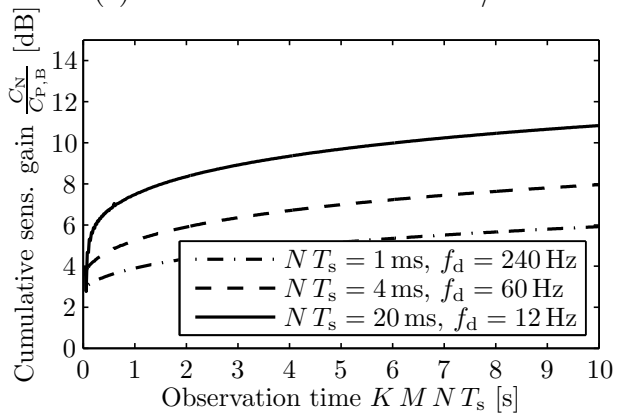

(e) Method B for GPS L1-C/A.

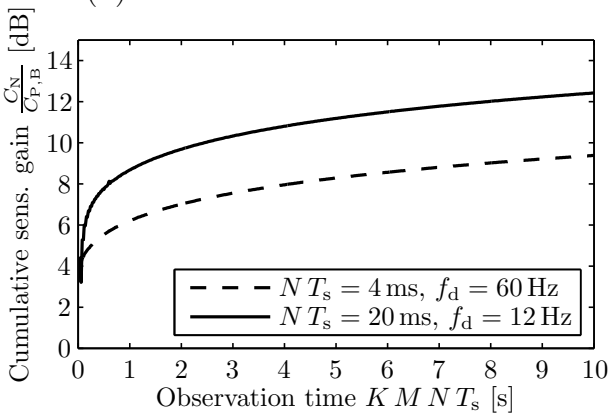

(f) Method B for Galileo E1-C.

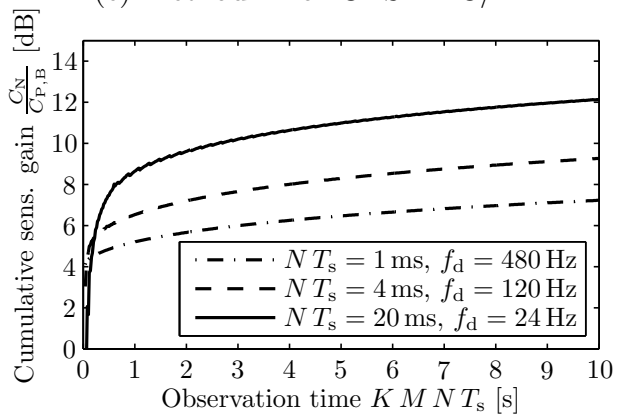

(g) Method B for GPS L1-C/A.

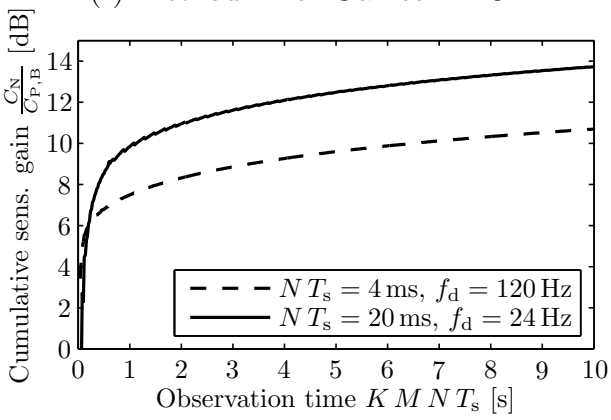

(h) Method B for Galileo E1-C.

Figure 6.5: Cumulative sensitivity gain of the phase mismatch correction technique versus the state-of-the-art noncoherent integration for $T_0 = 290\,\text{K}$, $F = 3\,\text{dB}$, $K = 10$, $P_f = 10^{-5}$, and $P_d = 90\,\%$.

6.5 Positioning Accuracy

The range variance for method A of the phase correction $\sigma^2_{\widehat{\rho},\mathrm{P,A}}$ has already been defined in (5.48) as a function of $\sigma^2_{\Delta,\mathrm{A}}$ and $\partial m_{\Delta,\mathrm{A}}/\partial\tau_\epsilon|_{\tau_\epsilon=0}$. The discrimination variance $\sigma^2_{\Delta,\mathrm{A}}$ is provided in (5.49) as a function of $m_{\Upsilon,\mathrm{E}} = m_\Upsilon|_{\widehat{\tau}=\widehat{\tau}_\mathrm{E}}$, $m_{\Upsilon,\mathrm{L}} = m_\Upsilon|_{\widehat{\tau}=\widehat{\tau}_\mathrm{L}}$, $\sigma^2_{\Upsilon,\mathrm{E}} = \sigma^2_\Upsilon|_{\widehat{\tau}=\widehat{\tau}_\mathrm{E}}$, and $\sigma^2_{\Upsilon,\mathrm{L}} = \sigma^2_\Upsilon|_{\widehat{\tau}=\widehat{\tau}_\mathrm{L}}$, where m_Υ and σ^2_Υ are derived in (6.3) and (5.32). With (5.54), the derivative of the discrimination mean for the adaptive integration technique can be derived as

$$\begin{aligned}\left.\frac{\partial m_{\Delta,\mathrm{A}}}{\partial\tau_\epsilon}\right|_{\tau_\epsilon=0} = &-8\,C\,\sigma_w^2\,R\!\left(\frac{\delta}{2}\right)\frac{N}{\eta\,T_\mathrm{c}}\Bigg[(2M-1)\left[\operatorname{sinc}^2\!(f_{\mathrm{d},0}\,N\,T_\mathrm{s})+\operatorname{sinc}^2\!(f_{\mathrm{d,K}-1}\,N\,T_\mathrm{s})\right]\\ &\qquad+\sum_{\kappa=1}^{K-2}2\,M\operatorname{sinc}^2\!(f_{\mathrm{d},\kappa}\,N\,T_\mathrm{s})\Bigg]\\ &-32\,C^2\,R^3\!\left(\frac{\delta}{2}\right)\frac{N}{\eta\,T_\mathrm{c}}\Bigg|\sum_{\kappa=1}^{K-1}\operatorname{sinc}(f_{\mathrm{d},\kappa}\,N\,T_\mathrm{s})\operatorname{sinc}(f_{\mathrm{d},\kappa-1}\,N\,T_\mathrm{s})\,\mathrm{e}^{\mathrm{j}\,\pi\,(f_{\mathrm{d},\kappa}+f_{\mathrm{d},\kappa-1})\,N\,T_\mathrm{s}-\mathrm{j}\,\widehat{\phi}_\kappa}\\ &\qquad+\sum_{\kappa=0}^{K-1}(M-1)\operatorname{sinc}^2\!(f_{\mathrm{d},\kappa}\,N\,T_\mathrm{s})\,\mathrm{e}^{\mathrm{j}\,2\,\pi\,f_{\mathrm{d},\kappa}\,N\,T_\mathrm{s}-\mathrm{j}\,\widehat{\phi}_\kappa}\Bigg|^2.\end{aligned}\tag{6.9}$$

In the same way, the range variance for method B of the phase correction, $\sigma^2_{\widehat{\rho},\mathrm{P,B}}$ is given in (5.55), with $\sigma^2_{\Delta,\mathrm{B}}$ provided in (5.56) as a function of $\sigma^2_{\Upsilon,\mathrm{I,E}} = \sigma^2_{\Upsilon,\mathrm{I}}|_{\widehat{\tau}=\widehat{\tau}_\mathrm{E}}$ and $\sigma^2_{\Upsilon,\mathrm{I,L}} = \sigma^2_{\Upsilon,\mathrm{I}}|_{\widehat{\tau}=\widehat{\tau}_\mathrm{L}}$. The inphase differential correlation noise variance $\sigma^2_{\Upsilon,\mathrm{I}}$ is derived in (6.4). Finally, the derivative of the discrimination function for method B is obtained from (5.59) and (6.3) as

$$\begin{aligned}\frac{\partial m_{\Delta,\mathrm{B}}}{\partial\tau_\epsilon} = &-8\,C\,R\!\left(\frac{\delta}{2}\right)\frac{N}{\eta\,T_\mathrm{c}}\Bigg[\sum_{\kappa=0}^{K-1}(M-1)\operatorname{sinc}^2\!(f_{\mathrm{d},\kappa}\,N\,T_\mathrm{s})\,\cos(2\,\pi\,f_{\mathrm{d},\kappa}\,N\,T_\mathrm{s}-\widehat{\phi}_\kappa)\\ &+\sum_{\kappa=1}^{K-1}\operatorname{sinc}(f_{\mathrm{d},\kappa}\,N\,T_\mathrm{s})\operatorname{sinc}(f_{\mathrm{d},\kappa-1}\,N\,T_\mathrm{s})\,\cos(\pi\,(f_{\mathrm{d},\kappa}+f_{\mathrm{d},\kappa-1})\,N\,T_\mathrm{s}-\widehat{\phi}_\kappa)\Bigg].\end{aligned}\tag{6.10}$$

Fig. 6.6 shows the standard deviations of the estimated ranges $\sigma_{\widehat{\rho},\mathrm{P,A}}$ and $\sigma_{\widehat{\rho},\mathrm{P,B}}$. The parameters $T_0 = 290\,\mathrm{K}$ and $F = 3\,\mathrm{dB}$ are motivated in Section 3.7, the parameter $K = 10$ in Section 5.4, and the parameters $\delta = 1/B$ and $B = 4.092\,\mathrm{MHz}$ in Section 3.14. In order to allow comparison with the previous results, the range estimation accuracies in Fig. 6.6 are also calculated for the common baseline $C_\mathrm{N}/\mathcal{N}_0$ values of Fig. 3.14.

6.6 Accuracy Improvement

Since the phase mismatch correction reduces the degradation of the correlation result, the correlation peak becomes larger in relation to the correlation noise. This improves the code discrimination and thus increases the ranging accuracy. The relative accuracies between the phase mismatch correction and the frequency offset correction, $\sigma_{\widehat{\rho},\mathrm{F,A}}/\sigma_{\widehat{\rho},\mathrm{P,A}}$ and $\sigma_{\widehat{\rho},\mathrm{F,B}}/\sigma_{\widehat{\rho},\mathrm{P,B}}$, are presented in Fig. 6.7. They are found by dividing the values of Fig. 5.6 by the values

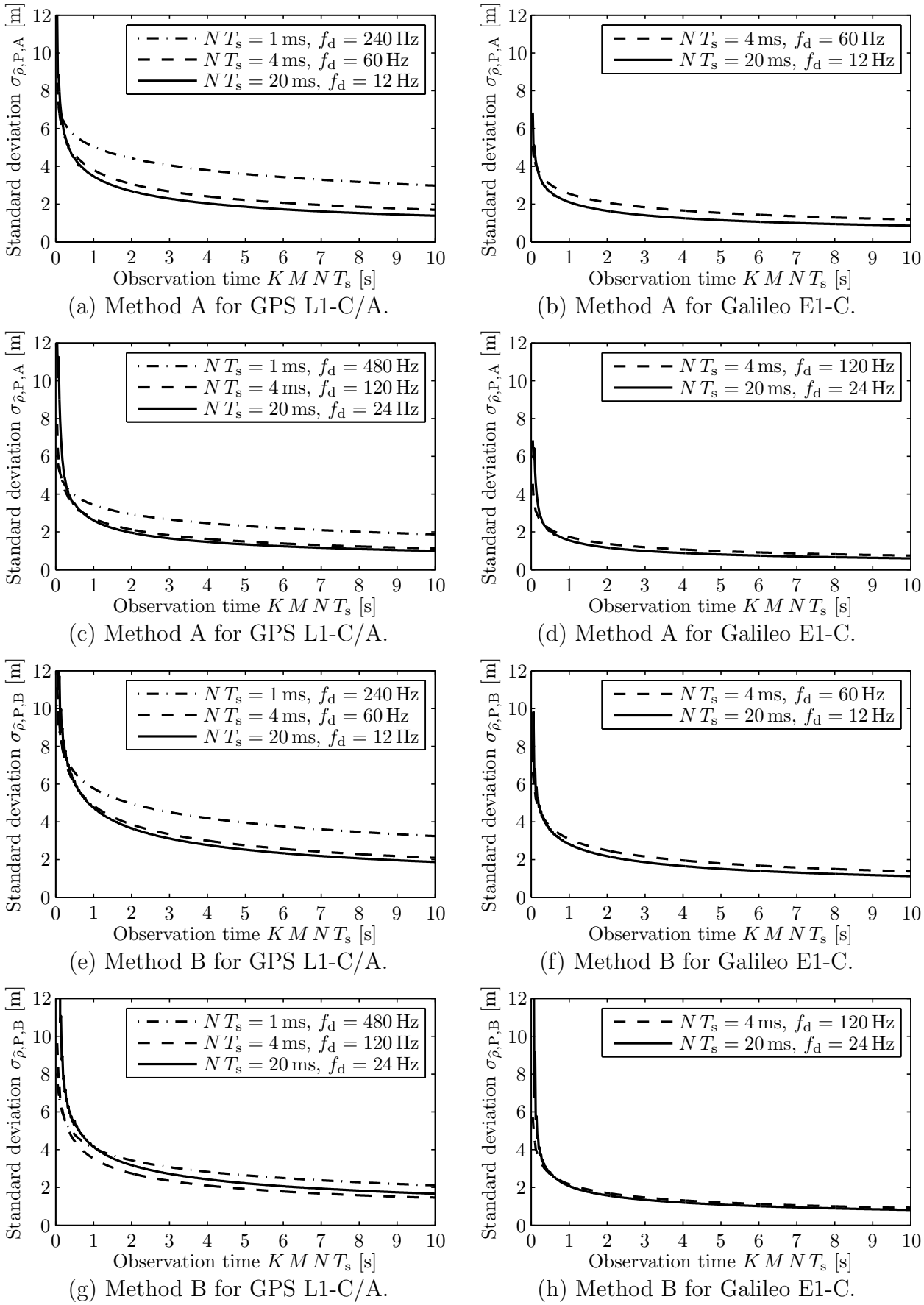

(a) Method A for GPS L1-C/A.
(b) Method A for Galileo E1-C.
(c) Method A for GPS L1-C/A.
(d) Method A for Galileo E1-C.
(e) Method B for GPS L1-C/A.
(f) Method B for Galileo E1-C.
(g) Method B for GPS L1-C/A.
(h) Method B for Galileo E1-C.

Figure 6.6: Range estimation accuracy with the phase mismatch correction technique for $T_0 = 290\,\mathrm{K}$, $F = 3\,\mathrm{dB}$, $K = 10$, $\delta = 1/B$, and $B = 4.092\,\mathrm{MHz}$.

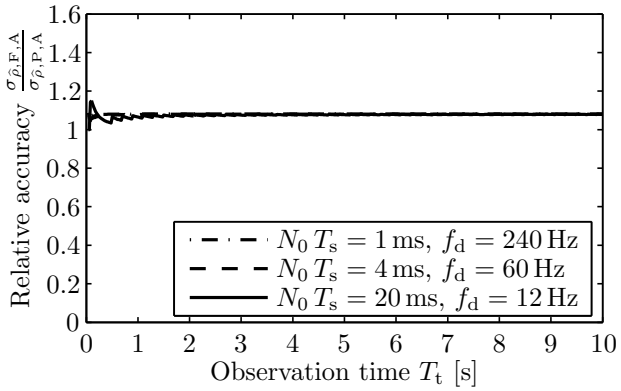

(a) Method A for GPS L1-C/A.

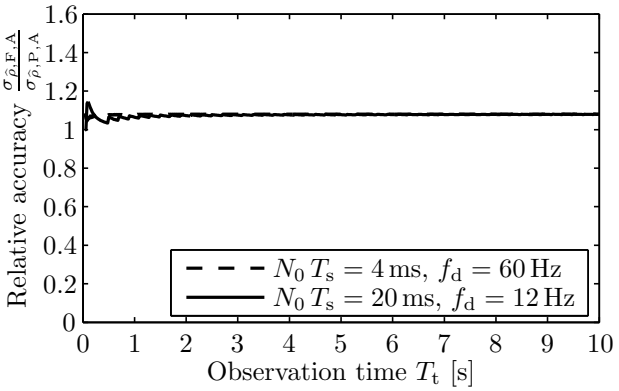

(b) Method A for Galileo E1-C.

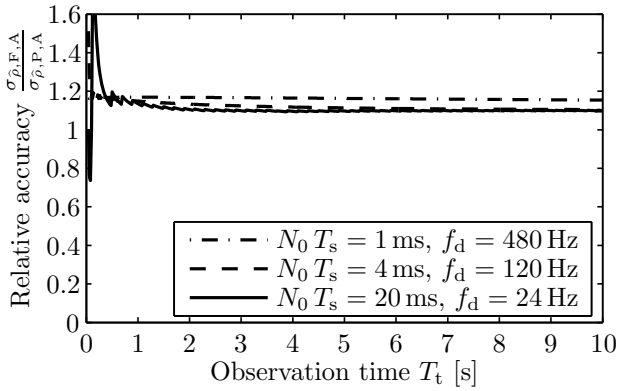

(c) Method A for GPS L1-C/A.

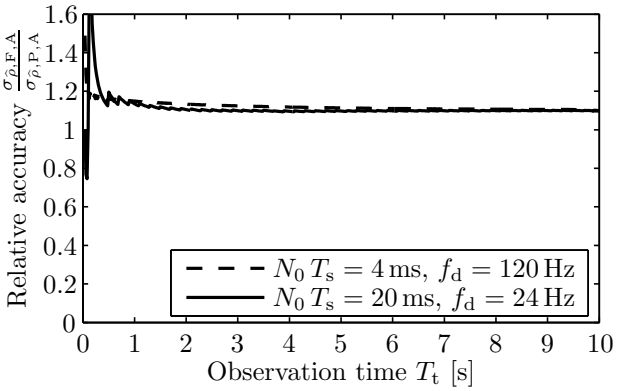

(d) Method A for Galileo E1-C.

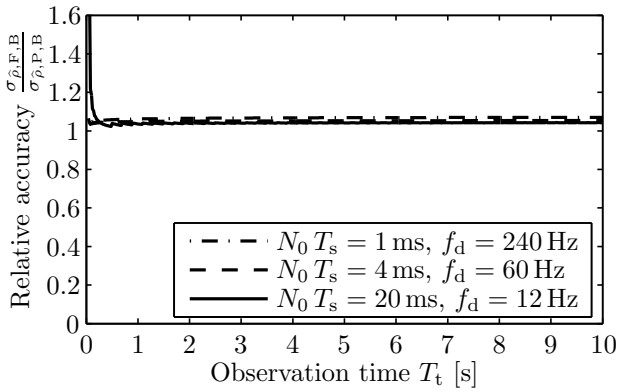

(e) Method B for GPS L1-C/A.

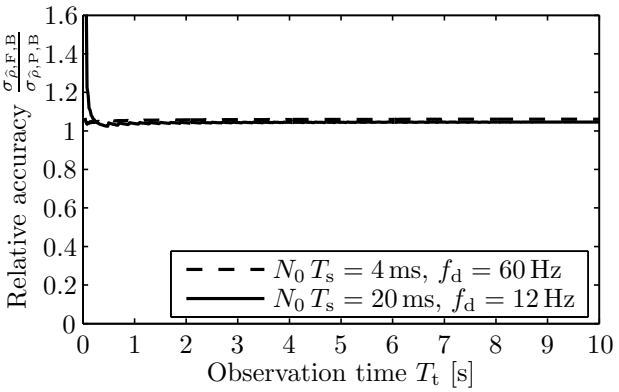

(f) Method B for Galileo E1-C.

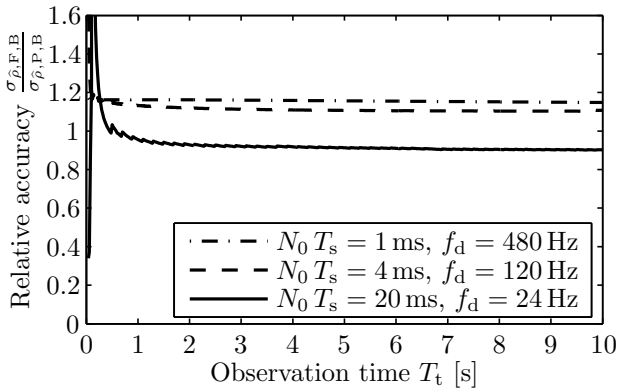

(g) Method B for GPS L1-C/A.

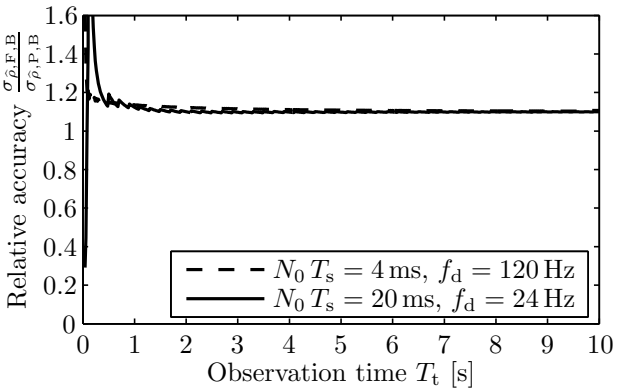

(h) Method B for Galileo E1-C.

Figure 6.7: Accuracy improvement of the phase mismatch correction technique for $T_0 = 290\,\mathrm{K}$, $F = 3\,\mathrm{dB}$, $K = 10$, $\delta = 1/B$, and $B = 4.092\,\mathrm{MHz}$.

of Fig. 6.6. Both methods, A and B, deliver an accuracy improvement of 15 % for long observation periods. It is thereby very stable over the range of observation periods. The accuracy gain exceeds 60 % for very short observation periods.

The cumulative relative accuracy of the phase mismatch correction technique versus the state-of-the-art noncoherent integration is shown in Fig. 6.8. The ratios $\sigma_{\hat{\rho},\mathrm{N}}/\sigma_{\hat{\rho},\mathrm{P,A}}$ and $\sigma_{\hat{\rho},\mathrm{N}}/\sigma_{\hat{\rho},\mathrm{P,B}}$ are thereby calculated based on the values in Fig. 3.21 and 6.6. The differential correlation improves the accuracy by 80 % and the frequency offset correction by 62 % for method A and 44 % for method B. The phase mismatch correction therefore improves the accuracy of the estimated ranges by as much as $1.8 \times 1.62 \times 1.15 - 1 = 235\,\%$ for method A and $1.8 \times 1.44 \times 1.15 - 1 = 198\,\%$ for method B.

6.7 Conclusion

The presented technique adaptively reduces the phase mismatch of the intermediate differential correlation results. The phase of the complex-valued differential correlation result is proportional to the residual frequency deviation and the coherent integration time. The underlying channel model for the simulations of this chapter incorporates a constant frequency offset, although the presented technique is also applicable to a dynamically changing frequency deviation. The frequency offset correction method presented in Chapter 5 incrementally reduces the residual frequency deviation. This leads to a fluctuation of the phase of the intermediate differential correlation results. The *phase mismatch correction* method of this chapter therefore adaptively realigns the correlation phases to improve the final differential correlation result. The analysis of this chapter shows that the phase mismatch correction method enhances the reception sensitivity by 0.7 dB for long observation periods and substantially more in excess of 1.5 dB for short observation periods. It adds up to a cumulative sensitivity gain versus the state-of-the noncoherent integration of 13.7 dB. The same sensitivity enhancement can also be achieved by just evaluating the inphase component of the final differential correlation result. This simplifies the hardware and software implementation considerably with the benefit of reduced implementation costs and power consumption. The reduction of the phase mismatch furthermore enables the adaptive integration technique of the next chapter, which yields a large sensitivity gain of 7.1 dB. The phase mismatch correction can also improve the positioning accuracy. The accuracy of the estimated satellite-receiver range can be increased by 15 %, which yields an improvement of the ranging accuracy versus the state-of-the-art noncoherent integration of 236 %. If just the inphase result is processed, the range accuracy is also increased by 15 % and a cumulative enhancement of 198 % when compared to the state-of-the-art results is achieved. The sensitivity and accuracy improvements in the presented simulations are not very large. This is the case for a constant frequency offset as it is simulated here. In case of a dynamically changing frequency deviation, e.g. from user motion or a drifting local oscillator, the sensitivity gain is substantially higher. The phase mismatch correction is furthermore necessary for the *adaptive integration interval* technique of the next chapter. The adaptive integration yields a very large sensitivity gain, but also causes very large phase fluctuations. It relies on the phase mismatch correction to realign the intermediate correlation results.

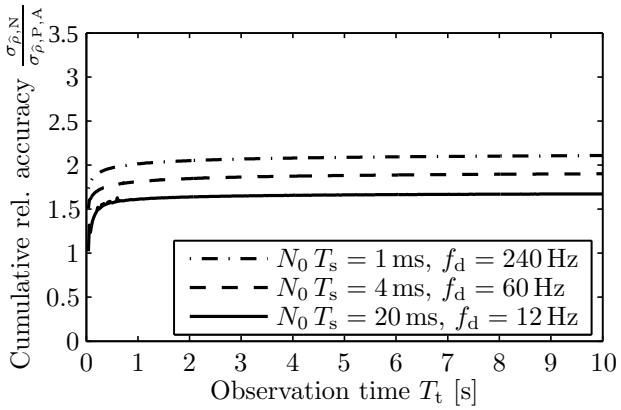

(a) Method A for GPS L1-C/A.

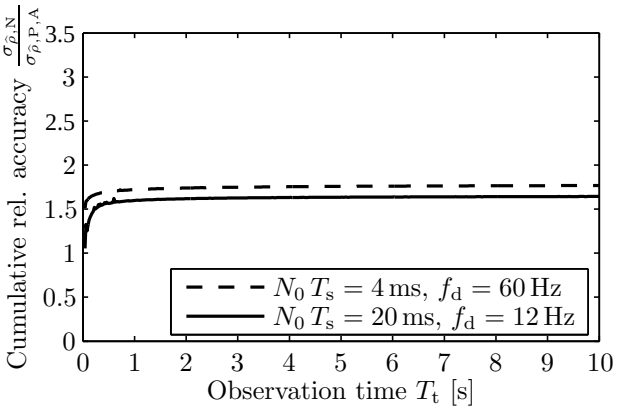

(b) Method A for Galileo E1-C.

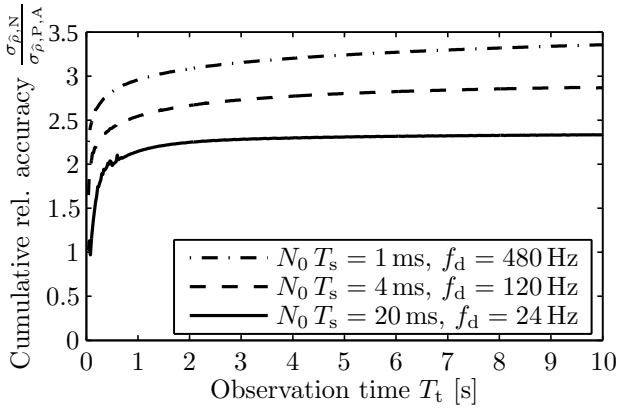

(c) Method A for GPS L1-C/A.

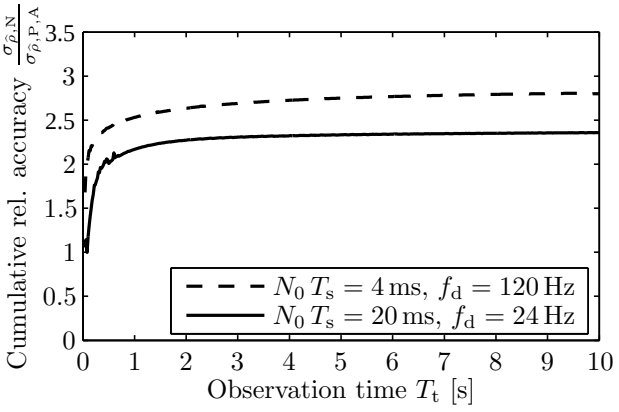

(d) Method A for Galileo E1-C.

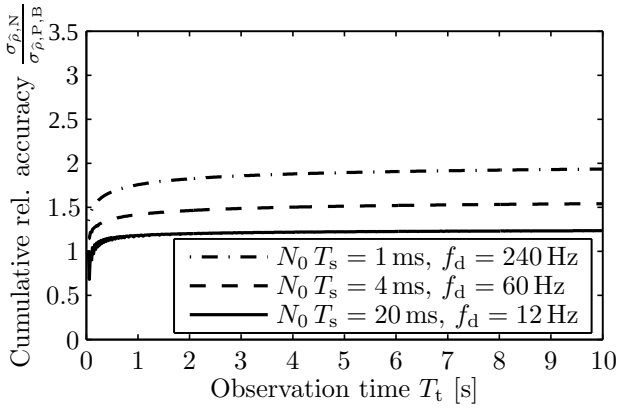

(e) Method B for GPS L1-C/A.

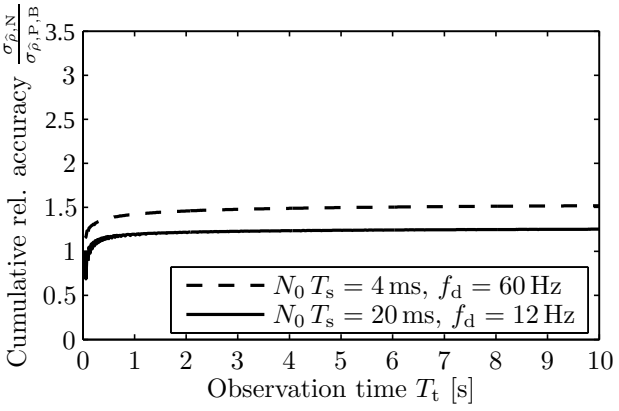

(f) Method B for Galileo E1-C.

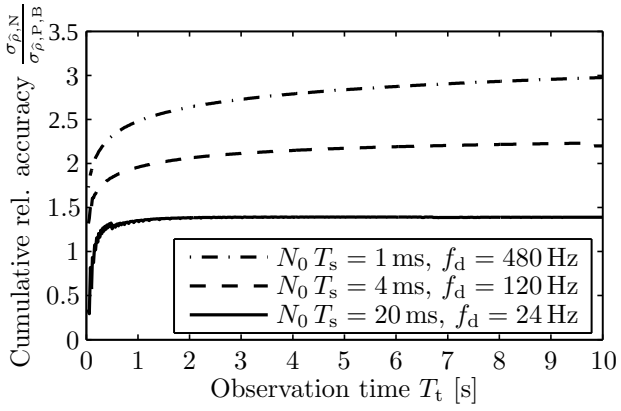

(g) Method B for GPS L1-C/A.

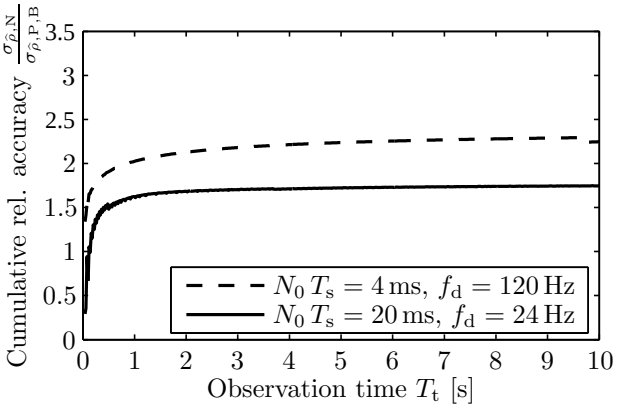

(h) Method B for Galileo E1-C.

Figure 6.8: Cumulative accuracy improvement of the phase mismatch correction technique versus the state-of-the-art noncoherent integration for $T_0 = 290\,\mathrm{K}$, $F = 3\,\mathrm{dB}$, $K = 10$, $\delta = 1/B$, and $B = 4.092\,\mathrm{MHz}$.

Chapter 7

Adaptive Integration Interval

The maximum coherent integration period is inversely proportional to the maximum frequency deviation. The higher the residual frequency deviation, the faster the signal phase rotates during the coherent integration process. The further the phase rotates during the coherent integration interval, the larger the sensitivity degradation when the samples are accumulated. The *frequency offset correction* of Chapter 5 incrementally reduces the residual frequency deviation. It is therefore also possible to incrementally increase the coherent integration period while the differential correlation process is still ongoing.

The *adaptive integration interval* technique of this chapter waits until the frequency correction has sufficiently converged. It increases the coherent integration period once the residual frequency deviation is sufficiently small. The reception sensitivity is thereby enhanced, since the coherent integration provides a higher correlation gain than the differential correlation. In case the frequency deviation increases again, the adaptive technique reduces the coherent integration interval.

7.1 Integration Number Adjustment

Adjusting the coherent integration interval as a function of the frequency deviation implies a transformation of the coherent integration number N to a time-variant variable N_κ. The intermediate correlation number M determines the accuracy of the frequency offset estimation and is also transformed into a time-variant variable M_κ, such that it can be adjusted as a function of N_κ. The signal flow diagram for the adaptive integration technique is presented in Fig. 7.1. When compared to the signal processing chain of the phase mismatch correction in Fig. 6.1, the additional block to calculate the integration numbers N_κ and M_κ becomes apparent. It bases its adjustment on the feedback path for the estimated phase $\widehat{\phi}_\kappa$.

In Chapter 5, an estimation method for the residual frequency deviation $f_{\mathrm{d},\mu}$ in the range $[-1/(2\,N_\kappa\,T_\mathrm{s}),\ 1/(2\,N_\kappa\,T_\mathrm{s})]$ is derived and analyzed. Modifying (5.4) yields

$$\widehat{f}_{\mathrm{d},\kappa} = \frac{\arg(\Psi_\kappa)}{2\,\pi\,N_\kappa\,T_\mathrm{s}} = \frac{\arg\left(\sum\limits_{\mu=W_\kappa+1}^{W_{\kappa+1}-1} s_\mu\,s_{\mu-1}^*\right)}{2\,\pi\,N_\kappa\,T_\mathrm{s}} \tag{7.1}$$

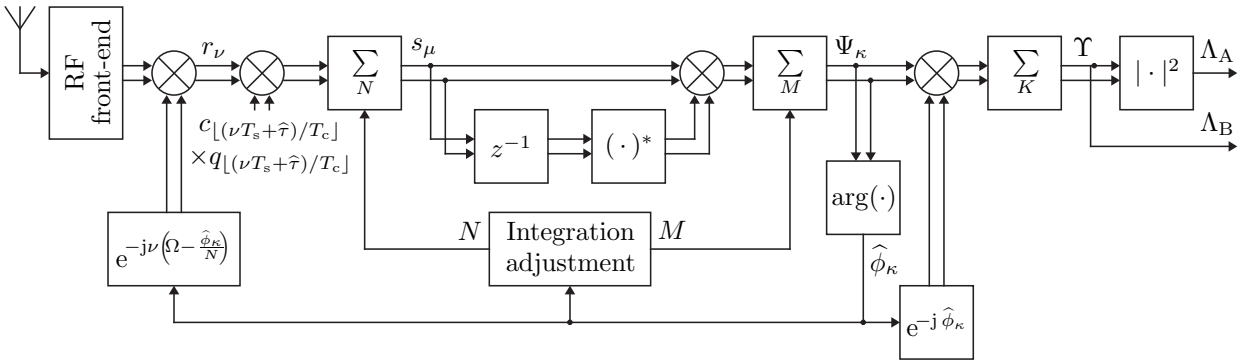

Figure 7.1: Receiver channel with the adaptive integration interval technique.

with the cumulative intermediate differential correlation number

$$W_{\kappa+1} = W_\kappa + M_\kappa \;, \quad W_0 = 0 \;. \tag{7.2}$$

Fig. 5.2 provides an overview of the frequency offset estimation accuracy. The initial intermediate correlation number M_0 has to be large enough to provide sufficiently long observation periods for the frequency offset estimation. This improves the estimation accuracy. Furthermore, the coherent integration number N_κ is only increased once the estimation of the frequency deviation has converged with sufficient accuracy. The next coherent integration number is then calculated as

$$\boxed{N_{\kappa+1} = \begin{cases} N_{\min} & ;\ \left\lfloor \frac{1}{8\,\widehat{f}_{\mathrm{d},\kappa}\,N_{\min}\,T_\mathrm{s}} \right\rfloor \leqslant 1 \\ \left\lfloor \frac{1}{8\,\widehat{f}_{\mathrm{d},\kappa}\,N_{\min}\,T_\mathrm{s}} \right\rfloor N_{\min} & ;\ 1 < \left\lfloor \frac{1}{8\,\widehat{f}_{\mathrm{d},\kappa}\,N_{\min}\,T_\mathrm{s}} \right\rfloor < \frac{N_{\max}}{N_{\min}} \\ N_{\max} & ;\ \text{else} \end{cases}} \;, \tag{7.3}$$

whereby the floor operation $\lfloor\cdot\rfloor$ rounds to the nearest integer smaller or equal to the argument. The minimum coherent integration number $N_{\min}$ ensures that at least one full code cycle is used for correlation. It is set to $1\,\mathrm{ms}/T_\mathrm{s}$ for GPS L1-C/A and $4\,\mathrm{ms}/T_\mathrm{s}$ for Galileo E1-C. The maximum coherent integration number $N_{\max}$ limits the coherent integration interval to the expected coherence time of the propagation channel. It should be chosen according to the Doppler spread, which is influenced by the dynamics of the receiver movement [75]. The coherence time is a statistical measure of the time duration over which the propagation channel is essentially invariant. A reasonable value of $N_{\max}$ for a static pedestrian receiver is $100\,\mathrm{ms}/T_\mathrm{s}$. The coherent integration number N_κ in (7.3) is only increased if the estimated frequency deviation is smaller than a quarter of the estimation range. Otherwise, the coherent integration period is decreased again. This case could happen for large estimation errors or if the frequency deviation varies due to fast receiver movement. The generous back-tracking property of (7.3) leads to a quick recovery from such situations.

In order to keep the total intermediate observation time $M_\kappa\,N_\kappa$ for the frequency offset estimation stable, the intermediate differential correlation number is set to

$$\boxed{M_{\kappa+1} = \begin{cases} 2 & ;\ \left\langle \frac{M_0\,N_0}{N_{\kappa+1}} \right\rangle \leqslant 2 \\ \left\langle \frac{M_0\,N_0}{N_{\kappa+1}} \right\rangle & ;\ \text{else} \end{cases}} \;, \tag{7.4}$$

with $\langle\cdot\rangle$ representing the rounding operation. As shown in Fig. 7.1, the final differential correlation result is denoted as Υ. From (3.38), (3.39), and (6.3), the expectation value of Υ for the adaptive integration interval method is derived as

$$\begin{aligned} m_\Upsilon &= \mathrm{E}\{\Upsilon\} \\ &= 2\,C\,\frac{R_0^2(\tau-\widehat{\tau})}{N_0^2}\left[\sum_{\kappa=0}^{K-1}(M_\kappa-1)\,N_\kappa^2\,\mathrm{sinc}^2(f_{\mathrm{d},\kappa}\,N_\kappa\,T_\mathrm{s})\,\mathrm{e}^{\mathrm{j}\,2\,\pi\,f_{\mathrm{d},\kappa}\,N_\kappa\,T_\mathrm{s}-\mathrm{j}\,\widehat{\phi}_\kappa}\right. \\ &\quad\left.+\sum_{\kappa=1}^{K-1}N_\kappa\,N_{\kappa-1}\,\mathrm{sinc}(f_{\mathrm{d},\kappa}\,N_\kappa\,T_\mathrm{s})\,\mathrm{sinc}(f_{\mathrm{d},\kappa-1}\,N_{\kappa-1}\,T_\mathrm{s})\,\mathrm{e}^{\mathrm{j}\,\pi\,(f_{\mathrm{d},\kappa}\,N_\kappa+f_{\mathrm{d},\kappa-1}\,N_{\kappa-1})\,T_\mathrm{s}-\mathrm{j}\,\widehat{\phi}_\kappa}\right]. \end{aligned} \tag{7.5}$$

where $R_0^2(\tau-\widehat{\tau})$ denotes the correlation function for the coherent integration number N_0 as specified in (3.28). With (3.42), (3.43), (3.51), and (5.32), the derivation of the combined variance of the inphase and quadrature components yields

$$\begin{aligned} \sigma_\Upsilon^2 &= \mathrm{E}\{|\Upsilon-\mathrm{E}\{\Upsilon\}|^2\} \\ &= \sum_{\kappa=0}^{K-1}(M_\kappa-1)\,\sigma_{w,\kappa}^4+\sum_{\kappa=1}^{K-1}\sigma_{w,\kappa}^2\,\sigma_{w,\kappa-1}^2 \\ &\quad+2\,C\,\frac{R_0^2(\tau-\widehat{\tau})}{N_0^2}\left[\sum_{\kappa=0}^{K-1}2\,(M_\kappa-1)\,\sigma_{w,\kappa}^2\,N_\kappa^2\,\mathrm{sinc}^2(f_{\mathrm{d},\kappa}\,N\,T_\mathrm{s})\right. \\ &\quad\left.+\sum_{\kappa=0}^{K-2}\sigma_{w,\kappa}^2\,N_{\kappa+1}^2\,\mathrm{sinc}^2(f_{\mathrm{d},\kappa+1}\,N\,T_\mathrm{s})+\sum_{\kappa=1}^{K-1}\sigma_{w,\kappa}^2\,N_{\kappa-1}^2\,\mathrm{sinc}^2(f_{\mathrm{d},\kappa-1}\,N\,T_\mathrm{s})\right] \end{aligned} \tag{7.6}$$

where the predetection noise variance

$$\sigma_{w,\kappa}^2 = 2\,N_\kappa\,k\,T_0\,B\,F \tag{7.7}$$

follows from (3.19). If only the inphase path is to be evaluated, a modification of (5.35) yields the variance of the inphase component of the differential correlation noise

$$\begin{aligned} \sigma_{\Upsilon,\mathrm{I}}^2 &= \mathrm{E}\{\Re\{\Upsilon-\mathrm{E}\{\Upsilon\}\}^2\} \\ &= \sum_{\kappa=0}^{K-1}\frac{(M_\kappa-1)\,\sigma_{w,\kappa}^4}{2}+\sum_{\kappa=1}^{K-1}\frac{\sigma_{w,\kappa}^2\,\sigma_{w,\kappa-1}^2}{2} \\ &\quad+C\,\frac{R_0^2(\tau-\widehat{\tau})}{N_0^2}\left[\sigma_{w,0}^2\,N_0^2\,\mathrm{sinc}^2(f_{\mathrm{d},0}\,N_0\,T_\mathrm{s})+\sigma_{w,K-1}^2\,N_{K-1}^2\,\mathrm{sinc}^2(f_{\mathrm{d},K-1}\,N_{K-1}\,T_\mathrm{s})\right. \\ &\quad+\sum_{\kappa=0}^{K-1}4\,(M_\kappa-2)\,\sigma_{w,\kappa}^2\,N_\kappa^2\,\mathrm{sinc}^2(f_{\mathrm{d},\kappa}\,N_\kappa\,T_\mathrm{s})\cos^2(2\,\pi\,f_{\mathrm{d},\kappa}\,N_\kappa\,T_\mathrm{s}-\widehat{\phi}_\kappa) \\ &\quad+\sum_{\kappa=0}^{K-2}\sigma_{w,\kappa}^2\left|N_{\kappa+1}\,\mathrm{sinc}(f_{\mathrm{d},\kappa+1}\,N_{\kappa+1}\,T_\mathrm{s})+N_\kappa\,\mathrm{sinc}(f_{\mathrm{d},\kappa}\,N_\kappa\,T_\mathrm{s})\,\mathrm{e}^{\mathrm{j}\,\pi\,(f_{\mathrm{d},\kappa+1}\,N_{\kappa+1}+3\,f_{\mathrm{d},\kappa}\,N_\kappa)\,T_\mathrm{s}-\mathrm{j}\,\widehat{\phi}_\kappa}\right|^2 \\ &\quad\left.+\sum_{\kappa=1}^{K-1}\sigma_{w,\kappa}^2\left|N_\kappa\,\mathrm{sinc}(f_{\mathrm{d},\kappa}\,N_\kappa\,T_\mathrm{s})+N_{\kappa-1}\,\mathrm{sinc}(f_{\mathrm{d},\kappa-1}\,N_{\kappa-1}\,T_\mathrm{s})\,\mathrm{e}^{\mathrm{j}\,\pi\,(3\,f_{\mathrm{d},\kappa}\,N_\kappa+f_{\mathrm{d},\kappa-1}\,N_{\kappa-1})\,T_\mathrm{s}-\mathrm{j}\,\widehat{\phi}_\kappa}\right|^2\right]. \end{aligned} \tag{7.8}$$

7.2 Reception Sensitivity

The reception sensitivity is again calculated for the two different decision statistics. The squared magnitude

$$\boxed{\Lambda_{\mathrm{A}} = |\Upsilon|^2 = \left| \sum_{\kappa=0}^{K-1} \sum_{\mu=W_\kappa}^{W_{\kappa+1}-1} s_\mu \, s_{\mu-1}^* \, \mathrm{e}^{-\mathrm{j}\,\widehat{\phi}_\kappa} \right|^2} \tag{7.9}$$

with $s_{-1} = 0$ is used for method A and the inphase component

$$\boxed{\Lambda_{\mathrm{B}} = \Re\{\Upsilon\} = \Re\left\{ \sum_{\kappa=0}^{K-1} \sum_{\mu=W_\kappa}^{W_{\kappa+1}-1} s_\mu \, s_{\mu-1}^* \, \mathrm{e}^{-\mathrm{j}\,\widehat{\phi}_\kappa} \right\}} \tag{7.10}$$

is used for method B.

As before, the detection threshold for method A, λ_{A}, is calculated with (5.38) by inserting $m_{\Upsilon,\mathrm{H}_0} = m_\Upsilon|_{R^2(\tau-\widehat{\tau})=R_{\mathrm{m}}^2}$ and $\sigma^2_{\Upsilon,\mathrm{H}_0} = \sigma^2_\Upsilon|_{R^2(\tau-\widehat{\tau})=R_{\mathrm{m}}^2}$ as specified in (7.5) and (7.6). The corresponding probability of detection $P_{\mathrm{d,A}}$ is then obtained from (5.40) by inserting $m_{\Upsilon,\mathrm{H}_1} = m_\Upsilon|_{R^2(\tau-\widehat{\tau})=N^2}$ and $\sigma^2_{\Upsilon,\mathrm{H}_1} = \sigma^2_\Upsilon|_{R^2(\tau-\widehat{\tau})=N^2}$. Similarly, the detection threshold for method B, λ_{B}, is calculated with (5.44), where $\sigma^2_{\Upsilon,\mathrm{I},\mathrm{H}_0} = \sigma^2_{\Upsilon,\mathrm{I}}|_{R^2(\tau-\widehat{\tau})=R_{\mathrm{m}}^2}$ is provided in (7.8). This yields the probability of detection $P_{\mathrm{d,B}}$ with (5.45) by inserting $\sigma^2_{\Upsilon,\mathrm{I},\mathrm{H}_1} = \sigma^2_{\Upsilon,\mathrm{I}}|_{R^2(\tau-\widehat{\tau})=N^2}$.

Chapter 3 introduces the differential correlation method, Chapter 4 the adaptive detection threshold, Chapter 5 the frequency offset correction, Chapter 6 the phase mismatch correction, and this chapter the adaptive integration interval. The reception sensitivity for $P_{\mathrm{d}} = 90\,\%$ of all these techniques combined is illustrated in Fig. 7.2. It shows the minimum carrier-to-noise PSD for method A, $C_{\mathrm{I,A}}/\mathcal{N}_0$, and method B, $C_{\mathrm{I,B}}/\mathcal{N}_0$, where a 90 % probability of detection can be maintained. The choice of $T_0 = 290\,\mathrm{K}$, $F = 3\,\mathrm{dB}$, $P_{\mathrm{f}} = 10^{-5}$, and $P_{\mathrm{d}} = 90\,\%$ in Fig. 7.2 is explained in detail in Section 3.7. The initial intermediate differential correlation number is chosen according to the setting in Section 5.4 as $M_0 = T_{\mathrm{t}}/(10\,N_0\,T_{\mathrm{s}})$, where

$$T_{\mathrm{t}} = \sum_{\kappa=0}^{K-1} M_\kappa \, N_\kappa \, T_{\mathrm{s}} \tag{7.11}$$

is the total observation period. This choice of M_0 corresponds to the value $K = 10$ in the last two chapters. The values for $N_0\,T_{\mathrm{s}}$ in the legend of each plot are the initial coherent integration periods that are incrementally increased with (7.3), when the initial frequency offset f_{d} is reduced with frequency correction technique of the Chapter 5. The minimum values $N_{\min}$ are chosen such that the coherent integration period covers exactly one spreading code period. The limit for the maximum coherent integration periods is $N_{\max}\,T_{\mathrm{s}} = 100\,\mathrm{ms}$. This value corresponds to a reasonable coherence time for a static pedestrian receiver, as elaborated in Section 7.1. While longer coherent integration periods would yield even better sensitivity, limiting the integration provides a higher receiver robustness and corresponds better to practical applications.

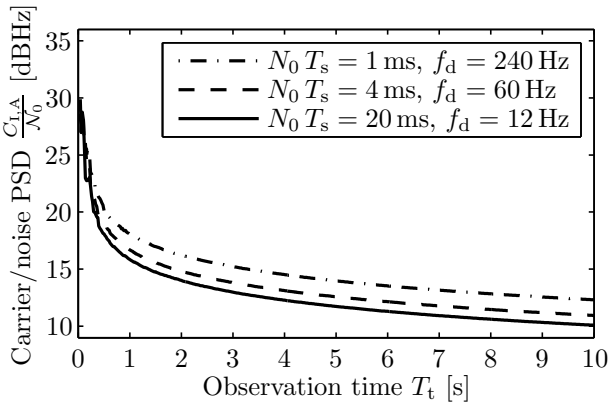

(a) Method A for GPS L1-C/A.

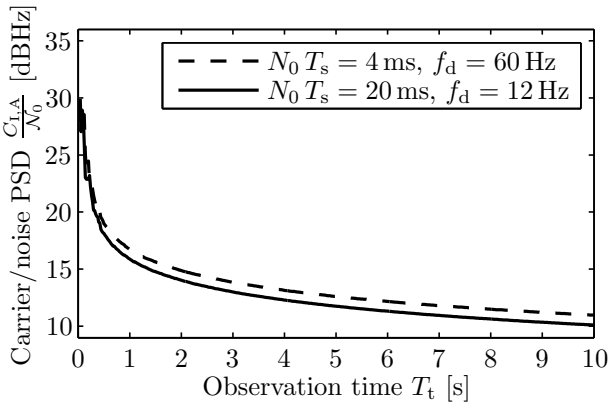

(b) Method A for Galileo E1-C.

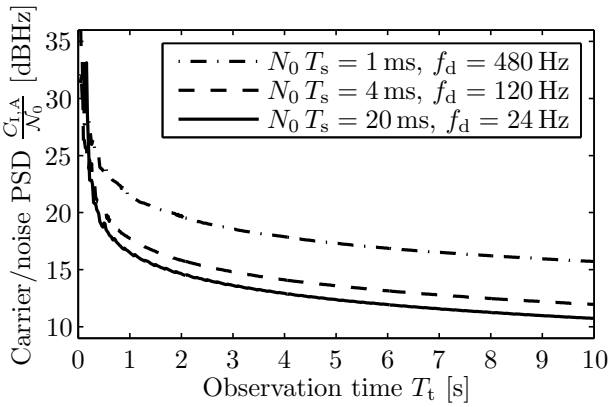

(c) Method A for GPS L1-C/A.

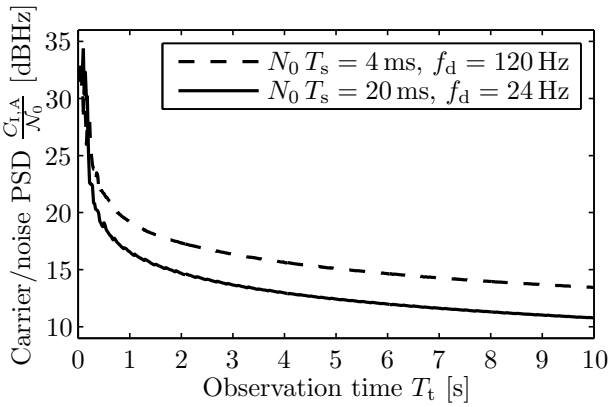

(d) Method A for Galileo E1-C.

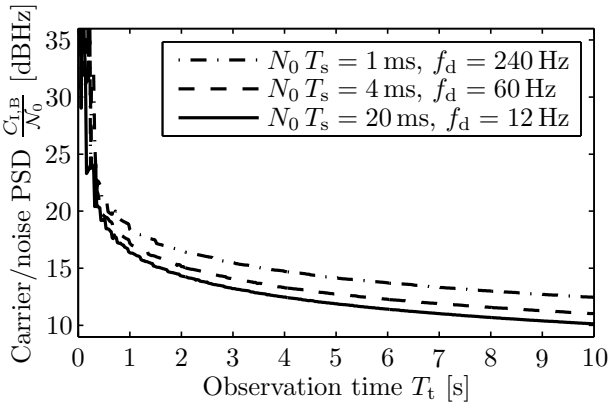

(e) Method B for GPS L1-C/A.

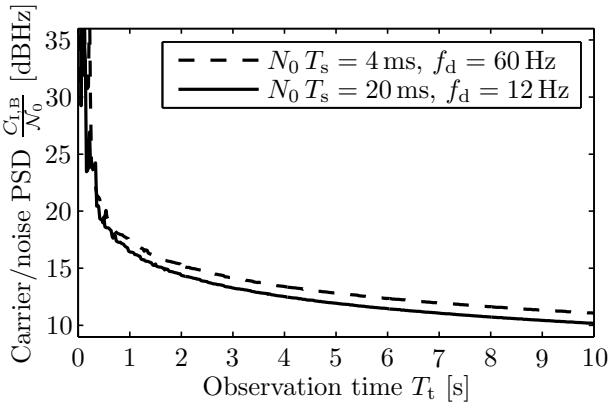

(f) Method B for Galileo E1-C.

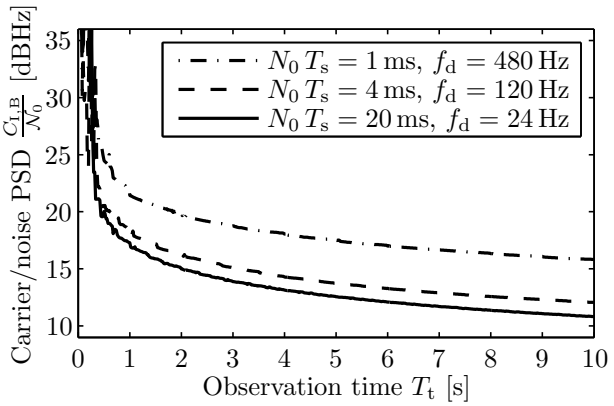

(g) Method B for GPS L1-C/A.

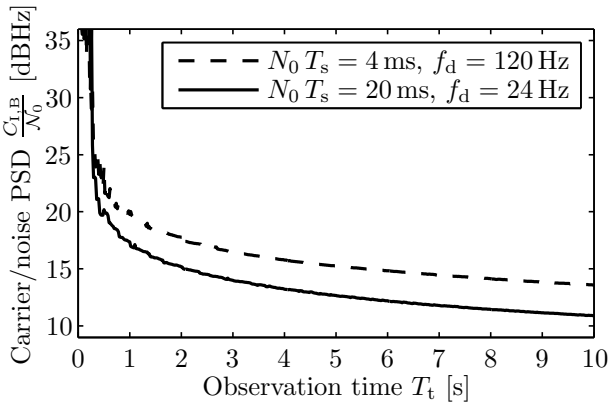

(h) Method B for Galileo E1-C.

Figure 7.2: Reception sensitivity with the adaptive integration interval technique for $T_0 = 290\,\mathrm{K}$, $F = 3\,\mathrm{dB}$, $M_0 = T_\mathrm{t}/(10\,N_0\,T_\mathrm{s})$, $N_{\mathrm{min,GPS}} = 1\,\mathrm{ms}/T_\mathrm{s}$, $N_{\mathrm{min,Galileo}} = 4\,\mathrm{ms}/T_\mathrm{s}$, $N_\mathrm{max}\,T_\mathrm{s} = 100\,\mathrm{ms}$, $P_\mathrm{f} = 10^{-5}$, and $P_\mathrm{d} = 90\,\%$.

7.3 Sensitivity Gain

The adaptive coherent integration interval exploits the convergence of the frequency deviation towards zero by incrementally increasing the coherent integration interval as a function of the estimated frequency deviation. It thereby yields a sensitivity gain, which is calculated in this section. The sensitivity gain in dB of the adaptive integration interval method is found by subtracting the values in Fig. 7.2 from the values in Fig. 6.3. As presented in Fig. 7.3, the gain for method A, $C_{\mathrm{P,A}}/C_{\mathrm{I,A}}$, amounts up to 7.1 dB, and the gain for method B, $C_{\mathrm{P,B}}/C_{\mathrm{I,B}}$, amounts up to 6.7 dB. The sensitivity gain is the largest for the shortest initial coherent integration interval $N_0\,T_\mathrm{s}$, since the maximum integration interval is limited at $N_{\max}\,T_\mathrm{s} = 100\,\mathrm{ms}$. The smallest initial value has the most room for increment and hence achieves the largest improvement. The longer initial coherent integration intervals saturate earlier. Nonetheless, the shortest initial coherent integration interval still delivers the largest frequency search bin. The adaptive integration interval does not affect the size of the frequency search bin. This is accomplished by a generous backtracking range. Only one quarter of the frequency estimation range leads to an increase in coherent integration time. Three quarters of the estimation range decrease the coherent integration period. The full magnitude of sensitivity improvement requires a certain settling time until the frequency offset correction has reduced the frequency deviation sufficiently. The adaptive integration method delivers its main improvement for intermediate and long observation periods.

The cumulative sensitivity gain of the adaptive detection threshold versus the state-of-the-art noncoherent integration can be obtained as the difference between the values in dB of Fig. 3.14 and 7.2. As is summarized in Fig. 7.4, the cumulative gain for method A, $C_{\mathrm{N}}/C_{\mathrm{I,A}}$, rises to 17.3 dB and the cumulative gain for method B, $C_{\mathrm{N}}/C_{\mathrm{I,B}}$, rises to 17.2 dB. Although methods A and B deliver almost the same reception sensitivity, their distinction is important since method B can be implemented with higher cost-efficiency and lower power consumption than method A. For the case of large frequency deviations, the cumulative gain is comprised of 1.5 dB by the differential correlation, 11.6 dB by the adaptive detection threshold, 1.5 dB by the frequency offset correction, 0.7 dB by the phase mismatch correction and 3.6 dB by the adaptive integration interval. However, the adaptive integration yields higher sensitivity improvements for shorter initial coherent integration periods. This leads to the effect that the cumulative sensitivity gain for $N\,T_\mathrm{s} = 1\,\mathrm{ms}$ and $f_\mathrm{d} = 240\,\mathrm{Hz}$ is 12.7 dB, while the cumulative gain for $N\,T_\mathrm{s} = 20\,\mathrm{ms}$ and $f_\mathrm{d} = 12\,\mathrm{Hz}$ is 13.6 dB, which is just 0.9 dB more. With the adaptive integration method, shorter initial coherent integration intervals might be beneficial in order to simplify the frequency search space. The resulting sensitivity reduction is only minor.

7.4 Positioning Accuracy

The range variance for method A of the adaptive integration $\sigma^2_{\hat{\rho},\mathrm{I,A}}$ is defined in (5.48) as a function of $\sigma^2_{\Delta,\mathrm{A}}$ and $\partial m_{\Delta,\mathrm{A}}/\partial\tau_\epsilon|_{\tau_\epsilon=0}$. The discrimination variance $\sigma^2_{\Delta,\mathrm{A}}$ is given in (5.49) as function of $m_{\Upsilon,\mathrm{E}} = m_\Upsilon|_{\hat{\tau}=\hat{\tau}_\mathrm{E}}$, $m_{\Upsilon,\mathrm{L}} = m_\Upsilon|_{\hat{\tau}=\hat{\tau}_\mathrm{L}}$, $\sigma^2_{\Upsilon,\mathrm{E}} = \sigma^2_\Upsilon|_{\hat{\tau}=\hat{\tau}_\mathrm{E}}$, and $\sigma^2_{\Upsilon,\mathrm{L}} = \sigma^2_\Upsilon|_{\hat{\tau}=\hat{\tau}_\mathrm{L}}$, where m_Υ and σ^2_Υ for the adaptive integration technique are derived in (7.5) and (7.6). The slope

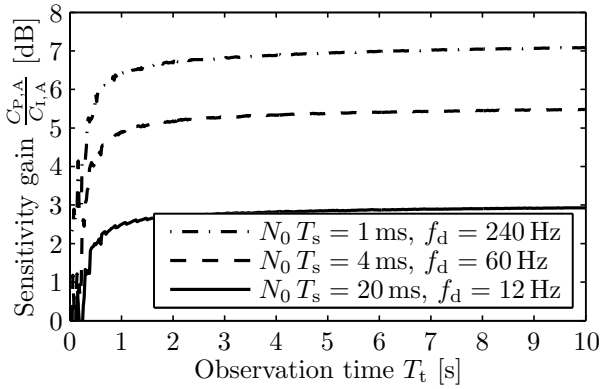

(a) Method A for GPS L1-C/A.

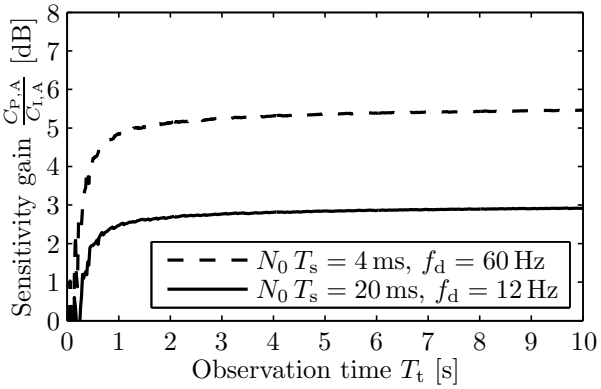

(b) Method A for Galileo E1-C.

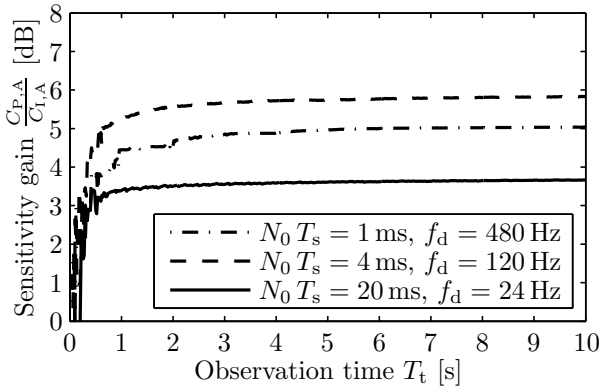

(c) Method A for GPS L1-C/A.

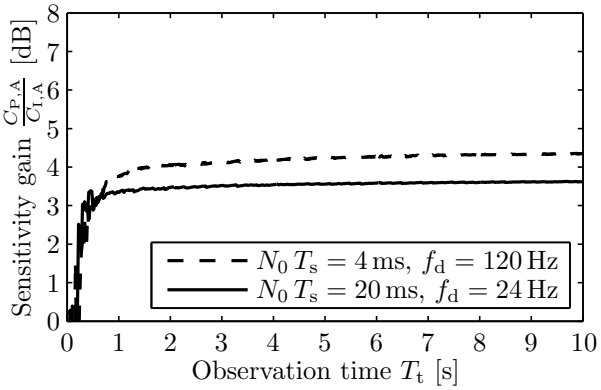

(d) Method A for Galileo E1-C.

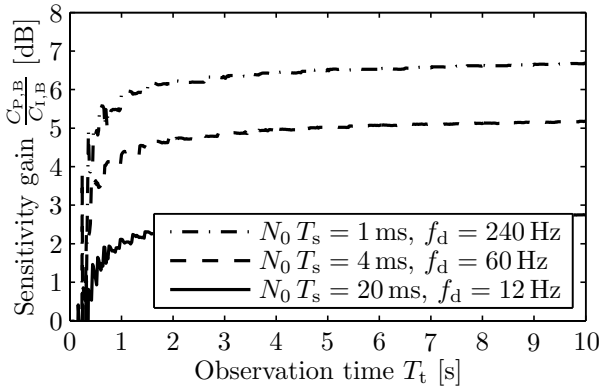

(e) Method B for GPS L1-C/A.

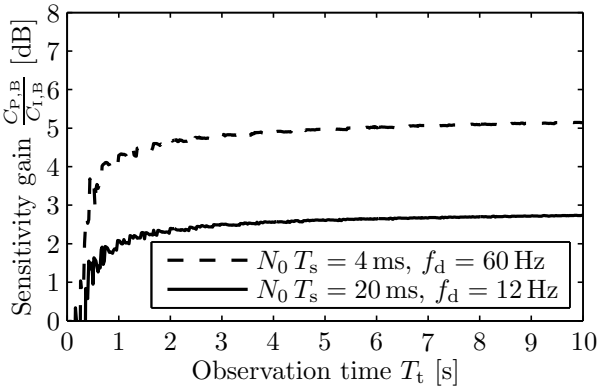

(f) Method B for Galileo E1-C.

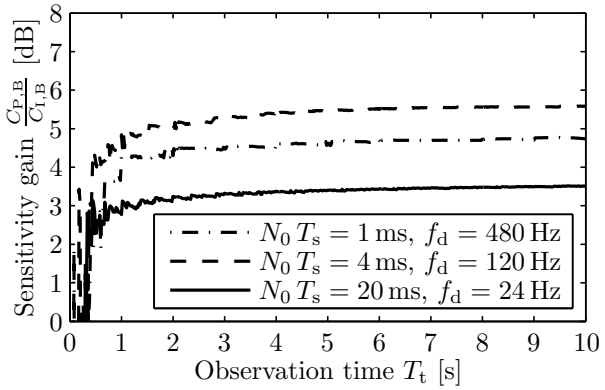

(g) Method B for GPS L1-C/A.

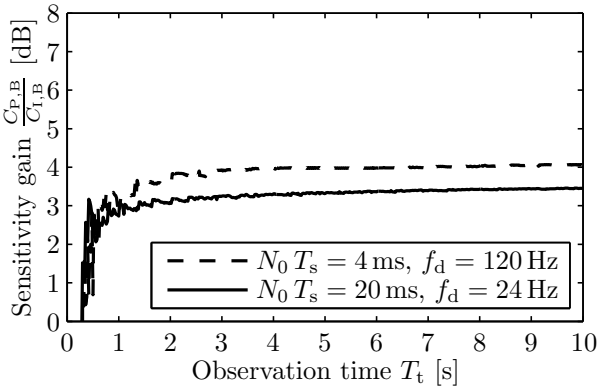

(h) Method B for Galileo E1-C.

Figure 7.3: Sensitivity gain of the adaptive integration interval technique for $T_0 = 290\,\mathrm{K}$, $F = 3\,\mathrm{dB}$, $M_0 = T_\mathrm{t}/(10\,N_0\,T_\mathrm{s})$, $N_{\mathrm{min,GPS}} = 1\,\mathrm{ms}/T_\mathrm{s}$, $N_{\mathrm{min,Galileo}} = 4\,\mathrm{ms}/T_\mathrm{s}$, $N_\mathrm{max}\,T_\mathrm{s} = 100\,\mathrm{ms}$, $P_\mathrm{f} = 10^{-5}$, and $P_\mathrm{d} = 90\,\%$.

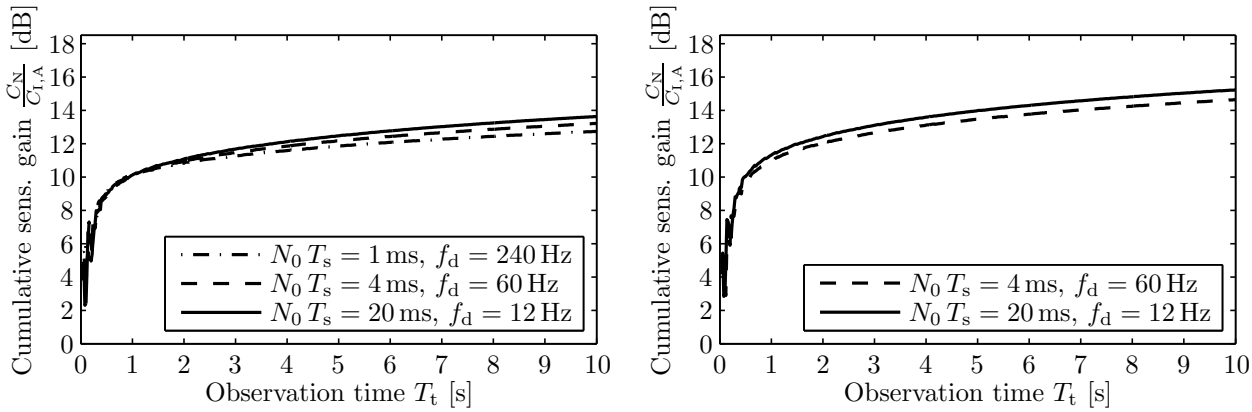

(a) Method A for GPS L1-C/A.

(b) Method A for Galileo E1-C.

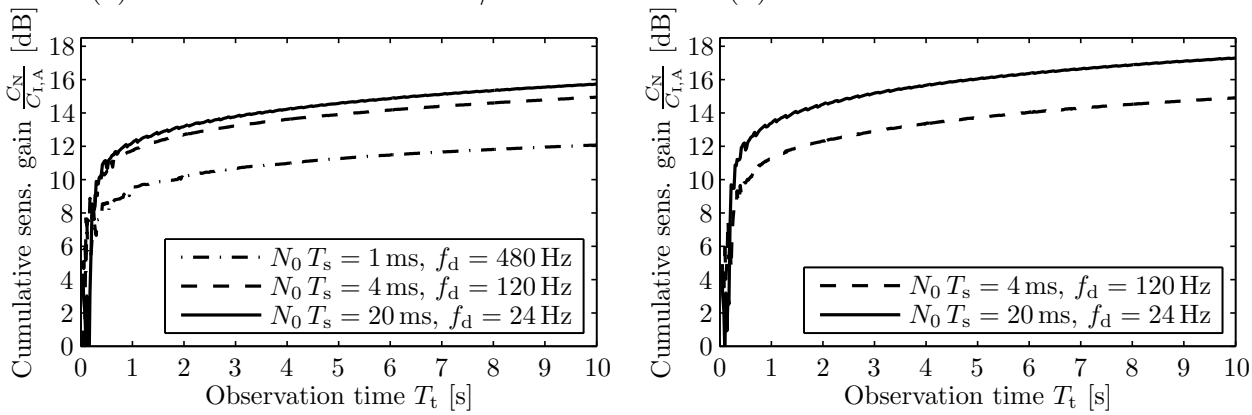

(c) Method A for GPS L1-C/A.

(d) Method A for Galileo E1-C.

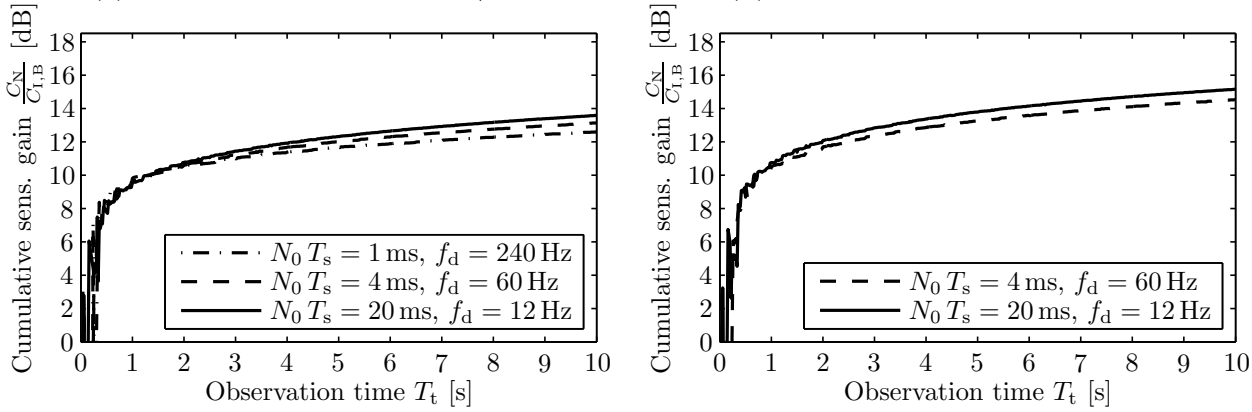

(e) Method B for GPS L1-C/A.

(f) Method B for Galileo E1-C.

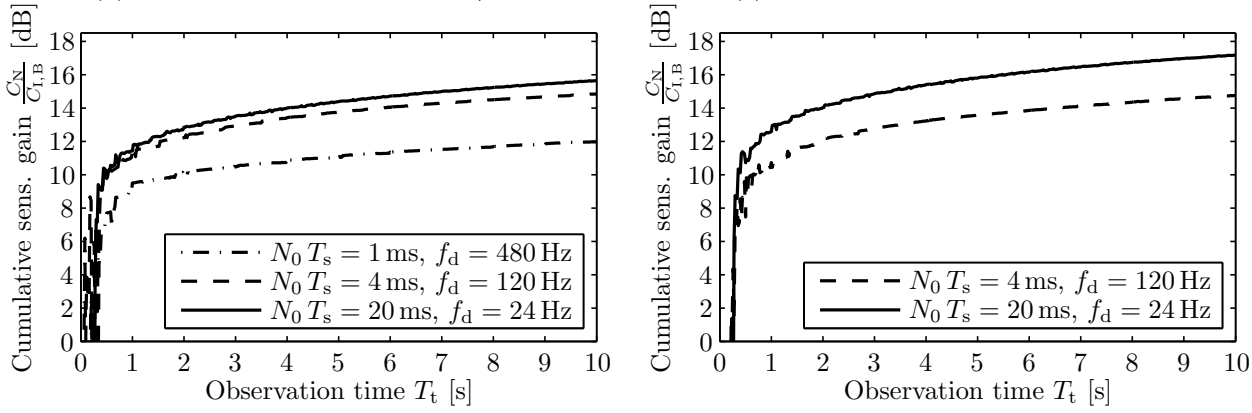

(g) Method B for GPS L1-C/A.

(h) Method B for Galileo E1-C.

Figure 7.4: Cumulative sensitivity gain of the adaptive integration interval technique versus the state-of-the-art noncoherent integration for $T_0 = 290\,\text{K}$, $F = 3\,\text{dB}$, $M_0 = T_t/(10\,N_0\,T_s)$, $N_{\min,\text{GPS}} = 1\,\text{ms}/T_s$, $N_{\min,\text{Galileo}} = 4\,\text{ms}/T_s$, $N_{\max}\,T_s = 100\,\text{ms}$, $P_f = 10^{-5}$, and $P_d = 90\,\%$.

of the discrimination mean can be derived with help of (5.52), (5.53), and (6.9) as

$$\begin{aligned}\left.\frac{\partial m_{\Delta,\mathrm{A}}}{\partial \tau_\epsilon}\right|_{\tau_\epsilon=0} &= -8\,C\,\frac{R_0\left(\frac{\delta}{2}\right)}{N_0\,\eta\,T_\mathrm{c}}\left[\sum_{\kappa=0}^{K-1} 2\,(M_\kappa-1)\,\sigma_{w,\kappa}^2\,N_\kappa^2\,\mathrm{sinc}^2(f_{\mathrm{d},\kappa}\,N_\kappa\,T_\mathrm{s})\right.\\ &\left.+\sum_{\kappa=0}^{K-2}\sigma_{w,\kappa}^2\,N_{\kappa+1}^2\,\mathrm{sinc}^2(f_{\mathrm{d},\kappa+1}\,N_{\kappa+1}\,T_\mathrm{s})+\sum_{\kappa=1}^{K-1}\sigma_{w,\kappa}^2\,N_{\kappa-1}^2\,\mathrm{sinc}^2(f_{\mathrm{d},\kappa-1}\,N_{\kappa-1}\,T_\mathrm{s})\right]\\ &-32\,C^2\,\frac{R_0^3\left(\frac{\delta}{2}\right)}{N_0^3\,\eta\,T_\mathrm{c}}\left|\sum_{\kappa=0}^{K-1}(M_\kappa-1)\,N_\kappa^2\,\mathrm{sinc}^2(f_{\mathrm{d},\kappa}\,N_\kappa\,T_\mathrm{s})\,\mathrm{e}^{\mathrm{j}\,2\,\pi\,f_{\mathrm{d},\kappa}\,N_\kappa\,T_\mathrm{s}-\mathrm{j}\,\widehat{\phi}_\kappa}\right.\\ &\left.+\sum_{\kappa=1}^{K-1}N_\kappa\,N_{\kappa-1}\,\mathrm{sinc}(f_{\mathrm{d},\kappa}\,N_\kappa\,T_\mathrm{s})\,\mathrm{sinc}(f_{\mathrm{d},\kappa-1}\,N_{\kappa-1}\,T_\mathrm{s})\,\mathrm{e}^{\mathrm{j}\,\pi\,(f_{\mathrm{d},\kappa}\,N_\kappa+f_{\mathrm{d},\kappa-1}\,N_{\kappa-1})\,T_\mathrm{s}-\mathrm{j}\,\widehat{\phi}_\kappa}\right|^2.\end{aligned} \tag{7.12}$$

As before, the range variance for method B of the adaptive integration, $\sigma_{\widehat{\rho},\mathrm{I,B}}^2$ is given by (5.55), with $\sigma_{\Delta,\mathrm{B}}^2$ presented in (5.56) as a function of $\sigma_{\Upsilon,\mathrm{I,E}}^2 = \sigma_{\Upsilon,\mathrm{I}}^2|_{\widehat{\tau}=\widehat{\tau}_\mathrm{E}}$ and $\sigma_{\Upsilon,\mathrm{I,L}}^2 = \sigma_{\Upsilon,\mathrm{I}}^2|_{\widehat{\tau}=\widehat{\tau}_\mathrm{L}}$. The inphase differential correlation noise variance $\sigma_{\Upsilon,\mathrm{I}}^2$ is derived in (7.8). Finally, the derivative of the discrimination function for method B is obtained from (6.10) and (7.5) as

$$\begin{aligned}\frac{\partial m_{\Delta,\mathrm{B}}}{\partial \tau_\epsilon} &= -8\,C\,\frac{R_0\left(\frac{\delta}{2}\right)}{N_0\,\eta\,T_\mathrm{c}}\left[\sum_{\kappa=0}^{K-1}(M_\kappa-1)\,N_\kappa^2\,\mathrm{sinc}^2(f_{\mathrm{d},\kappa}\,N_\kappa\,T_\mathrm{s})\,\cos\!\left(2\,\pi\,f_{\mathrm{d},\kappa}\,N_\kappa\,T_\mathrm{s}-\widehat{\phi}_\kappa\right)\right.\\ &\left.+\sum_{\kappa=1}^{K-1}N_\kappa\,N_{\kappa-1}\,\mathrm{sinc}(f_{\mathrm{d},\kappa}\,N_\kappa\,T_\mathrm{s})\,\mathrm{sinc}(f_{\mathrm{d},\kappa-1}\,N_{\kappa-1}\,T_\mathrm{s})\,\cos\!\left(\pi(f_{\mathrm{d},\kappa}\,N_\kappa+f_{\mathrm{d},\kappa-1}\,N_{\kappa-1})\,T_\mathrm{s}-\widehat{\phi}_\kappa\right)\right].\end{aligned} \tag{7.13}$$

This completes the derivation of the standard deviations of the estimated receiver-satellite ranges $\sigma_{\widehat{\rho},\mathrm{I,A}}$ and $\sigma_{\widehat{\rho},\mathrm{I,B}}$, which are illustrated in Fig. 7.5. The same baseline $C_\mathrm{N}/\mathcal{N}_0$ function in Fig. 3.14 as for all previous accuracy plots has been used to enable direct comparison. The parameters $T_0 = 290\,\mathrm{K}$ and $F = 3\,\mathrm{dB}$ are introduced in Section 3.7, the parameters $M_0 = T_\mathrm{t}/(10\,N_0\,T_\mathrm{s})$, $N_{\min,\mathrm{GPS}} = 1\,\mathrm{ms}/T_\mathrm{s}$, $N_{\min,\mathrm{Galileo}} = 4\,\mathrm{ms}/T_\mathrm{s}$, and $N_\mathrm{max}\,T_\mathrm{s} = 100\,\mathrm{ms}$ in Section 7.2, and the parameters $\delta = 1/B$ and $B = 4.092\,\mathrm{MHz}$ in Section 3.14.

7.5 Accuracy Improvement

When the frequency deviation decreases and the coherent integration interval is increased, then the signal-to-noise ratio for the code discrimination increases as well. The increased signal strength leads to an improved positioning accuracy, which is presented in this section. Dividing the values in Fig. 6.6 by the values in Fig. 7.5 yields the accuracy improvement of the the adaptive integration technique. The resulting relative accuracies $\sigma_{\widehat{\rho},\mathrm{P,A}}/\sigma_{\widehat{\rho},\mathrm{I,A}}$ and $\sigma_{\widehat{\rho},\mathrm{P,B}}/\sigma_{\widehat{\rho},\mathrm{I,B}}$ are shown in Fig. 7.6. The accuracy of the estimated receiver-satellite distance is improved with the adaptive integration technique by up to 114 % for method A and 66 % for method B. The shortest initial coherent integration interval $N_0\,T_\mathrm{s}$ delivers the highest improvement in ranging accuracy, since it has the most headroom for the extended integration,

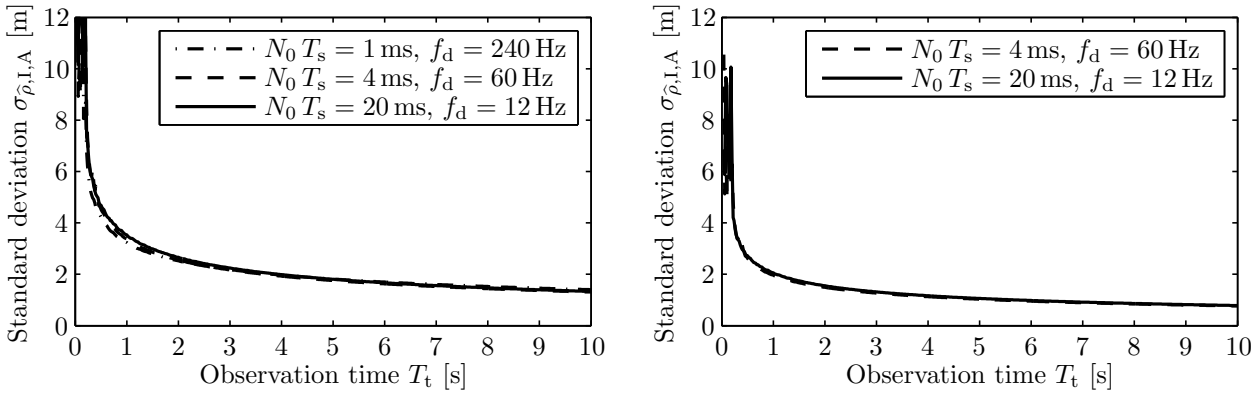

(a) Method A for GPS L1-C/A.

(b) Method A for Galileo E1-C.

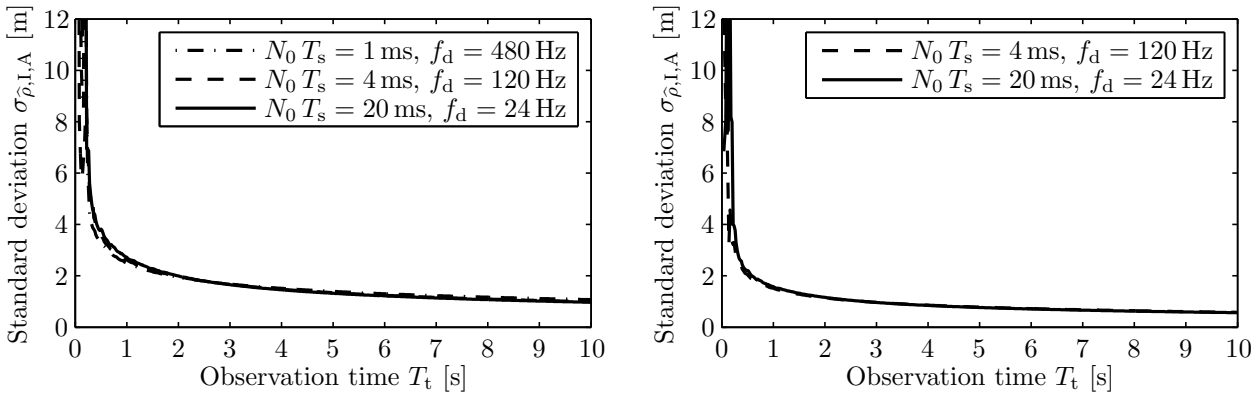

(c) Method A for GPS L1-C/A.

(d) Method A for Galileo E1-C.

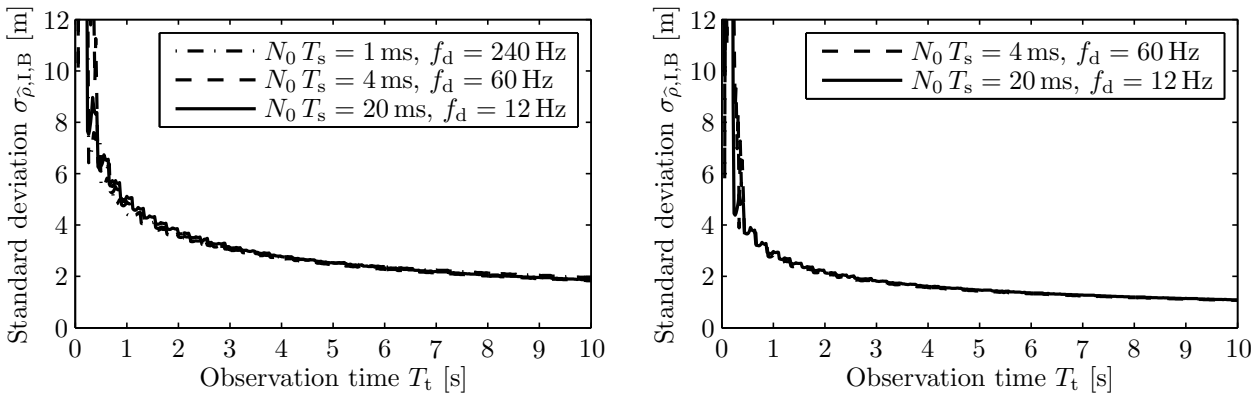

(e) Method B for GPS L1-C/A.

(f) Method B for Galileo E1-C.

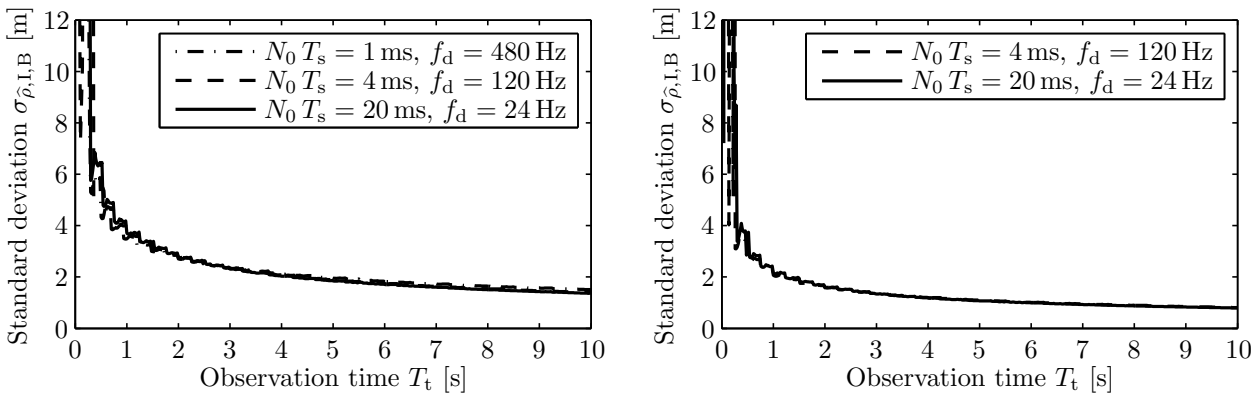

(g) Method B for GPS L1-C/A.

(h) Method B for Galileo E1-C.

Figure 7.5: Range estimation accuracy with the adaptive integration interval technique for $T_0 = 290\,\mathrm{K}$, $F = 3\,\mathrm{dB}$, $M_0 = T_\mathrm{t}/(10\,N_0\,T_\mathrm{s})$, $N_{\min,\mathrm{GPS}} = 1\,\mathrm{ms}/T_\mathrm{s}$, $N_{\min,\mathrm{Galileo}} = 4\,\mathrm{ms}/T_\mathrm{s}$, $N_\mathrm{max}\,T_\mathrm{s} = 100\,\mathrm{ms}$, $\delta = 1/B$, and $B = 4.092\,\mathrm{MHz}$.

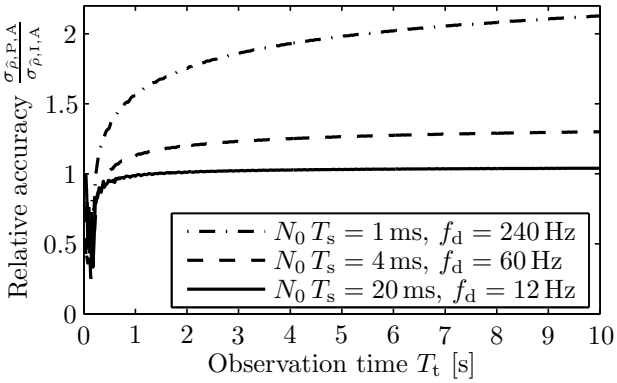

(a) Method A for GPS L1-C/A.

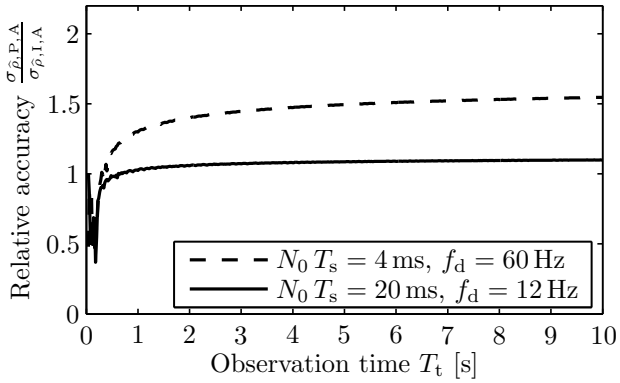

(b) Method A for Galileo E1-C.

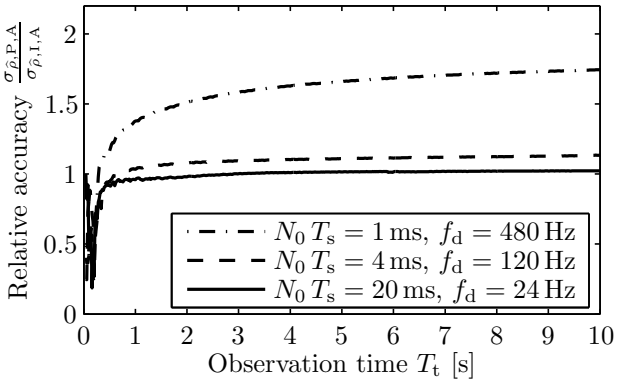

(c) Method A for GPS L1-C/A.

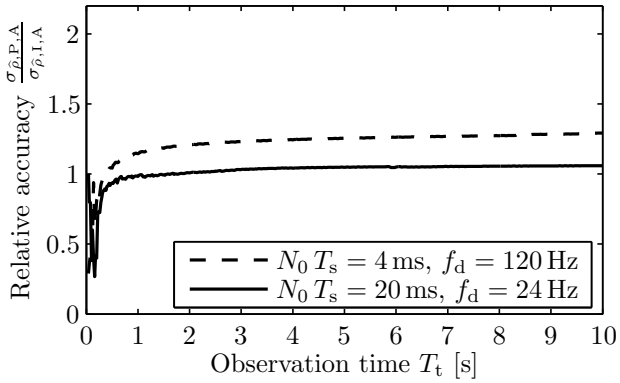

(d) Method A for Galileo E1-C.

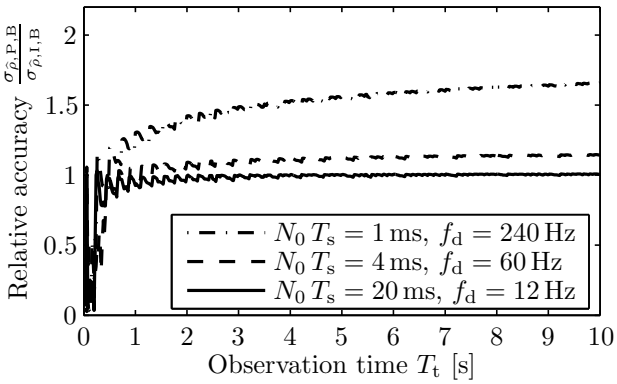

(e) Method B for GPS L1-C/A.

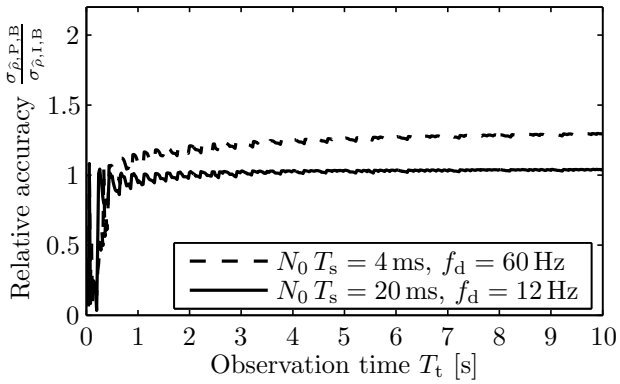

(f) Method B for Galileo E1-C.

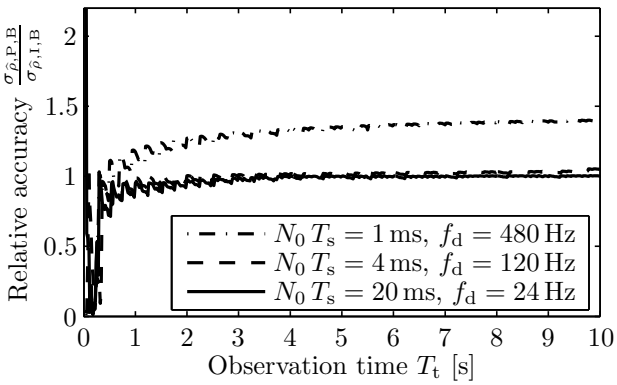

(g) Method B for GPS L1-C/A.

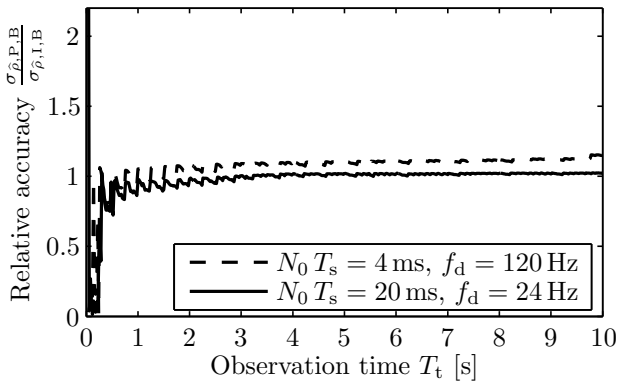

(h) Method B for Galileo E1-C.

Figure 7.6: Accuracy improvement of the adaptive integration interval technique for $T_0 = 290\,\mathrm{K}$, $F = 3\,\mathrm{dB}$, $M_0 = T_\mathrm{t}/(10\,N_0\,T_\mathrm{s})$, $N_{\mathrm{min,GPS}} = 1\,\mathrm{ms}/T_\mathrm{s}$, $N_{\mathrm{min,Galileo}} = 4\,\mathrm{ms}/T_\mathrm{s}$, $N_\mathrm{max}\,T_\mathrm{s} = 100\,\mathrm{ms}$, $\delta = 1/B$, and $B = 4.092\,\mathrm{MHz}$.

which is bound by $N_{\max} T_s = 100\,\text{ms}$. This bound has practical reasons, since the propagation channel has a limited coherence time, even for a static receiver. It is elaborated in more detail in Section 7.1. It should be noted that the shortest initial coherent integration not only yields the largest accuracy improvement, but also tolerates the largest initial frequency deviation. It can observed in Fig. 7.5, that the different initial coherent integration intervals deliver almost the same range accuracy. With the adaptive integration it is hence useful to start with a short initial coherent integration in order to allow for a large initial frequency deviation. For intermediate and long observation periods, there is barely any difference in the resulting range accuracy.

The cumulative relative accuracy of the phase mismatch correction versus the state-of-the-art noncoherent integration is presented in Fig. 7.7. The ratios of the values in Fig. 3.21 and 7.5 yield the cumulative relative accuracies $\sigma_{\hat{\rho},\text{N}}/\sigma_{\hat{\rho},\text{I,A}}$ and $\sigma_{\hat{\rho},\text{N}}/\sigma_{\hat{\rho},\text{I,B}}$. The differential correlation improves the accuracy by 80 %, the frequency offset correction by 62 % for method A and 44 % for method B, the phase mismatch correction by 15 %, and the adaptive integration by 74 % for method A and 40 % for method B. The combination of all these techniques increases the accuracy of the final estimated range by up to $1.8 \times 1.62 \times 1.15 \times 1.74 - 1 = 483\,\%$ of the initial value with method A and $1.8 \times 1.44 \times 1.15 \times 1.4 - 1 = 317\,\%$ with method B.

7.6 Conclusion

A method to adaptively adjust the coherent integration interval in respect to the residual frequency deviation is introduced in this chapter. Since the residual frequency deviation leads to a continuous phase rotation of the baseband signal samples, the coherent integration interval can only be chosen as long as the residual frequency deviation permits. The previously presented frequency offset correction method reduces the residual frequency deviation and therefore enables the *adaptive integration interval* technique. The extended coherent integration interval delivers a very large signal-to-noise ratio improvement. The initial size of the frequency search bin is thereby maintained without a constraint. The generous backtracking range of three quarters of the the frequency estimation range yields a high reliability of the adaptive integration technique. In case of a sudden increase in frequency deviation, e.g. due to fast changes in receiver motion, the coherent integration period is reduced again. The presented method enhances the reception sensitivity by up to 7.1 dB, when the maximum coherent integration interval is bound by 100 ms. It enhances the cumulative sensitivity gain versus the state-of-the-art noncoherent integration to 17.3 dB. The increased signal-to-noise ratio also leads to a higher accuracy of the correlation peak estimation, which increases the accuracy of the receiver-satellite range by 114 %. The cumulative accuracy improvement reaches 483 % as compared to the state-of-the-art noncoherent integration. Due to the phase mismatch correction, positioning based on the just the inphase component of the differential correlation result is also possible. This method achieves around the same cumulative reception sensitivity improvement of 17.2 dB versus the state-of-the-art and thereby reduces implementation costs and power consumption. The improvement in positioning accuracy is somewhat less with 66 %, which yields a cumulative improvement of 317 % versus the state-of-the-art noncoherent integration.

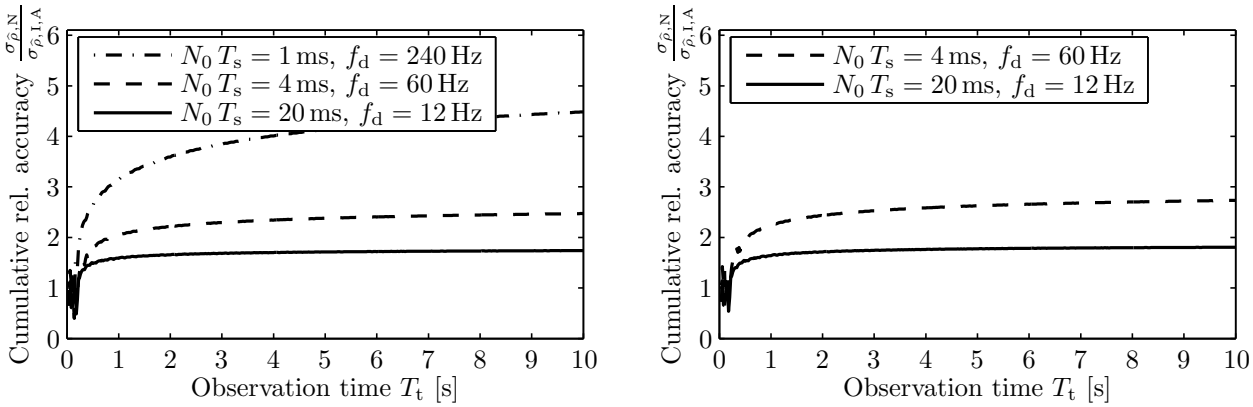

(a) Method A for GPS L1-C/A.

(b) Method A for Galileo E1-C.

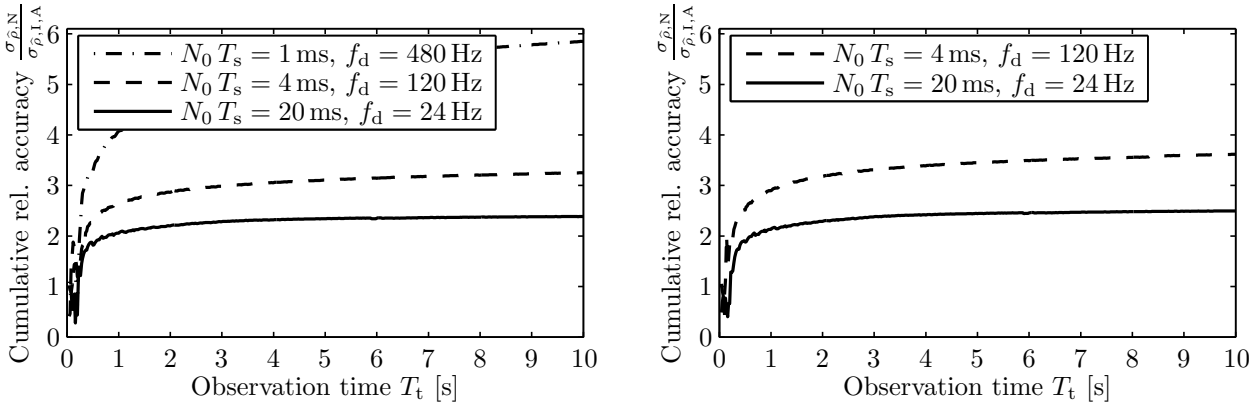

(c) Method A for GPS L1-C/A.

(d) Method A for Galileo E1-C.

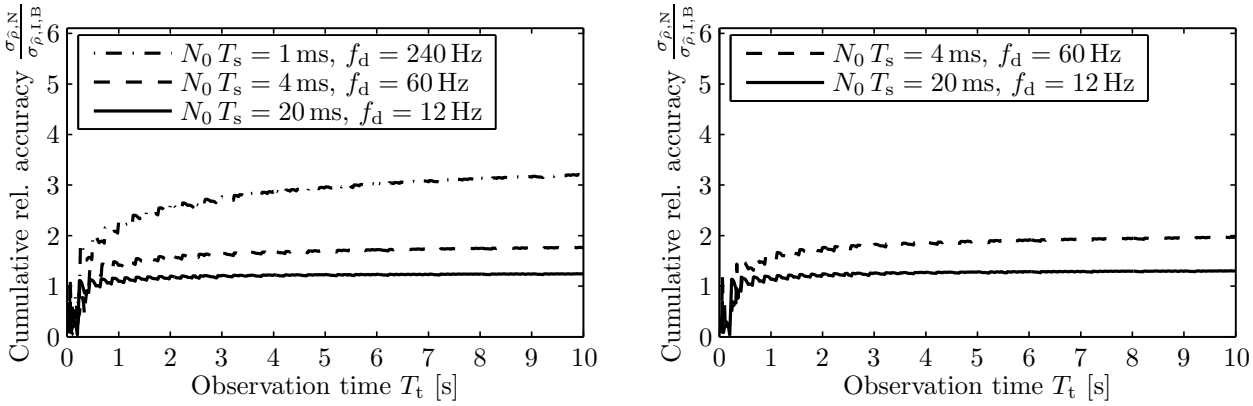

(e) Method B for GPS L1-C/A.

(f) Method B for Galileo E1-C.

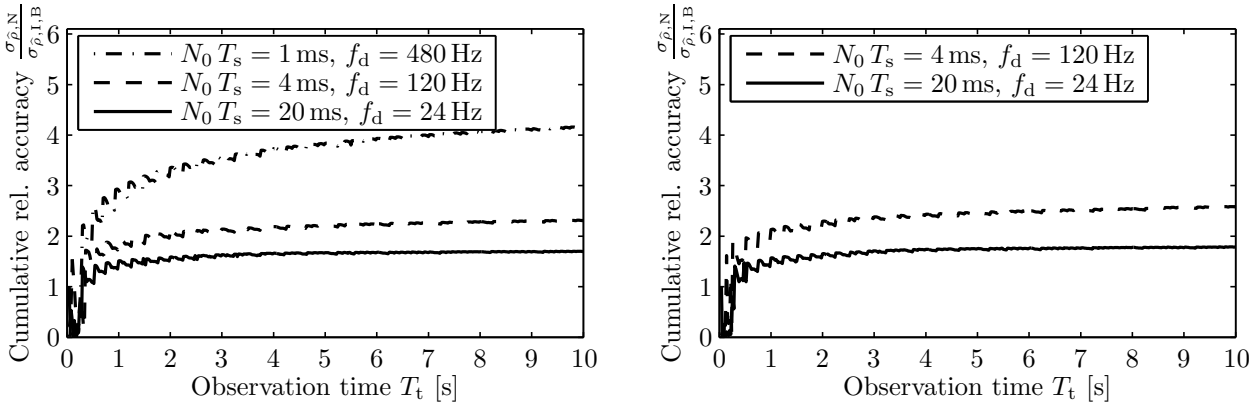

(g) Method B for GPS L1-C/A.

(h) Method B for Galileo E1-C.

Figure 7.7: Cumulative accuracy improvement of the adaptive integration interval technique versus the state-of-the-art noncoherent integration for $T_0 = 290\,\mathrm{K}$, $F = 3\,\mathrm{dB}$, $M_0 = T_\mathrm{t}/10\,N_0\,T_\mathrm{s}$, $N_\mathrm{max}\,T_\mathrm{s} = 100\,\mathrm{ms}$, $\delta = 1/B$, and $B = 4.092\,\mathrm{MHz}$.

Chapter 8

Multipath Fading Mitigation

As introduced in Chapter 1, satellite navigation is becoming increasingly important for location based services and emergency caller location. Both applications require positioning in urban and indoor areas, where obstacles give rise to reflections, diffraction, and scattering. These obstacles are often near the receiver and lead to multipath signal propagation. Measurement campaigns have shown that most multipath components are within an excess delay of less than 500 ns, which corresponds to an excess distance of 150 m [12, 76, 77]. Multiple signal echoes therefore combine at the receiver antenna with a sub-chip distance. Depending on their phase offset, they cause constructive or destructive interference. This then leads to a widely varying amplitude of the combined multipath signal. The resulting fading process degrades the receiver performance. It is shown in this chapter that the negative impact of the fading process can be reduced by adaptively adjusting the detection threshold with the presented *multipath fading mitigation* method.

8.1 Fading Adaptation

As introduced in Section 3.7, GPS receivers typically employ the Neyman-Pearson detection criterion, where the false detection probability P_f must not exceed a fixed number. Then for the given false detection probability, the probability of detection P_d is maximized. The detection threshold λ is therefore chosen as low as possible, without exceeding the maximum false detection probability. False detection is caused by out-of-phase correlation and additive noise.

In relevant environments for mobile phone positioning, the power distribution of the received signal can be modelled with a Rice distribution [41, 78, 79]. The multipath fading modifies both the correlation peak and the out-of-phase autocorrelation values. If the detection threshold is not adjusted, the fading correlation peak changes the probability of detection. At the same time, the fading out-of-phase autocorrelation values lead to a changed false detection probability, which is different from the admissible level. The multipath fading mitigation method of this chapter therefore estimates the differential correlation variance $\sigma^2_{\Psi,\mathrm{H}_0}$ and mean magnitude $|m_{\Psi,\mathrm{H}_0}|$. This allows to optimally adjust the detection threshold

to the fading characteristic of the Galileo/GPS signal. The false detection probability is kept at the admissible level and the probability of detection is maximized. The knowledge of the fading characteristic can thus be used to recover a large portion of the receiver performance.

The magnitude of a complex-valued GAUSSIAN distributed variable θ with the expectation value

$$m_\theta = \mathrm{E}\{\theta\} \; , \tag{8.1}$$

and the combined real and complex variance

$$\sigma_\theta^2 = \mathrm{E}\big\{|\theta - m_\theta|^2\big\} \tag{8.2}$$

obeys the RICE distribution [28]

$$p_{|\theta|}(\alpha) = \begin{cases} \frac{2\,\alpha}{\sigma_\theta^2} \exp\Big(-\frac{\alpha^2+|m_\theta|^2}{\sigma_\theta^2}\Big)\; \mathrm{I}_0\Big(\frac{2\,|m_\theta|\,\alpha}{\sigma_\theta^2}\Big) \; , & \alpha \geqslant 0 \\ 0 \; , & \text{else} \; , \end{cases} \tag{8.3}$$

with

$$\alpha = |\theta| \; . \tag{8.4}$$

The modified BESSEL function of first kind and zero order is denoted by $\mathrm{I}_0(\cdot)$ and specified in (3.57). The RICE distribution is frequently used to model multipath fading in urban and indoor environments [41, 78, 79]. The fading signal is thereby characterized by the RICE factor

$$\mathcal{K} = \frac{|m_\theta|^2}{\sigma_\theta^2} \; . \tag{8.5}$$

To model a fading Galileo/GPS signal, its definition in (3.8) is modified to

$$r_\nu = \sqrt{2\,C}\, c_{\lfloor(\nu\,T_\mathrm{s}+\tau)/T_\mathrm{c}\rfloor}\, q_{\lfloor(\nu\,T_\mathrm{s}+\tau)/T_\mathrm{c}\rfloor}\, \mathrm{e}^{\,\mathrm{j}\,(2\,\pi\,f_\mathrm{d}\,\nu\,T_\mathrm{s}+\varphi_\mathrm{c})}\, \theta_\nu + n_\nu \; , \tag{8.6}$$

where θ_ν describes the fading characteristic. The received line-of-sight signal power is described by C. The fading variable θ has the mean magnitude

$$|m_\theta| = |\mathrm{E}\{\theta\}| = 1 \; . \tag{8.7}$$

The line-of-sight signal is superimposed by multiple time-varying reflections, which form the fading process around the line-of-sight signal. The variance of the fading variable

$$\sigma_\theta^2 = \mathrm{E}\big\{|\theta - m_\theta|^2\big\} = \frac{1}{\mathcal{K}} \tag{8.8}$$

follows from (8.5) and (8.7). It is subsequently assumed that the coherent integration interval $N\,T_\mathrm{s}$ is chosen to be no longer than the coherence time of the multipath propagation channel, such that the fading variable θ_ν can be approximated to be constant during each coherent integration interval. By making the additional assumption that the fading variable is uncorrelated between integration intervals, the computation becomes mathematically better traceable. With (3.14) and (3.31), the coherently integrated predetection result is derived as

$$\boxed{\begin{aligned} s_\mu &= \sum_{\nu=\mu\,N}^{(\mu+1)\,N-1} r_\nu\, c_{\lfloor(\nu\,T_\mathrm{s}+\widehat{\tau})/T_\mathrm{c}\rfloor}\, q_{\lfloor(\nu\,T_\mathrm{s}+\widehat{\tau})/T_\mathrm{c}\rfloor} \\ &\simeq \sqrt{2\,C}\, R(\tau-\widehat{\tau})\, \mathrm{sinc}(f_\mathrm{d}\,N\,T_\mathrm{s})\, \mathrm{e}^{\,\mathrm{j}\,[(2\,\mu+1)\,\pi\,f_\mathrm{d}\,N\,T_\mathrm{s}+\varphi_\mathrm{c}]}\, \theta_{N\mu} + w_\mu \end{aligned}} \; . \tag{8.9}$$

The GAUSSIAN variables $\theta_{N\mu}$ and w_μ in (8.9) lead to a GAUSSIAN distributed variable s_μ with the mean

$$m_{s_\mu} = \mathrm{E}\{s_\mu\} = \sqrt{2\,C}\,R(\tau-\widehat{\tau})\,\mathrm{sinc}(f_\mathrm{d}\,N\,T_\mathrm{s})\,\mathrm{e}^{\mathrm{j}\,[(2\,\mu+1)\,\pi\,f_\mathrm{d}\,N\,T_\mathrm{s}+\varphi_\mathrm{c}]}\,m_\theta \tag{8.10}$$

and the variance

$$\sigma^2_{s_\mu} = \mathrm{E}\big\{|s_\mu - \mathrm{E}\{s_\mu\}|^2\big\} = 2\,C\,R^2(\tau-\widehat{\tau})\,\mathrm{sinc}^2(f_\mathrm{d}\,N\,T_\mathrm{s})\,\sigma^2_\theta + \sigma^2_w\,. \tag{8.11}$$

The differential correlation result is calculated as

$$\Psi = \sum_{\mu=1}^{M-1} s_\mu\,s^*_{\mu-1}\,. \tag{8.12}$$

Its expectation value is derived from (3.39), (8.7), and (8.10) as

$$\boxed{\begin{aligned} m_\Psi &= \mathrm{E}\{\Psi\} = (M-1)\,m_{s_\mu}\,m^*_{s_{\mu-1}} \\ &= 2\,(M-1)\,C\,R^2(\tau-\widehat{\tau})\,\mathrm{sinc}^2(f_\mathrm{d}\,N\,T_\mathrm{s})\,\mathrm{e}^{\mathrm{j}\,2\,\pi\,f_\mathrm{d}\,N\,T_\mathrm{s}} \end{aligned}}\,. \tag{8.13}$$

The correlation variance for the RICE fading channel is derived from (3.51), (8.8), and (8.11) as

$$\boxed{\begin{aligned} \sigma^2_\Psi &= \mathrm{E}\big\{|\Psi - \mathrm{E}\{\Psi\}|^2\big\} = (M-1)\left(\sigma^4_{s_\mu} + 2\,\sigma^2_{s_\mu}\,|m_{s_\mu}|^2\right) \\ &= (M-1)\Bigg[\sigma^4_w + 4\,C^2\,R^4(\tau-\widehat{\tau})\,\mathrm{sinc}^4(f_\mathrm{d}\,N\,T_\mathrm{s})\,\frac{2\,\mathcal{K}+1}{\mathcal{K}^2} \\ &\qquad + 4\,C\,\sigma^2_w\,R^2(\tau-\widehat{\tau})\,\mathrm{sinc}^2(f_\mathrm{d}\,N\,T_\mathrm{s})\,\frac{\mathcal{K}+1}{\mathcal{K}}\Bigg] \end{aligned}}\,. \tag{8.14}$$

8.2 Optimal Detection Threshold

If the detection threshold λ that is defined in (3.65) as

$$\lambda = P^{-1}_{\Lambda,\mathrm{H}_0}(1-P_\mathrm{f}) = \frac{\sigma^2_{\Psi,\mathrm{H}_0}}{2}\left[\mathrm{Q}^{-1}_{1,\beta}\left(\sqrt{\frac{2\,|m_{\Psi,\mathrm{H}_0}|^2}{\sigma^2_{\Psi,\mathrm{H}_0}}},\,P_\mathrm{f}\right)\right]^2 \tag{8.15}$$

is calculated for a line-of-sight signal and then applied to signals received from a RICE multipath fading channel, the resulting probability of false detection P_f specified in (3.63) as

$$P_\mathrm{f} = \Pr\{\Lambda \geqslant \lambda|\mathrm{H}_0\} = 1 - P_{\Lambda|\mathrm{H}_0}(\lambda) = \mathrm{Q}_1\left(\sqrt{\frac{2\,|m_{\Psi,\mathrm{H}_0}|^2}{\sigma^2_{\Psi,\mathrm{H}_0}}},\,\sqrt{\frac{2\,\lambda}{\sigma^2_{\Psi,\mathrm{H}_0}}}\right) \tag{8.16}$$

is above the admissible level. Fig. 8.1 shows P_f as a function of the RICE factor $\mathcal{K}$. The detection threshold λ in Fig. 8.1 has been calculated to yield $P_\mathrm{f} = 10^{-5}$ for a non-fading signal. This is the standard approach for state-of-the-art receivers. However, once the RICE factor drops below 100, the false alarm probability starts to increase. The probability of false alarm is almost a magnitude too large for $\mathcal{K} = 10$. For low RICE factors, the false

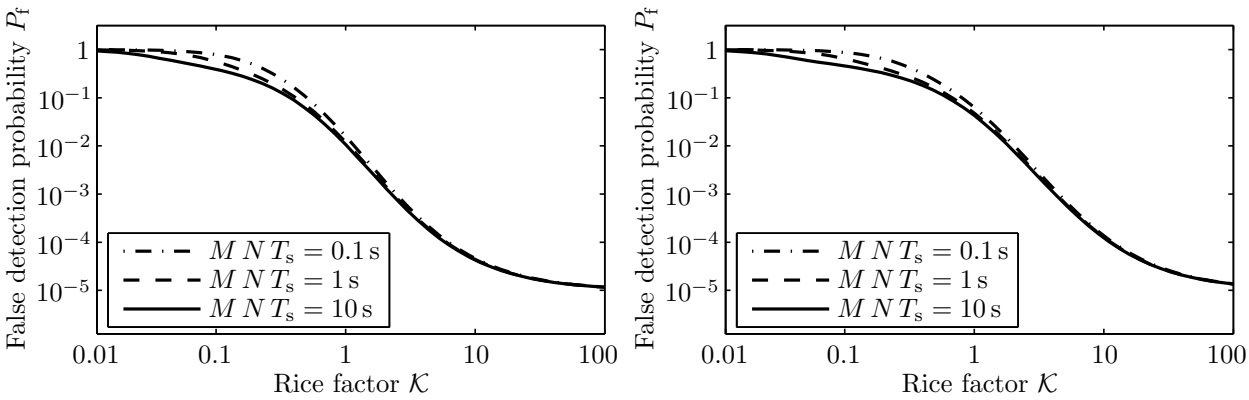

(a) GPS L1-C/A. (b) Galileo E1-C.

Figure 8.1: Probability of false detection without threshold adaptation for $T_0 = 290\,\mathrm{K}$, $F = 3\,\mathrm{dB}$, $N\,T_\mathrm{s} = 20\,\mathrm{ms}$, and $C/\mathcal{N}_0 = 45\,\mathrm{dBHz}$.

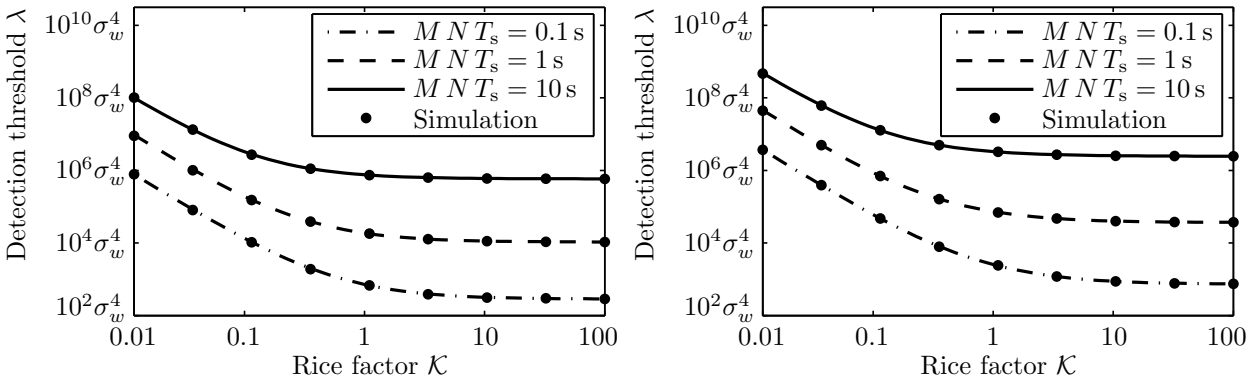

(a) GPS L1-C/A. (b) Galileo E1-C.

Figure 8.2: Optimal detection threshold λ for Rice fading for $T_0 = 290\,\mathrm{K}$, $F = 3\,\mathrm{dB}$, $N\,T_\mathrm{s} = 20\,\mathrm{ms}$, $C/\mathcal{N}_0 = 45\,\mathrm{dBHz}$, and $B = 4.092\,\mathrm{MHz}$.

alarm probability approaches 100 %, which means that false acquisition leading to severe positioning errors is almost guaranteed.

In order for the false detection probability P_f in (8.16) to exactly reach the permissable level, the detection threshold λ in (8.15) has to be calculated as a function of the actual Rice factor $\mathcal{K}$ of the propagation channel, where $m_{\Psi,\mathrm{H}_0} = m_\Psi|_{R^2(\tau-\widehat{\tau})=R_\mathrm{m}^2}$ is specified in (8.13) and $\sigma^2_{\Psi,\mathrm{H}_0} = \sigma^2_\Psi|_{R^2(\tau-\widehat{\tau})=R_\mathrm{m}^2}$ is given in (8.14). A low Rice factor $\mathcal{K}$ requires a high detection threshold λ and a high Rice factor requires a low detection threshold. In Fig. 8.2, the optimal detection threshold is presented as a function of the Rice factor. It must be high enough not to lead to a violation of the maximum allowed P_f. Using this threshold will maintain a constant false alarm probability $P_\mathrm{f} = 10^{-5}$ for all possible Rice factors.

The Rice factor can be estimated with different methods [80, 81, 82]. However, none of them is required here, since the detection threshold estimation method of Chapter 4 can also be applied to Rice fading channels. It can calculate the optimal detection threshold for the actual Rice factor of the propagation channel, as will be shown subsequently. With this technique, the estimated differential correlation mean

$$|\widehat{m}_{\Psi,\mathrm{H}_0}|^2 = \frac{1}{\vartheta^4}\sqrt{2\,\mathcal{M}_1^2 - \mathcal{M}_2} \tag{8.17}$$

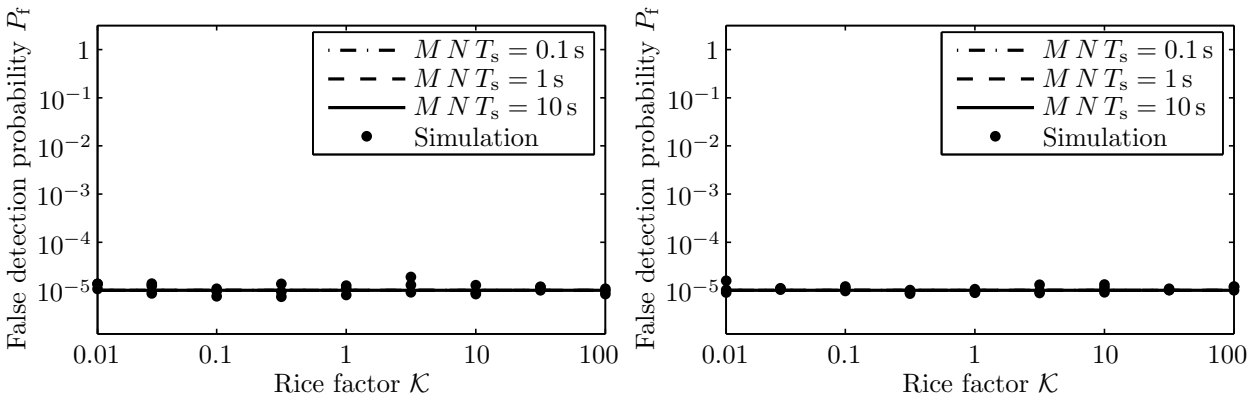

(a) GPS L1-C/A. (b) Galileo E1-C.

Figure 8.3: Probability of false detection with threshold adaptation for $T_0 = 290\,\mathrm{K}$, $F = 3\,\mathrm{dB}$, $N\,T_\mathrm{s} = 20\,\mathrm{ms}$, and $C/\mathcal{N}_0 = 45\,\mathrm{dBHz}$.

of (4.15) and the estimated differential correlation variance

$$\widehat{\sigma}^2_{\Psi,\mathrm{H}_0} = (M-1)\,\widehat{\sigma}^4_w + 2\,\widehat{\sigma}^2_w\,|\widehat{m}_{\Psi,\mathrm{H}_0}| \tag{8.18}$$

of (4.20) are calculated with help of the first moment

$$\mathcal{M}_1 = \frac{1}{D - 2\,\lceil T_\mathrm{c}/T_\mathrm{s}\rceil + 1}\left[\sum_{\nu=1}^{\hat{\imath}-\lceil T_\mathrm{c}/T_\mathrm{s}\rceil}\Lambda_\nu + \sum_{\nu=\hat{\imath}+\lceil T_\mathrm{c}/T_\mathrm{s}\rceil}^{D}\Lambda_\nu\right] \simeq \mathrm{E}\{\Lambda\}\,\big|_{\tau\neq\widehat{\tau}} \tag{8.19}$$

in (4.13), the second moment

$$\mathcal{M}_2 = \frac{1}{D - 2\,\lceil T_\mathrm{c}/T_\mathrm{s}\rceil + 1}\left[\sum_{\nu=1}^{\hat{\imath}-\lceil T_\mathrm{c}/T_\mathrm{s}\rceil}\Lambda^2_\nu + \sum_{\nu=\hat{\imath}+\lceil T_\mathrm{c}/T_\mathrm{s}\rceil}^{D}\Lambda^2_\nu\right] \simeq \mathrm{E}\big\{\Lambda^2\big\}\,\big|_{\tau\neq\widehat{\tau}} \tag{8.20}$$

in (4.14), and

$$\widehat{\sigma}^2_w = -\frac{\vartheta^2\,|\widehat{m}_{\Psi,\mathrm{H}_0}|}{M-1} + \sqrt{\frac{\vartheta^4\,|\widehat{m}_{\Psi,\mathrm{H}_0}|^2}{(M-1)^2} + \frac{\mathcal{M}_1 - \vartheta^4\,|\widehat{m}_{\Psi,\mathrm{H}_0}|^2}{(M-1)}}\,. \tag{8.21}$$

in (4.19). Fig. 8.2 compares the optimal detection threshold for RICE fading channels versus a simulation of the estimated threshold with (8.17) and (8.18). The simulation utilizes 1021×4 different code phase bins for the GPS L1-C/A signal and 4090×4 code phase bins for the Galileo E1-C signal, due to the front-end bandwidth of four times the chip rate. This corresponds to a simple full epoch code search and works well for the whole range of RICE factors. As can be seen in Fig. 8.2, the detection threshold for fading signals with a low RICE factor is higher than for non-fading signals with a very high RICE factor. Cross-correlation is not an issue here, since the multipath fading mitigation only increases the detection threshold and does not decrease it. The *adaptive detection threshold* method in Chapter 4, which actually decreases the threshold, already takes care of the cross-correlation. The simulated detection thresholds of Fig. 8.2 are furthermore translated into the resulting false detection probabilities in Fig. 8.3. It can be seen that the false alarm probability is kept constant at $P_\mathrm{f} = 10^{-5}$. This is the primary target of the multipath fading mitigation

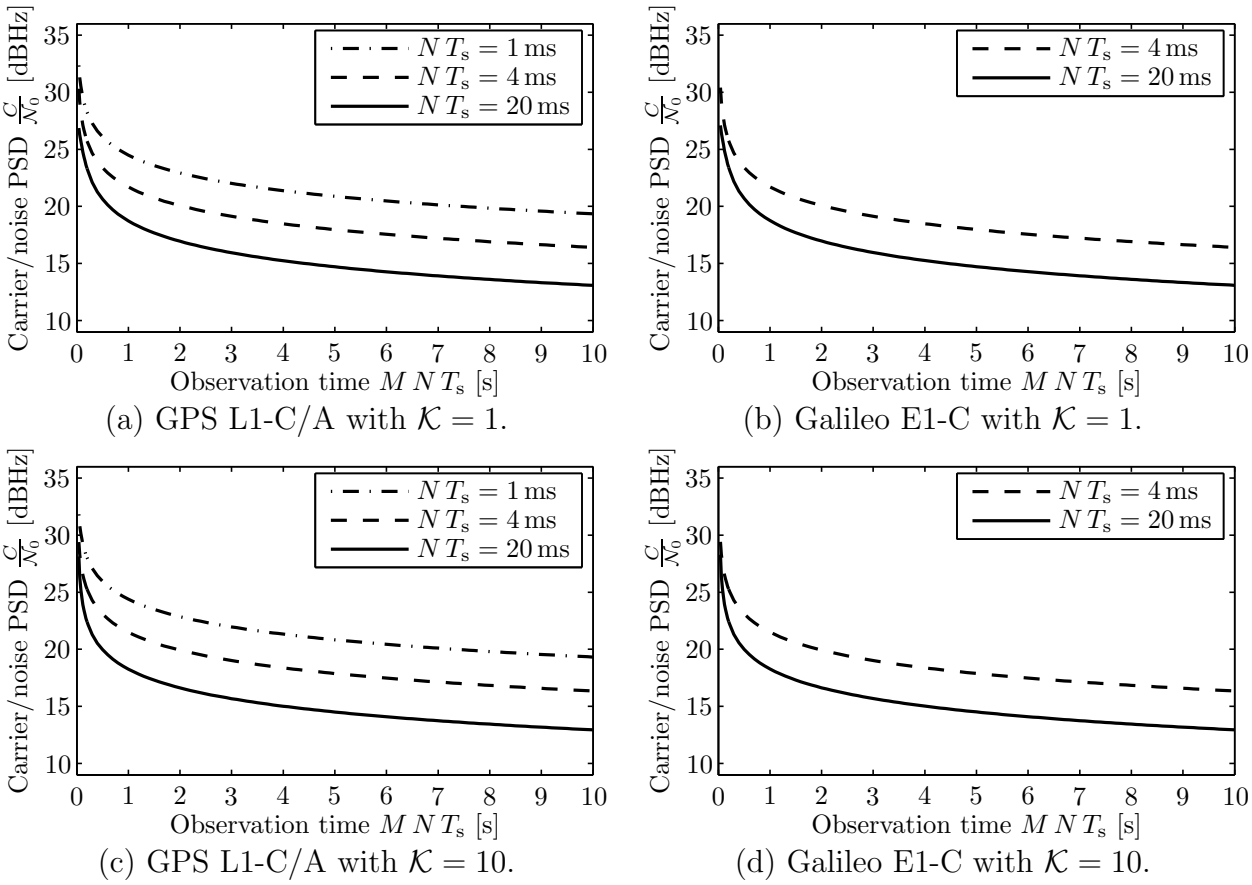

(a) GPS L1-C/A with $\mathcal{K} = 1$.

(b) Galileo E1-C with $\mathcal{K} = 1$.

(c) GPS L1-C/A with $\mathcal{K} = 10$.

(d) Galileo E1-C with $\mathcal{K} = 10$.

Figure 8.4: Reception sensitivity with the multipath fading mitigation technique for $T_0 = 290\,\mathrm{K}$, $F = 3\,\mathrm{dB}$, $P_\mathrm{f} = 10^{-5}$, and $P_\mathrm{d} = 90\,\%$.

technique. The simulations in Fig. 8.2 and 8.3 do not make use of any of the approximations in this thesis. They simulate the results for actual white GAUSSIAN noise samples combined with the Galileo/GPS satellite signal at the input of the receiver chain in Fig. 3.3. As can be seen, the simulations match very well with the theoretical derivations. Fig. 8.3 shows that the multipath fading mitigation works effectively. The RICE fading does not increase the probability of false acquisition any more, as previously in Fig. 8.1. The false alarm probability is at the permissable level of $P_\mathrm{f} = 10^{-5}$ for the whole range of different RICE factors.

8.3 Reception Sensitivity

Fig. 8.4 shows the reception sensitivity achieved by the optimal detection threshold λ of Fig. 8.2. The choice of the receiver parameters $T_0 = 290\,\mathrm{K}$, $F = 3\,\mathrm{dB}$, $P_\mathrm{f} = 10^{-5}$, and $P_\mathrm{d} = 90\,\%$ has been motivated in Section 3.7. The decision statistic

$$\boxed{\Lambda = |\Psi|^2 = \left| \sum_{\mu=1}^{M-1} s_\mu \, s_{\mu-1}^* \right|^2} \tag{8.22}$$

results in the detection probability

$$P_{\mathrm{d}} = \Pr\{\Lambda \geqslant \lambda | \mathrm{H}_1\} = 1 - P_{\Lambda|\mathrm{H}_1}(\lambda) = \mathrm{Q}_1\left(\sqrt{\frac{2\,|m_{\Psi,\mathrm{H}_1}|^2}{\sigma^2_{\Psi,\mathrm{H}_1}}}, \sqrt{\frac{2\,\lambda}{\sigma^2_{\Psi,\mathrm{H}_1}}}\right) \tag{8.23}$$

as specified in (3.66) by applying

$$m_{\Psi,\mathrm{H}_1} = m_{\Psi}\big|_{R^2(\tau-\widehat{\tau})=N^2}\,, \quad \sigma^2_{\Psi,\mathrm{H}_1} = \sigma^2_{\Psi}\big|_{R^2(\tau-\widehat{\tau})=N^2}\,. \tag{8.24}$$

The reception sensitivity in Fig. 8.4 corresponds to $P_{\mathrm{d}} = 90\,\%$. The figure is provided to show how the RICE fading influences the receiver sensitivity. It can be observed that the sensitivity degrades slightly for lower $\mathcal{K}$. However, this effect is barely noticeable since the degradation is really minor. The reason for it is the increase in detection threshold to prevent false acquisition due to fading behavior.

8.4 Conclusion

The presented *multipath fading mitigation* method estimates the optimal detection threshold for different fading channels. It dynamically adjusts well over a wide range of different RICE factors. The optimal detection threshold is lower for signals with a high RICE factor. A relevant multipath proportion leads to a low RICE factor and the optimal detection threshold is set at a higher level to prevent excessive false detections. If the detection threshold for a line-of-sight signal was applied to a strongly fading signal, false detections would occur frequently. The adaptive detection threshold technique therefore automatically calculates the optimal detection threshold for any RICE factor of the propagation channel.

Chapter 9

Conclusion

Location based services and emergency caller location require high service availability in deep urban and moderate indoor environments. Severe attenuation of Galileo/GPS signals in these environments mandates enhanced reception sensitivity. Long signal integration periods are the key to improving the reception sensitivity. However, the maximum coherent integration interval is limited by residual frequency deviation. The state-of-the-art enhanced sensitivity method is *noncoherent integration*, which tolerates a certain amount of frequency deviation.

This work has introduced the *differential correlation* technique. Because differential correlation multiplies statistically independent noise samples, it provides a sensitivity gain of 1.5–2.9 dB over the noncoherent integration. Additionally, differential correlation also provides an estimate of the residual frequency deviation. This property is utilized to build a *frequency offset correction* loop. It incrementally reduces the frequency deviation while the correlation process is ongoing. This in turn causes phase rotations within the correlation process. The *phase mismatch correction* resolves this issue. The incremental reduction of the frequency offset allows for an incremental extension of the coherent integration intervals. The *adaptive integration interval* technique causes very large phase fluctuations. The phase mismatch correction resolves this problem as well. All techniques combined advance the sensitivity gain to 17.3 dB beyond the published state-of-the-art method. However, this sensitivity gain can only be fully realized with an *adaptive detection threshold*. This thesis has therefore presented a method to estimate the mean and variance of the differential correlation result. It keeps a constant probability of false detection while maximizing the reception sensitivity. The differential correlation provides the strongest sensitivity gain for short observation intervals, while the frequency offset and phase mismatch corrections yield the highest benefit for intermediate observation periods. The adaptive integration interval and the adaptive detection threshold achieve the biggest improvement for long observation periods, where they provide the major share of the sensitivity gain.

At the same time, a sufficiently high positioning accuracy should be maintained to enable location based services and emergency caller location. The correlation scheme has an influence on the positioning accuracy. Each satellite to receiver distance is calculated based on the location of the correlation peak. As the satellite signal becomes weaker, the correlation function becomes noisier, which in turn leads to larger positioning errors. Since the

techniques of this thesis increase the correlation gain, positioning accuracy is also improved. The differential correlation by itself increases the accuracy of each satellite to receiver distance by 80 %. The combination of all techniques presented, improves the range accuracy by 483 %. While the benefit of the differential correlation and frequency offset correction is already present for short and intermediate observation periods, the adaptive integration interval yields the highest accuracy increase for long observation periods.

Urban and indoor environments frequently cause multipath fading signals, which leads to a substantially increased false alarm probability with state-of-the-art noncoherent integration. The adaptive detection threshold technique of this work, however, not only compensates for variations in the signal-to-noise ratio, it also mitigates the multipath fading behavior and maintains a constant false alarm probability.

Many location based services also require low power consumption. The major signal processing blocks of this thesis have therefore been implemented in a microchip design. The Appendix summarizes the resulting silicon area and power consumption. The phase mismatch correction rotates the correlation peak towards the inphase path. The subsequent quadrature path may then be omitted to reduce implementation expenses and current consumption with only minor impact on the reception sensitivity. The sensitivity gain may also be traded off to reduce the observation period and thereby the power consumption. If the noncoherent integration was also advanced with the adaptive detection threshold, the combined techniques of this thesis can still achieve the same reception sensitivity in only one tenth of the observation period.

In summary, the techniques presented in this thesis aim at improving the service availability, accuracy, and power efficiency of positioning with Galileo and GPS.

Appendix A

Semiconductor Implementation Characteristics

The mandate for emergency caller location and the prospected revenues with location based services increasingly leads to GPS receivers being integrated into cellular telephones. The majority of future Galileo receivers are also expected to become integrated into mobile phones. The size constraints of cellular phones require highly integrated semiconductor solutions. The most important requirement for a successful integration of a Galileo/GPS receiver into mobile phones is low cost. The cost of microchips can be reduced by shrinking the silicon area. This can be accomplished by the optimum choice of the quantization resolutions in the digital baseband section and by the reuse of hardware resources within the integrated circuits.

Since satellite navigation receivers for indoor applications are usually designed to host the equivalent of several thousand correlation channels, the benefit of reducing the bit sizes and reusing the signal processing blocks is substantial. The optimum quantization resolutions for the differential correlation technique, as well as for the state-of-the-art noncoherent integration method are therefore derived in this chapter. Furthermore, the required amount of signal processing units can be also substantially reduced. This is accomplished by operating the hardware resources with an increased clock rate and multiplexing different signal processing paths through the same hardware.

The implementation of the differential correlation and the noncoherent integration methods in hardware description language allows the synthesizing of the signal processing units into a complementary metal-oxide semiconductor (CMOS) technology. This chapter presents the resulting silicon area, power consumption, quantization loss, and timing characteristics for a 90 nm CMOS process. In order to obtain these results, the respective floating point algorithms are first converted into a fixed point representation and then implemented with the Verilog hardware description language. The units are verified with the Mentor Graphics ModelSim before they are synthesized into digital CMOS circuits with the Synopsys Design Compiler. This tool allows the analysis of the circuit timing characteristics and the silicon area. Based on the synthesis results, the power consumption of the silicon circuits is simulated with the Sequence Power Theater.

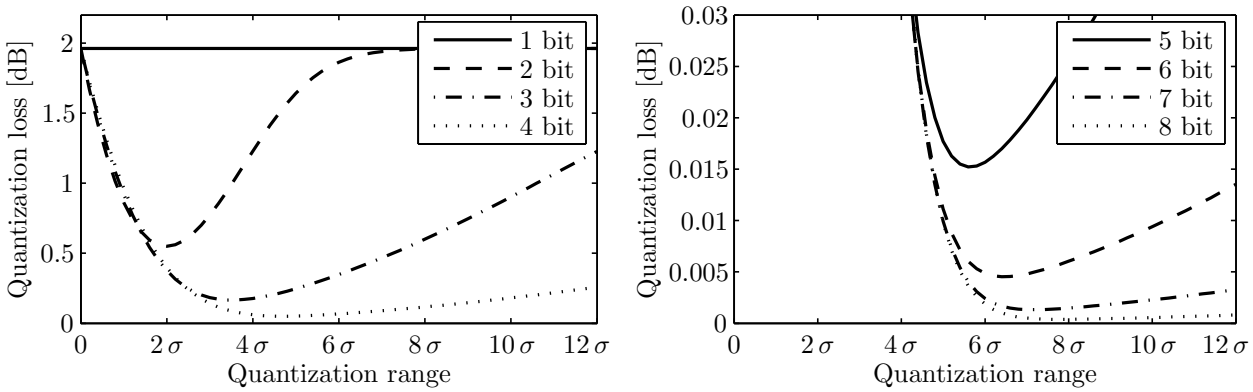

(a) 1–4 bit resolution. (b) 5–8 bit resolution.

Figure A.1: Quantization loss for a uniform ADC with mid-riser characteristic.

The simulations begin with low clock frequencies and extend up to extremely high clock frequencies, as long as the timing slack remains positive. The inputs of all units are directly connected to the processing logic and the output signals are stored into flip-flops. This allows the different units to operate asynchronously from each other, where the signal requires one clock period to propagate through each processing block.

A.1 Analog to Digital Conversion

The differential correlation technique and the noncoherent integration method use the same signal processing chain up to the coherently integrated predetection results. The choice of the quantization resolution for the Analog-to-Digital Conversion (ADC) is determined by the trade-off between the implementation complexity and Signal-to-Noise Ratio (SNR) degradation. High quantization resolutions offer lower SNR degradation, but introduce substantial implementation expenses. This is because they require every consecutive digital signal processing stage to operate with correspondingly larger bit ranges. Fig. A.1 shows the quantization loss for a uniform ADC with mid-riser characteristic as a function of the number of output bits. The quantization range is given as a multiple of the input standard deviation σ. The optimal quantization range for signals with very low SNR depends almost entirely on the standard deviation of the input signal, which is denoted by σ in Fig. A.1.

Table A.1 summarizes the optimum quantization range and the resulting implementation degradation for a given number of output bits. The output quantization resolution specifies how many bits are used to decode the output signal, the quantization range specifies which range is covered before the saturation takes place, and the quantization loss specifies the resulting SNR degradation.

A.2 Despreading

The despreading stage does not cause any implementation loss, as it only multiplies the input signal with a series of ± 1. If the signal encoding is chosen symmetrical around zero with a

Output quantization resolution	Optimal quantization range	Minimal quantization loss
1 bit	n/a	1.96 dB
2 bit	[-0.99 σ, 0.99 σ]	0.55 dB
3 bit	[-1.76 σ, 1.76 σ]	0.17 dB
4 bit	[-2.35 σ, 2.35 σ]	0.050 dB
5 bit	[-2.82 σ, 2.82 σ]	0.015 dB
6 bit	[-3.23 σ, 3.23 σ]	0.0045 dB
7 bit	[-3.58 σ, 3.58 σ]	0.0013 dB
8 bit	[-3.93 σ, 3.93 σ]	0.00038 dB

Table A.1: Quantization characteristics for the ADC unit.

Silicon area	Timing slack	Leakage power	Dynamic power
51.7 μm^2	$T_\mathrm{s} - 0.175\,\mathrm{ns}$	30.1 nW	$\frac{9.49 \times 10^{-14}\,\mathrm{W}}{T_\mathrm{s}}$

Table A.2: Synthesis results for the despreading unit.

Silicon area	Timing slack	Leakage power	Dynamic power
458 μm^2	$T_\mathrm{s} - 0.585\,\mathrm{ns}$	244 nW	$\frac{5.31 \times 10^{-13}\,\mathrm{W}}{T_\mathrm{s}}$

Table A.3: Synthesis results for the Gold code generation unit.

single bit marking the sign and the remaining bits the magnitude, then the despreading stage has to only perform an exclusive-or (XOR) operation between the input signal bit and the despreading code. Table A.2 shows the total silicon area, power consumption, and timing slack for different clock frequencies of the despreading unit.

The results show that a single despreading unit could in principle support the entire search of all code delays. The received signal would be applied at the input and the entire reference code would be stepped through within one chip period of the received signal. During the next chip period of the received signal, the reference code would start with a shift of one chip and again step through the entire code. The reference code generator would thus have to run through the entire code plus one chip within the period of one chip of the received signal. Table A.3 presents the implementation characteristics of the GPS L1-C/A Gold code generator for different clock frequencies. It shows that the code generator could in principle also support this multiplexing scheme where the despreading and code generation unit are reused for the despreading with all code delays.

	Accumulation number	Output quantization resolution	Output quantization range	Theoretical quantization loss	Simulated quantization loss
GPS L1-C/A	2045	6 bit	[-2047, 2047]	0.063 dB	0.060 dB
GPS L1-C/A	40900	6 bit	[-4095, 4095]	0.013 dB	0.014 dB
Galileo E1-C	8180	6 bit	[-4095, 4095]	0.063 dB	0.063 dB
Galileo E1-C	40900	6 bit	[-4095, 4095]	0.013 dB	0.016 dB

Table A.4: Quantization characteristics for the coherent accumulation unit.

Silicon area	Timing slack	Leakage power	Dynamic power
$760\,\mu\mathrm{m}^2$	$T_\mathrm{s} - 2.89\,\mathrm{ns}$	485 nW	$\frac{1.06 \times 10^{-12}\,\mathrm{W}}{T_\mathrm{s}}$

Table A.5: Synthesis results for the coherent accumulation unit.

	Output quantization resolution	Output quantization range	Theoretical quantization loss	Simulated quantization loss
GPS L1-C/A	8 bit	[-1023, 1023]	0.010 dB	0.010 dB
GPS L1-C/A	8 bit	[-1023, 1023]	0.008 dB	0.008 dB
Galileo E1-C	8 bit	[-1023, 1023]	0.005 dB	0.005 dB
Galileo E1-C	8 bit	[-1023, 1023]	0.010 dB	0.011 dB

Table A.6: Quantization characteristics for the differential product unit.

A.3 Coherent Accumulation

The coherent accumulation stage integrates N samples of the input signal. The output requires a higher quantization resolution than the input, because the signal-to-noise ratio is also higher at the output. Furthermore, due to the increased mean and standard deviation at the output, a quantization step size larger than one is required. Table A.4 summarizes the quantization characteristics and the resulting loss for the coherent accumulation. Table A.5 presents the results of the semiconductor synthesis of the coherent accumulation unit.

A.4 Differential Product

The differential product unit multiplies each input sample with the complex-conjugate of the previous input sample. The complex-valued differential product is implemented with three multiplications, one addition, and two subtractions. In order to reduce the silicon area, the three multiplication operations are calculated by a single multiplier in time multiplex operation. Table A.6 summarizes the quantization results for the differential product and Table A.7 presents the synthesis results.

Silicon area	Timing slack	Leakage power	Dynamic power
$4839\,\mu\mathrm{m}^2$	$T_\mathrm{s} - 3.73\,\mathrm{ns}$	$3.13\,\mu\mathrm{W}$	$\frac{3.35 \times 10^{-12}\,\mathrm{W}}{T_\mathrm{s}}$

Table A.7: Synthesis results for the differential product unit.

	Accumulation number	Output quantization resolution	Output quantization range	Theoretical quantization loss	Simulated quantization loss
GPS L1-C/A	100	8 bit	[-511, 511]	0.001 dB	0.002 dB
Galileo E1-C	100	8 bit	[-511, 511]	0.002 dB	0.002 dB

Table A.8: Quantization characteristics for the differential accumulation unit.

Silicon area	Timing slack	Leakage power	Dynamic power
$895\,\mu\mathrm{m}^2$	$T_\mathrm{s} - 2.06\,\mathrm{ns}$	530 nW	$\frac{9.82 \times 10^{-13}\,\mathrm{W}}{T_\mathrm{s}}$

Table A.9: Synthesis results for the differential accumulation unit.

A.5 Differential Accumulation

The differential products are further accumulated to form the differential correlation result. Since the differential correlation result is then processed in software, the output resolution of the differential accumulation stage is 8 bit, which results in an additional quantization loss of just around 0.002 dB. The quantization characteristics of the differential accumulation unit are summarized in Table A.8, while the synthesis results are presented in Table A.9.

A.6 Squared Magnitude

The inphase and quadrature components of the input are squared and added together by the squared magnitude stage. The internal squaring hardware is thereby reused for both squaring operations in time multiplex mode. Table A.10 shows the quantization results, while Table A.11 summarizes the CMOS semiconductor synthesis outcome.

A.7 Noncoherent Accumulation

The final step for the noncoherent integration method is to raise the signal-to-noise ratio of the detection statistic by means of noncoherent accumulation. This accumulator hardware only has to process positive numbers, since its input is supplied from the squared magnitude unit. It can hence be implemented with less silicon area than the differential accumulation unit. The silicon area is displayed in Table A.13 together with the timing and power characteristics, while the quantization loss is found in Table A.12.

	Output quantization resolution	Output quantization range	Theoretical quantization loss	Simulated quantization loss
GPS L1-C/A	7 bit	$[0, 1023]$	0.005 dB	0.004 dB
GPS L1-C/A	7 bit	$[0, 1023]$	0.004 dB	0.012 dB
Galileo E1-C	7 bit	$[0, 1023]$	0.002 dB	0.001 dB
Galileo E1-C	7 bit	$[0, 1023]$	0.005 dB	0.014 dB

Table A.10: Quantization characteristics for the squared magnitude unit.

Silicon area	Timing slack	Leakage power	Dynamic power
$876\,\mu\text{m}^2$	$T_\text{s} - 1.84\,\text{ns}$	555 nW	$\frac{1.3 \times 10^{-12}\,\text{W}}{T_\text{s}}$

Table A.11: Synthesis results for the squared magnitude unit.

	Accumulation number	Output quantization resolution	Output quantization range	Theoretical quantization loss	Simulated quantization loss
GPS L1-C/A	100	8 bit	$[0, 2047]$	0.003 dB	0.003 dB
Galileo E1-C	100	8 bit	$[0, 2047]$	0.003 dB	0.003 dB

Table A.12: Quantization characteristics for the noncoherent accumulation unit.

Silicon area	Timing slack	Leakage power	Dynamic power
$721\,\mu\text{m}^2$	$T_\text{s} - 2\,\text{ns}$	416 nW	$\frac{8.73 \times 10^{-13}\,\text{W}}{T_\text{s}}$

Table A.13: Synthesis results for the noncoherent accumulation unit.

A.8 Conclusion

The Appendix presents the semiconductor implementation characteristics for differential correlation and noncoherent integration. The quantization resolutions are a trade-off between maximizing the signal-to-noise ratio and minimizing the silicon area. The resulting quantization degradation is sufficiently low for enhanced sensitivity Galileo/GPS receivers. A large number of correlation results can be calculated simultaneously by running the hardware units with an increased clock rate and multiplexing the data streams. The timing slack of the CMOS synthesis results can be analyzed in order to estimate the degree of parallelization required for single shot positioning. When compared with the desired sample rates, the timing slack indicates how many correlation channels can be served in parallel by the respective unit. The simulations of the power consumption allow an estimate of the battery drain by the receiver circuit. The silicon area does not increase with the clock frequency as long as the timing slack is positive. Combined with the required degree of parallelization, the synthesized silicon area is important for the business case of the microchip.

Acronyms, Mathematical Symbols, and Variables

Acronyms

3D	three-dimensional (p. 12)
ADC	Analog to Digital Conversion (p. 122)
BOC	Binary Offset Carrier (p. 15)
BPSK	Binary Phase Shift Keying (p. 16)
dB	decibel (p. 1)
dBHz	Hertz in decibel (p. 31)
dBm	miliwatt in decibel (p. 1)
FFT	Fast Fourier Transform (p. 9)
GPS	Global Positioning System (p. 1)
GSM	Global System for Mobile Communications (p. 1)
Hz	Hertz (p. 16)
K	Kelvin (p. 18)
kHz	kilohertz (p. 6)
km	kilometer (p. 5)
m	meter (p. 12)
MAP	Maximum A Posteriori (p. 6)
MHz	Megahertz (p. 6)
ML	Maximum Likelihood (p. 6)
MMSE	Minimum Mean Squared Error (p. 6)
ms	millisecond (p. 7)
mW	milliwatt (p. 1)
nW	nanowatt (p. 7)
PSD	Power Spectral Density (p. 16)
RF	Radio Frequency (p. 8)
s	second (p. 5)
SNR	Signal-to-Noise Ratio (p. 122)
UMTS	Universal Mobile Telecommunications Services (p. 1)
W	Watt (p. 1)
WLSE	Weighted Least Square Error (p. 5)

Mathematical Symbols

$\operatorname{argmax}(\cdot)$	maximum argument (p. 6, eq. 2.10)
$\operatorname{argmin}(\cdot)$	minimum argument (p. 5, eq. 2.8)
$\cos(\cdot)$	sinus function (p. 17, eq. 3.4)
$\delta(\cdot)$	DIRAC delta distribution (p. 24, eq. 3.44)
$\operatorname{erfc}(\cdot)$	complementary error function (p. 69, eq. 5.17)
$\exp(\cdot)$	exponential function (p. 18, eq. 3.10)
$\mathrm{E}\{\cdot\}$	expectation value (p. 18, eq. 3.11)
$\Gamma(\cdot)$	GAMMA function (p. 27, eq. 3.56)
$\Im\{\cdot\}$	imaginary part (p. 18, eq. 3.10)
$\mathrm{I}_\kappa(\cdot)$	modified BESSEL function of the first kind and order κ (p. 27, eq. 3.57)
j	complex operator $\sqrt{-1}$ (p. 17, eq. 3.8)
J	JACOBIAN determinant (p. 68, eq. 5.9)
$\mathrm{K}_0(\cdot)$	modified BESSEL function of the second kind and zero order (p. 24, eq. 3.45)
m_α	expectation value of α (p. 23, eq. 3.38)
$\Pr\{\cdot\}$	probability (p. 29, eq. 3.63)
$p_\alpha(\cdot)$	probability density function of α (p. 24, eq. 3.44)
$P_\alpha(\cdot)$	cumulative probability density function of α (p. 50, eq. 4.3)
$\Phi(\mathrm{j}\,\omega)$	characteristic function (p. 42, eq. 3.104)
$\mathrm{Q}_\kappa(\cdot,\,\cdot)$	MARCUM-Q function of order κ (p. 28, eq. 3.59)
$\mathrm{Q}^{-1}_{\kappa,\beta}(\cdot,\,\cdot)$	inverse κ-th order MARCUM-Q function with respect to its second argument (p. 30, eq. 3.65)
$\operatorname{rect}(\cdot)$	rectangular function (p. 17, eq. 3.6)
$\Re\{\cdot\}$	real part (p. 6, eq. 2.10)
$\mathbb{R}^3$	three-dimensional real number space (p. 5)
$\operatorname{sign}(\cdot)$	signum function (p. 15, eq. 3.3)
$\sin(\cdot)$	sinus function (p. 15, eq. 3.3)
$\operatorname{sinc}(\alpha)$	sinus of $\pi\,\alpha$ divided by $\pi\,\alpha$ (p. 20, eq. 3.26)
σ_α	standard deviation of α (p. 5, eq. 2.8)
z^{-1}	delay element (p. 14)
$\mathbb{Z}$	integer number space (p. 4)
$\simeq$	approximately equal (p. 5, eq. 2.4)
$(\cdot)^*$	complex conjugate (p. 14)
$\hat{\alpha}$	estimated value of α (p. 5, eq. 2.8)
$\|\cdot\|_2$	EUCLIDIAN norm (p. 5, eq. 2.2)
$\|\cdot\|$	magnitude (p. 5, eq. 2.7)
$\pm$	plus or minus (p. 6)
$\langle\cdot\rangle$	rounding to the nearest integer (p. 5, eq. 2.6)
$\lfloor\cdot\rfloor$	rounding to the nearest integer less or equal (p. 9, eq. 2.13)
$\lceil\cdot\rceil$	rounding to the nearest integer more or equal (p. 56, eq. 4.13)

Latin Variables

B	front-end bandwidth (p. 18, eq. 3.11)
c	speed of light (p. 5, eq. 2.2)
$c(t)$	time-continuous spreading code (p. 20, eq. 3.28)
c_ν	sampled spreading code (p. 15, eq. 3.1)
C	carrier power (p. 15, eq. 3.1)
C_D	carrier power for $P_\mathrm{d} = 90\,\%$ with differential correlation (p. 31)
$C_\mathrm{F,A}$	carrier power for $P_\mathrm{d} = 90\,\%$ with frequency offset correction using method A (p. 74)
$C_\mathrm{F,B}$	carrier power for $P_\mathrm{d} = 90\,\%$ with frequency offset correction using method B (p. 74)
$C_\mathrm{I,A}$	carrier power for $P_\mathrm{d} = 90\,\%$ with adaptive integration interval using method A (p. 102)
$C_\mathrm{I,B}$	carrier power for $P_\mathrm{d} = 90\,\%$ with adaptive integration interval using method B (p. 102)
C_N	carrier power for $P_\mathrm{d} = 90\,\%$ with noncoherent integration (p. 35)
$C_\mathrm{P,A}$	carrier power for $P_\mathrm{d} = 90\,\%$ with phase mismatch correction using method A (p. 89)
$C_\mathrm{P,B}$	carrier power for $P_\mathrm{d} = 90\,\%$ with phase mismatch correction using method B (p. 89)
$C_\mathrm{T,D}$	carrier power for $P_\mathrm{d} = 90\,\%$ with adaptive detection threshold for differential correlation (p. 59)
$C_\mathrm{T,E}$	carrier power for $P_\mathrm{d} = 90\,\%$ with adaptive detection threshold and estimation error (p. 60)
$C_\mathrm{T,N}$	carrier power for $P_\mathrm{d} = 90\,\%$ with adaptive detection threshold for noncoherent integration (p. 61)
$d_{\mathrm{s},\mu}$	data bit stream after coherent integration (p. 19, eq. 3.21)
d_μ	data bit stream (p. 15, eq. 3.1)
D	number of code phase bins of the receiver (p. 9)
f	frequency (p. 18, eq. 3.9)
f_c	carrier frequency (p. 17, eq. 3.4)
f_d	frequency deviation (p. 18, eq. 3.9)
$f_{\mathrm{d},\kappa}$	time-variant frequency deviation (p. 67, eq. 5.2)
f_D	Doppler frequency shift (p. 17, eq. 3.4)
f_LO	local oscillator frequency (p. 9, eq. 2.12)
$f_{\mathrm{LO},\kappa}$	time-variant local oscillator frequency (p. 70, eq. 5.24)
F	front-end noise figure (p. 18, eq. 3.11)
G	number of spreading code periods per data bit period (p. 15, eq. 3.2)
H_0	hypothesis 0 (p. 29, eq. 3.62)
H_1	hypothesis 1 (p. 29, eq. 3.62)
k	Boltzman constant (p. 18, eq. 3.12)
K	third accumulation number (p. 71, eq. 5.28)
$\mathcal{K}$	Rice factor (p. 113, eq. 8.5)

K_S	number of visible satellites (p. 5, eq. 2.8)
L	primary spreading code length (p. 4, eq. 2.1)
$m_{\widehat{f}_{\mathrm{d},\kappa}}$	expectation value of the estimated frequency deviation (p. 69, eq. 5.22)
m_Δ	expectation value of the discrimination function (p. 39, eq. 3.84)
$m_{\Delta,\mathrm{A}}$	expectation value of the discrimination function for method A (p. 79, eq. 5.52)
$m_{\Delta,\mathrm{B}}$	expectation value of the discrimination function for method B (p. 80, eq. 5.58)
$m_{\Lambda,\mathrm{E}}$	expectation value of the early decision statistic (p. 39, eq. 3.79)
$m_{\Lambda,\mathrm{L}}$	expectation value of the late decision statistic (p. 39, eq. 3.81)
$m_{\widehat{\phi}_\kappa}$	expectation value of the estimated phase of the differential correlation result (p. 88, eq. 6.5)
m_Ψ	expectation value of the differential correlation result (p. 22, eq. 3.33)
$m_{\Psi,\mathrm{E}}$	expectation value of the early differential correlation result (p. 39, eq. 3.80)
m_{Ψ,H_0}	expectation value of the differential correlation result for hypothesis 0 (p. 29, eq. 3.64)
m_{Ψ,H_1}	expectation value of the differential correlation result for hypothesis 1 (p. 30, eq. 3.67)
$m_{\Psi,\mathrm{L}}$	expectation value of the late differential correlation result (p. 39, eq. 3.82)
$m_{\widehat{\tau}}$	expectation value of the estimated code delay (p. 40, eq. 3.90)
m_θ	expectation value of a Gaussian distributed variable (p. 113, eq. 8.1)
m_Υ	expectation value of the final differential correlation result (p. 71, eq. 5.31)
$m_{\Upsilon,\mathrm{E}}$	expectation value of the early final differential correlation result (p. 79, eq. 5.50)
$m_{\Upsilon,\mathrm{H}_0}$	expectation value of the final differential correlation result for hypothesis 0 (p. 74, eq. 5.39)
$m_{\Upsilon,\mathrm{H}_1}$	expectation value of the final differential correlation result for hypothesis 1 (p. 74, eq. 5.41)
$m_{\Upsilon,\mathrm{L}}$	expectation value of the late final differential correlation result (p. 79, eq. 5.51)
M	second accumulation number (p. 10, eq. 2.15)
M_κ	time-variant second accumulation number (p. 100, eq. 7.4)
$\mathcal{M}_1$	first moment (p. 56, eq. 4.13)
$\mathcal{M}_2$	second moment (p. 56, eq. 4.14)
n	additive white Gaussian noise in lowpass equivalent notation (p. 18, eq. 3.10)
n_bp	additive white Gaussian noise in bandpass notation (p. 17, eq. 3.4)
n_ν	sampled additive white Gaussian noise in lowpass equivalent notation (p. 17, eq. 3.8)
N	coherent accumulation number (p. 9, eq. 2.13)
$\mathcal{N}_0$	noise power spectral density (p. 18, eq. 3.12)
N_κ	time-variant coherent accumulation number (p. 100, eq. 7.3)
N_max	maximum coherent integration number (p. 100, eq. 7.3)
$p(t)$	spreading pulse form (p. 15, eq. 3.1)

$\mathbf{p}_\mathrm{a}$	approximate receiver location (p. 5, eq. 2.4)
$p_n(\,\cdot\,,\,\cdot\,)$	probability distribution of the complex-valued GAUSSIAN noise (p. 18, eq. 3.10)
$\mathbf{p}_\mathrm{r}$	receiver location (p. 5, eq. 2.2)
$\mathbf{p}_\mathrm{s}^{(\kappa)}$	satellite location (p. 5, eq. 2.2)
$p_\gamma(\,\cdot\,)$	normal product distribution (p. 24, eq. 3.44)
$p_\Lambda(\,\cdot\,)$	probability distribution of the decision statistic (p. 27, eq. 3.55)
$p_{\widehat{\phi}_\kappa}(\,\cdot\,)$	probability distribution of the estimated phase of the intermediate differential correlation result (p. 68, eq. 5.15)
$p_{\Psi_\kappa}(\,\cdot\,,\,\cdot\,)$	probability distribution of the intermediate differential correlation result (p. 68, eq. 5.10)
$p_{\lvert\theta\rvert}(\,\cdot\,)$	RICE distribution (p. 113, eq. 8.3)
P_d	probability of detection (p. 30, eq. 3.66)
$P_\mathrm{d,A}$	probability of detection for method A (p. 74, eq. 5.40)
$P_\mathrm{d,B}$	probability of detection for method B (p. 74, eq. 5.45)
P_f	probability of false detection (p. 29, eq. 3.63)
$P_\mathrm{f,A}$	probability of false detection for method A (p. 73, eq. 5.38)
$P_\mathrm{f,B}$	probability of false detection for method B (p. 74, eq. 5.42)
$P_\Lambda(\,\cdot\,)$	cumulative probability distribution of the decision statistic (p. 28, eq. 3.58)
$q(t)$	time-continuous BOC subcarrier (p. 15, eq. 3.3)
q_ν	sampled BOC subcarrier (p. 17, eq. 3.8)
$r(t)$	time-continuous received signal in lowpass equivalent notation (p. 6, eq. 2.9)
$r_\mathrm{bp}(t)$	time-continuous received signal in bandpass notation (p. 17, eq. 3.4)
r_ν	sampled received signal in lowpass equivalent notation (p. 17, eq. 3.8)
$R(\,\cdot\,)$	correlation function (p. 20, eq. 3.28)
$R_0(\,\cdot\,)$	correlation function for the coherent integration number N_0 (p. 101, eq. 7.5)
R_m	maximum out-of-phase autocorrelation value (p. 21)
s_μ	predetection samples (p. 18, eq. 3.14)
t	time (p. 5, eq. 2.2)
t_0	transmission time (p. 4, eq. 2.1)
t_a	approximate time (p. 5, eq. 2.5)
t_ϵ	satellite clock error (p. 4, eq. 2.1)
T_0	noise temperature (p. 18, eq. 3.12)
T_c	spreading chip period (p. 4, eq. 2.1)
T_d	data bit period (p. 15, eq. 3.1)
T_i	coherent integration period (p. 6, eq. 2.9)
T_t	total observation period (p. 102, eq. 7.11)
T_p	propagation period (p. 17, eq. 3.4)
T_s	sample period (p. 9, eq. 2.12)
u	GAUSSIAN distributed part of the differential correlation result (p. 22, eq. 3.34)
U	secondary spreading code length (p. 16)
v	normal product distributed part of the differential correlation result (p. 22, eq. 3.35)

w_μ	zero-mean white GAUSSIAN noise component of the predetection samples (p. 19, eq. 3.16)
$x(t)$	time-continuous transmit signal in lowpass equivalent notation (p. 15, eq. 3.1)
y_μ	deterministic signal component of the predetection samples (p. 21, eq. 3.31)
y_{μ,H_0}	deterministic signal component of the predetection samples for hypothesis 0 (p. 33, eq. 3.71)
y_{μ,H_1}	deterministic signal component of the predetection samples for hypothesis 1 (p. 33, eq. 3.73)
Y	number of frequency bins of the receiver (p. 9, eq. 2.12)

Greek Variables

α	function variable (p. 20, eq. 3.26)
β	function variable (p. 21, eq. 3.29)
δ	distance between the early and late code delay (p. 39, eq. 3.86)
Δ	code discrimination function (p. 39, eq. 3.83)
η	correction factor for BPSK or BOC modulation (p. 40, eq. 3.93)
ι	correlation path index (p. 9, eq. 2.13)
κ	sample index (p. 66, eq. 5.1)
λ	detection threshold (p. 29, eq. 3.62)
λ_A	detection threshold for method A (p. 73, eq. 5.38)
λ_B	detection threshold for method B (p. 74, eq. 5.44)
Λ	decision statistic (p. 9, eq. 2.14)
Λ_A	decision statistic for method A (p. 73, eq. 5.36)
Λ_B	decision statistic for method B (p. 73, eq. 5.37)
Λ_E	early decision statistic (p. 39, eq. 3.79)
Λ_L	late decision statistic (p. 39, eq. 3.81)
μ	sample index (p. 9, eq. 2.13)
ν	sample index (p. 9, eq. 2.13)
Ω	digital down-conversion factor (p. 9, eq. 2.12)
Ω_κ	time-variant digital down-conversion factor (p. 71, eq. 5.26)
ϕ_κ	phase of the intermediate differential correlation result (p. 68, eq. 5.8)
Ψ	differential correlation result (p. 22, eq. 3.32)
Ψ_E	early differential correlation result (p. 39, eq. 3.79)
Ψ_L	late differential correlation result (p. 39, eq. 3.81)
Ψ_κ	intermediate differential correlation result (p. 66, eq. 5.1)
ρ	distance between receiver and satellite (p. 5, eq. 2.2)
σ_n	standard deviation of the additive white GAUSSIAN noise (p. 18, eq. 3.11)
$\sigma_{\widehat{f}_{\mathrm{d},\kappa}}$	standard deviation of the estimated frequency deviation (p. 69, eq. 5.23)
σ_w	standard deviation of the noise component of the predetection samples (p. 19, eq. 3.19)

σ_{Δ} standard deviation of the discrimination function (p. 41, eq. 3.99)

$\sigma_{\Delta,\mathrm{A}}$ standard deviation of the discrimination function for method A (p. 79, eq. 5.49)

$\sigma_{\Delta,\mathrm{B}}$ standard deviation of the discrimination function for method B (p. 80, eq. 5.56)

$\sigma_{\widehat{\phi}_\kappa}$ standard deviation of the estimated phase of the intermediate differential correlation result (p. 88, eq. 6.6)

σ_{Ψ} combined standard deviation of the inphase and quadrature components of the differential correlation result (p. 26, eq. 3.51)

$\sigma_{\Psi,\mathrm{E}}$ combined standard deviation of the inphase and quadrature components of the early differential correlation result (p. 39, eq. 3.80)

$\sigma_{\Psi,\mathrm{H}_0}$ combined standard deviation of the inphase and quadrature components of the differential correlation result for hypothesis 0 (p. 29, eq. 3.64)

$\sigma_{\Psi,\mathrm{H}_1}$ combined standard deviation of the inphase and quadrature components of the differential correlation result for hypothesis 1 (p. 30, eq. 3.67)

$\sigma_{\Psi,\mathrm{I}}$ standard deviation of the inphase component of the differential correlation result (p. 26, eq. 3.49)

$\sigma_{\Psi,\mathrm{L}}$ combined standard deviation of the inphase and quadrature components of the late differential correlation result (p. 39, eq. 3.82)

$\sigma_{\Psi,\mathrm{Q}}$ standard deviation of the quadrature component of the differential correlation result (p. 26, eq. 3.50)

$\sigma_{\widehat{\rho}}$ standard deviation of the range estimate (p. 43, eq. 3.109)

$\sigma_{\widehat{\rho},\mathrm{D}}$ standard deviation of the range estimate for differential correlation (p. 43, eq. 3.109)

$\sigma_{\widehat{\rho},\mathrm{F,A}}$ standard deviation of the range estimate for frequency offset correction with method A (p. 79, eq. 5.48)

$\sigma_{\widehat{\rho},\mathrm{F,B}}$ standard deviation of the range estimate for frequency offset correction with method B (p. 80, eq. 5.55)

$\sigma_{\widehat{\rho},\mathrm{I,A}}$ standard deviation of the range estimate for adaptive integration interval with method A (p. 104)

$\sigma_{\widehat{\rho},\mathrm{I,B}}$ standard deviation of the range estimate for adaptive integration interval with method B (p. 107)

$\sigma_{\widehat{\rho},\mathrm{N}}$ standard deviation of the range estimate for noncoherent integration (p. 46, eq. 3.122)

$\sigma_{\widehat{\rho},\mathrm{P,A}}$ standard deviation of the range estimate for phase mismatch correction with method A (p. 94, eq. 6.5)

$\sigma_{\widehat{\rho},\mathrm{P,B}}$ standard deviation of the range estimate for phase mismatch correction with method B (p. 94, eq. 6.5)

$\sigma_{\widehat{\tau}}$ standard deviation of the estimated code delay (p. 40, eq. 3.91)

σ_{θ} standard deviation of a Gaussian distributed variable (p. 113, eq. 8.2)

σ_{Υ} combined standard deviation of the inphase and quadrature components of the final differential correlation result (p. 72, eq. 5.32)

$\sigma_{\Upsilon,\mathrm{E}}$ combined standard deviation of the inphase and quadrature components of the early final differential correlation result (p. 79, eq. 5.50)

$\sigma_{\Upsilon,\mathrm{H}_0}$ combined standard deviation of the inphase and quadrature components of the final differential correlation result for hypothesis 0 (p. 74, eq. 5.39)

$\sigma_{\Upsilon,\mathrm{H}_1}$ combined standard deviation of the inphase and quadrature components of the final differential correlation result for hypothesis 1 (p. 74, eq. 5.41)

$\sigma_{\Upsilon,\mathrm{I}}$ standard deviation of the inphase component of the final differential correlation result (p. 73, eq. 5.35)

$\sigma_{\Upsilon,\mathrm{I,E}}$ standard deviation of the inphase component of the early final differential correlation result (p. 80, eq. 5.57)

$\sigma_{\Upsilon,\mathrm{I},\mathrm{H}_0}$ standard deviation of the inphase component of the final differential correlation result for hypothesis 0 (p. 74, eq. 5.43)

$\sigma_{\Upsilon,\mathrm{I},\mathrm{H}_1}$ standard deviation of the inphase component of the final differential correlation result for hypothesis 1 (p. 74, eq. 5.46)

$\sigma_{\Upsilon,\mathrm{I,L}}$ standard deviation of the inphase component of the late final differential correlation result (p. 80, eq. 5.57)

$\sigma_{\Upsilon,\mathrm{L}}$ combined standard deviation of the inphase and quadrature components of the late final differential correlation result (p. 79, eq. 5.51)

τ code phase (p. 4, eq. 2.1)

τ_ϵ initial mean code phase estimation error (p. 39, eq. 3.85)

τ_E early code phase (p. 39, eq. 3.80)

τ_L late code phase (p. 39, eq. 3.82)

θ GAUSSIAN distributed variable (p. 113, eq. 8.1)

φ_c carrier phase (p. 17, eq. 3.4)

φ_μ phase of the deterministic signal component of the predetection samples (p. 71, eq. 5.30)

ς integer multiple (p. 4, eq. 2.1)

ϑ scaling factor (p. 57, eq. 4.15)

Bibliography

[1] W. C. Stone, "Electromagnetic signal attenuation in construction materials," NISTIR 6055, National Institute of Standards, USA, Gaithersburg, MD, USA, 1997.

[2] G. MacGougan, G. Lachapelle, R. Klukas, K. Siu, L. Garin, J. Shewfelt, and G. Cox, "Performance analysis of a stand-alone high-sensitivity receiver," *GPS Solutions*, vol. 6, no. 3, pp. 179–195, Dec. 2002.

[3] J. Collin, H. Kuusniemi, O. Mezentsev, G. MacGougan, and G. Lachapelle, "HSGPS under heavy signal masking – Accuracy and availability analysis," in *Proc. Nordic Radionavigation Conference*, Dec. 2003.

[4] "Navstar GPS space segment: Navigation user interfaces," IS-GPS-200, Rev. D, Navstar GPS Joint Program Office, El Segundo, CA, USA, Mar. 2006.

[5] "Galileo open service: Signal in space interface control document," GAL OS SIS ICD/D.0, European Space Agency / Galileo Joint Undertaking, Brussels, Belgium, May 2006.

[6] A. Cameron, "100 million strong: Industry eyes LBS tipping point," *GPS World*, vol. 16, no. 5, pp. 38–39, May 2005.

[7] M. W. Thelander, "The 411 on E-911 (LBS, A-GPS, EOTD and TDOA)," Signals Ahead, vol. 2, no. 12, Signals Research Group, Oakland, CA, USA, Jun. 2005.

[8] "Navigation market status 2005," Strategy Analytics, Newton, MA, USA, Oct. 2005.

[9] B. Clark and M. Basso, "Mobile location vendors strive to meet E911 accuracy," T-17-0494, Gartner Inc., Stamford, CT, USA, Jul. 2002.

[10] A. Schmitz-Peiffer, S. Martin, N. Vincent, J. Daigremont, and N. Paul, "Galileo local component for location based services," in *Proc. European Navigation Conference GNSS*, Jun. 2003, paper 315.

[11] J. Swann, E. Chatre, and D. Ludwig, "Galileo: Benefits for location based services," *Journal of Global Positioning Systems*, vol. 1, no. 2, pp. 58–66, Dec. 2003.

[12] F. Pérez-Fontán, B. Sanmartín, A. Steingass, A. Lehner, E. Selva, J Kubista, and B. Arbesser-Rastburg, "Measurements and modeling of the satellite-to-indoor channel for Galileo," in *Proc. European Navigation Conference GNSS*, May 2004, paper 88.

[13] H. Kuusniemi and G. Lachapelle, "GNSS signal reliability testing in urban and indoor environments," in *Proc. ION National Technical Meeting*, Jan. 2004, pp. 210–224.

[14] "Technical specification group radio access network; Stage 2 functional specification of user equipment (UE) positioning in UTRAN," 3GPP TS 25.305, 3rd Generation Partnership Project, Jun. 2005.

[15] "Technical specification group GSM/EDGE radio access network; Location services (LCS); Broadcast network assistance for enhanced observed time difference (E-OTD) and global positioning system (GPS) positioning methods," 3GPP TS 44.035, 3rd Generation Partnership Project, Feb. 2005.

[16] "Position determination service for CDMA2000 spread spectrum systems," 3GPP2 C.S0022-A, 3rd Generation Partnership Project 2, Mar. 2004.

[17] J. La Mance and J. De Solas, "Assisted GPS: A low-infrastructure approach," *GPS World*, vol. 13, no. 3, pp. 46–51, Mar. 2002.

[18] M. Monnerat, R. Couty, N. Vincent, O. Huez, and E. Chatre, "The assisted GNSS, technology and applications," in *Proc. ION GNSS Int. Technical Meeting of the Satellite Division*, Sep. 2004, pp. 2479–2488.

[19] D. Akopian and J. Syrjärinne, "A network aided iterated LS method for GPS positioning and time recovery without navigation message decoding," in *Proc. IEEE Position Location and Navigation Symposium*, Apr. 2002, pp. 77–84.

[20] N. Sirola and J. Syjärinne, "GPS position can be computed without the navigation data," in *Proc. ION GPS Int. Technical Meeting of the Satellite Division*, Sep. 2002, pp. 2741–2744.

[21] N. Agarwal, J. Basch, P. Beckmann, P. Bharti, S. Bloebaum, S. Casadei, A. Chou, P. Enge, W. Fong, N. Hathi, W. Mann, A. Sahai, J. Stone, J. Tsitsiklis, and B. Van Roy, "Algorithms for GPS operation indoors and downtown," *GPS Solutions*, vol. 6, no. 3, pp. 149–160, Dec. 2002.

[22] R. Bryant, "Assisted GPS: Using cellular telephone networks for GPS anywhere," *GPS World*, vol. 16, no. 5, pp. 40–46, May 2005.

[23] M. Moeglein and N. Krasner, "An introduction to SnapTrack server-aided GPS technology," in *Proc. ION GPS Int. Technical Meeting of the Satellite Division*, Sep. 1998, pp. 333–342.

[24] S. Singh, M. E. Cannon, R. Klukas, and G. Cox, "Field test assessment of assisted GPS and high sensitivity GPS receivers under weak/degraded signal conditions," in *Proc. ION GNSS Int. Technical Meeting of the Satellite Division*, Sep. 2005, pp. 2930–2943.

[25] J. Syrjärinne, "Wireless-assisted GPS: Keeping time with mobiles," *GPS World*, vol. 12, no. 1, pp. 22–31, Jan. 2001.

[26] P. Axelrad and R. G. Brown, *Global Positioning System: Theory and Applications*. Washington, DC, USA: American Institute of Aeronautics and Astronautics, 1996, vol. 1, ch. 9: GPS Navigation Algorithms, pp. 409–433.

[27] A. Polydoros and S. Glisic, *Code Division Multiple Access Communications*. Norwell, MA, USA: Kluwer Academic Publishers, 1995, ch. 4: Code Synchronization: A Review of Principles and Techniques, pp. 115–137.

[28] J. G. Proakis, *Digital Communications*, 4th ed. New York, NY, USA: McGraw-Hill, 2001.

[29] J. J. Spilker Jr. and B. W. Parkinson, *Global Positining System: Theory and Applications*. Washington, DC, USA: American Institute of Aeronautics and Astronautics, 1996, vol. 1, ch. 3: GPS Signal Structure and Theoretical Performance, pp. 57–119.

[30] A. J. Van Dierendonk, *Global Positining System: Theory and Applications*. Washington, DC, USA: American Institute of Aeronautics and Astronautics, 1996, vol. 1, ch. 8: GPS Receivers, pp. 329–407.

[31] P. Ward, *Understanding GPS: Principles and Applications*. Norwood, MA, USA: Artech House Publishers, 1996, ch. 5: Satellite Signal Acquisition and Tracking, pp. 119–208.

[32] F. van Diggelen and C. Abraham, "Indoor GPS technology," in *Proc. CTIA Wireless Convention*, May 2001.

[33] H. Mathis, P. Flammant, and A. Thiel, "An analytic way to optimize the detector of a post-correlation FFT acquisition algorithm," in *Proc. ION GPS/GNSS Int. Technical Meeting of the Satellite Division*, Sep. 2003, pp. 689–699.

[34] K. Tanaka, T. Muto, K. Hori, M. Wakamori, K. Teranishi, H. Takahashi, M. Sawada, and M. Ronning, "A high performance GPS solution for mobile use," in *Proc. ION GPS Int. Technical Meeting of the Satellite Division*, Sep. 2002, pp. 1648–1655.

[35] Z. Biacs, G. Marshall, M. Moeglein, and W. Riley, "The Qualcom/SnapTrack wireless-assisted GPS hybrid positioning system and results from initial commercial deployments," in *Proc. ION GPS Int. Technical Meeting of the Satellite Division*, Sep. 2002, pp. 378–384.

[36] C.-W. Park, S. Choi, and J. Yoon, "FFT based high sensitivity indoor GPS receiver technologies using CDMA cellular network," in *Proc. ION GNSS Int. Technical Meeting of the Satellite Division*, Sep. 2004, pp. 428–435.

[37] P. Anderson, G. Whitworth, V. Ashe, and T. Carter, "DSP and GPS combination for mobile communication platforms," in *Proc. ION GNSS Int. Technical Meeting of the Satellite Division*, Sep. 2004, pp. 1006–1012.

[38] A. C. von Ancken, R. D. Williams, and M. H. Salinas, "A coarse/fine search PN code acquisition scheme," *IEEE Transactions on Aerospace and Electronic Systems*, vol. 37, no. 1, pp. 280–285, Jan. 2001.

[39] A. Lakhzouri, E. S. Lohan, and M. Renfors, "Reduced-complexity time-domain correlation for acquisition and tracking of BOC-modulated signals," in *Proc. ESA Workshop on Satellite Navigation User Equipment Technology*, Dec. 2004.

[40] D. Akopian and S. Agaian, "A fast matched filter in time domain," in *Proc. IEEE Position Location and Navigation Symposium*, Apr. 2004, pp. 455–460.

[41] N. F. Krasner, G. Marshall, and W. Riley, "Position determination using hybrid GPS/cellphone ranging," in *Proc. ION GPS Int. Technical Meeting of the Satellite Division*, Sep. 2002, pp. 165–176.

[42] M. O'Donnell, T. Watson, J. Fisher, S. Simpson, G. Brodin, E. Bryant, and D. Walsh, "Galileo performance: GPS interoperability and discriminators for urban and indoor environments," *GPS World*, vol. 14, no. 6, pp. 38–45, Jun. 2003.

[43] F. Dovis, "Innovative hybrid NAV/COM solution for improving accuracy and availability of user positioning," in *Proc. European Navigation Conference GNSS*, Apr. 2003, paper 118.

[44] B. Eissfeller, C. Tiberius, T. Pany, and G. Heinrichs, "Real-time kinematic in the light of GPS modernization and Galileo," *Galileo's World*, pp. 28–34, Autumn 2002.

[45] Y. Feng, "Combined Galileo and GPS: A technical perspective," *Journal of Global Positioning Systems*, vol. 2, no. 1, pp. 67–72, Dec. 2003.

[46] H. Meyr, M. Moeneclaey, and S. A. Fechtel, *Digital Communication Receivers: Synchronization, Channel Estimation, and Signal Processing*. Somerset, NJ, USA: John Wiley and Sons, 1998.

[47] M. H. Zarrabizadeh and E. S. Sousa, "A differentially coherent PN code acquisition receiver for cdma systems," *IEEE Transactions on Communications*, vol. 45, no. 11, pp. 1456–1465, Nov. 1997.

[48] "Navstar space segment: User segment L5 interfaces," ICD-GPS-705, Rev. 3, Navstar GPS Joint Program Office, El Segundo, CA, USA, Sep. 2005.

[49] K. W. Martin, "Complex signal processing is not complex," *IEEE Transactions on Circuits and Systems*, vol. 51, no. 9, pp. 1823–1836, Sep. 2004.

[50] R. B. Langley, "GPS receiver system noise," *GPS World*, vol. 8, no. 6, pp. 40–45, Jun. 1997.

[51] K. J. Quirk and M. Srinivasan, "Analysis of sampling and quantization effects on the performance of PN code tracking loops," in *IEEE Int. Conference on Communications*, vol. 3, May 2002, pp. 1480–1484.

[52] R. Gold, "Maximal recursive sequences with 3-valued recursive cross-correlation functions," *IEEE Transactions on Information Theory*, vol. 14, no. 1, pp. 154–156, Jan. 1968.

[53] E. W. Weisstein, *CRC Concise Encyclopedia of Mathematics*, 2nd ed. Baco Raton, FL, USA: Chapman & Hall/CRC, 2002.

[54] M. Abramowitz and I. A. Stegun, Eds., *Handbook of Mathematical Functions with Formulas, Graphs, and Mathematical Tables*. New York, NY, USA: Dover Publications, 1965.

[55] A. Papoulis and S. U. Pillai, *Probability, Random Variables and Stochastic Processes*, 4th ed. New York, NY, USA: McGraw-Hill, 2002.

[56] M. K. Simon, *Probability Distributions Involving Gaussian Random Variables*. Norwell, MA, USA: Kluwer Academic Publishers, 2002.

[57] W. H. Press, S. A. Teukolsky, V. W. T, and F. B. P, *Numerical Recipies in C++: The Art of Scientific Computing*. Cambridge, UK: Campbridge University Press, 2002.

[58] A. J. Van Dierendonck, P. Fenton, and T. Ford, "Theory and performance of narrow correlator spacing in a GPS receiver," *Navigation: Journal of the ION*, vol. 39, no. 3, pp. 265–283, Fall 1992.

[59] J. J. Spilker Jr. and B. W. Parkinson, *Global Positining System: Theory and Applications*. Washington, DC, USA: American Institute of Aeronautics and Astronautics, 1996, vol. 1, ch. 7: Fundamentals of Signal Tracking Theory, pp. 245–327.

[60] J. W. Betz and K. R. Kolodziejski, "Extended theory of early-late code tracking for a bandlimited GPS receiver," *Navigation: Journal of the ION*, vol. 47, no. 3, pp. 211–226, Fall 2000.

[61] J. K. Holmes, "Code tracking loop performance including the effects of channel filtering and Gaussian interference," in *Proc. IAIN World Congress*, Jun. 2000, pp. 382–398.

[62] P. Fan and M. Darnell, *Sequence Design for Communications Applications*. Somerset, UK: Research Studies Press, 1996.

[63] P. Ward, *Understanding GPS: Principles and Applications*. Norwood, MA, USA: Artech House Publishers, 1996, ch. 4: GPS Satellite Signal Characteristics, pp. 83–117.

[64] E. P. Glennon and A. G. Dempster, "A review of GPS cross-correlation mitigation techniques," in *Proc. GNSS Int. Symposium on GNSS/GPS*, Dec. 2004.

[65] P. G. Mattos, "Solutions to the cross-correlation and oscillator stability problems for indoor C/A code GPS," in *Proc. ION GNSS Int. Technical Meeting of the Satellite Division*, Sep. 2003, pp. 654–659.

[66] G. Heinrichs, A. Schmid, A. Neubauer, G. Rohmer, F. Förster, J. A. Ávila Rodríguez, T. Pany, B. Eissfeller, H. Ehm, and R. Weigel, "HIGAPS: A highly integrated Galileo/GPS chipset for consumer applications," *GPS World*, vol. 15, no. 9, pp. 38–47, Sep. 2004.

[67] D. R. Pauluzzi and N. C. Beaulieu, "A comparison of SNR estimation techniques for the AWGN channel," *IEEE Transactions on Communications*, vol. 48, no. 10, pp. 1681–1691, Oct. 2000.

[68] M. K. Simon and S. Dolinar, "Improving SNR estimation for autonomous receivers," *IEEE Transactions on Communications*, vol. 53, no. 6, pp. 1063–1073, Jun. 2005.

[69] P. D. Groves, "GPS signal to noise measurement in weak signal and high interference environments," in *Proc. ION GNSS Int. Technical Meeting of the Satellite Division*, Sep. 2005, pp. 643–658.

[70] E. Serpedin, A. Chevreuil, G. B. Giannakis, and P. Loubaton, "Blind channel and carrier frequency offset estimation using periodic modulation precoders," *IEEE Transactions on Signal Processing*, vol. 48, no. 8, pp. 2389–2405, Aug. 2000.

[71] Y. Wang, E. Serpedin, and P. Ciblat, "Optimal blind nonlinear least-squares carrier phase and frequency offset estimation for general QAM modulations," *IEEE Transactions on Wireless Communications*, vol. 2, no. 5, pp. 1040–1054, Sep. 2003.

[72] U. Tureli, P. J. Honan, and H. Liu, "Low-complexity nonlinear least squares carrier offset estimator for OFDM: Identifiability, diversity and performance," *IEEE Transactions on Signal Processing*, vol. 52, no. 9, pp. 2441–2452, Sep. 2004.

[73] P. Ciblat and L. Vandendrope, "Blind carrier frequency offset estimation for noncircular constellation-based transmissions," *IEEE Transactions on Signal Processing*, vol. 51, no. 5, pp. 1378–1389, May 2003.

[74] W. Gander and W. Gautschi, "Adaptive quadrature - revisited," *BIT Numerical Mathematics*, vol. 40, no. 1, pp. 84–101, Mar. 2000.

[75] T. S. Rappaport, *Wireless Communications - Principles and Practice*. Upper Saddle River, NJ, USA: Prentice Hall, 1996.

[76] A. Steingass and A. Lehner, "Measuring the navigation multipath channel - A statistical analysis," in *Proc. ION GNSS Int. Technical Meeting of the Satellite Division*, Sep. 2004, pp. 1157–1164.

[77] A. Jahn, S. Buonomo, S. M, and L. E, "Narrow- and wide-band channel characterization for land mobile satellite systems: Experimental results at L-band," in *Proc. Int. Mobile Satellite Conference*, Jun. 1995, pp. 115–121.

[78] A. Lehner and A. Steingass, "A novel channel model for land mobile satellite navigation," in *Proc. ION GNSS Int. Technical Meeting of the Satellite Division*, Sep. 2005, pp. 2132–2138.

[79] R. Ercek, P. De Doncker, and F. Grenez, "Study of pseudo-range error due to non-line-of-sight-multipath in urban canyons," in *Proc. ION GNSS Int. Technical Meeting of the Satellite Division*, Sep. 2005, pp. 1083–1094.

[80] K. K. Talukdar and W. D. Lawing, "Estimation of the parameters of the Rice distribution," *Journal of the Accoustical Society of America*, vol. 89, no. 3, pp. 1193–1197, Mar. 1991.

[81] L. J. Greenstein, M. D. G, and V. Erceg, "Moment-method estimation of the Ricean K-factor," *IEEE Communications Letters*, vol. 6, no. 3, pp. 175–176, Jun. 1999.

[82] C. Tepedelenlioglu, A. Abdi, and G. B. Giannakis, "The Ricean K factor: Estimation and performance analysis," *IEEE Transactions on Wireless Communications*, vol. 2, no. 4, pp. 799–819, Jul. 2003.

Publications

[1] A. Schmid and A. Neubauer, "Comaprison of the sensitivity limits for GPS and Galileo receivers in multipath scenarios," in *Proc. IEEE Position Location and Navigation Symposium*, Apr. 2004, pp. 503–509.

[2] A. Schmid and A. Neubauer, "Theoretical minimal bounds for single shot measurement thresholds of the Galileo and GPS open signals in multipath fading environments," in *Proc. European Navigation Conference GNSS*, May 2004, paper 20.

[3] G. Heinrichs, N. Lemke, A. Schmid, A. Neubauer, R. Kronberger, G. Rohmer, F. Förster, T. Pany, J. A. Ávila Rodríguez, B. Eissfeller, H. Ehm, and R. Weigel, "HIGAPS - A large-scale integrated combined Galileo/GPS chipset for the consumer market," in *Proc. European Navigation Conference GNSS*, May 2004, paper 52.

[4] A. Schmid and A. Neubauer, "Signal estimation technique for enhanced sensitivity navigation receivers," in *Proc. European Radio Navigation Systems and Services*, June 2004.

[5] A. Schmid and A. Neubauer, "Evaluation of Galileo BOC modulation versus GPS BPSK modulation in multipath propagation scenarios," in *Proc. European Radio Navigation Systems and Services*, June 2004.

[6] G. Heinrichs, N. Lemke, A. Schmid, A. Neubauer, R. Kronberger, G. Rohmer, F. Förster, J. A. Ávila Rodríguez, T. Pany, B. Eissfeller, H. Ehm, and R. Weigel, "Galileo/GPS receiver architecture for high sensitivity acquisition," in *Proc. Int. Symposium on Signals Systems and Electronics*, Aug. 2004.

[7] A. Schmid and A. Neubauer, "Performance evaluation of differential correlation for single shot measurement positioning," in *Proc. ION GNSS Int. Technical Meeting of the Satellite Division*, Sept. 2004, pp. 1998–2009.

[8] A. Schmid and A. Neubauer, "Channel estimation technique for positioning accuracy improvement in multipath propagation scenarios," in *Proc. ION GNSS Int. Technical Meeting of the Satellite Division*, Sept. 2004, pp. 1195–1202.

[9] A. Schmid, A. Neubauer, H. Ehm, R. Weigel, N. Lemke, G. Heinrichs, J. A. Ávila Rodríguez, R. Kanituh, T. Pany, B. Eissfeller, G. Rohmer, B. Niemann, and M. Overbeck, "Enabling location based services with a combined Galileo/GPS receiver architecture," in *Proc. ION GNSS Int. Technical Meeting of the Satellite Division*, Sept. 2004, pp. 1468–1479.

[10] G. Heinrichs, A. Schmid, A. Neubauer, G. Rohmer, F. Förster, J. A. Ávila Rodríguez, T. Pany, B. Eissfeller, H. Ehm, and R. Weigel, "HIGAPS: A highly integrated Galileo/GPS chipset for consumer applications," *GPS World*, vol. 15, no. 9, pp. 38–47, Sept. 2004.

[11] A. Schmid, A. Neubauer, H. Ehm, R. Weigel, G. Heinrichs, N. Lemke, J. Winkel, J. A. Ávila Rodríguez, T. Pany, G. Rohmer, and P. Nagel, "A combined Galileo/GPS receiver architecture for consumer market applications," in *Proc. ESA Satellite Navigation User Equipment Technology*, Dec. 2004.

[12] A. Schmid, C. Günther, and A. Neubauer, "Rice factor estimation for GNSS reception sensitivity improvement in multipath fading environments," in *Proc. Workshop on Positioning, Navigation, and Communication*, Mar. 2005, pp. 93–98.

[13] A. Schmid and A. Neubauer, "Differential correlation for Galileo/GPS receivers," in *Proc. IEEE Int. Conference on Acoustics Speech and Signal Processing*, vol. 3, Mar. 2005, pp. 953–956.

[14] H. Ehm, R. Weigel, A. Schmid, A. Neubauer, N. Lemke, G. Heinrichs, J. Winkel, R. Kaniuth, J. A. Ávila Rodríguez, T. Pany, and B. Eissfeller, "HIGAPS - A highly integrated receiver architecture with enhanced sensitivity for combined Galileo/GPS reception," in *Proc. Int. Conference on Integrated Navigation Systems*, May 2005.

[15] A. Schmid and A. Neubauer, "Carrier to noise power estimation for enhanced sensitivity Galileo/GPS receivers," in *Proc. IEEE Vehicular Technology Conference*, May 2005.

[16] A. Schmid, C. Günther, and A. Neubauer, "Frequency offset estimation for Galileo/GPS receivers based on differential correlation," in *Proc. IEEE Statistical Signal Processing*, July 2005.

[17] A. Schmid, A. Neubauer, H. Ehm, R. Weigel, G. Heinrichs, N. Lemke, J. Winkel, J. A. Ávila Rodríguez, R. Kaniuth, T. Pany, B. Eissfeller, G. Rohmer, and M. Overbeck, "Combined Galileo/GPS architecture for enhanced sensitivity reception," *AEÜ Int. Journal of Electronics and Communications*, vol. 59, no. 5, pp. 297–306, July 2005.

[18] H. Ehm, A. Schmid, A. Neubauer, C. Günther, and R. Weigel, "A simulation model for Galileo/GPS receivers including the RF front-end," in *Proc. European Navigation Conference GNSS*, July 2005, paper 402.

[19] R. Kaniuth, B. Eissfeller, N. Lemke, G. Heinrichs, H. Ehm, R. Weigel, A. Schmid, A. Neubauer, and P. Nagel, "Single shot positioning with the HIGAPS receiver," in *Proc. European Navigation Conference GNSS*, July 2005, paper 547.

[20] A. Schmid, C. Günther, and A. Neubauer, "Adaptive phase correction loop for enhanced acquisition sensitivity," in *Proc. ION GNSS Int. Technical Meeting of the Satellite Division*, Sept. 2005, pp. 168–177.

[21] A. Schmid, A. Neubauer, H. Ehm, R. Weigel, and C. Günther, "Galileo/GPS receiver fixed-point implementation using conventional and differential correlation," in *Proc. ION GNSS Int. Technical Meeting of the Satellite Division*, Sept. 2005, pp. 1945–1956.

[22] R. Kaniuth, B. Eissfeller, N. Lemke, G. Heinrichs, H. Ehm, R. Weigel, A. Schmid, A. Neubauer, and P. Nagel, "A snap-shot positioning approach for a high integrated GPS/Galileo chipset," in *Proc. ION GNSS Int. Technical Meeting of the Satellite Division*, Sept. 2005, pp. 1153–1159.

[23] A. Schmid, C. Günther, and A. Neubauer, "Adaptive frequency correction method for enhanced sensitivity CDMA acquisition," in *Proc. IEEE Global Telecommunications*, Nov. 2005.